Structural Effects on the Kinetics and Thermodynamics of Making and Breaking O–O Bonds

Dylan Meamber Rogers

A dissertation

submitted in partial fulfillment of the

requirements for the degree of

Doctor of Philosophy

University of Washington

2023

Reading Committee:

Julia A. Kovacs, Chair

Brandi Cossairt

Dianne Xiao

Program Authorized to Offer Degree:

Chemistry

University of Washington

Abstract

Structural Effects on the Kinetics and Thermodynamics of Making and Breaking O–O Bonds

Dylan Meamber Rogers

Chair of the Supervisory Committee:
Prof. Julia Kovacs
Chemistry

Nature has developed enzymes over millennia that perform difficult chemical transformations in mild conditions, using structural controls to aid in the generation of powerful reactive intermediates. Metalloenzymes such as cysteine dioxygenase (CDO) and isopenicillin N synthase (IPNS) use thiolate ligands coordinated to their metal centers to bind dioxygen and produce strong oxidants in the form of Fe^{III}-superoxo and and high-valent Fe-oxo species. The similar active sites of CDO and IPNS afford different chemistry due to small variations in their ligands stabilizing different intermediates. Similarly, nitrile hydratase (NHase) uses dioxygen to modify the thiolates in its coordination sphere to allow for the binding of nitriles and their transformations to amides. Dioxygen is produced by the oxygen-evolving complex (OEC) via the process of water splitting, a thermodynamically difficult process that Nature accomplishes via a cubane cluster of manganese and calcium atoms. This cluster separates that process into

thermodynamically simpler steps which allow for the generation of dioxygen using the energy from light.

To examine the factors that allow for the broadly different reactivity performed by CDO, IPNS, and NHase, a structurally constrained iron complex $[Fe^{III}(S_2{}^{Me2}N_3(Et,Pr)]^+$ is produced and its interactions with oxo-atom donors to produce a sulfenate species is characterized and compared to the less constrained complex $[Fe^{III}(S_2{}^{Me2}N_3(Pr,Pr)]^+$. At low temperatures, an oxo-atom donor adduct species is observed before formation of that sulfenate, and inhibition studies imply the existence of an intermediate Fe^V-oxo. This species is investigated via computational methods, and it is found that the constrained ligand produces a less stable oxo species.

The reduced complex $Fe^{II}(S_2{}^{Me2}N_3(Et,Pr)$ and its reactivity with dioxygen are also characterized kinetically and thermodynamically by stopped-flow UV/visible spectroscopy, finding evidence that an Fe^{III}-superoxo is formed. Compared to $Fe^{II}(S_2{}^{Me2}N_3(Pr,Pr)$, the superoxo is formed much more quickly and much more favorably. This superoxo species is transient and further reacts with either the solvent or itself, although the product species could not be characterized. Reactivity with oxygen in the presence of an excess of weak C–H bonds or with deuterated solvent was not found to change the rate of this species' decay, indicating that the process occurring could be an intramolecular process. Computational studies support the possibility of a intramolecular process.

The influence of a *cis* or *trans* thiolate is examined via the generation of the asymmetric mixed alkoxide/thiolate complexes $Fe^{II}(S^{Me2}O^{Me2}N_3(Pr,Pr))$ and $[Fe^{III}(S^{Me2}O^{Me2}N_3(Pr,Pr))]^+$ were synthesized, and their reactivity with oxo-atom donors and dioxygen was examined. Similar to the bis-thiolate complexes, intermediates were observed with oxo-atom donor and oxygen reactivity, but products could not be isolated. The preference for binding a substrate *cis* or *trans* to a thiolate

was studied through computational methods, finding structural evidence that *trans* binding is preferred and predicted spectral evidence that *cis* binding is preferred.

Factors influencing the structural flexibility of the OEC were examined using a series of model cubane complexes with varying ligand environments. By modifying the exogenous ligands of the cubane in small ways, dramatic changes are observed in the structural parameters of the cubane as a whole, demonstrating a potential way the OEC controls its structural arrangement during the process of water oxidation.

Acknowledgements

I have so much to be thankful for, and so many people to thank for helping me complete this journey I've been on. Foremost, I need to give my deepest thanks to my research advisor Prof. Julie Kovacs, there were many times where I felt stuck or needed help to figure out what was going with my reactions, and my conversations with her were always invaluable for turning that corner and making a breakthrough. It's in large part thanks to her that I've grown so much as a scientist, and her passion for her chemistry helped to keep me going when I could not keep myself going. I also know I need to thank her for her patience with me, thank you for pushing me every day to be a better scientist.

I also need to thank the members of the Kovacs group that I worked with and who helped me learn and understand better in our every conversation. Thanks to Dr. Ben Leipzig, Dr. Maike Lundahl, Dr. Maksym Dedushko, Dr. Penny Poon, Dr. Alexandra Downing, Dr. Maria Greiner, Erin Hanada, Julian Smith-Jones, Paige Gannon, Bennet Karel, Tony Vazquez, Chris Woodburn, Chris Lowe, and Douglas Baumgardner, your support and friendship during my graduate career was a huge part of what kept me going. I'll miss the Excited State Café, even if the coffee we made in lab was never really any good, sitting down and talking about the experiments we were up to always was.

The entire Department of Chemistry at the University of Washington has been crucial to my success here, the support from the Inorganic Division especially. While I always dreaded having to prepare to give a Division Meeting talk, the feedback I received every time made the whole process worth it. I know several breakthroughs I made in my research were the direct result of a good question someone asked me after a presentation or in the hall a few days later. Speaking of the hall, the entire third floor of the Chemistry Building has been such a fantastic community,

it's been fantastic knowing that if I don't understand something an expert is just a few doors away and they're always happy to help answer whatever silly question I have. Thanks especially to the Velian, Cossairt, and Xiao groups and the students therein, I'm so appreciative of the openness and collaborative nature of the department and the friends I've made because of it. Thanks to my committee: Profs. Julie Kovacs, Brandi Cossairt, Dianne Xiao, Stefan Stoll, and Ed Lazowska for shepherding me through this process and helping me all along the way, also to the professors of the department and to all of the professors I worked with or learned from, both at the University of Washington and in my undergrad career at Northwestern University. Especially to Prof. Danna Freedman, thank you for taking a chance on a second year undergrad and starting my career in chemistry!

My friends have been such incredible support through my time in graduate school, and I want to thank them profusely for all that they've done for me. Thanks to Jon Kephart and Ben Mitchell especially, it's been the best going through graduate school with you both, and I'm first of all so appreciative of how you've helped me learn and grow, and secondly I'm so proud of you both for the people you are the work you're doing, you're both stars! Thanks to my friends outside of graduate school as well, I'm very lucky in that you're too numerous to name, if you're reading this you certainly made a difference in my life and I don't think I'll ever be able to truly express how grateful I am that you're in my life. Whether it's trivia or climbing or friends from undergrad or high school, I'm thankful for your friendships and I'm looking forward to the adventures to come.

Thank you so much to my family, who have been there for me since the beginning of my life. Thank you, Mom and Dad, I wouldn't be the person I am today if not for you both and thank you for always believing in me and pushing me and giving me the opportunities I've had. Thanks

to Blake and Kyle for believing in me and being there for me, and for letting me compete with you when we were growing up together, you two are also a large part of why I'm happy with the person I've become today. I love you all, and thanks for helping me become who I am!

As I've been writing this dissertation my cat Gumshoe has been scampering around the room and lying next to me and meowing a whole lot at me, I'm writing down for posterity that yes as soon as I'm done writing this he's getting treats and cuddles. Gumbo, once you learn how to read you can see why I haven't had as much time as you want me to have to play with you, I've been hard at work! He's the best, I love that guy.

If you're reading this, I need to thank you most of all. I hope you enjoy it!

List of Figures

List of Tables

List of Schemes

List of Numbered Complexes

1	$Fe^{II}(S_2{}^{Me2}N_3(Pr,Pr))$
2	$[Fe^{III}(S_2{}^{Me2}N_3(Pr,Pr))]^+$
2-PNO	$[Fe^{III}(S_2{}^{Me2}N_3(Pr,Pr))(PNO)]^+$
2-superoxo	$[Fe^{III}(S_2{}^{Me2}N_3(Pr,Pr))(O_2)]$
2-hydroperoxo	$[Fe^{III}(S_2{}^{Me2}N_3(Pr,Pr))(OOH)]$
3	$[Fe^{III}(S_2{}^{Me2}N_3(Et,Pr))]^+$
3-PNO	$[Fe^{III}(S_2{}^{Me2}N_3(Et,Pr))(PNO)]^+$
3-superoxo	$[Fe^{III}(S_2{}^{Me2}N_3(Et,Pr))(O_2)]$
3-hydroperoxo	$[Fe^{III}(S_2{}^{Me2}N_3(Et,Pr))(OOH)]$
4	$[Fe^{III}(S_2{}^{Me2}N_3(Et,Pr)\text{-}S^{pers}]PF_6$
5	$[Fe^{III}(\eta^2\text{-}S^{Me2}O)(S^{Me2}N_3(Pr,Pr)](PF_6)$
6	$[Fe^{III}(\eta^2\text{-}S^{Me2}O)(S^{Me2}N_3(Et,Pr)](PF_6)$
7	$[Fe^{III}(\eta^2\text{-}S^{Me2}S)(S^{Me2}N_3(Pr,Pr)](PF_6)$
8	$Fe^{II}(S_2{}^{Me2}N_3(Et,Pr))$
9	$Fe^{II}(S^{Me2},O^{Me2}N_2NH(Pr,Pr))$
10	$[Fe^{III}(S^{Me2},O^{Me2}N_2NH(Pr,Pr))](PF_6)$
11	Mn(hydroxyphenyldiimine)(Cl)
12	$[(en)NaMn_3O_4(L_3)(OH)]$
13	$[(en)NaMn_3O_4(L_3)(OMe)]$
14	$[(py)NaMn_3O_4(L_3)(OH)]$

Glossary

δ	isomer shift
Å	Ångström
ACV	δ-(l-α-aminoadipyl)-l-cysteinyl-d-valine
Ag	silver
amu	atomic mass unit
$^{Asp}O^-$	aspartic acid
ATR	attenuated total reflectance
AZADOL	2-hydroxy-2-azaadamantane
Ba	barium
BDE	bond dissociation energy
bpy	2,2'-bipyridine
°C	degree Celsius
Ca	calcium
CDO	cysteine dioxygenase
CHD	1,4-cyclohexadiene
cm^{-1}	wavenumber
Co	cobalt
CO_2	carbon dioxide
CT	charge transfer
CV	cyclic voltammetry
$^{Cys}S^-$	cysteine
D	deuterium
Da	dalton
DCM	dichloromethane
DFT	density functional theory
DHA	9,10-dihydroanthracene
EAS	electron absorbance spectroscopy
E_a	activation energy
en	ethylenediamine

eV	electronvolt
EPR	electron paramagnetic resonance
ESI-MS	electrospray-ionization mass spectroscopy
Et_2O	diethyl ether
EtOH	ethanol
EXAFS	extended X-ray absorption fine structure
ε	extinction coefficient
Fe	iron
FT	Fourier transform
G	gauss
ΔG	Gibbs free energy
GHz	gigahertz
$GluO^-$	Glutamic acid
H	hydrogen
Δ*H*	enthalpy
$\Delta H^{\ddagger}$	enthalpy of activation
H_2O	water
H_2O_2	hydrogen peroxidej
HAT	hydrogen atom transfer
^{His}N	histidine
HS	high-spin
HOMO	highest occupied molecular orbital
Hz	Hertz
$IArF_5$	pentafluoroiodobenzene
IBX-ester	isopropyl 2-iodoxybenzoate
IPNS	isopenicillin N synthase
J	coupling constant
K	Kelvin
KO_2	potassium superoxide
L	liter
LS	low-spin

LUMO	lowest occupied molecular orbital
MeCN	acetonitrile
MeOH	methanol
MHz	megahertz
Mn	manganese
N_3^-	azide anion
NHase	nitrile hydratase
nm	nanometer
NMR	nuclear magnetic resonance
NTO	natural transition orbital
NO	Nitric oxide
$O^{\bullet}$	oxyl radical
$O_2^{\bullet-}$	superoxide anion
OEC	oxygen-evolving complex
OIAr	oxo atom donor
OH^-	hydroxide
OMe^-	methoxide
OTf^-	trifluoromethanesulfonate
ORTEP	Oak Ridge Thermal-Ellipsoid Program
PDB	protein data bank
PFIB	pentafluoroiodosylbenzene
PhI	iodobenzene
PhIO	iodosylbenzene
pK_a	acid dissociation constant
PNO	pyridine-N-oxide
ppm	parts per million
PPh_3	triphenylphosphine
PSII	photosystem II
Ru	ruthenium
QM/MM	quantum mechanics/molecular moduling
rRaman	resonance Raman

ΔS	entropy
$\Delta S^{\ddagger}$	entropy of activation
SCE	saturated calomel electrode
Sr	strontium
TD-DFT	time-dependent density functional theory
TFA	trifluoroacetic acid
THF	tetrahydrofuran
TMC	1,4,8,11-tetramethyl-1,4,-8,11-tetraaza cyclotetradecane
TMS	tetramethylsilane
tren	tris(2-aminoethyl)amine
UV/Vis	UV-visible
V	volt
XAS	X-ray absorption spectroscopy
XFEL	X-ray free electron laser
XRD	X-ray diffraction
μ_B	Bohr magneton
μ_{eff}	magnetic moment
σ^2_{oct}	octahedral angle variance
τ	five-coordinate geometry index
χ_T	magnetic susceptibility

Chapter 1. Making and Breaking Oxygen-Oxygen Bonds in Nature

1.1. Bioinorganic Chemistry

Nature has developed enzymes over the course of billions of years to perform complex chemical syntheses to sustain life.[1] These transformations are of interest for industrial applications as widely varying as waste remediation to pharmaceutical synthesis as well as developing a better understanding of biochemical processes in our own bodies so that more effective therapies can be created. Enzymes usually require narrow ranges of pH and temperature to properly function, which limits their direct usefulness for industrial applications. Additionally, enzymes typically have very high selectivity for specific substrates due to a variety of inherent physical or electronic structures, further limiting the usefulness of individual enzymes for performing chemistry on broad classes of molecules.[2]

Metalloenzymes as a class are of great interest due to their wide range of functionalities, ranging from cellular replication, dioxygen (O_2) transport, water oxidation and photosynthesis, to the biosynthesis of neurotransmitters.[3,4] The reactivity of each metalloenzyme is determined by the unique environment of the metal within the metalloenzyme, including the primary and secondary coordination spheres around the active site and the surrounding protein scaffold and its water channels.[5] By studying the function of these enzymes, we can elucidate how the metal ion's environment modulates its reactivity and use that knowledge to develop better catalysts for industrial applications and therapeutics. However, studying these enzymes *in vivo* has severe limitations due to the temperature, and pH range limitations of enzymes, as well as their large size, complexity, solubility restrictions, and the short lifetimes of most reactive intermediates.

Using synthetic biomimetic models offers an aid to better study protein mechanisms. By designing small molecule models that mimic the proteins' active sites, these synthetic complexes

can be very useful tools to investigate the reactions catalyzed by the enzymes as part of their biological system. These models have the capacity to mimic the coordination environment of the active site and through a variety of synthetic means can be tuned to observe reactive intermediates within the fundamental steps in the metalloenzyme's reactivity. The knowledge gained from the study of these biomimetic model complexes provides insight into biochemical pathways and can inspire the design of efficient, robust, and earth-abundant catalysts, as well as assist the rational design of engineered enzymes.[6]

1.2. Breaking O-O Bonds in Nature

Many of the most important chemical transformations for life involve the use of dioxygen as a convenient source for oxidizing a metal center, for the modulation of the electronic structure of an associated metal, or for the incorporation and use of oxygen atoms in essential molecules of biological systems. There are many enzymes which have been tuned by Nature over millennia to effectively bind and use dioxygen. Several motifs occur repeatedly in these enzymes, with the most common being the heme environment; a porphyrin ring coordinating a metal (typically an iron or cobalt atom) over which electron density can be spread.[7] This porphyrin ring is analogous to four planar coordinated and linked histidine residues, with two open sites.[7,8] In many systems, a fifth coordination site is ligated with a cysteine to increase the reactivity and allow for the cleavage of

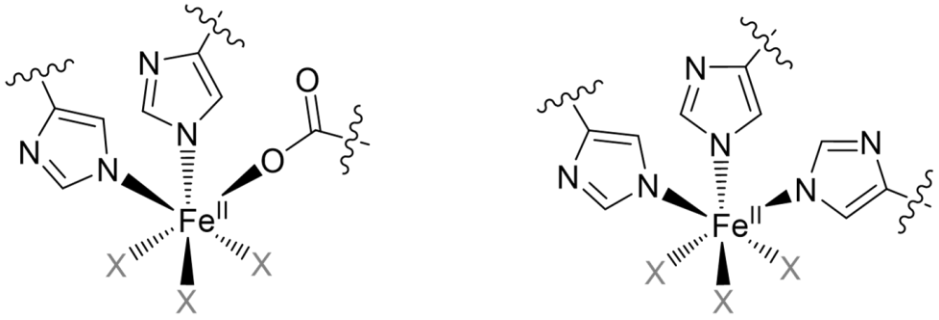

Figure 1-1. Diagrams of 2-His-1-carboxylate facial triad (left) and three histidine triad (right).

strong C-H bonds in hydrocarbons (as in the P450 family of enzymes). The non-heme environmental motif typically contains histidines, carboxylates (as aspartic acid), and occasionally cysteine in a 2-His-1-carboxylate facial triad pocket, although there are several examples with a three histidine triad (**Figure 1-1**).[9–11]

Dioxygen activation in Nature frequently involves a monomeric or a dimeric iron center, which activate oxygen in similar ways.[12–16] A general scheme for the activation of dioxygen by a single Fe^{II} center involves the Fe^{II} center first binding dioxygen and undergoing a one electron oxidation to form an Fe^{III}-superoxo (Fe^{III}-$O_2^{\bullet}$). This binding involves the formally spin-forbidden process of changing triplet dioxygen to singlet dioxygen, which requires the presence of a metal in order to transfer an electron at ambient conditions.[17,18] This Fe^{III}-superoxo can act to abstract a hydrogen atom from a nearby substrate or act as a powerful oxidant. When it performs H-atom abstraction (HAT), it becomes an Fe^{III}-hydroperoxo with a weaker and more activated O-O bond which can undergo homolytic or heterolytic cleavage to form an Fe^{IV}- or Fe^{V}-oxo, respectively. Both of those high-valent iron oxo species have been shown to be competent oxidants, and they can also both perform a second HAT reaction to form an Fe^{III}-hydroxide (**Scheme 1-1**).[19–22] The iron oxo can also be trapped by a neighboring thiolate ligand to oxygenate a sulfur, and the structure of the enzyme in question has major influence on the specific processes that occur.

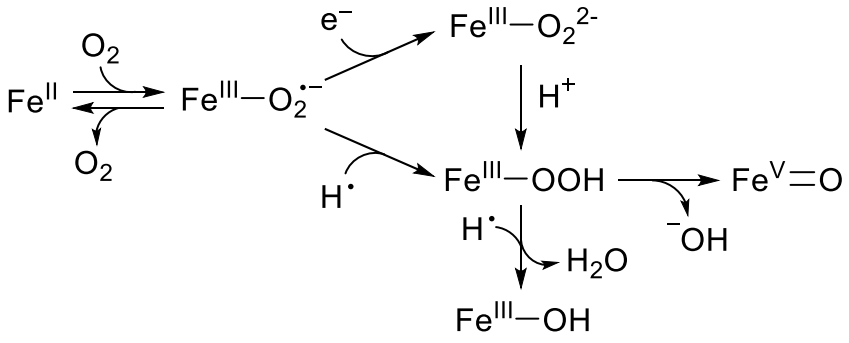

Scheme 1-1. General scheme for the activation of dioxygen by Fe^{II} and the resulting oxidative products.

Understanding how varied enzymatic systems use oxygen as a tool to accomplish their difficult chemical transformations can help us to discover new and more efficient pathways to generate important moelecules. There are a few major families of non-heme oxygen-interacting enzymes, those being monooxygenases, dioxygenases, and biosynthetic oxidases.[11] The dioxygenase family comprises many enzymes which add two oxygen atoms, both from dioxygen, to their substrate. The extradiol dioxygenases bind a catecholic substrate and oxygen in adjacent sites, which allows the dioxygen to directly transfer an electron to the substrate via the iron, creating two radicals which can recombine to form an Fe^{II}-bound alkylperoxo intermediate.[23–25] The substrates undergo a rearrangement to form a lactone with concomitant heterolytic O-O bond cleavage, and a further ring opening via hydrolysis of this lactone by the remaining oxygen atom derived from O_2. Throughout this process, the iron center is not itself oxidized or reduced, remaining as a ferrous center for the duration of the catalytic cycle.[26,27] The Rieske *cis*-diol-forming dioxygenases act similarly, directly adding both atoms of dioxygen to adjacent carbons of an unactivated aromatic ring. This requires O_2 to be activated to a more powerful form in order to successfully attack the aromatic ring. These dioxygenases perform this with a mononuclear iron which binds the substrate and dioxygen coupled with a 2Fe-2S cluster subunit which stores an additional electron for the reaction.[28] They are proposed to perform this transformation via formation of first an Fe^{III}-hydroperoxo and then an Fe^{v}-oxo-hydroxo which then transfers those oxygen atoms to the aromatic substrate. At the end of the cycle, both the mononuclear iron center and the 2Fe-2S cluster are oxidized by one electron each.[29,30] Dioxygenases also are used to add oxygen atoms to aliphatic substrates using 2-oxo acid as a cosubstrate.[31] There, a single Fe^{II} center coordinates both the 2-oxo acid cosubstrate and dioxygen, forming an Fe^{III}-superoxo which attacks the cosubstrate and performs homolytic bond cleavage to then afford an Fe^{IV}-oxo species. This

high valent oxo abstracts a hydrogen atom from the substrate to create an Fe^{III}-hydroxo species which rebounds to restore the resting enzyme and add the second atom from dioxygen to the substrate.[32,33]

The monooxygenases act similarly, adding only one of the two atoms in dioxygen to the substrate and the other to a cofactor. Like the 2-oxo acid dioxygenases, dioxygen is activated by an Fe^{II} center, but unlike the dioxygenases, an Fe^{II}-superoxo is only transiently formed on the way to a peroxo-bridged Fe^{II}-O-O-cofactor species.[34] This undergoes heterolytic O-O bond cleavage to produce an Fe^{IV}-oxo that does electrophilic aromatic substitution on the substrate to produce its product.[35] The oxidase family also uses dioxygen in a variety of ways, but similar to the strategies previously discussed. Dioxygen is bound and activated by the iron center, whereupon it can produce a high-valent iron oxo species which can do a second part of a reaction and form an oxidized product. Unlike oxygenases, no atoms from dioxygen are incorporated in final products, rather, dioxygen is only used as a source of oxidizing equivalents to produce highly potent reactive intermediates. These enzymes complete their wide variety of reactivity using the same general materials and the same general coordination environments (2-His-1-carboxylate), which indicates the major role that steric and electronic effects play in modulating the reactivity that occurs, and how a deep understanding of how each factor influences the final product is required to be able to apply these to artificial systems.[36,37]

Of the wide variety of oxygen-activating iron enzymes, those that bind and activate O_2 in a cysteine thiolate-coordinate non-heme environment such as nitrile hydratase (NHase), cysteine dioxygenase (CDO), and isopenicillin N synthase (IPNS) are of particular interest for study. Both CDO and IPNS catalyze the O_2-promoted oxidation of cysteinates (RS^-), reactions which are thermodynamically favored but kinetically slow in the absence of a transition metal catalyst, due

to the process being spin-forbidden.[38] Both enzymes are proposed to bind O_2 to afford highly reactive ferric-superoxo intermediates, which can be used to form β-lactam rings as in IPNS[39] or to oxidize cysteine to cysteine sulfenic acid as in CDO.[40–42] Nitrile hydratase is also notable due to its post-translational modification of its cysteine residues to form sulfenic and sulfinic acids which are necessary for it to catalyze the transformation of nitriles to their corresponding amides.[12]

1.3. Nitrile Hydratase

1.3.1. Background

Nitrile hydratase is somewhat of an outlier in non-heme iron thiolate enzymes in that it does not use dioxygen in its catalytic cycle, rather using it to alter the characteristics of cysteine residues bound to the active site in order to accomplish its reactivity. Nitrile hydratases contain either Fe^{III} or Co^{III} centers and they catalyze the stereoselective hydration of nitriles to amides, an industrially useful function which transforms what may otherwise be a waste product into important chemical precursors like acrylamide, which is itself used to make a variety of polymers useful to industry.[43,44] Performing this process enzymatically is cheaper and more selective than using a copper-catalyzed hydrolysis method, and allows the process to be performed at ambient conditions.[45] Nitrile hydratases also find use in wastewater treatment, converting toxic and very common chemicals such as acetonitrile, acrylonitrile, and benzonitrile which are often found in industrial waste streams to their corresponding amides, which can be further decomposed to less harmful carboxylic acids.[43,46]

1.3.2. Structure of Nitrile Hydratase

The nitrile hydratase enzyme's active site is composed of three cysteine residues, one serine residue (all from the α subunit of the enzyme), and two arginine residues (from the β subunit of the enzyme), with the three cysteines and two main chain amide nitrogen atoms bound to a central Fe^{III} or Co^{III} atom (**Figure 1-2**).[47] A sixth coordination site is occupied by a nitric oxide molecule in the inactive state, which can be photolyzed away and replaced with a suitable substrate. This binding motif is ubiquitous in NHases,[48,49] and is post-translationally modified to contain a cysteine-sulfinic acid (-SO_2H) and cysteine-sulfenic acid (-SOH), remaining inactive unless these oxygens are incorporated.[50–52] The process of oxidizing these cysteine residues occurs quickly and only once per enzyme *in vivo*, precluding direct study of the enzyme. A recent EPR and mass spectrometry study on an Fe peptide fragment has indicated that it proceeds by first oxidizing a high-spin Fe^{II} center with dioxygen, which matures through singly-, doubly- and then triply-oxidized peptides until a low-spin Fe^{III} center is formed.[53] Oxidizing the complex further leads to loss of function,[54,55] indicating that the cysteine-sulfenic acid is involved in the catalytic cycle and does more than modulate the electronic structure of the metal center.[56,57]

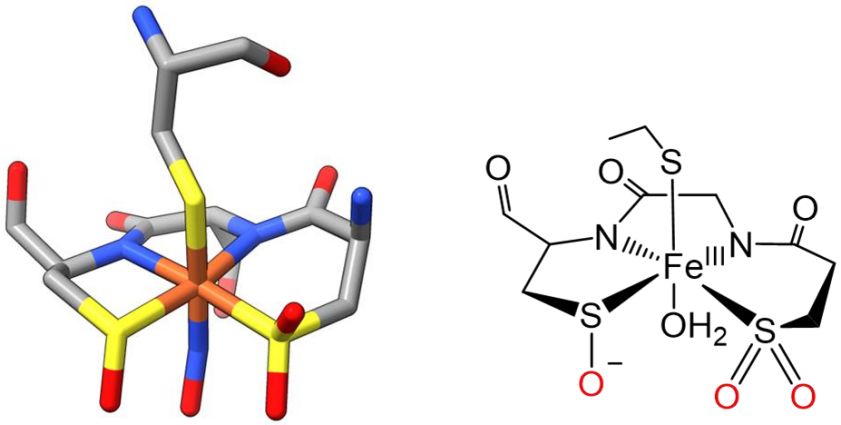

Figure 1-2. Depictions of the post-translationally modified active site of nitrile hydratase. Left: Crystallographic structure of NO-bound NHase (PDB ID: 2AHJ).[187] Left: schematic drawing of water-bound NHase.

1.3.3. Mechanism of Nitrile Hydratase

The proposed mechanisms for NHase enzymes use the cysteine-sulfenic acid moiety to nucleophilically attack a bound nitrile substrate in order to form a five-membered ring structure (**Scheme 1-2**).[57,58] In one mechanism, a nitrile exchanges for the water bound to the sixth coordination site of the metal center. It is then nucleophilically attacked by the nearby cysteine-sulfenic acid to afford a five-membered imidate ring.[59] The sulfenic acid sulfur is then attacked by the unmodified cysteine thiolate to form a disulfide bond, concomitantly breaking the S-O bond and opening the ring. The imidic acid formed by this isomerizes to an amide through a series of proton transfers,[60] and can be released by the enzyme to bind a new substrate. The newly-formed disulfide is attacked by water to regenerate the active catalyst.[57] The disulfide switch that is invoked in this mechanism is not supported by much experimental evidence, and other proposed mechanisms follow a similar route but regenerate the catalyst differently, either using a water molecule to simultaneously transfer protons to allow imidic acid isomerization and break the disulfide bond,[58] or avoiding formation of a disulfide bond entirely by having a cysteine-sulfenic

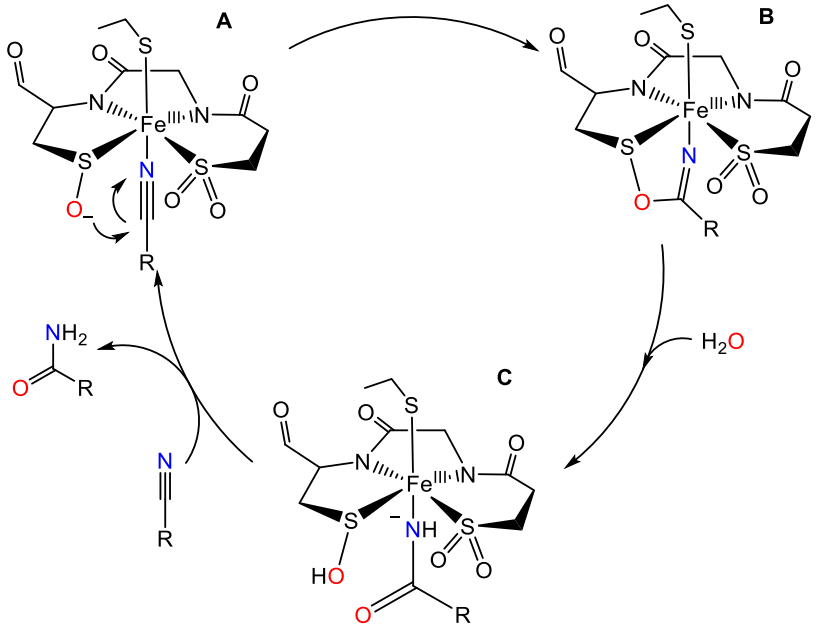

Scheme 1-2. Proposed reaction mechanism of nitrile hydratase.

acid attack the nitrile substrate unassisted, followed by a similar regeneration of the active catalyst with a concerted reformation of the cysteine-sulfenic acid and amide isomerization through an external water molecule.[61] The ambiguity of the mechanism highlights the need for further research into the reactive mechanism in order to be able to produce new catalysts for the economical transformation of nitriles to amides.

1.3.4. Model Chemistry

Due to the lack of directly observable evidence for the mechanism of catalysis and the formation of the active site of NHases, model complexes which oxygenate sulfur are a valuable area for study. Due to the difficulty of selectively oxygenating sulfur atoms, whether singly or doubly or triply, there are few reported complexes with mixed sulfinate/sulfenates, none of which involve an iron center,[62–66] and there are only a few singly oxygenated (sulfenate) complexes compared to doubly (sulfinate) or triply (sulfonate) complexes.[67,68] Currently, there are no functional model complexes for nitrile hydratase, but mixed N/S Fe complexes have allowed investigation into the behavior of NHase and related enzymes.

The first step of NHase's activity involves the photolabilization of a nitric oxide molecule in order to make the active site available for binding of the nitrile substrate. Mascharak and coworkers have reported a 3N/2S square pyramidal iron complex which in its unmodified state does not release NO when photoexcited in noncoordinating solvents. When its aromatic thiolates were oxidized by (1S)-(+)-(10-camphorsulfonyl)oxaziridine, NO can be released by photoexcitation (**Figure 1-4**, left).[69] This indicates that lowering the electron density at the iron center by oxygenating the coordinated sulfurs likely plays a role in the activity of NHase.

In addition to allowing the photolabilization of NO, the oxygenation of bound sulfur atoms has been shown to alter the magnetic and electronic properties of the metal center by several model complexes. In the Kovacs group alone, the role of thiolates in modulating the electronic structure of the metal center has been thoroughly explored.[64,70–74] The first of these complexes, $[Fe^{III}(ADIT)_2]^+$, is a six-coordinate N4/2S iron complex with two identical thiolate ligands (**Figure 1-3**, left). One of these two ligands can be oxidized with *tert*-butyl N-sulfonyloxaziridine, the product of which is stable and able to be isolated and crystallographically characterized. This product, $[Fe^{III}(ADIT)(ADIT\text{-}O)]^+$, has one of the two sulfur atoms oxygenated, and changes the color of the complex from green to purple, indicating that the oxygenation has a major effect on the irons' electronic structure (**Figure 1-3**, center right). XAS, X-ray crystallography, and DFT calculations show that the unmodified sulfur atom increases in covalency and that the π-interactions of the modified sulfur atom are lost. This oxygenated thiolate can be protonated with a strong acid to form $[Fe^{III}(ADIT)(ADIT\text{-}OH)]^{2+}$, and its sulfur to metal charge transfer band redshifts slightly, as an -S-OH ligand is weaker than an -S-O$^-$ ligand (**Figure 1-3**, right). The original $[Fe^{III}(ADIT)_2]^+$ can also be protonated with strong acid, which similarly to the oxygen addition also blue shifts the sulfur to metal charge transfer band, indicating a similar compensatory effect occurs with this process (**Figure 1-3**, center left).[70] Throughout this process, $[Fe^{III}(ADIT)_2]^+$ and derivatives demonstrate a potential role of the thiolate in NHase, with the complex staying in

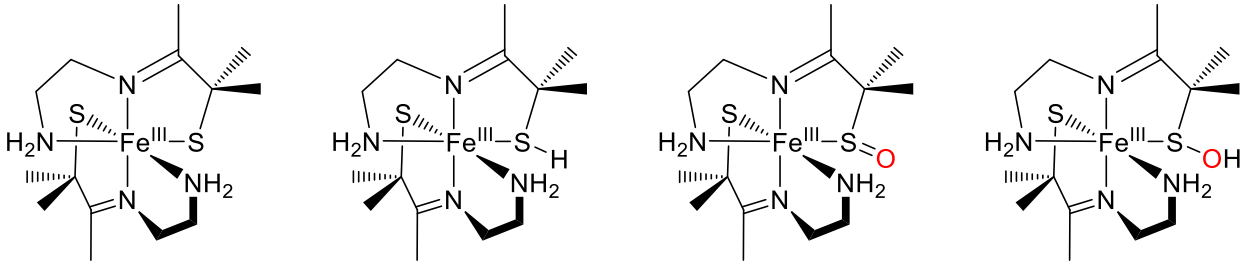

Figure 1-3. $[Fe^{III}(ADIT)_2]^+$, $[Fe^{III}(ADIT)(ADIT\text{-}H)]^{2+}$, $[Fe^{III}(ADIT)(ADIT\text{-}O)]^+$, and $[Fe^{III}(ADIT)(ADIT\text{-}OH)]^{2+}$.[70]

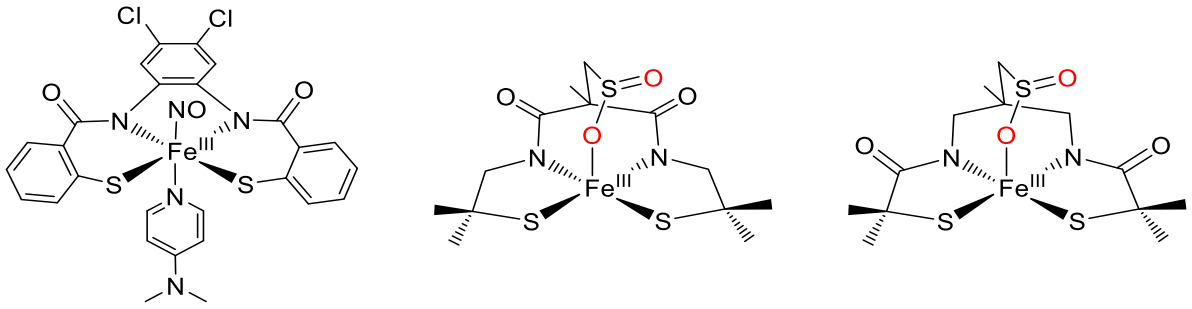

Figure 1-4. Selected model complexes for nitrile hydratase $[(Cl_2PhPepS)Fe(NO)(DMAP)]^-$ by the Mascharak group,[69] $[Fe^{III}(L\text{-}O_2)]^{2-}$ by the Chottard group,[73,75] and $[Fe^{III}((tame\text{-}N_2SO_2^{Me2})]^{2-}$ by the Kovacs group.[73,75]

the +3 oxidation state with a low spin-state, as NHase requires for catalytic activity. The bis-thiolate ligated $[Fe^{III}(S_2^{Me2}N_3(Pr,Pr))]^+$ complex was shown to behave similarly, with the oxygenated $[Fe^{III}(\eta^2\text{-}S^{Me2}O)(S^{Me2})N_3(Pr,Pr)]^+$ also shifting electron density away from the metal ion towards the oxygen atom.[74]

While their contribution is important to the role of the thiolate in NHase and related enzymes, none of the above complexes feature a 2N/3S environment as NHase does. Two similar complexes developed by the Chottard group and the Kovacs group can be used to examine the mechanism by which NHase enzymes are post-translationally modified to their active forms (**Figure 1-4**, center and right).[73,75] Both of these complexes feature a square-pyramidal tris-thiolate-ligated Fe^{III} complex that interacts readily with dioxygen, as is proposed that NHase does. Addition of O_2 results to either complex results in the apical thiolate being doubly oxygenated and the equatorial thiolates remaining untouched. Neither complex was shown to be capable of binding a sixth ligand opposite the modified thiolate, and as such neither is catalytically active.

While there are still no small molecule models with first-row transition metals which perform the hydration of nitriles, there has recently been reported a cobalt-containing NHase analogue which performs the hydrolysis of isocyanides, a similar reaction which Fe-type NHases are capable of performing. The Masuda group developed a complex with a cobalt ion in a square

pyramidal 2N/3S environment. By exposing this complex to air during its synthesis, they produce a quadruply-oxygenated species with two sulfinates. This complex can coordinate *tert*-butyl isocyanide, and in basic aqueous solutions, will catalytically produce *tert*-butyl amine, albeit with small turnover numbers. Using DFT calculations, they find that the reaction proceeds via nucleophilic attack of a water molecule on the activated isocyanide substrate.[76,77] While this does not agree with most accepted probable mechanisms for the hydration of nitriles by nitrile hydratase, it does show the value of using small-molecule models to investigate the behavior and characteristics of more complicated enzymes.

1.4. Cysteine Dioxygenase

1.4.1. Background

Cysteine dioxygenase is a more traditional non-heme iron thiolate enzyme which uses dioxygen in its mechanism to catalyze the transformation of cysteine to cysteine sulfinic acid.[41,78,79] It is used biologically to regulate the concentration of cysteine,[80] the buildup of which has been implicated in the advancement of neurodegenerative diseases such as Alzheimer's and Parkinson's[81] and in the progression of certain cancers.[82] CDO is a member of the class of thiol dioxygenases that catalyze the transformation of specific thiol containing substrates to their

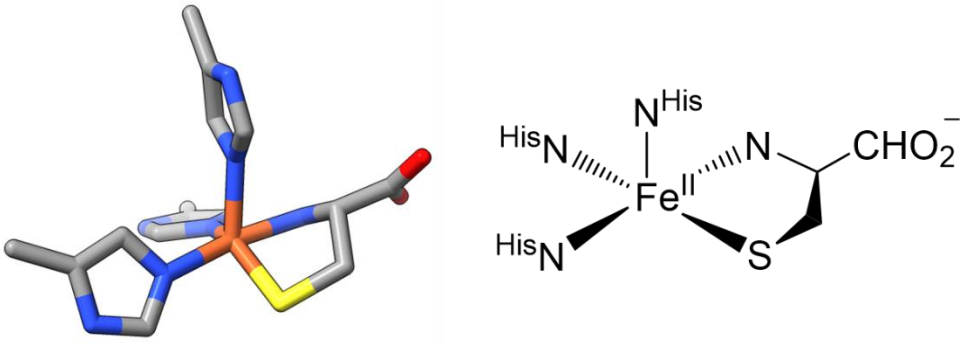

Figure 1-5. Depictions of the active site of cysteine dioxygenase. Left: crystallographic structure of human CDO (PDB ID: 2IC1).[188] Right: schematic drawing of the active site of CDO.

corresponding sulfinic acids.[83] While prevalent in mammals and important in the catabolism of cysteine, CDO is somewhat new to detailed examination, with the first crystal structure of the native iron-containing enzyme only being published in 2006.[84]

1.4.2. Structure of Cysteine Dioxygenase

Cysteine dioxygenase is another outlier to the normal 2-His-1-carboxylate binding motif of many iron dioxygenases, replacing the carboxylate with a third histidine residue in a facial triad.[84,85] X-ray crystallographic studies have revealed an Fe^{II} metal center bound to those histidines, one water molecule, and a free cysteine bound to the metal via the sulfur and the nitrogen (**Figure 1-5**).[84,85] However, as crystallographic measurements are not necessarily indicative of the structure of the enzyme as it performs catalysis, there was some doubt whether this complex represented the active site in part of the catalytic cycle. Resonance Raman, magnetic circular dichroism,[42] and Mössbauer studies[86] were used to demonstrate that binding of cysteine is the initial step in the catalytic cycle of CDO, and further, that the resting state is a high-spin Fe^{II} ion.

1.4.3. Mechanism of Cysteine Dioxygenase

The mechanism of cysteine dioxygenase is not known unequivocally, however, there are a few competing potential mechanisms with supporting evidence. In the resting state, the active site consists of the Fe^{II} center bound to the three histidines, whereupon a free cysteine binds to the Fe^{II} ion (**Scheme 1-3**). The binding of the sulfur was shown by theoretical calculations to lower the energetic barrier to the activation of dioxygen by the iron.[87,88] An Fe^{III}-superoxo intermediate by dioxygen binding *cis* to the cysteine's sulfur, which was confirmed by the Pierce group using single-turnover experiments on the native enzyme.[89] This superoxo intermediate is proposed by theoretical quantum mechanics/molecular mechanics (QM/MM) models to attack the neighboring

thiolate with its distal oxygen to produce an unusual four-membered RS-Fe^{II}-O-O ring structure,[88] with some evidence indicating the Fe^{III}-superoxo and subsequent cyclic structure are stabilized by a crosslinked tyrosine and cysteine nearby to the active site.[90,91] This proposed bicyclic structure then cleaves the O-O bond heterolytically to form a high-valent Fe^{IV}-oxo and a singly oxygenated sulfenate. This S=O bond can be rotated out of the way to allow the oxo atom to migrate on to the cysteine sulfur to afford the cysteine sulfinate bound to an Fe^{II} center.

It is difficult to gather spectroscopic evidence for these proposed intermediates of the enzyme due to temperature and solvent constraints inherent to enzymes. Through the use of a combination of spectroscopic and computational studies, however, Jameson and coworkers were able to find some evidence of either the Fe^{III}-superoxo species or the Fe^{II}-peroxythiolate bicyclic intermediate.[92] Using transient absorption spectroscopy they were able to observe an intermediate

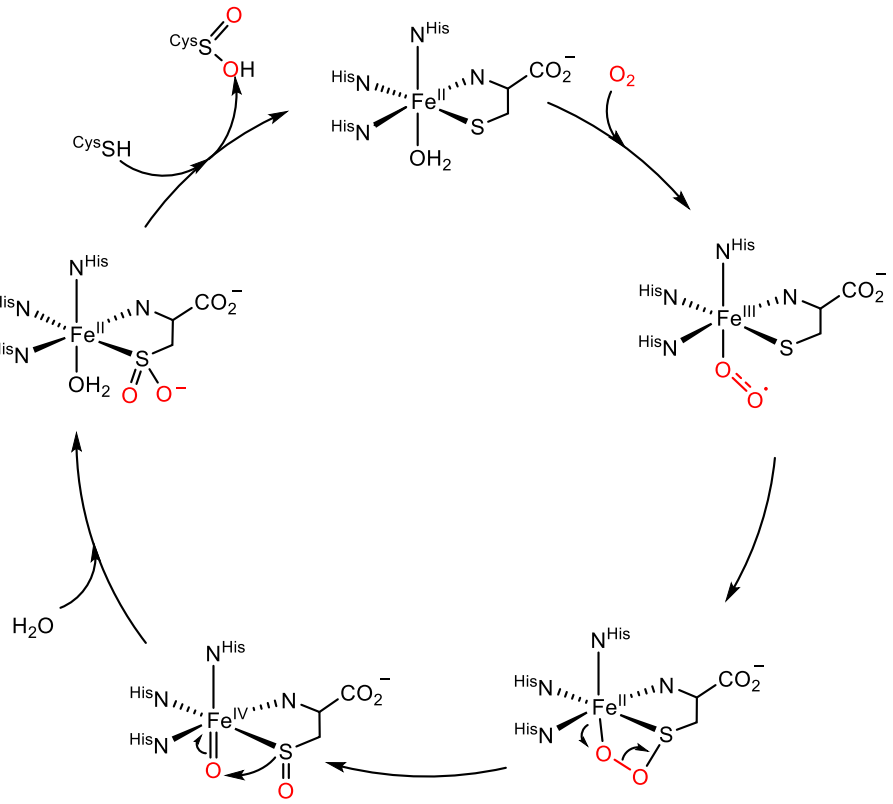

Scheme 1-3. Proposed reaction mechanism of cysteine dioxygenase.

with peaks at 500 and 640 nm which disappeared within 20 milliseconds. TD-DFT calculations of the Fe^{III}-superoxo and Fe^{II}-peroxythiolate were found to be substantially similar to the observed spectrum, however, there was not enough evidence to definitively assign it to either structure. Using insight from a model Fe^{III}-superoxo complex developed by the Kovacs group that will be discussed in the next section, it is likely that this transient spectrum can be assigned as the Fe^{III}-superoxo rather than a Fe^{II}-peroxythiolate.[22] As of yet there remains no directly observed evidence for either the Fe^{II}-peroxythiolate or the Fe^{IV}-oxo that have been proposed in the mechanism.

1.4.4. Model Chemistry

Most Fe^{II}-thiolate model complexes that react with dioxygen tend to produce oxygenation of the central iron atom rather than behave similar to CDO where the thiolate is oxygenated. Fe-oxo clusters are commonly formed, or disulfide bonds are created. It was only as recently as 2010 when the Goldberg group reported a model complex which accomplished sulfur oxygenation starting with an Fe^{II}-SR complex and dioxygen (**Figure 1-6**, left). Further, isotopic labeling studies showed that the only source of oxygen atoms on the thiolato sulfur was from dioxygen,[93] which has also been reported for CDO through $^{18}O_2$ isotope studies.[94] Since then, there have been several reported models which mimic the structure and function of CDO, most employing scorpionate-style ligands, such as the trispyrazolylborato Fe^{II} complex reported by Limberg and coworkers which mimics the 3-His-1-cysteine structure of CDO with the trispyrazoloylborato ligand and L-

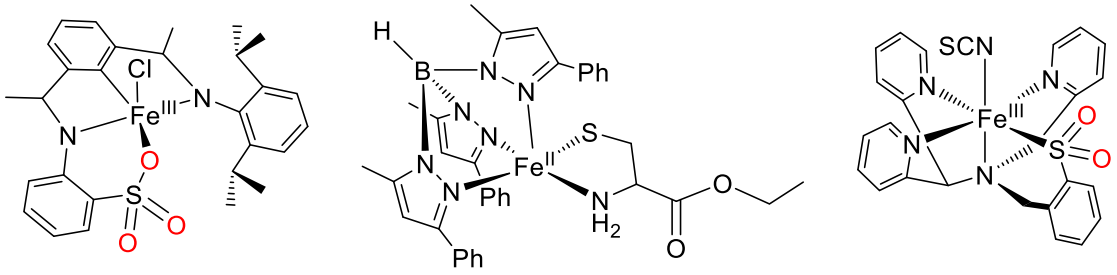

Figure 1-6. Selected model complexes for cysteine dioxygenase $[Fe^{II}(LN_3SO_3)]^+$ by the Goldberg group,[93] $[Tp^{Me,Ph}FeCysOEt]$ by the Limberg group,[95] and $[Fe^{II}(N_3PySO_2)(NCS)]$ by the Goldberg group.[96]

cysteine ethyl ester, and produces a sulfinic acid when reacted with dioxygen (**Figure 1-6**, center).[95] The Goldberg group has reported a complex featuring a pentadentate 4N/1S ligand based on the N4Py ligand with one pendant pyridine replaced with a phenylthiolate group. Reacting this Fe^{II} complex with dioxygen generated a doubly oxygenated sulfinato complex similar to the cysteine sulfinic acid produced by CDO (**Figure 1-6**, right).[96] The Goldberg group has also used the tridentate triazacyclononane (TACN) ligand to produce an Fe^{II}(TACN) aminobenzenethiolate complex that oxygenated the ligated sulfur when exposed to dioxygen.[97]

While complexes that mimic the coordination and chemistry of CDO are no longer uncommon, there are very few reported and characterized non-heme Fe^{III}-superoxo complexes. The Fiedler group recently reported that their trispyrazoloylborato-ligated Fe^{II} complex with a less reactive substrate (2-aminothiophenolate) reacted with dioxygen to form an Fe^{III}-superoxo which they were able to characterize by low temperature electronic absorption and resonance Raman experiments. Like CDO with this substrate, this Fe^{III}-superoxo was also found to not oxygenate the sulfur atom, instead following an alternate pathway resulting in 2-aminophenyl disulfide.[98] The Kovacs group has also reported an Fe^{III}-superoxo generated from dioxygen, using the $[Fe^{II}(S_2{}^{Me2}N_3(Pr,Pr))]$ complex. This complex was characterized with resonance Raman, low temperature electronic absorption, Mössbauer spectroscopies and DFT calculations that proved formation of an antiferromagnetically coupled Fe^{III}-superoxo species. When warmed to -40 °C, this species does perform oxygenation of the coordinated sulfur atom, similar to CDO. However, there is evidence that this complex accomplishes this via a mechanism which involves abstracting a hydrogen atom to form an Fe^{III}-hydroperoxo, which will be discussed in a later section.[22] The Kovacs group has also reported an Fe^{III}-superoxo formed with dioxygen using a different ligand system, $[Fe^{III}(S^{Me2}N_4(tren))(O_2)]^+$. This complex also does not oxygenate sulfur, instead forming

a μ-oxo dimer; but there is evidence that it forms this dimer via a mechanism involving formation of an Fe^{IV}-oxo species, similar a proposed intermediate of CDO.[99,100]

1.5. Isopenicillin N Synthase

1.5.1. Background

Isopenicillin N synthase is an iron biosynthetic oxidase which uses dioxygen as an oxidant to form isopenicillin N, a precursor to all β-lactam type antibiotics, which are the most widely used class of antibiotic in the world.[101] It does this transformation without the assistance of any cofactors, managing the four-electron oxidation of its δ-(l-α-aminoadipyl)-l-cysteinyl-d-valine (ACV) substrate only by control of the iron center's electronic structure and the steric profile of the active site.[102] These β-lactam rings are the key to the penicillin family's bactericidal nature, as they act by inhibiting the synthesis of bacterial cell walls, acting as an irreversible inhibitor of DD-peptidase, the enzyme responsible for the final crosslinking step of the cell wall construction.[103–105] Currently, the β-lactam family of antibiotics is produced via bulk fermentation of the relevant fungi, an efficient but limiting method which is constrained by only being able to produce naturally occurring antibiotics.[106] The ability of IPNS to perform this ring closure to produce a highly strained β-lactam fused to a thiazolidine ring is of great interest, as current methods[107] in β-lactam synthesis require very particular materials, such as the Staudinger synthesis[108] requiring a ketene and imine cyclization[109] or employing complications such as photoinduced rearrangements[110] or radical cyclizations.[111] Deepening our understanding of the mechanism of IPNS will be crucial for discovering new catalysts to perform these sorts of difficult reactions under mild conditions.

1.5.2. Structure of Isopenicillin N Synthase

Isopenicillin N synthase uses the standard 2-His-1-carboxylate binding motif, containing an Fe^{II} metal center coordinated to two histidines, one aspartic acid, a carbonyl from a neighboring glutamine, and in the resting state, two water molecules (**Figure 1-7**).[112,113] The substrate ACV binds through the thiolate, displacing the glutamine and affording the active form of the enzyme.[114,115] In order for IPNS to use dioxygen as an oxidant and not form oxygenated products, the enzyme's secondary structure contains several steric and electrostatic controls, enclosing the metal center with a hydrophobic cavity within the protein and isolating the reactive complex and subsequent intermediates from the external environment.[116,117] DFT studies have shown that these steric controls help to preclude the formation of a bridged Fe-O-O-S structure seen in the mechanism of CDO and to force the products of the reaction away from the more thermodynamically favorable sulfur oxidation products and to the more difficult H-atom abstraction products.[118] The ACV substrate additionally aids in this, contributing to steric controls with its dangling valine residue, and assisting in binding dioxygen as superoxide via charge donation to the iron center.[119,120]

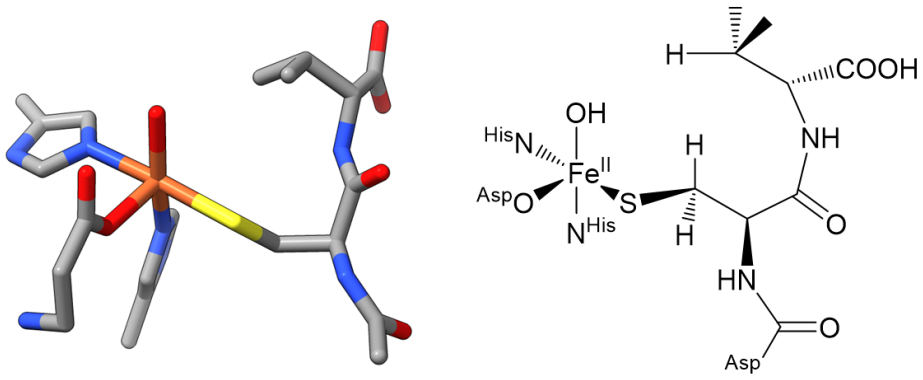

Figure 1-7. Depictions of the ACV-bound active site of isopenicillin N synthase. Left: crystallographic structure of substrate-bound IPNS (PDB ID: IBK0).[189] Right: Schematic drawing of substrate-bound IPNS.

1.5.3. Mechanism of Isopenicillin N Synthase

Dioxygen is used in the mechanism of IPNS to sequentially produce two powerful oxidants, an Fe^{III}-superoxo and an Fe^{IV}-oxo which perform two hydrogen atom abstractions in order to form a β-lactam ring fused to a thiazolidine ring (**Scheme 1-4**). This process begins with the displacement of the glutamine and binding of ACV to the iron center via the thiol sulfur, which lowers the redox potential of the iron and facilitates the binding of dioxygen opposite to the aspartic acid.[39] The newly formed Fe^{III}-superoxo can then abstract the hydrogen from the β-carbon of ACV to form a thioaldehyde and an Fe^{III}-hydroperoxo. These mediate the closure of the β-lactam ring while also generating an Fe^{IV}-oxo intermediate,[121–123] which can perform a second hydrogen atom abstraction from the valinyl β-carbon to make a tertiary radical species that can close the thiazolidine ring to afford the product isopenicillin N.[117,124–126]

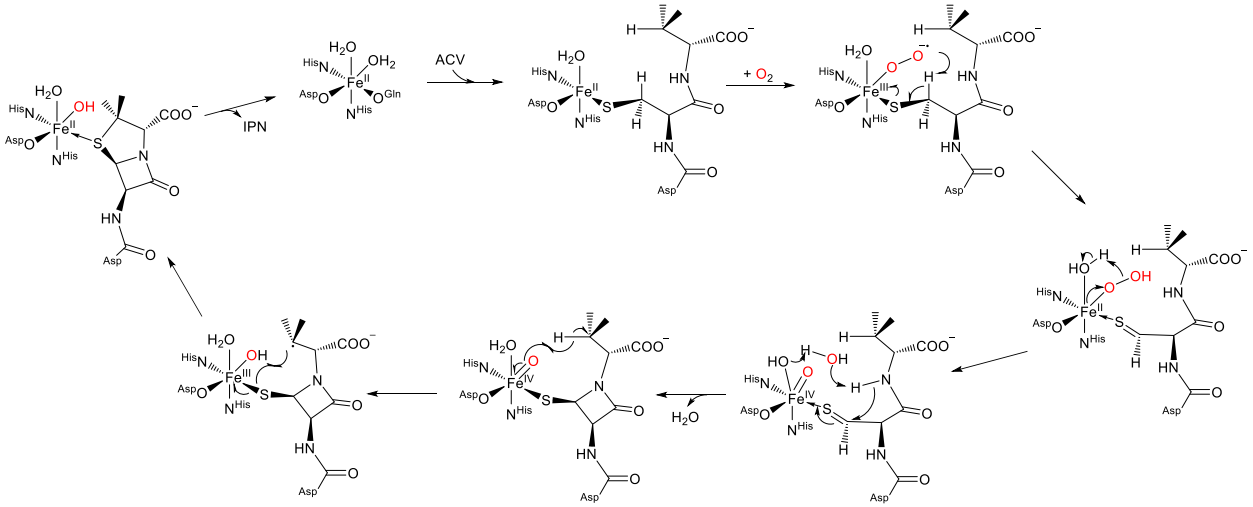

Scheme 1-4. Proposed reaction mechanism of isopenicillin N synthase.

Like CDO, the reactive intermediates in IPNS have been difficult to directly observe. The Fe^{III}-superoxo species has been observed with a combination of transient-state-kinetics, stopped-flow absorption, and freeze-quench Mössbauer spectroscopies.[120] Selectively deuterating the cysteine residue of ACV leads to a longer lifetime of the first intermediate species generated by the interaction of the ACV-bound Fe^{II} complex, allowing Mössbauer spectroscopy to be used to

identify it as a high-spin Fe^{III} magnetically coupled to a superoxide radical. Accumulation of this Fe^{III}-superoxo species also precedes the accumulation of the Fe^{IV}-oxo intermediate, which is independently identified as such by Mössbauer spectroscopy. Kinetic isotope experiments carried out with selective deuteration of the valine residue of ACV shows a large effect on the decay of this intermediate with no effect on its formation or the formation or decay of the previous Fe^{III}-superoxo intermediate. These intermediates were also identified crystallographically using substrate analogues which cannot complete the bicyclization. Replacing the valine residue with a methylcysteine showed formation of the β-lactam and formation of a metal-bound sulfoxide, indicating oxidation of the sulfur by the Fe^{IV}-oxo,[125] and replacing the internal amine which is involved in formation of the β-lactam ring with an ester causes an thiocarboxylate to be formed, indicating a hydrogen atom abstraction to form a Fe^{III}-hydroperoxo followed by nucleophilic attack by the hydroperoxide on the thioaldehyde to form a thiocarboxylic acid.[127]

1.5.4. Model Chemistry

IPNS carries out two sequential C-H bond cleavages by high energy intermediates, and it is no surprise that a small molecule model which can perform both has not yet been reported. Using an Fe^{IV}-oxo as an oxidant is quite common, occurring frequently in Nature as the active oxidant in the heme iron enzyme family of cytochrome P450[128] and in a wide variety of non-heme iron enzymes including taurine:α-ketoglutarate dioxygenase (TauD), prolyl-4-hydroxylase, and halogenase CytC3.[129–131] Fe^{IV}-oxo species also occur frequently in biomimetic models of enzymes, being frequently invoked as active oxidants and occasionally even reported in a crystal structure, and they are the subject of numerous reports and reviews.[99,132–136] Ferric superoxides acting as agents for hydrogen atom abstraction are much more rare, as they prefer as previously discussed to oxidize adjacent sulfurs. The first reported non-heme mononuclear iron-superoxo complex was

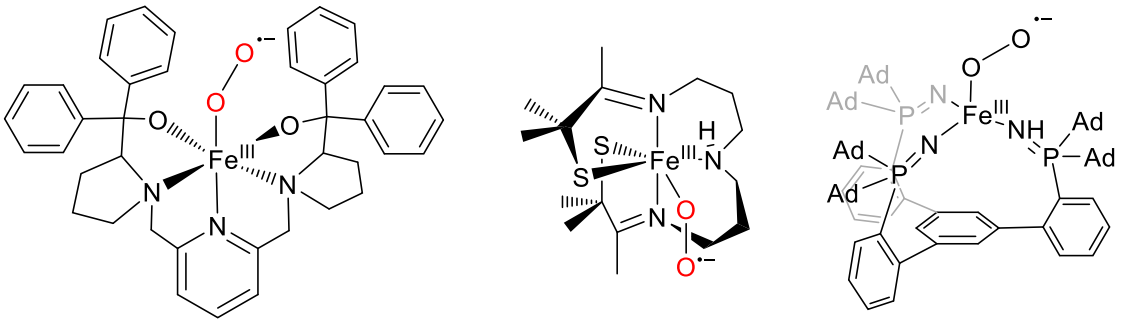

Figure 1-8. Selected model complexes for isopenicillin N synthase [Fe^{III}(BDPP)(O_2)] by the Lee group,[137] [Fe^{III}($S_2{}^{Me2}N_3$(Pr,Pr))(O_2)] by the Kovacs group,[22] and [(L^{Ad}H)FeO_2] by the Rittle group.[141]

reported in 2014 by the Lee group, using a pentadentate 3N/2O ligand to support an Fe^{II} metal ion which reacted with dioxygen at low temperatures to afford an Fe^{III}-superoxo species. They were able to characterize this by resonance Raman and Mössbauer spectroscopies, and show that it was capable of abstracting a hydrogen atom from 9,10-dihydroanthracene (BDE = 78 kcal/mol) (**Figure 1-8**, left).[137,138] The previously discussed Fe^{III}-superoxo reported by the Kovacs group forms an Fe^{III}-superoxo complex and in THF will convert to a putative Fe^{III}-hydroperoxo, with an observed deuterium isotope effect of k_H/k_D = 4.8, similar to that of IPNS (k_H/k_D = 5.6) (**Figure 1-8**, center).[22]

Other Fe^{III}-superoxos have been reported, as in the proposed mechanism of IPNS. The Hikichi group in 2015 reported a 5N trispyrazoloylborato- and imidazolylborato-ligated Fe^{II} center which reacted with dioxygen to form an Fe^{III}-superoxo capable of abstracting hydrogen atoms from bonds with C-H bond strengths less than 72.6 kcal/mol.[139] The Nam group in 2014 reported a 4N square planar tetraamido macrocylic ligand complexed Fe^{II} center which reacted with dioxygen to form a side-on (η^2) Fe^{III}-superoxo complex that did not activate the C-H bonds of hydrocarbons such as cyclohexadiene (BDE = 76.0 kcal/mol) and xanthene (BDE = 75.2 kcal/mol), but that it did show evidence of activating O-H bonds of 2,4-di-*tert*-butylphenol (BDE = 85.9).[138,140] The Rittle group in 2021 reported a 3N trigonal Fe^{II} complex based on a

phosphinimide scaffold ligand which similarly was shown to activate dioxygen to form a tetrahedral Fe^{III}-superoxo capable of activating the N-H bond of diphenylhydrazine (BDE = 73.1 kcal/mol) to produce azobenzene and as of yet uncharacterized iron products (**Figure 1-8**, right).[141] These complexes, with the exception of the complex reported by the Kovacs group, do not include a sulfur coordinated to the iron center like IPNS does, and additionally unlike IPNS they are only capable of abstracting hydrogen atoms from weak bonds. IPNS has the benefit of a dedicated support structure inside the enzyme to preclude side products from forming, as well as to carefully manage the electronic structure of the iron in the active site, allowing the abstraction of methylene C-H bond (BDE = 93 kcal/mol), where the model complexes are subject to the whim of solvent interactions and a much more flexible ligand environment.

1.6. Forming O-O Bonds in Nature

In order to use dioxygen as a convenient source of oxidizing equivalents, energy must first be stored in its chemical bonds. For millennia, the atmosphere of Earth was composed of the relatively inert gases nitrogen and carbon dioxide and potentially methane.[142] About 3.5 billion years ago, the first photosynthetic life forms began to produce gaseous oxygen from the abundant water, and the Earth's atmosphere was forever changed from a weakly reducing environment to a strongly oxidizing one.[143] This was catastrophic for almost everything living at the time, causing dramatic cooling due to the oxidation of the strong greenhouse gas methane to the weaker carbon dioxide and leading to a series of ice ages,[144] but also providing an extremely convenient and powerful source of chemical energy to the first eukaryotes.[145]

Photosynthesis, the process of storing the energy of light from the sun via splitting water into dioxygen and carbohydrates, is the process which has allowed complex life and civilization to flourish both by producing oxygen essential to cellular respiration and the variety of combustion

reactions that power our modern world, and by generating the organic molecules plants use for growth.[146] The heart of this process is the water-splitting reaction, which takes two equivalents of water and "splits" them into one equivalent of dioxygen and two equivalents of hydrogen, at the cost of about 350 kJ/mol produced.[147,148] This is a high energy cost to pay in one step, and Nature has developed a catalyst which breaks this process up into more surmountable parts, which additionally allows the reaction to take place at ambient conditions with the only energy input necessary coming from the sun.

1.7. The Oxygen-Evolving Complex

1.7.1. Background

The way Nature performs the water-splitting reaction is through a tetramanganese calcium cubane cluster known as the oxygen-evolving complex (OEC), located in the protein complex photosystem II (PSII). First isolated from cyanobacteria and found there and in chloroplasts, the OEC is remarkably invariant across the locations that it is found in.[149] It is the only natural system on Earth that provides organisms with the oxygen they breathe or otherwise consume, and it provides a model for the exploitation of efficient solar energy to produce a sort of solar fuel.[150] In the absence of any sort of catalyst in aqueous solution, the water splitting reaction can still be accomplished by application of high electric potential: first one hydrogen atom is removed from a water, generating a hydroxyl radical at the cost of about 2.8 eV (a 680 nm visible red photon is about 1.8 eV). For 0.7 eV more, this hydroxyl radical and another water molecule can shed another hydrogen atom to form hydrogen peroxide, to which another 1 eV added and two hydrogen atoms lost will produce dioxygen.[151] This is somewhat of a problem, as the drastically differing energetic costs for each step would seem to require unique machinery to deliver each different oxidative

step, however, Nature has managed to use the OEC cluster to tune the energetics of this sequence to make them all require approximately the same energy to accomplish.

1.7.2. Structure of the Oxygen-Evolving Complex

The oxygen-evolving complex consists of a cluster of four manganese atoms and one calcium atom bound together by a variety of bridging oxo atoms to form a Mn_3CaO_4 cubane with a "dangling" manganese atom, attached to the greater cubane via another oxo bridge (**Figure 1-9**). A variety of crystallographic studies have determined that the cubane is not completely symmetric, with Mn-O bond distances being in the range of 1.8-2.1 Å and Ca-O bond distances being about 2.4-2.5 Å. The cluster has four associated water molecules, two of which are bound to the dangling manganese Mn4, the other two of which are bound to the central calcium atom. These water molecules have been speculated to be the substrates of the reaction, although there is not strong evidence for any particular water as of yet. Substitution of the calcium ion for a similar strontium or barium ion results in greatly decreased or no oxygen-evolving function of the cluster, indicating that the calcium plays some role in the reactivity of the OEC.[152,153]

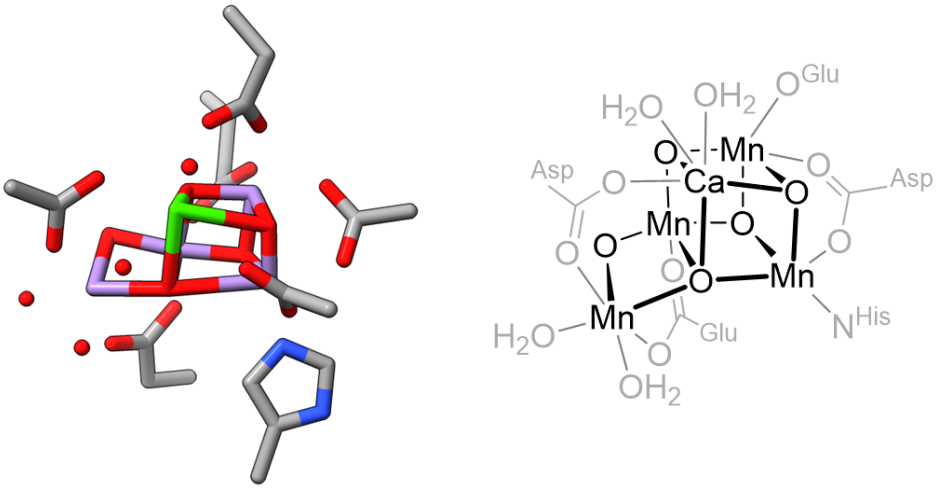

Figure 1-9. Depictions of the active site of the oxygen-evolving complex. Left: crystallographic structure of the OEC with surrounding protein residues (PDB ID: 5B5E).[190] Right: Schematic drawing of the OEC with surrounding protein residues.

The metal ion cluster is supported by a variety of amino acid residues, largely glutamic acids and aspartic acids bound bidentate to two metals across a face of the cubane. There are two histidine residues near the cubane as well, one of them bound to Mn1, and one of them not directly coordinated to the cluster. Additionally, there is a tyrosine residue termed Y_Z which is situated between the cubane cluster and the reaction center of photosystem II and has been implicated as both the delivery mechanism for oxidizing equivalents to the cluster and as an important part of a hydrogen bonding network that may function as an exit channel for the protons created by the water splitting process. There are two chloride atoms in the vicinity of the cubane cluster with indeterminate function, substitution of which with bromide atoms did not inhibit oxygen evolution but substitution with iodine did, indicating that they are involved in the mechanism of water splitting in some way but potentially only to keep the coordination structure of the cubane intact or as part of the egress pathway of the protons.[154,155]

1.7.3. Mechanism of the Oxygen-Evolving Complex

Despite extensive study, the exact mechanism of oxygen formation by the OEC is not completely understood. However, the generalities of the mechanism have been known for quite some time due to pioneering light-flash experiments by Joliot and Kok, resulting in the description of the catalytic cycle known as the Kok cycle (sometimes Joliot-Kok cycle) (**Scheme 1-5**).[156,157] The Kok cycle has five states denoted by the letter S and a number *i* indicating the amount of oxidizing equivalents stored in the cluster. This cycle starts at S_0 with three manganese ions in the +3 state and one in the +4, and goes up to the S_4 state, with three in the +4 state and one in the +5 (alternatively, all four manganese atoms in the +4 oxidation state and an oxyl somewhere in the cluster).[158] Upon formation of this S_4 state, the enzyme spontaneously converts back to the S_0 state

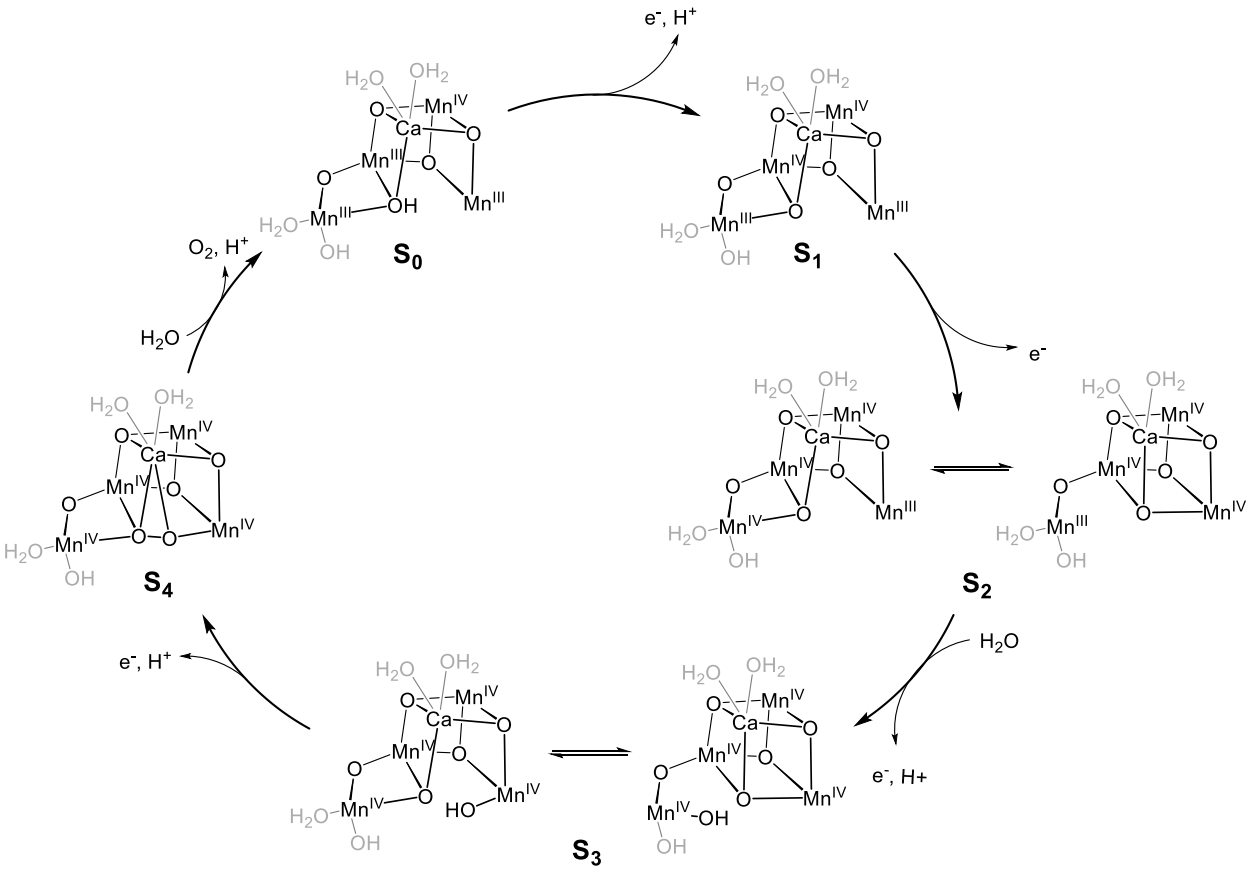

Scheme 1-5. The mechanism of the oxygen evolving complex, including "open" and "closed" conformers in the S_2 and S_3 states.

with concomitant release of a molecule of O_2. Because of the transient nature of the S_4 state and the extreme difficulty of characterizing the S_3 state due to its instability,[159] the exact mechanism of dioxygen formation is unknown. Many mechanisms of O-O bond formation have been proposed, but two leading mechanisms are the radical coupling mechanism wherein two Mn^{IV}-oxyl radicals couple to form a peroxo intermediate,[160] and a nucleophilic attack mechanism where Ca^{II}-OH nucleophilically attacks a Mn^{V}-oxo to form an O-O bond.[161,162]

During the Kok cycle, the OEC is structurally flexible, and that flexibility is likely important to its function. EPR and computational studies have shown that the S_2 and S_3 states exist in two interconvertible forms, an "open" form where the central oxygen atom O5 is closer to the dangling manganese, and a "closed" form where O5 is closer to the rest of the cubane.[163]

Additionally, depending on whether S_2 is "open" or "closed", the OEC exists in a low- or high-spin form respectively.[164,165] Whether the cubane cluster is "open" or "closed" during the S_2 to S_3 transition has important implications regarding potential reaction mechanisms, how and where substrate waters bind, and when and from where protons must be removed.[166] The "open" and "closed" forms of the S_2 state have also been proposed to be part of a gating mechanism which regulates access to higher S_i states to raise the effectiveness of the catalyst.[167] The reason for this flexibility is currently not entirely understood, but it has been proposed to be due to Jahn-Teller effects.[168] The S_3 state is also heterogeneous, but it has not been fully probed and it remains unclear whether its forms are interconvertible.[169]

1.7.4. Model Chemistry

The pursuit of an artificial oxygen-evolving catalyst is not new, and there are a wide variety of model complexes that can be sorted into either structural or functional analogues of the OEC. The two groups rarely overlap, and many functional models do not include manganese atoms. The first designed molecule known to function as a catalyst for water oxidation is the famous ruthenium "blue dimer" from Meyer and coworkers[170,171] which uses an oxo-bridged ruthenium pair to catalytically oxidize water in the presence of excess Ce^{IV} oxidant (**Figure 1-10**, left).[172] Since the publication of the blue dimer, there have been a wide variety of successful catalysts for oxygen evolution at a small scale, ranging from electrocatalytic generation of O_2 with metal oxide materials[173] to molecular species with a variety of transition metal centers that have been extensively reviewed.[174–177] Notably, there are also a range of Mn_4O_4 complexes which are capable of performing the oxygen evolution reaction. These clusters typically operate using some variation on a "butterfly" mechanism wherein two oxygens are coupled across a face of an Mn_4O_4 cubane and subsequently released, generating dioxygen and an open Mn_4O_2 structure which is repaired by

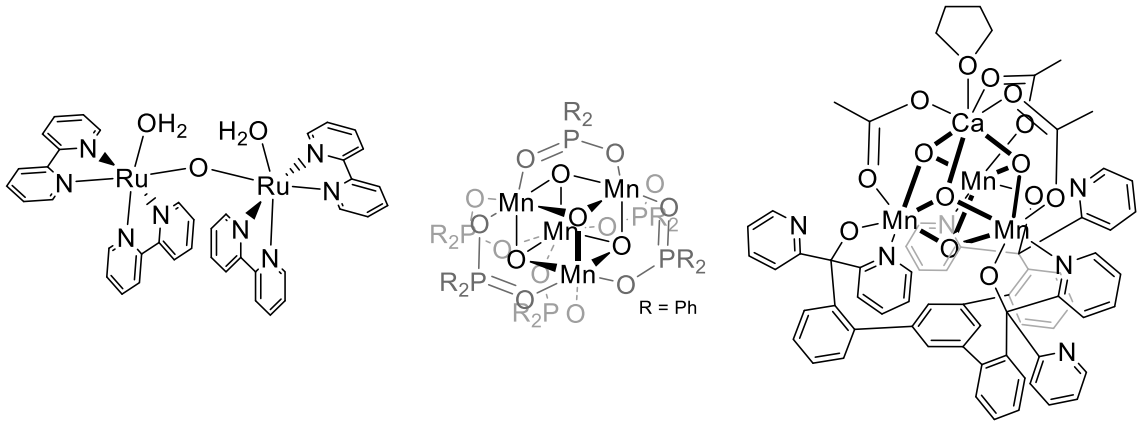

Figure 1-10. Selected model complexes for the OEC. $[(bpy)_2(OH_2)RuORu(OH_2)(bpy)_2]^{4+}$ by the Meyer group,[170,171] $[Mn_4O_4((C_6H_5)_2PO_2)_6]$ by the Dismukes group,[178] and $LMn^{IV}_3CaO_4(OAc)_3(THF)$ by the Agapie group.[179]

the incorporation and subsequent oxidation of water molecules (**Figure 1-10**, center).[178] These analogues prove the possibility of dioxygen generation by high-valent manganese clusters, but rely on self-assembly and do not include a calcium atom, which is known to be crucial to the function of the OEC. Further, the degree of structural flexibility required to proceed through the "butterfly" mechanism is not present in the OEC.

With the publication of high-resolution crystal structures of the OEC, more directly relevant structural models have been able to be developed. The Agapie group has developed a series of transition metal cubanes that model the core cubane both including and not including a calcium atom or analogue for a calcium atom (**Figure 1-10**, right).[179] Using a multinucleating polydentate ligand platform, they have been able to produce $Mn^3M_1O_4$ cubanes, where M = Mn, Sr, Zn, Sc, Y, Ca, Fe, Co, Ni, Cu, Lu, Yb, Tb, Dy, Eu, Gd, Nd, Ce, and La.[179–184] The lanthanide series was used to probe the effect of redox-inactive metal centers (such as the calcium found in the OEC) on the electronic properties of the nearby manganese ions, and it was found that increasing the atomic radius of the metal center decreased the redox potential of the complex as a whole.[181] This echoes what was found in studies replacing the calcium atom in the native OEC

with strontium or barium, where replacement altered the redox structure of the complex.[152] Replacement of the calcium atom for another redox-inactive metal such as Zn or Sc similarly show a decrease in redox potential with a decrease in metal ion Lewis acidity.[184] Regardless of the identity of the fourth metal in these structural analogues, none of them function as competent catalysts for the oxygen evolution reaction, however, they can be used to create heterogenous material electrocatalysts which do.[183]

There are very few structural models that incorporate the "dangling" manganese atom of the OEC. The Agapie group found that by oxidizing a cubane to an $Mn^{IV}_3GdO_4$ or $Mn^{IV}_3CaO_4$ complex desymmetrizes it and creates a unique basic oxygen site which can be used to attach a fifth metal to the cubane.[185] As of yet, the only fifth metal they have added is Ag^+, which they have found creates a close structural mimic to the active site of the OEC, but they have not demonstrated any oxygen evolution capability. The Zhao group used self-assembly techniques to create a Mn_4CaO cubane which mimics the S_1 state of the OEC. They found that their synthetic complex had five accessible redox states, similar to the OEC, and that it can be chemically oxidized to an S_2 equivalent state. Oxidizing the complex increases the potential required to oxidize each sequential step, which may indicate that the purpose of deprotonating the OEC may be to lower the redox potential of subsequent oxidation steps.[186] Similarly to the Agapie group, they did not find that this complex was capable of performing the oxygen evolution reaction.

1.8. Conclusions

Biomimetic modeling of the active sites of enzymes can allow a greater understanding of their mechanisms and what parts of the active site are required for functionality. In particular, due to the high reactivity and efficacy of enzymes consuming or producing dioxygen, biomimetic models are valuable in making determinations of how and why enzymes react the way they do. In

cases such as the structural similarity and reactive differences of IPNS and CDO, biomimetic modeling can be used to examine both the formation of highly reactive Fe^{III}-superoxo intermediates and to determine why one uses that reactive intermediate to oxygenate sulfur and the other uses the same intermediate in a very similar coordination environment to perform hydrogen atom abstraction. Through these models, we can achieve greater clarity on the purpose of ligands included in the active sites of these complexes, and how they affect the electronic structure of the metal to allow the enzyme to perform its transformations.

1.9. References

(1) Maret, W. The Metals in the Biological Periodic System of the Elements: Concepts and Conjectures. *Int. J. Mol. Sci.* **2016**, *17* (1), 66. DOI:10.3390/ijms17010066

(2) Williams, R. J. P. Bio-Inorganic Chemistry: Its Conceptual Evolution. *Coord. Chem. Rev.* **1990**, *100* (C), 573–610. DOI: 10.1016/0010-8545(90)85020-S

(3) Lippard, S. J.; Berg, J. M. *Principles of Bioinorganic Chemistry*; University Science Books: Mill Valley, CA, 1994

(4) Holm, R. H.; Kennepohl, P.; Solomon, E. I. Structural and Functional Aspects of Metal Sites in Biology. *Chem. Rev.* **1996**, *96* (7), 2239–2314. DOI: 10.1021/cr9500390

(5) Tainer, J. A.; Roberts, V. A.; Getzoff, E. D. Metal-Binding Sites in Proteins. *Curr. Opin. Biotechnol.* **1991**, *2* (4), 582–591. DOI: 10.1016/0958-1669(91)90084-I

(6) Lutz, S. Beyond Directed Evolution-Semi-Rational Protein Engineering and Design. *Curr. Opin. Biotechnol.* **2010**, *21* (6), 734–743. DOI: 10.1016/j.copbio.2010.08.011

(7) Huang, X.; Groves, J. T. Oxygen Activation and Radical Transformations in Heme Proteins and Metalloporphyrins. *Chem. Rev*. **2018**, *118* (5), 2491–2553 DOI: 10.1021/acs.chemrev.7b00373

(8) Finnigan, J. D.; Young, C.; Cook, D. J.; Charnock, S. J.; Black, G. W. Cytochromes P450 (P450s): A Review of the Class System with a Focus on Prokaryotic P450s. *Adv. Protein. Chem. Struct. Biol.* **2020**, *122*, 289–320. DOI: 10.1016/bs.apcsb.2020.06.005

(9) Solomon, E. I.; Decker, A.; Lehnert, N. Non-Heme Iron Enzymes: Contrasts to Heme Catalysis. *P. Nat. Acad. Sci.* **2003**, *100* (7), 3589–3594. DOI: 10.1073/pnas.0336792100

(10) Bruijnincx, P. C. A.; van Koten, G.; Klein Gebbink, R. J. M. Mononuclear Non-Heme Iron Enzymes with the 2-His-1-Carboxylate Facial Triad: Recent Developments in Enzymology and Modeling Studies. *Chem. Soc. Rev.* **2008**, *37* (12), 2716–2744. DOI: 10.1039/b707179p

(11) Kovaleva, E. G.; Lipscomb, J. D. Versatility of Biological Non-Heme Fe(II) Centers in Oxygen Activation Reactions. *Nat. Chem. Biol*. **2008**, *4*, 186–193. DOI: 10.1038/nchembio.71

(12) Kovacs, J. A. Synthetic Analogues of Cysteinate-Ligated Non-Heme Iron and Non-Corrinoid Cobalt Enzymes. *Chem. Rev*. **2004**, *104* (2), 825–848. DOI: 10.1021/cr020619e

(13) Murakami, T.; Nojiri, M.; Nakayama, H.; Dohmae, N.; Takio, K.; Odaka, M.; Endo, I.; Nagamune, T.; Yohda, M. Post-Translational Modification Is Essential for Catalytic Activity of Nitrile Hydratase. *Protein Sci.* **2000**, *9* (5), 1024–1030 DOI: 10.1110/ps.9.5.1024

(14) Tamanaha, E.; Zhang, B.; Guo, Y.; Chang, W. C.; Barr, E. W.; Xing, G.; St Clair, J.; Ye, S.; Neese, F.; Bollinger, J. M.; Krebs, C. Spectroscopic Evidence for the Two C-H-Cleaving Intermediates of Aspergillus Nidulans Isopenicillin N Synthase. *J. Am. Chem. Soc.* **2016**, *138* (28), 8862–8874. DOI: 10.1021/jacs.6b04065

(15) Tchesnokov, E. P.; Faponle, A. S.; Davies, C. G.; Quesne, M. G.; Turner, R.; Fellner, M.; Souness, R. J.; Wilbanks, S. M.; De Visser, S. P.; Jameson, G. N. L. An Iron-Oxygen Intermediate Formed during the Catalytic Cycle of Cysteine Dioxygenase. *Chem. Comm.* **2016**, *52* (57), 8814–8817. DOI: 10.1039/c6cc03904a

(16) Nelp, M. T.; Song, Y.; Wysocki, V. H.; Bandarian, V. A Protein-Derived Oxygen Is the Source of the Amide Oxygen of Nitrile Hydratases. *J. Biol. Chem.* **2016**, *291* (15), 7822–7829. DOI: 10.1074/jbc.M115.704791

(17) Minaev, B. F.; Ågren, H.; Minaeva, V. O. Spin-Orbit Coupling in Enzymatic Reactions and the Role of Spin in Biochemistry. In *Handbook of Computational Chemistry*; Springer International Publishing, 2017; pp 1557–1587. DOI: 10.1007/978-3-319-27282-5_29

(18) Minaev, B. F.; Minaeva, V. O.; Ågren, H. Spin-Orbit Coupling in Enzymatic Reactions and the Role of Spin in Biochemistry. In *Handbook of Computational Chemistry*; Springer Netherlands, 2012; pp 1067–1094. https://doi.org/10.1007/978-94-007-0711-5_29

(19) Hohenberger, J.; Ray, K.; Meyer, K. The Biology and Chemistry of High-Valent Iron-Oxo and Iron-Nitrido Complexes. *Nat. Commun*. **2012**, 1–13. DOI: 10.1038/ncomms1718

(20) Krebs, C.; Fujimori, D. G.; Walsh, C. T.; Bollinger, J. M. Non-Heme Fe(IV)-Oxo Intermediates. In *Accounts Chem. Res.* **2007**, *40*, 484–492. DOI: 10.1021/ar700066p

(21) Blakeley, M. N. Insights into Dioxygen Activation by Biomimetic Alkyl Thiolate-Ligated Iron Complexes, University of Washington, Seattle, WA, 2019.

(22) Blakely, M. N.; Dedushko, M. A.; Poon, P. C. Y.; Villar-Acevedo, G.; Kovacs, J. A. Formation of a Reactive, Alkyl Thiolate-Ligated FeIII-Superoxo Intermediate Derived from Dioxygen. *J. Am. Chem. Soc.* **2019**, *141*, 1867-1870. DOI: 10.1021/jacs.8b12670

(23) Sanvoisin, J.; Langley, G. J.; Bugg, T. D. H. Mechanism of Extradiol Catechol Dioxygenases: Evidence for a Lactone Intermediate in the 2,3-Dihydroxyphenylpropionate 1,2-Dioxygenase Reaction. *J. Am. Chem. Soc.* **1995**, *117* (29), 7836–7837. DOI: 10.1021/ja00134a041

(24) Arciero, D. M.; Lipscomb, J. D. Binding of 17O-Labeled Substrate and Inhibitors to Protocatechuate 4,5-Dioxygenase-Nitrosyl Complex. Evidence for Direct Substrate Binding to the Active Site Fe2+ of Extradiol Dioxygenases. *J. Biol. Chem.* **1986**, *261* (5), 2170–2178. DOI: 10.1016/s0021-9258(17)35913-6

(25) Shu, L.; Chiou, Y. M.; Orville, A. M.; Miller, M. A.; Lipscomb, J. D.; Que, L. X-Ray Absorption Spectroscopic Studies of the Fe(II) Active Site of Catechol 2,3-Dioxygenase. Implications for the Extradiol Cleavage Mechanism. *Biochemistry* **1995**, *34* (20), 6649–6659. DOI: 10.1021/bi00020a010

(26) Siegbahn, P. E. M.; Haeffner, F. Mechanism for Catechol Ring-Cleavage by Non-Heme Iron Extradiol Dioxygenases. *J. Am. Chem. Soc.* **2004**, *126* (29), 8919–8932. DOI: 10.1021/ja0493805

(27) Deeth, R. J.; Bugg, T. D. H. A Density Functional Investigation of the Extradiol Cleavage Mechanism in Non-Heme Iron Catechol Dioxygenases. *J. Biol. Inorg. Chem.* **2003**, *8* (4), 409–418. DOI: 10.1007/s00775-002-0430-7

(28) Karlsson, A.; Parales, J. V.; Parales, R. E.; Gibson, D. T.; Eklund, H.; Ramaswamy, S. Crystal Structure of Naphthalene Dioxygenase: Side-on Binding of Dioxygen to Iron. *Science* **2003**, *299* (5609), 1039–1042. DOI: 10.1126/science.1078020

(29) Ohta, T.; Chakrabarty, S.; Lipscomb, J. D.; Solomon, E. I. Near-IR MCD of the Nonheme Ferrous Active Site in Naphthalene 1,2-Dioxygenase: Correlation to Crystallography and

Structural Insight into the Mechanism of Rieske Dioxygenases. *J. Am. Chem. Soc.* **2008**, *130* (5), 1601–1610. DOI: 10.1021/ja074769o

(30) Pavel, E. G.; Martins, L. J.; Ellis, W. R.; Solomon, E. I. Magnetic Circular Dichroism Studies of Exogenous Ligand and Substrate Binding to the Non-Heme Ferrous Active Site in Phthalate Dioxygenase. *Chem. Biol.* **1994**, *1* (3), 173–183. DOI: 10.1016/1074-5521(94)90007-8

(31) Hausinger, R. P. Fe(II)/α-Ketoglutarate-Dependent Hydroxylases and Related Enzymes. *Crit. Rev. Biochem. Mol.* **2004**, *39*, 21–68. DOI: 10.1080/10409230490440541

(32) Price, J. C.; Barr, E. W.; Tirupati, B.; Bollinger, J. M.; Krebs, C. The First Direct Characterization of a High-Valent Iron Intermediate in the Reaction of an α-Ketoglutarate-Dependent Dioxygenase: A High-Spin Fe(IV) Complex in Taurine/α-Ketoglutarate Dioxygenase (TauD) from Escherichia Coli. *Biochemistry* **2003**, *42* (24), 7497–7508. DOI: 10.1021/bi030011f

(33) Ryle, M. J.; Padmakumar, R.; Hausinger, R. P. Stopped-Flow Kinetic Analysis of Escherichia Coli Taurine/α- Ketoglutarate Dioxygenase: Interactions with α Ketoglutarate, Taurine, and Oxygen. *Biochemistry* **1999**, *38* (46), 15278–15286. DOI: 10.1021/bi9912746

(34) Pavon, J. A.; Fitzpatrick, P. F. Insights into the Catalytic Mechanisms of Phenylalanine and Tryptophan Hydroxylase from Kinetic Isotope Effects on Aromatic Hydroxylation. *Biochemistry* **2006**, *45* (36), 11030–11037. DOI: 10.1021/bi0607554

(35) Fitzpatrick, P. F. Tetrahydropterin-Dependent Amino Acid Hydroxylases. *Annu. Rev. Biochem.* **1999**, *68*, 355–381. DOI: 10.1146/annurev.biochem.68.1.355

(36) Clifton, I. J.; McDonough, M. A.; Ehrismann, D.; Kershaw, N. J.; Granatino, N.; Schofield, C. J. Structural Studies on 2-Oxoglutarate Oxygenases and Related Double-Stranded β-

Helix Fold Proteins. *J. Inorg. Biochem*. **2006**, *4*, 644–669. DOI: 10.1016/j.jinorgbio.2006.01.024

(37) Koehntop, K. D.; Emerson, J. P.; Que, L. The 2-His-1-Carboxylate Facial Triad: A Versatile Platform for Dioxygen Activation by Mononuclear Non-Heme Iron(II) Enzymes. *J. Biol. Inorg. Chem*. **2005**, *10*, 87–93. DOI: 10.1007/s00775-005-0624-x

(38) Kovacs, J. A. How Iron Activates O2. *Science* **2003**, *299*, 1024–1025. DOI: 10.1126/science.1081792

(39) Roach, P. L.; Clifton, I. J.; Hensgens, C. M.; Shibiata, N.; Shofield, C. J.; Haju, J.; Baldwin, J. E. Structure of Isopenicillin N Synthase Complexed with Substrate and the Mechanism of Penicillin Formation. *Nature* **1997**, *387*, 827-830. DOI: 10.1038/42990

(40) Aluri, S.; De Visser, S. P. The Mechanism of Cysteine Oxygenation by Cysteine Dioxygenase Enzymes. *J. Am. Chem. Soc.* **2007**, *129* (48), 14846–14847. DOI: 10.1021/ja0758178

(41) Joseph, C. A.; Maroney, M. J. Cysteine Dioxygenase: Structure and Mechanism. *Chem. Comm.* **2007**, 3338–3349. DOI: 10.1039/b702158e

(42) Gardner, J. D.; Pierce, B. S.; Fox, B. G.; Brunold, T. C. Spectroscopic and Computational Characterization of Substrate-Bound Mouse Cysteine Dioxygenase: Nature of the Ferrous and Ferric Cysteine Adducts and Mechanistic Implications. *Biochemistry* **2010**, *49* (29), 6033–6041. DOI: 10.1021/bi100189h

(43) Li, T.; Liu, J.; Bai, R.; Ohandja, D. G.; Wong, F. S. Biodegradation of Organonitriles by Adapted Activated Sludge Consortium with Acetonitrile-Degrading Microorganisms. *Water Res* **2007**, *41* (15), 3465–3473. 10.1016/j.watres.2007.04.033

(44) Ohara, T.; Sato, T.; Shimizu, N.; Prescher, G.; Schwind, H.; Weiberg, O.; Marten, K.; Greim, H.; Shaffer, T. D.; Nandi, P. Acrylic Acid and Derivatives. In *Ullmann's Encyclopedia of Industrial Chemistry*; Wiley, 2020; pp 1–21. DOI: 10.1002/14356007.a01_161.pub4

(45) Herth, G.; Schornick, G.; L. Buchholz, F. Polyacrylamides and Poly(Acrylic Acids). In *Ullmann's Encyclopedia of Industrial Chemistry*; Wiley-VCH Verlag GmbH & Co. KGaA: Weinheim, Germany, 2015; pp 1–16. 10.1002/14356007.a21_143.pub2

(46) Wyatt, J. M.; Knowles, C. J. Microbial Degradation of Acrylonitrile Waste Effluents: The Degradation of Effluents and Condensates from the Manufacture of Acrylonitrile. *Int. Biodeterior. Biodegradation* **1995**, *35* (1–3), 227–248. DOI: 10.1016/0964-8305(95)00031-Y

(47) Nagashima, S.; Nakasako, M.; Dohmae, N.; Tsujimura, M.; Takio, K.; Odaka, M.; Yohda, M.; Kamiya, N.; Endo, I. Novel Non-Heme Iron Center of Nitrile Hydratase with a Claw Setting of Oxygen Atoms. *Nat. Struct. Biol*. **1998**, *5*, 347–351. DOI: 10.1038/nsb0598-347

(48) Miyanaga, A.; Fushinobu, S.; Ito, K.; Wakagi, T. Crystal Structure of Cobalt-Containing Nitrile Hydratase. *Biochem. Biophys. Res. Commun.* **2001**, *288* (5), 1169–1174. DOI: 10.1006/bbrc.2001.5897

(49) Nishiyama, M.; Horinouchi, S.; Kobayashi, M.; Nagasawa, T.; Yamada, H.; Beppu, T. Cloning and Characterization of Genes Responsible for Metabolism of Nitrile Compounds from Pseudomonas Chloraraphis B23. *J. Bacteriol.* **1991**, *173* (8), 2465–2472. DOI: 10.1128/jb.173.8.2465-2472.1991

(50) Dey, A.; Chow, M.; Taniguchi, K.; Lugo-Mas, P.; Davin, S.; Maeda, M.; Kovacs, J. A.; Odaka, M.; Hodgson, K. O.; Hedman, B.; Solomon, E. I. Sulfur K-Edge XAS and DFT

Calculations on Nitrile Hydratase: Geometric and Electronic Structure of the Non-Heme Iron Active Site. *J. Am. Chem. Soc.* **2006**, *128* (2), 533–541. DOI: 10.1021/ja0549695

(51) Tsujimura, M.; Odaka, M.; Nakayama, H.; Dohmae, N.; Koshino, H.; Asami, T.; Hoshino, M.; Takio, K.; Yoshida, S.; Maeda, M.; Endo, I. A Novel Inhibitor for Fe-Type Nitrile Hydratase: 2-Cyano-2-Propyl Hydroperoxide. *J. Am. Chem. Soc.* **2003**, *125* (38), 11532–11538. DOI: 10.1021/ja035018z

(52) Murakami, T.; Nojiri, M.; Nakayama, H.; Dohmae, N.; Takio, K.; Odaka, M.; Endo, I.; Nagamune, T.; Yohda, M. Post-Translational Modification Is Essential for Catalytic Activity of Nitrile Hydratase. *Protein Sci.* **2000**, *9* (5), 1024–1030. DOI: 10.1110/ps.9.5.1024

(53) Ogutu, I. R. A. M.; Holz, R. C.; Bennett, B. Insight into the Maturation Process of the Nitrile Hydratase Active Site. *Inorg. Chem.* **2021**, *60* (8), 5432–5435. DOI: 10.1021/acs.inorgchem.0c02924

(54) Tsujimura, M.; Odaka, M.; Nakayama, H.; Dohmae, N.; Koshino, H.; Asami, T.; Hoshino, M.; Takio, K.; Yoshida, S.; Maeda, M.; Endo, I. A Novel Inhibitor for Fe-Type Nitrile Hydratase: 2-Cyano-2-Propyl Hydroperoxide. *J. Am. Chem. Soc.* **2003**, *125* (38), 11532–11538. DOI: 10.1021/ja035018z

(55) Murakami, T.; Nojiri, M.; Nakayama, H.; Dohmae, N.; Takio, K.; Odaka, M.; Endo, I.; Nagamune, T.; Yohda, M. Post-Translational Modification Is Essential for Catalytic Activity of Nitrile Hydratase. *Protein Sci.* **2000**, *9* (5), 1024–1030. DOI: 10.1110/ps.9.5.1024

(56) Arakawa, T.; Kawano, Y.; Katayama, Y.; Nakayama, H.; Dohmae, N.; Yohda, M.; Odaka, M. Structural Basis for Catalytic Activation of Thiocyanate Hydrolase Involving Metal-

Ligated Cysteine Modification. *J. Am. Chem. Soc.* **2009**, *131* (41), 14838–14843. DOI: 10.1021/ja903979s

(57) Hopmann, K. H. Full Reaction Mechanism of Nitrile Hydratase: A Cyclic Intermediate and an Unexpected Disulfide Switch. *Inorg. Chem.* **2014**, *53* (6), 2760–2762. DOI: 10.1021/ic500091k

(58) Kayanuma, M.; Shoji, M.; Yohda, M.; Odaka, M.; Shigeta, Y. Catalytic Mechanism of Nitrile Hydratase Subsequent to Cyclic Intermediate Formation: A QM/MM Study. *J. Phys. Chem. B* **2016**, *120* (13), 3259–3266. DOI: 10.1021/acs.jpcb.5b11363

(59) Martinez, S.; Wu, R.; Sanishvili, R.; Liu, D.; Holz, R. The Active Site Sulfenic Acid Ligand in Nitrile Hydratases Can Function as a Nucleophile. *J. Am. Chem. Soc.* **2014**, *136* (4), 1186–1189. DOI: 10.1021/ja410462j

(60) Hopmann, K. H.; Guo, J. D.; Himo, F. Theoretical Investigation of the First-Shell Mechanism of Nitrile Hydratase. *Inorg. Chem.* **2007**, *46* (12), 4850–4856. DOI: 10.1021/ic061894c

(61) Yamanaka, Y.; Kato, Y.; Hashimoto, K.; Iida, K.; Nagasawa, K.; Nakayama, H.; Dohmae, N.; Noguchi, K.; Noguchi, T.; Yohda, M.; Odaka, M. Time-Resolved Crystallography of the Reaction Intermediate of Nitrile Hydratase: Revealing a Role for the Cysteinesulfenic Acid Ligand as a Catalytic Nucleophile. *Angew. Chem. Int. Ed.* **2015**, *54* (37), 10763–10767. DOI: 10.1002/anie.201502731

(62) Dilworth, J. R.; Zheng, Y.; Lu, S.; Wu, Q. Preparation and Characterization of a Novel Asymmetrically Oxidized Complex of 2-(Diphenylphosphino)-Benzenethiol with Ruthenium. The Crystal and Molecular Structure of [Ru(2-Ph2PC6H4S)·(2-Ph2PC6H4S-

OH)(2-Ph2PC6H4SO2)]·1/2H2O. *Transit. Metal Chem.* **1992**, *17* (4), 364–368. DOI: 10.1007/BF02910910

(63) Buonomo, R. M.; Font, I.; Maguire, M. J.; Reibenspies, J. H.; Tuntulani, T.; Darensbourg, M. Y. Study of Sulfinate and Sulfenate Complexes Derived from the Oxygenation of Thiolate Sulfur in [1,5-Bis(2-Mercapto-2-Methylpropyl)-1,5-Diazacyclooctanato(2—)]Nickel(II). *J. Am. Chem. Soc.* **1995**, *117* (3), 963–973. DOI: 10.1021/ja00108a013

(64) Kung, I.; Schweitzer, D.; Shearer, J.; Taylor, W. D.; Jackson, H. L.; Lovell, S.; Kovacs, J. A. How Do Oxidized Thiolate Ligands Affect the Electronic and Reactivity Properties of a Nitrile Hydratase Model Compound? *J. Am. Chem. Soc.* **2000**, *122* (34) 8299–8300. DOI: 10.1021/ja0017561

(65) Masitas, C. A.; Mashuta, M. S.; Grapperhaus, C. A. Asymmetric Oxygenation of a Ruthenium Dithiolate Mimics the Mixed Sulfenato/Sulfinato Donor Sets of Nitrile Hydratase and Thiocyanate Hydrolase. *Inorg. Chem.* **2010**, *49* (12), 5344–5346. DOI: 10.1021/ic100414c

(66) Aucott, S. M.; Milton, H. L.; Robertson, S. D.; Slawin, A. M. Z.; Walker, G. D.; Woollins, J. D. Platinum Complexes of Naphthalene-1,8-Dichalcogen and Related Polyaromatic Hydrocarbon Ligands. *Chem.-Eur. J.* **2004**, *10* (7), 1666–1676. DOI: 10.1002/chem.200305352

(67) Ekanayake, D. M.; Fischer, A. A.; Elwood, M. E.; Guzek, A. M.; Lindeman, S. v.; Popescu, C. v.; Fiedler, A. T. Nonheme Iron-Thiolate Complexes as Structural Models of Sulfoxide Synthase Active Sites. *Dalton Trans.* **2020**, *49* (48), 17745–17757. DOI: 10.1039/d0dt03403g

(68) McQuilken, A. C.; Goldberg, D. P. Sulfur Oxygenation in Biomimetic Non-Heme Iron-Thiolate Complexes. *Dalton Trans.* **2012**, *36*, 10883–10899. DOI: 10.1039/c2dt30806a

(69) Rose, M. J.; Betterley, N. M.; Mascharak, P. K. Thiolate S-Oxygenation Controls Nitric Oxide (NO) Photolability of a Synthetic Iron Nitrile Hydratase (Fe-NHase) Model Derived from Mixed Carboxamide/Thiolate Ligand. *J. Am. Chem. Soc.* **2009**, *131* (24), 8340–8341. DOI: 10.1021/ja9004656

(70) Lugo-Mas, P.; Dey, A.; Xu, L.; Davin, S. D.; Benedict, J.; Kaminsky, W.; Hodgson, K. O.; Hedman, B.; Solomon, E. I.; Kovacs, J. A. How Does Single Oxygen Atom Addition Affect the Properties of an Fe-Nitrile Hydratase Analogue? The Compensatory Role of the Unmodified Thiolate. *J. Am. Chem. Soc.* **2006**, *128* (34), 11211–11221. DOI: 10.1021/ja062706k

(71) Shoner, S. C.; Barnhart, D.; Kovacs, J. A. A Model for the Low-Spin, Non-Heme, Thiolate-Ligated Iron Site of Nitrile Hydratase. *Inorg. Chem.* **1995**, *34*, 4517–4518. DOI: 10.1021/ic00122a001

(72) Ellison, J. J.; Nienstedt, A.; Shoner, S. C.; Barnhart, D.; Cowen, J. A., Kovacs, J. A. Reactivity of Five-Coordinate Models for the Thiolate-Ligated Fe Site of Nitrile Hydratase. *J. Am. Chem. Soc.* **1998**, *120* (23), 5691–5700. DOI: 10.1021/ja973129q

(73) Lugo-Mas, P.; Taylor, W.; Schweitzer, D.; Theisen, R. M.; Xu, L.; Shearer, J; Swartz, R. D.; Gleaves, M. C.; DiPasquale, A.; Kaminsky, W.; Kovacs, J. A. Properties of Square-Pyramidal Alkyl−Thiolate Fe^{III} Complexes, Including an Analogue of the Unmodified Form of Nitrile Hydratase. *Inorg. Chem.* **2008**, *47*, 11228-11236. DOI: 10.1021/ic801704n

(74) Villar-Acevedo, G.; Lugo-Mas, P.; Blakely, M. N.; Rees, J. A.; Ganas, A. S.; Hanada, E. M.; Kaminsky, W.; Kovacs, J. A. Metal-Assisted Oxo Atom Addition to an Fe(III)-Thiolate. *J. Am. Chem. Soc.* **2017**, *139*, 119-129. DOI: 10.1021/jacs.6b03512

(75) Heinrich, L.; Li, Y.; Vaissermann, J.; Chottard, G.; Chottard, J.-C. A Pentacoordinated Di-N-Carboxamido-Dithiolato-O-Sulfinato-Iron(III) Complex Related to the Metal Site of Nitrile Hydratase. *Angew. Chem. Int. Ed.* **1999**, *38* (23), 3526–3528. DOI: 10.1002/(SICI)1521-3773(19991203)38:23<3526::AID-ANIE3526>3.0.CO;2-Z

(76) Ozawa, T.; Ikeda, T.; Yano, T.; Arii, H.; Yamaguchi, S.; Funahashi, Y.; Jitsukawa, K.; Masuda, H. Coordination of a Water Molecule to a Square-Pyramidal N2S 3-Type Co(III) Complex Directed to an Active Site of Nitrile Hydratase. *Chem. Lett.* **2005**, *34* (1), 18–19. DOI: 10.1246/cl.2005.18

(77) Yano, T.; Wasada-Tsutsui, Y.; Ikeda, T.; Shibayama, T.; Kajita, Y.; Inomata, T.; Funahashi, Y.; Ozawa, T.; Masuda, H. Co(III) Complexes with N2S3-Type Ligands as Structural/Functional Models for the Isocyanide Hydrolysis Reaction Catalyzed by Nitrile Hydratase. *Inorg. Chem.* **2018**, *57* (8), 4277–4290. DOI: 10.1021/acs.inorgchem.6b02324

(78) Aluri, S.; de Visser, S. P. The Mechanism of Cysteine Oxygenation by Cysteine Dioxygenase Enzymes. *J. Am. Chem. Soc.* **2007**, *129* (48), 14846–14847. DOI: 10.1021/ja0758178

(79) Pierce, B. S.; Gardner, J. D.; Bailey, L. J.; Brunold, T. C.; Fox, B. G. Characterization of the Nitrosyl Adduct of Substrate-Bound Mouse Cysteine Dioxygenase by Electron Paramagnetic Resonance: Electronic Structure of the Active Site and Mechanistic Implications. *Biochemistry* **2007**, *46* (29), 8569–8578. DOI: 10.1021/bi700662d

(80) Stipanuk, M. H. SULFUR AMINO ACID METABOLISM: Pathways for Production and Removal of Homocysteine and Cysteine. *Annu. Rev. Nutr.* **2004**, *24* (1), 539–577. DOI: 10.1146/annurev.nutr.24.012003.132418

(81) Heafield, M. T.; Fearn, S.; Steventon, G. B.; Waring, R. H.; Williams, A. C.; Sturman, S. G. Plasma Cysteine and Sulphate Levels in Patients with Motor Neurone, Parkinson's and Alzheimer's Disease. *Neurosci. Lett.* **1990**, *110* (1–2), 216–220. DOI: 10.1016/0304-3940(90)90814-P

(82) Jeschke, J.; O'Hagan, H. M.; Zhang, W.; Vatapalli, R.; Calmon, M. F.; Danilova, L.; Nelkenbrecher, C.; van Neste, L.; Bijsmans, I. T. G. W.; van Engeland, M.; Gabrielson, E.; Schuebel, K. E.; Winterpacht, A.; Baylin, S. B.; Herman, J. G.; Ahuja, N. Frequent Inactivation of Cysteine Dioxygenase Type 1 Contributes to Survival of Breast Cancer Cells and Resistance to Anthracyclines. *Clin. Cancer Res.* **2013**, *19* (12), 3201–3211. DOI: 10.1158/1078-0432.CCR-12-3751

(83) Stipanuk, M. H.; Simmons, C. R.; Karplus, P. A.; Dominy, J. E. Thiol Dioxygenases: Unique Families of Cupin Proteins. *Amino Acids* **2011**, *41*, 91–102. DOI: 10.1007/s00726-010-0518-2

(84) Simmons, C. R.; Liu, Q.; Huang, Q.; Hao, Q.; Begley, T. P.; Karplus, P. A.; Stipanuk, M. H. Crystal Structure of Mammalian Cysteine Dioxygenase: A Novel Mononuclear Iron Center for Cysteine Thiol Oxidation. *J. Biol. Chem.* **2006**, *281* (27), 18723–18733. DOI: 10.1074/jbc.M601555200

(85) Joseph, C. A.; Maroney, M. J. Cysteine Dioxygenase: Structure and Mechanism. *Chem. Comm.* **2007**, *32*, 3338–3349. DOI: 10.1039/b702158e.

(86) Tchesnokov, E. P.; Wilbanks, S. M.; Jameson, G. N. L. A Strongly Bound High-Spin Iron(II) Coordinates Cysteine and Homocysteine in Cysteine Dioxygenase. *Biochemistry* **2012**, *51* (1), 257–264. DOI: 10.1021/BI201597W

(87) de Visser, S. P.; Straganz, G. D. Why Do Cysteine Dioxygenase Enzymes Contain a 3-His Ligand Motif Rather than a 2His/LAsp Motif like Most Nonheme Dioxygenases? *J. Phys. Chem. A* **2009**, *113* (9), 1835–1846. DOI: 10.1021/JP809700F

(88) Kumar, D.; Thiel, W.; de Visser, S. P. Theoretical Study on the Mechanism of the Oxygen Activation Process in Cysteine Dioxygenase Enzymes. *J. Am. Chem. Soc.* **2011**, *133* (11), 3869–3882. DOI: 10.1021/ja107514f

(89) Crawford, J. A.; Li, W.; Pierce, B. S. Single Turnover of Substrate-Bound Ferric Cysteine Dioxygenase with Superoxide Anion: Enzymatic Reactivation, Product Formation, and a Transient Intermediate. *Biochemistry* **2011**, *50* (47), 10241–10253. DOI: 10.1021/BI2011724

(90) Li, J.; Koto, T.; Davis, I.; Liu, A. Probing the Cys-Tyr Cofactor Biogenesis in Cysteine Dioxygenase by the Genetic Incorporation of Fluorotyrosine. *Biochemistry* **2019**, *58* (17), 2218–2227. DOI: 10.1021/acs.biochem.9b00006

(91) Li, J.; Griffith, W. P.; Davis, I.; Shin, I.; Wang, J.; Li, F.; Wang, Y.; Wherritt, D. J.; Liu, A. Cleavage of a Carbon–Fluorine Bond by an Engineered Cysteine Dioxygenase. *Nat. Chem. Biol.* **2018**, *14* (9), 853–860. DOI: 10.1038/s41589-018-0085-5

(92) Tchesnokov, E. P.; Faponle, A. S.; Davies, C. G.; Quesne, M. G.; Turner, R.; Fellner, M.; Souness, R. J.; Wilbanks, S. M.; de Visser, S. P.; Jameson, G. N. L. An Iron–Oxygen Intermediate Formed during the Catalytic Cycle of Cysteine Dioxygenase. *Chem. Comm.* **2016**, *52* (57), 8814–8817. DOI: 10.1039/C6CC03904A

(93) Jiang, Y.; Widger, L. R.; Kasper, G. D.; Siegler, M. A.; Goldberg, D. P. Iron(II)-Thiolate S -Oxygenation by O2: Synthetic Models of Cysteine Dioxygenase. *J. Am. Chem. Soc.* **2010**, *132* (35), 12214–12215. DOI: 10.1021/JA105591Q

(94) Lombardini, J. B.; Singer, T. P.; Boyer, P. D. Cysteine Oxygenase: II. Studies on the Mechanism of the Reaction with 18Oxygen. *J. Biol. Chem.* **1969**, *244* (5), 1172–1175. DOI: 10.1016/S0021-9258(18)91825-9

(95) Sallmann, M.; Siewert, I.; Fohlmeister, L.; Limberg, C.; Knispel, C. A Trispyrazolylborato Iron Cysteinato Complex as a Functional Model for the Cysteine Dioxygenase. *Angew. Chem. Int. Ed.* **2012**, *51* (9), 2234–2237. DOI: 10.1002/ANIE.201107345

(96) McQuilken, A. C.; Jiang, Y.; Siegler, M. A.; Goldberg, D. P. Addition of Dioxygen to an N 4S(Thiolate) Iron(II) Cysteine Dioxygenase Model Gives a Structurally Characterized Sulfinato-Iron(II) Complex. *J. Am. Chem. Soc.* **2012**, *134* (21), 8758–8761. DOI: 10.1021/JA302112Y

(97) Gordon, J. B.; McGale, J. P.; Prendergast, J. R.; Shirani-Sarmazeh, Z.; Siegler, M. A.; Jameson, G. N. L.; Goldberg, D. P. Structures, Spectroscopic Properties, and Dioxygen Reactivity of 5- and 6-Coordinate Nonheme Iron(II) Complexes: A Combined Enzyme/Model Study of Thiol Dioxygenases. *J. Am. Chem. Soc.* **2018**, *140* (44), 14807–14822. DOI: 10.1021/JACS.8B08349

(98) Fischer, A. A.; Lindeman, S. V; Fiedler, A. T. A Synthetic Model of the Nonheme Iron–Superoxo Intermediate of Cysteine Dioxygenase. *Chem. Comm.* **2018**, *54* (80), 11344–11347. DOI: 10.1039/C8CC06247A

(99) Dedushko, M. A.; Greiner, M. B.; Downing, A. N.; Coggins, M.; Kovacs, J. A. Electronic Structure and Reactivity of Dioxygen-Derived Aliphatic Thiolate-Ligated Fe-Peroxo and Fe(IV) Oxo Compounds. *J. Am. Chem. Soc.* **2021**. DOI: 10.1021/jacs.1c07656

(100) Dedushko, M. A.; Pikul, J. H.; Kovacs, J. A. Superoxide Oxidation by a Thiolate-Ligated Iron Complex and Anion Inhibition. *Inorg Chem* **2021**, *60* (10), 7250–7261. DOI: 10.1021/acs.inorgchem.1c00336

(101) Cohen, G.; Shiffman, D.; Mevarech, M.; Aharonowitz, Y. Microbial Isopenicillin N Synthase Genes: Structure, Function, Diversity and Evolution. *Trends Biotechnol.* **1990**, *8* (C), 105–111. DOI: 10.1016/0167-7799(90)90148-Q

(102) Peck, S. C.; van der Donk, W. A. Go It Alone: Four-Electron Oxidations by Mononuclear Non-Heme Iron Enzymes. *J. Biol. Inorg. Chem.* **2016**, *22* (2), 381–394. DOI: 10.1007/S00775-016-1399-Y

(103) Fisher, J. F.; Meroueh, S. O.; Mobashery, S. Bacterial Resistance to β-Lactam Antibiotics: Compelling Opportunism, Compelling Opportunity. *Chem. Rev*. **2005**, *105* (2), 395–424. DOI: 10.1021/cr030102i

(104) Bush, K.; Bradford, P. A. β-Lactams and β-Lactamase Inhibitors: An Overview. *Cold Spring Harb. Perspect. Med.* **2016**, *6* (8), a025247. DOI: 10.1101/cshperspect.a025247

(105) Pandey, N.; Cascella, M. Beta Lactam Antibiotics. *Antibiotic Discovery and Development* **2022**, 79–117. DOI: 10.1007/978-1-4614-1400-1_3

(106) Elander, R. P. Industrial Production of β-Lactam Antibiotics. *Appl. Microbiol. Biot.* **2003**, *61*, 385–392. DOI: 10.1007/s00253-003-1274-y

(107) France, S.; Weatherwax, A.; Taggi, A. E.; Lectka, T. Advances in the Catalytic, Asymmetric Synthesis of β-Lactams. *Acc. Chem. Res.* **2004**, *37* (8), 592–600. DOI: 10.1021/ar030055g

(108) Staudinger, H. Zur Kenntniss Der Ketene. Diphenylketen. *Justus. Liebigs. Ann. Chem.* **1907**, *356* (1–2), 51–123. DOI: 10.1002/jlac.19073560106

(109) Palomo, C.; Aizpurua, J. M.; Ganboa, I.; Oiarbide, M. Asymmetric Synthesis of β-Lactams by Staudinger Ketene-Imine Cycloaddition Reaction. *Eur. J. Org. Chem.* **1999**, *12*, 3223–3235. DOI: 10.1002/(SICI)1099-0690(199912)1999:12<3223::AID-EJOC3223>3.0.CO;2-1

(110) Toda, F.; Miyamoto, H.; Inoue, M.; Yasaka, S.; Matijasic, I. Enantioselective Photocyclization of Amides to β-Lactam Derivatives in Inclusion Crystals with an Optically Active Host. *J. Org. Chem.* **2000**, *65* (9), 2728–2732. DOI: 10.1021/jo991832m

(111) Ishibashi, H.; Kameoka, C.; Kodama, K.; Ikeda, M. Asymmetric Radical Cyclization Leading to β-Lactams: Stereoselective Synthesis of Chiral Key Intermediates for Carbapenem Antibiotics PS-5 and Thienamycin. *Tetrahedron* **1996**, *52* (2), 489–502. DOI: 10.1016/0040-4020(95)00902-7

(112) Hegg, E. L.; Jr, L. Q. The 2-His-1-Carboxylate Facial Triad - An Emerging Structural Motif in Mononuclear Non-Heme Iron(II) Enzymes. *Eur. J. Biochem.* **1997**, *250* (3), 625–629. DOI: 10.1111/j.1432-1033.1997.t01-1-00625.x

(113) Roach, P. L.; Clifton, I. J.; Fülöp, V.; Harlos, K.; Barton, G. J.; Hajdu, J.; Andersson, I.; Schofield, C. J.; Baldwin, J. E. Crystal Structure of Isopenicillin N Synthase Is the First from a New Structural Family of Enzymes. *Nature* **1995**, *375* (6533), 700–704. DOI: 10.1038/375700a0

(114) Roach, P. L.; Clifton, I. J.; Hensgens, C. M. H.; Shibata, N.; Long, A. J.; Strange, R. W.; Hasnain, S. S.; Schofield, C. J.; Baldwin, J. E.; Hajdu, J. Anaerobic Crystallisation of an

Isopenicillin N Synthase . Fe(II) . Substrate Complex Demonstrated by X-Ray Studies. *Eur. J. Biochem.* **1996**, *242* (3), 736–740. DOI: 10.1111/j.1432-1033.1996.0736r.x

(115) Roach, P. L.; Clifton, I. J.; Hensgens, C. M. H.; Shibata, N.; Schofield, C. J.; Hajdu, J.; Baldwin, J. E. Structure of Isopenicillin N Synthase Complexed with Substrate and the Mechanism of Penicillin Formation. *Nature* **1997**, *387* (6635), 827–830. DOI: 10.1038/42990

(116) Roach, P. L.; Clifton, I. J.; Fülöp, V.; Harlos, K.; Barton, G. J.; Hajdu, J.; Andersson, I.; Schofield, C. J.; Baldwin, J. E. Crystal Structure of Isopenicillin N Synthase Is the First from a New Structural Family of Enzymes. *Nature* **1995**, *375* (6533), 700–704. DOI: 10.1038/375700a0

(117) McNeill, L. A.; Brown, T. J. N.; Sami, M.; Clifton, I. J.; Burzlaff, N. I.; Claridge, T. D. W.; Adlington, R. M.; Baldwin, J. E.; Rutledge, P. J.; Schofield, C. J. Terminally Truncated Isopenicillin N Synthase Generates a Dithioester Product: Evidence for a Thioaldehyde Intermediate during Catalysis and a New Mode of Reaction for Non-Heme Iron Oxidases. *Chem.-Eur. J.* **2017**, *23* (52), 12815–12824. DOI: 10.1002/chem.201701592

(118) Goudarzi, S.; Babicz, J. T.; Kabil, O.; Banerjee, R.; Solomon, E. I. Spectroscopic and Electronic Structure Study of ETHE1: Elucidating the Factors Influencing Sulfur Oxidation and Oxygenation in Mononuclear Nonheme Iron Enzymes. *J. Am. Chem. Soc.* **2018**, *140* (44), 14887–14902. DOI: 10.1021/jacs.8b09022

(119) Brown, C. D.; Neidig, M. L.; Neibergall, M. B.; Lipscomb, J. D.; Solomon, E. I. VTVH-MCD and DFT Studies of Thiolate Bonding to {FeNO}7/ {FeO2}8 Complexes of Isopenicillin N Synthase: Substrate Determination of Oxidase versus Oxygenase Activity

in Nonheme Fe Enzymes. *J. Am. Chem. Soc.* **2007**, *129* (23), 7427–7438. DOI: 10.1021/ja071364v

(120) Tamanaha, E.; Zhang, B.; Guo, Y.; Chang, W. C.; Barr, E. W.; Xing, G.; St Clair, J.; Ye, S.; Neese, F.; Bollinger, J. M.; Krebs, C. Spectroscopic Evidence for the Two C-H-Cleaving Intermediates of Aspergillus Nidulans Isopenicillin N Synthase. *J. Am. Chem. Soc.* **2016**, *138* (28), 8862–8874. DOI: 10.1021/jacs.6b04065

(121) Wirstam, M.; Siegbahn, P. E. M. A Mechanistic Study of Isopenicillin N Formation Using Density Functional Theory. *J. Am. Chem. Soc.* **2000**, *122* (35), 8539–8547. DOI: 10.1021/JA001103K

(122) Lundberg, M.; Siegbahn, P. E. M.; Morokuma, K. The Mechanism for Isopenicillin N Synthase from Density-Functional Modeling Highlights the Similarities with Other Enzymes in the 2-His-1-Carboxylate Family. *Biochemistry* **2008**, *47* (3), 1031–1042. DOI: 10.1021/BI701577Q

(123) Lundberg, M.; Kawatsu, T.; Vreven, T.; Frisch, M. J.; Morokuma, K. Transition States in a Protein Environment - ONIOM QM:MM Modeling of Isopenicillin N Synthesis. *J. Chem. Theory Comput.* **2009**, *5* (1), 222–234. DOI: 10.1021/CT800457G

(124) Chapman, N. C.; Rutledge, P. J. Isopenicillin N Synthase: Crystallographic Studies. *ChemBioChem* **2021**, *22* (10), 1687–1705. DOI: 10.1002/CBIC.202000743

(125) Burzlaff, N. I.; Rutledge, P. J.; Clifton, I. J.; Hensgens, C. M.; Pickford, M.; Adlington, R. M.; Roach, P. L.; Baldwin, J. E. The Reaction Cycle of Isopenicillin N Synthase Observed by X-Ray Diffraction. *Nature* **1999**, *401*, 721-724. DOI: 10.1038/44400

(126) Ge, W.; Clifton, I. J.; Stok, J. E.; Adlington, R. M.; Baldwin, J. E.; Rutledge, P. J. Isopenicillin N Synthase Mediates Thiolate Oxidation to Sulfenate in a Depsipeptide

Substrate Analogue: Implications for Oxygen Binding and a Link to Nitrile Hydratase? *J. Am. Chem. Soc.* **2008**, *130*, 10096-10102. DOI: 10.1021/ja8005397

(127) Ogle, J. M.; Clifton, I. J.; Rutledge, P. J.; Elkins, J. M.; Burzlaff, N. I.; Adlington, R. M.; Roach, P. L.; Baldwin, J. E. Alternative Oxidation by Isopenicillin N Synthase Observed by X-Ray Diffraction. *Chem. Biol.* **2001**, *8* (12), 1231–1237. DOI: 10.1016/S1074-5521(01)00090-4

(128) Makris, T. M.; Koenig, K. von; Schlichting, I.; Sligar, S. G. The Status of High-Valent Metal Oxo Complexes in the P450 Cytochromes. *J. Inorg. Biochem.* **2006**, *100* (4), 507–518. DOI: 10.1016/J.JINORGBIO.2006.01.025

(129) Galonić, D. P.; Barr, E. W.; Walsh, C. T.; Bollinger, J. M.; Krebs, C. Two Interconverting Fe(IV) Intermediates in Aliphatic Chlorination by the Halogenase CytC3. *Nat. Chem. Biol.* **2007**, *3* (2), 113–116. DOI: 10.1038/nchembio856

(130) Hoffart, L. M.; Barr, E. W.; Guyer, R. B.; Bollinger, J. M.; Krebs, C. Direct Spectroscopic Detection of a C-H-Cleaving High-Spin Fe(IV) Complex in a Prolyl-4-Hydroxylase. *P. Natl. Acad. Sci. USA* **2006**, *103* (40), 14738–14743. DOI: 10.1073/PNAS.0604005103

(131) Bollinger, J. M.; Krebs, C. Stalking Intermediates in Oxygen Activation by Iron Enzymes: Motivation and Method. *J. Inorg. Biochem.* **2006**, *100* (4), 586–605. DOI: 10.1016/J.JINORGBIO.2006.01.022

(132) Nam, W. High-Valent Iron(IV)-Oxo Complexes of Heme and Non-Heme Ligands in Oxygenation Reactions. *Acc. Chem. Res.* **2007**, *40* (7), 522–531. DOI: 10.1021/AR700027F

(133) Shan, X.; Que, L. High-Valent Nonheme Iron-Oxo Species in Biomimetic Oxidations. *J. Inorg. Biochem.* **2006**, *100* (4), 421–433. DOI: 10.1016/J.JINORGBIO.2006.01.014

(134) McDonald, A. R.; Que, L. High-Valent Nonheme Iron-Oxo Complexes: Synthesis, Structure, and Spectroscopy. *Coord. Chem. Rev.* **2013**, *257* (2), 414–428. DOI: 10.1016/J.CCR.2012.08.002

(135) Ray, K.; Pfaff, F. F.; Wang, B.; Nam, W. Status of Reactive Non-Heme Metal-Oxygen Intermediates in Chemical and Enzymatic Reactions. *J. Am. Chem. Soc.* **2014**, *136* (40), 13942–13958. DOI: 10.1021/JA507807V

(136) Sahu, S.; Goldberg, D. P. Activation of Dioxygen by Iron and Manganese Complexes: A Heme and Nonheme Perspective. *J. Am. Chem. Soc.* **2016**, *138* (36), 11410–11428. DOI: 10.1021/JACS.6B05251

(137) Chiang, C. W.; Kleespies, S. T.; Stout, H. D.; Meier, K. K.; Li, P. Y.; Bominaar, E. L.; Que, L.; Münck, E.; Lee, W. Z. Characterization of a Paramagnetic Mononuclear Nonheme Iron-Superoxo Complex. *J. Am. Chem. Soc.* **2014**, *136* (31), 10846–10849. DOI: 10.1021/JA504410S

(138) Luo, Y.-R. *Comprehensive Handbook of Chemical Bond Energies*; Press, C. R. C., Ed.; Taylor and Francis Group: Boca Raton, FL, 2007.

(139) Oddon, D.; Chiba, Y.; Nakazawa, D.; Ohta, T.; Ogura, T.; Hikichi, S. Characterization of Mononuclear Non-Heme Iron(III)-Superoxo Complex with a Five-Azole Ligand Set. *Angew. Chem. Int. Ed.* **2015**, *54* (25), 7336–7339. DOI: 10.1002/ANIE.201502367

(140) Hong, S.; Sutherlin, K. D.; Park, J.; Kwon, E.; Siegler, M. A.; Solomon, E. I.; Nam, W. Crystallographic and Spectroscopic Characterization and Reactivities of a Mononuclear Non-Haem Iron(III)-Superoxo Complex. *Nat. Comm.* **2014**, *5* (1), 1–7. DOI: 10.1038/ncomms6440

(141) Winslow, C.; Lee, H. B.; Field, M. J.; Teat, S. J.; Rittle, J. Structure and Reactivity of a High-Spin, Nonheme Iron(III)-Superoxo Complex Supported by Phosphinimide Ligands. *J. Am. Chem. Soc.* **2021**, *143* (34), 13686–13693. DOI: 10.1021/JACS.1C05276

(142) Shaw, G. H. Earth's Atmosphere – Hadean to Early Proterozoic. *Geochemistry* **2008**, *68* (3), 235–264. DOI: 10.1016/J.CHEMER.2008.05.001

(143) Baumgartner, R. J.; van Kranendonk, M. J.; Wacey, D.; Fiorentini, M. L.; Saunders, M.; Caruso, S.; Pages, A.; Homann, M.; Guagliardo, P. Nano−porous Pyrite and Organic Matter in 3.5-Billion-Year-Old Stromatolites Record Primordial Life. *Geology* **2019**, *47* (11), 1039–1043. DOI: 10.1130/G46365.1

(144) Kopp, R. E.; Kirschvink, J. L.; Hilburn, I. A.; Nash, C. Z. The Paleoproterozoic Snowball Earth: A Climate Disaster Triggered by the Evolution of Oxygenic Photosynthesis. *P. Natl. Acad. Sci. USA* **2005**, *102* (32), 11131–11136. DOI: 10.1073/PNAS.0504878102

(145) Gross, J.; Bhattacharya, D. Uniting Sex and Eukaryote Origins in an Emerging Oxygenic World. *Biol. Direct* **2010**, *5* (1), 1–20. DOI: 10.1186/1745-6150-5-53

(146) Barber, J. Photosynthetic Energy Conversion: Natural and Artificial. *Chem. Soc. Rev.* **2008**, *38* (1), 185–196. DOI: 10.1039/B802262N

(147) Armstrong, F. A. Why Did Nature Choose Manganese to Make Oxygen? *Philos. T. Roy. Soc. B.* **2008**, *363* (1494), 1263–1270. DOI: 10.1098/rstb.2007.2223

(148) Renger, G. Light Induced Oxidative Water Splitting in Photosynthesis: Energetics, Kinetics and Mechanism. *J. Photoch. Photobio. B*. **2011**, *104,* 35–43. DOI: 10.1016/j.jphotobiol.2011.01.023

(149) Raval, M. K.; Biswal, B.; Biswal, U. C. The Mystery of Oxygen Evolution: Analysis of Structure and Function of Photosystem II, the Water-Plastoquinone Oxido-Reductase. *Photosynth. Res.* **2005**, *85*, 267–293. DOI: 10.1007/s11120-005-8163-4

(150) Nocera, D. G. The Artificial Leaf. *Acc. Chem. Res.* **2012**, *45* (5), 767–776. DOI: 10.1021/ar2003013

(151) Anderson, A. B.; Albu, T. v. Ab Initio Determination of Reversible Potentials and Activation Energies for Outer-Sphere Oxygen Reduction to Water and the Reverse Oxidation Reaction. *J. Am. Chem. Soc.* **1999**, *121* (50), 11855–11863. DOI: 10.1021/ja992735d

(152) Yocum, C. F. The Calcium and Chloride Requirements of the O2 Evolving Complex. *Coordin. Chem. Rev.* **2008**, *252*, 296–305. DOI: 10.1016/j.ccr.2007.08.010

(153) Cox, N.; Pantazis, D. A.; Neese, F.; Lubitz, W. Biological Water Oxidation. *Acc. Chem. Res.* **2013**, *46* (7), 1588–1596. DOI: 10.1021/ar3003249

(154) Murray, J. W.; Maghlaoui, K.; Kargul, J.; Ishida, N.; Lai, T. L.; Rutherford, A. W.; Sugiura, M.; Boussac, A.; Barber, J. X-Ray Crystallography Identifies Two Chloride Binding Sites in the Oxygen Evolving Centre of Photosystem II. *Energy Environ. Sci.* **2008**, *1* (1), 161–166. DOI: 10.1039/b810067p

(155) Kawakami, K.; Umena, Y.; Kamiya, N.; Shen, J. R. Location of Chloride and Its Possible Functions in Oxygen-Evolving Photosystem II Revealed by X-Ray Crystallography. *P. Natl. Acad. Sci. USA* **2009**, *106* (21), 8567–8572. DOI: 10.1073/pnas.0812797106

(156) KOK, B.; FORBUSH, B.; McGLOIN, M. COOPERATION OF CHARGES IN PHOTOSYNTHETIC O2 EVOLUTION–I. A LINEAR FOUR STEP MECHANISM. *Photochem. Photobiol.* **1970**, *11* (6), 457–475. DOI: 10.1111/j.1751-1097.1970.tb06017.x

(157) Joliot, P.; Barbieri, G.; Chabaud, R. UN NOUVEAU MODELE DES CENTRES PHOTOCHIMIQUES DU SYSTEME II. *Photochem. Photobiol.* **1969**, *10* (5), 309–329. DOI: 10.1111/j.1751-1097.1969.tb05696.x

(158) Cox, N.; Retegan, M.; Neese, F.; Pantazis, D. A.; Boussac, A.; Lubitz, W. Electronic Structure of the Oxygen-Evolving Complex in Photosystem II Prior to O-O Bond Formation. *Science* **2014**, *345* (6198), 804–808. DOI: 10.1126/science.1254910

(159) Hatakeyama, M.; Ogata, K.; Fujii, K.; Yachandra, V. K.; Yano, J.; Nakamura, S. Structural Changes in the S3 State of the Oxygen Evolving Complex in Photosystem II. *Chem. Phys. Lett.* **2016**, *651*, 243–250. DOI: 10.1016/j.cplett.2016.03.010

(160) Siegbahn, P. E. M. O-O Bond Formation in the S4 State of the Oxygen-Evolving Complex in Photosystem II. *Chem.-Eur. J.* **2006**, *12* (36), 9217–9227. DOI: 10.1002/chem.200600774

(161) McEvoy, J. P.; Brudvig, G. W. Water-Splitting Chemistry of Photosystem II. *Chem. Rev.* **2006**, *106* (11), 4455–4483. DOI: 10.1021/cr0204294

(162) Betley, T. A.; Wu, Q.; Van Voorhis, T.; Nocera, D. G. Electronic Design Criteria for O-O Bond Formation via Metal-Oxo Complexes. *Inorg. Chem.* **2008**, *47* (6), 1849–1861. DOI: 10.1021/ic701972n

(163) Retegan, M.; Krewald, V.; Mamedov, F.; Neese, F.; Lubitz, W.; Cox, N.; Pantazis, D. A. A Five-Coordinate Mn(IV) Intermediate in Biological Water Oxidation: Spectroscopic Signature and a Pivot Mechanism for Water Binding. *Chem. Sci.* **2016**, *7* (1), 72–84. DOI: 10.1039/c5sc03124a

(164) Haddy, A.; Lakshmi, K. V.; Brudvig, G. W.; Frank, H. A. Q-Band EPR of the S2 State of Photosystem II Confirms an S = 5/2 Origin of the X-Band g = 4.1 Signal. *Biophys. J.* **2004**, *87* (4), 2885–2896. DOI: 10.1529/biophysj.104.040238

(165) Pantazis, D. A.; Ames, W.; Cox, N.; Lubitz, W.; Neese, F. Two Interconvertible Structures That Explain the Spectroscopic Properties of the Oxygen-Evolving Complex of Photosystem II in the S2 State. *Angew. Chem. Int. Ed.* **2012**, *51* (39), 9935–9940. DOI: 10.1002/anie.201204705

(166) Ibrahim, M.; Fransson, T.; Chatterjee, R.; Cheah, M. H.; Hussein, R.; Lassalle, L.; Sutherlin, K. D.; Young, I. D.; Fuller, F. D.; Gul, S.; Kim, I. S.; Simon, P. S.; de Lichtenberg, C.; Chernev, P.; Bogacz, I.; Pham, C. C.; Orville, A. M.; Saichek, N.; Northen, T.; Batyuk, A.; Carbajo, S.; Alonso-Mori, R.; Tono, K.; Owada, S.; Bhowmick, A.; Bolotovsky, R.; Mendez, D.; Moriarty, N. W.; Holton, J. M.; Dobbek, H.; Brewster, A. S.; Adams, P. D.; Sauter, N. K.; Bergmann, U.; Zouni, A.; Messinger, J.; Kern, J.; Yachandra, V. K.; Yano, J. Untangling the Sequence of Events during the S2 → S3 Transition in Photosystem II and Implications for the Water Oxidation Mechanism. *P. Natl. Acad. Sci. USA* **2020**, *117* (23), 12624–12635. DOI: 10.1073/pnas.2000529117

(167) Pantazis, D. A. Missing Pieces in the Puzzle of Biological Water Oxidation. *ACS Catal*. **2018**, *8* (10) 9477–9507. DOI: 10.1021/acscatal.8b01928

(168) Ames, W.; Pantazis, D. A.; Krewald, V.; Cox, N.; Messinger, J.; Lubitz, W.; Neese, F. Theoretical Evaluation of Structural Models of the S 2 State in the Oxygen Evolving Complex of Photosystem II: Protonation States and Magnetic Interactions. *J. Am. Chem. Soc.* **2011**, *133* (49), 19743–19757. DOI: 10.1021/ja2041805

(169) Boussac, A.; Rutherford, A. W.; Sugiura, M. Electron Transfer Pathways from the S2-States to the S3-States Either after a Ca2 +/Sr2 + or a Cl-/I- Exchange in Photosystem II from Thermosynechococcus Elongatus. *Biochim. Biophys. Acta Bioenerg.* **2015**, *1847* (6–7), 576–586. DOI: 10.1016/j.bbabio.2015.03.006

(170) Gersten, S. W.; Samuels, G. J.; Meyer, T. J. Catalytic Oxidation of Water by an Oxo-Bridged Ruthenium Dimer. *J. Am. Chem. Soc.* **1982**, *104* (14), 4029–4030. DOI: 10.1021/ja00378a053

(171) Binstead, R. A.; Chronister, C. W.; Ni, J.; Hartshorn, C. M.; Meyer, T. J. Mechanism of Water Oxidation by the μ-Oxo Dimer [(Bpy)2(H2O)Ru(III)ORu(III)(OH2)(Bpy)2]4+. *J. Am. Chem. Soc.* **2000**, *122* (35), 8464–8473. DOI: 10.1021/ja993235n

(172) Liu, F.; Concepcion, J. J.; Jurss, J. W.; Cardolaccia, T.; Templeton, J. L.; Meyer, T. J. Mechanisms of Water Oxidation from the Blue Dimer to Photosystem II. *Inorg. Chem*. **2008**, *47* (6), 1727–1752. DOI: 10.1021/ic701249s

(173) Matsumoto, Y.; Sato, E. Electrocatalytic Properties of Transition Metal Oxides for Oxygen Evolution Reaction. *Mater. Chem. Phys.* **1986**, *14* (5), 397–426. DOI: 10.1016/0254-0584(86)90045-3

(174) Brimblecombe, R.; Dismukes, G. C.; Swiegers, G. F.; Spiccia, L. Molecular Water-Oxidation Catalysts for Photoelectrochemical Cells. *Dalton Trans.* **2009**, *43*, 9374–9384. DOI: 10.1039/B912669D

(175) Wieghardt, K. The Active Sites in Manganese-Containing Metalloproteins and Inorganic Model Complexes. *Angew. Chem. Int. Ed.* **1989**, *28* (9), 1153–1172. DOI: 10.1002/ANIE.198911531

(176) Cady, C. W.; Crabtree, R. H.; Brudvig, G. W. Functional Models for the Oxygen-Evolving Complex of Photosystem II. *Coord. Chem. Rev.* **2008**, *252* (3–4), 444–455. DOI: 10.1016/J.CCR.2007.06.002

(177) McEvoy, J. P.; Brudvig, G. W. Water-Splitting Chemistry of Photosystem II. *Chem. Rev.* **2006**, *106* (11), 4455–4483. DOI: 10.1021/CR0204294

(178) Dismukes, G. C.; Brimblecombe, R.; Felton, G. A. N.; Pryadun, R. S.; Sheats, J. E.; Spiccia, L.; Swiegers, G. F. Development of Bioinspired Mn4O4-Cubane Water Oxidation Catalysts: Lessons from Photosynthesis. *Acc. Chem. Res.* **2009**, *42* (12), 1935–1943. DOI: 10.1021/AR900249X

(179) Kanady, J. S.; Tsui, E. Y.; Day, M. W.; Agapie, T. A Synthetic Model of the Mn 3Ca Subsite of the Oxygen-Evolving Complex in Photosystem II. *Science* **2011**, *333* (6043), 733–736. DOI: 10.1126/science.1206036

(180) Tsui, E. Y.; Agapie, T. Reduction Potentials of Heterometallic Manganese-Oxido Cubane Complexes Modulated by Redox-Inactive Metals. *P. Natl. Acad. Sci. USA* **2013**, *110* (25), 10084–10088. DOI: 10.1073/pnas.1302677110

(181) Lin, P. H.; Takase, M. K.; Agapie, T. Investigations of the Effect of the Non-Manganese Metal in Heterometallic-Oxido Cluster Models of the Oxygen Evolving Complex of Photosystem II: Lanthanides as Substitutes for Calcium. *Inorg. Chem.* **2015**, *54* (1), 59–64. DOI: 10.1021/ic5015219

(182) Tsui, E. Y.; Kanady, J. S.; Agapie, T. Synthetic Cluster Models of Biological and Heterogeneous Manganese Catalysts for O2 Evolution. *Inorg. Chem.* **2013**, *52* (24), 13833–13848. DOI: 10.1021/ic402236f

(183) Suseno, S.; McCrory, C. C. L.; Tran, R.; Gul, S.; Yano, J.; Agapie, T. Molecular Mixed-Metal Manganese Oxido Cubanes as Precursors to Heterogeneous Oxygen Evolution Catalysts. *Chem.-Eur. J.* **2015**, *21* (38), 13420–13430. DOI: 10.1002/chem.201501104

(184) Lionetti, D.; Suseno, S.; Tsui, E. Y.; Lu, L.; Stich, T. A.; Carsch, K. M.; Nielsen, R. J.; Goddard, W. A.; Britt, R. D.; Agapie, T. Effects of Lewis Acidic Metal Ions (M) on Oxygen-Atom Transfer Reactivity of Heterometallic Mn 3 MO 4 Cubane and Fe 3 MO(OH) and Mn 3 MO(OH) Clusters. *Inorg. Chem.* **2019**, *58* (4), 2336–2345. DOI: 10.1021/acs.inorgchem.8b02701

(185) Kanady, J. S.; Lin, P. H.; Carsch, K. M.; Nielsen, R. J.; Takase, M. K.; Goddard, W. A.; Agapie, T. Toward Models for the Full Oxygen-Evolving Complex of Photosystem II by Ligand Coordination to Lower the Symmetry of the Mn3CaO4 Cubane: Demonstration That Electronic Effects Facilitate Binding of a Fifth Metal. *J. Am. Chem. Soc.* **2014**, *136* (41), 14373–14376. DOI: 10.1021/ja508160x

(186) Zhang, C.; Chen, C.; Dong, H.; Shen, J. R.; Dau, H.; Zhao, J. A Synthetic Mn4Ca-Cluster Mimicking the Oxygen-Evolving Center of Photosynthesis. *Science* **2015**, *348* (6235), 690–693. DOI: 10.1126/science.aaa6550

(187) Nagashima, S.; Nakasako, M.; Dohmae, N.; Tsujimura, M.; Takio, K.; Odaka, M.; Yohda, M.; Kamiya, N.; Endo, I. Novel Non-Heme Iron Center of Nitrile Hydratase with a Claw Setting of Oxygen Atoms. *Nat. Struct. Biol.* **1998**, *5* (5), 347–351. DOI: 10.1038/nsb0598-347

(188) Ye, S.; Wu, X.; Wei, L.; Tang, D.; Sun, P.; Bartlam, M.; Rao, Z. An Insight into the Mechanism of Human Cysteine Dioxygenase: KEY ROLES OF THE THIOETHER-

BONDED TYROSINE-CYSTEINE COFACTOR. *J. Biol. Chem.* **2007**, *282* (5), 3391–3402. DOI: 10.1074/JBC.M609337200

(189) Roach, P. L.; Clifton, I. J.; Hensgens, C. M. H.; Shibata, N.; Schofield, C. J.; Hajdu, J.; Baldwin, J. E. Structure of IsopenicillinN Synthase Complexed with Substrate and the Mechanism Of Penicillin Formation. *Nature* **1997**, *387* (6635), 827–830. DOI: 10.1038/42990

(190) Tanaka, A.; Fukushima, Y.; Kamiya, N. Two Different Structures of the Oxygen-Evolving Complex in the Same Polypeptide Frameworks of Photosystem II. *J. Am. Chem. Soc.* **2017**, *139* (5), 1718–1721. DOI: 10.1021/jacs.6b0966

Chapter 2. Ligand Constraint Effects on Oxo-Atom Addition

2.1. Introduction

Previous work in the biomimetic modeling of non-heme iron enzymes by the Kovacs group has led to the development of a series of related complexes featuring thiolates in the coordination sphere. Initially, the properties of nitrile hydratase were probed with $[Fe^{III}(ADIT)_2]^+$,[1] an N_4S_2 complex which matched the structural and electronic properties of NHase. It features a low-spin $S = 1/2$ iron center arising from the covalent contributions of the Fe-S bonds. $[Fe^{III}(ADIT)_2]^+$ also has an electronic spectrum that is substantially similar to that of NHase, with an absorption band at approximately 700 nm matching the 710 nm band of NHase.[2] This complex could be reacted with a suitable oxo-atom donor such as *N*-sulfonyloxaziridine to produce a singly oxygenated $[Fe^{III}(ADIT)(ADIT\text{-}O)]^+$ complex mimicking the oxidized sulfur atoms found in NHase (**Scheme 2-1**).[3] This complex retained the $S = 1/2$ spin state of the base complex, with the weakening of the iron-sulfenate bond being compensated for by the unmodified thiolate. Its electronic absorption spectrum differs somewhat dramatically from the base complex, with the 700 nm band shifting to 575 nm as a result of the reduced π interactions. When this S=O bond is protonated to form an S-OH by HBF_4, the spin state is still maintained, and the absorption maximum shifts from 575 nm to 622 nm due to the renewed π interactions. This complex demonstrated the possibilities that

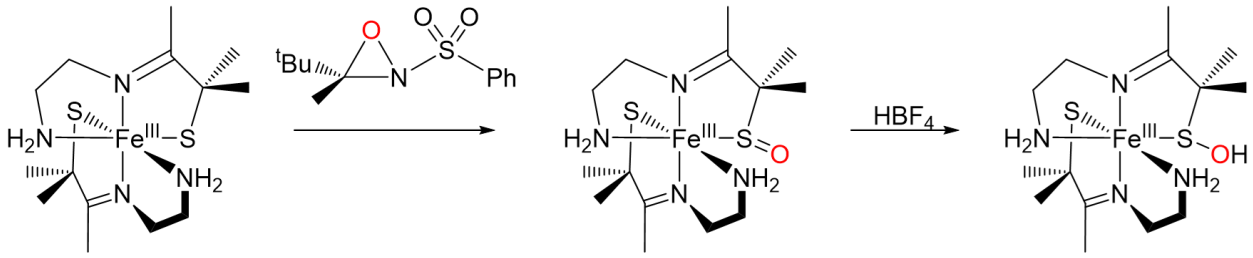

Scheme 2-1. Addition of tert-butyl N-sulfonyloxaziridine to $[Fe^{III}(ADIT)_2]^+$ to produce a sulfenate and its subsequent protonation by HBF_4.

cysteinates may help to modulate the pK_a, lability of ligands, and the redox potentials of the metal center.

A drawback of the $[Fe^{III}(ADIT)_2]^+$ system is that it is by design six-coordinate with no labile ligands, unlike the active sites it models, which contain one or more labile group to allow them to perform their catalysis. A series of N_3S_2 chiral helical ligands was developed in order to provide an open coordination site while also precluding the formation of thiolate-bridged dimers or oligomers. These ligands are derived from a Schiff-base condensation involving an amine such as bis(3-aminopropyl)amine and a carbonyl with a nearby thiolate such as 3-mercapto-3-methyl-2-butanone to form a helical chain which encloses a metal center (**Scheme 2-2**). These ligands mimic a bound cysteine residue in an enzyme and allow modifications such as methylation of the ligand backbone, shortening or lengthening of the amine linker to control steric effects, and the presence of methyl groups or hydrogen atoms β to the coordinating thiolates.[4,5] A survey of several complexes $[M^{II}S_2{}^{R2}N_3(Pr,Pr)]$—where M = Fe, Co, Ni, or Zn and R = H or Me—found that the helicity and angular distortion of the ligand was generally correlated with the ionic radius of the metal center.[4]

The oxidized iron and cobalt complexes of this series were initially used to study the properties of nitrile hydratase, a class of enzyme which performs catalysis using either an iron or cobalt center.[6,7] It was found that $Fe^{II}(S_2{}^{Me2}N_2NH(Pr,Pr))$ (**Figure 2-1**, **1**) was a pale yellow-green

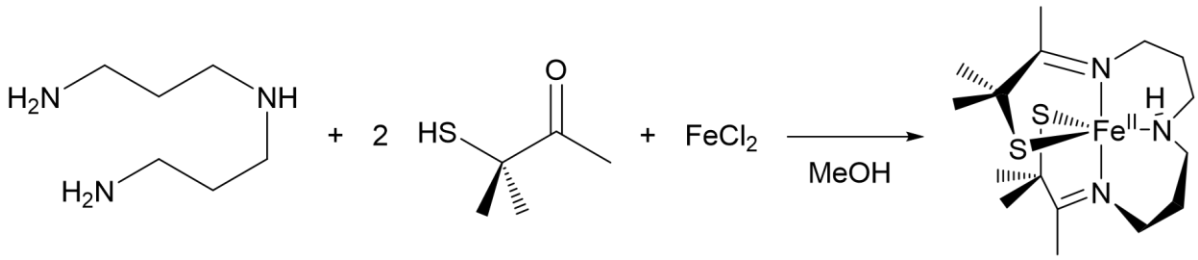

Scheme 2-2. General synthesis of bis-thiolate ligated iron complexes, specifically $Fe^{II}(S_2{}^{Me2}N_2NH(Pr,Pr))$ (**1**).

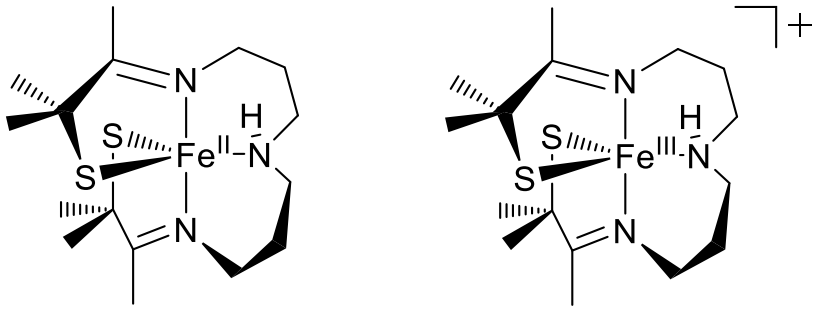

Figure 2-1. $Fe^{II}(S_2^{Me2}N_2NH(Pr,Pr))$ (**1**) (left) and $[Fe^{III}(S_2^{Me2}N_2NH(Pr,Pr))]^+$ (**2**) (right).

complex with λ_{max} (ε, $M^{-1}cm^{-1}$) = 359 nm (820) that can be oxidized to $[Fe^{III}(S_2^{Me2}N_2NH(Pr,Pr))](PF_6)$ (**Figure 2-1**, **2**) by ferrocenium hexafluorophosphate ($FcPF_6$). **2** is a red/brown complex with λ_{max} (ε, $M^{-1}cm^{-1}$) = 416 nm (4200).[4] This complex has a low-spin S = 1/2 ground state at low temperatures, with a higher spin state becoming thermally accessible around 150 K, similar to what was found for NHase.[8] While it does not bind nitriles, **2** does reversibly coordinate azide, forming a yellow-green complex at low temperatures with λ_{max} (ε, $M^{-1}cm^{-1}$) = 330 (7400), 460 (2200), and 708 nm (1600) and reforming **2** when warmed to room temperature.[9] The cobalt analogue, $[Co^{III}(S_2^{Me2}N_2NH(Pr,Pr))](PF_6)$ binds thiocyanates, azide, and ammonia, but not nitriles.[10,11] Oxidizing one of the two thiolates by air to a sulfinate produces $[Co^{III}(S^{Me2}(S^{O2})N_3(Pr,Pr))]^+$, which does not bind azide or thiocyanate due to a change in geometry which forces a substrate to bind *trans* to the sulfinate and thus to experience the stronger *trans* effect of the sulfinate. Oxidizing the remaining thiolate to a sulfenate produces $[Co(III)((\eta^2\text{-}SO)(S^{O2})N_3(Pr,Pr))]^+$, which is unreactive to previously discussed substrates.[12]

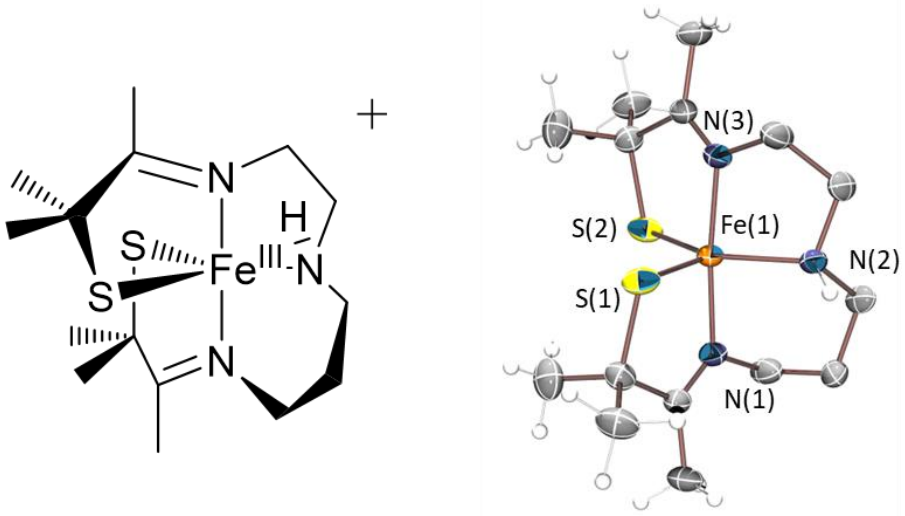

Figure 2-2. Schematic drawing (left) and ORTEP diagram (right) of $[Fe^{III}(S_2{}^{Me2}N_3(Et,Pr))]^+$ (**3**). Thermal ellipsoids at 50% probability level.

By removing a methylene unit from the amide backbone of **2**, the electronically similar but sterically constrained complex $[Fe^{III}(S_2{}^{Me2}N_3(Et,Pr))](PF_6)$ (**Figure 2-2**, **3**) is formed. Compared to **2**, it retains the same five-coordinate N_3S_2 environment, but has a S–Fe–N bond angle 9.5° wider (141.8° vs 132.3°), giving it a relatively more open sixth coordination site. **2** is largely trigonal bipyramidal with $\tau = 0.763$, whereas **3** is closer to square pyramidal with $\tau = 0.456$. This complex retains the $S = 1/2$ spin state over a wider range of temperatures than **2** does. Limiting the flexibility of the complex in this way also has effects on the electronic structure of the complex due to the modified orbital overlap; it is reduced at -455 mV vs SCE in MeOH compared to -400 mV for **2**.[5]

Like **2**, **3** is capable of binding a variety of substrates. It binds azide, as **2** does, in the open sixth coordination site of the S–Fe–N angle, *cis* to one sulfur and *trans* to the other. In **3**, azide was bound irreversibly in DCM, THF, and MeCN; but reversibly in MeOH, requiring low temperatures to generate appreciable amounts of the azide bound complex. The more constrained **3** was found to bind azide much more quickly and strongly than **2** in a variety of solvents.[5] More notably, **3** was found to bind a much wider variety of substrates than **2**, coordinating nitriles (the substrate of NHase), alcohols, thiocyanates, and amides (the product of NHase). When a substrate is bound to

the sixth coordination site, it is typically accompanied by the growth of a peak in the range of 700-900 nm in the electronic absorption spectrum and a more rhombic EPR spectrum with a wider range of *g* values compared to the five-coordinate complex.[13]

More recent work in the Kovacs group has focused on this class of complexes as biomimetic models of cysteine dioxygenase (CDO).[14] Work with **2** and oxo-atom donors such as iodosylbenzene and isopropyl 2-iodoxybenzoate has shown that **2** forms an Fe-oxo-atom-donor adduct species at low temperature, which goes on to form a singly oxygenated Fe–S–O cyclic sulfenate species. Further, this reaction was found to be inhibited by the presence of azide ligated to the metal center, indicating that the reaction involves direct coordination to the metal center.[14] The exact mechanism of sulfur oxidation has yet to be experimentally proven, however, there is some evidence that an Fe^{V}-oxo species is formed before converting to the sulfenate species, which has also been invoked in proposed mechanisms of cysteine oxidation by CDO.

2.2. Experimental

General Methods

All reactions were performed under one atmosphere of nitrogen in a glovebox or using standard Schlenk techniques unless otherwise indicated. Reagents purchased from commercial vendors were of the highest purity available and used without further purification. Pentane, toluene, diethyl ether (Et_2O), tetrahydrofuran (THF), acetonitrile (MeCN), and dichloromethane (DCM) were rigorously degassed and purified using solvent purification columns housed in a custom stainless-steel cabinet, dispensed a stainless steel Schlenk line (GlassContour). Methanol was distilled from magnesium turnings and iodine and degassed prior to use. 3-mercapto-3-methyl-2-butanone was synthesized according to literature precedent.[4] IBX-ester and pentafluoroiodosylbenzene were synthesized as described previously.[15–18]

^{1}H-NMR spectra were recorded on a Bruker AV-300, AV-301, or AV-500 FT-NMR spectrometer. Chemical shifts are reported in ppm and coupling constants (*J*) in Hz. EPR spectra were recorded on a Bruker EMX CW-EPR spectrometer equipped with a crysostat operating at X-band frequency at 120 K or a Bruker EMXnano CW-EPR spectrometer equipped with a cryostat operating at X-band frequency at 120 K. The EPR spectra were simulated using EasySpin (version 5.2.35),[19] a MATLAB package developed by Stoll and Schweiger (The MathWorks, Massachusetts, USA). Electrospray ionization mass spectrometry (ESI-MS) was performed on a Bruker Esquire LC-Ion Trap. Low-temperature electronic absorption spectra were recorded using a Varian Cary 50 or Agilent Cary 60 spectrophotometer equipped with either a fiber optic cable connected to a "dip" attenuated total reflection probe (C-technologies), with a custom built two-necked solution sample holder equipped with a threaded glass connector (sized to fit the dip probe) and purged with argon, or a UNISOKU CoolSpek USP-203 cryostat.

Calculations were performed using the ORCA v. 4.2.1 quantum chemistry package developed by Neese and coworkers,[20,21] and employed the polarized triple-zeta basis set def2-TZVP, the def2/J auxiliary basis set for Coulomb fitting, and the atom-pairwise dispersion correction of Grimme (D3BJ).[22] Tight convergence criteria were required for self-consistent field (SCF) solutions. The Grid4 (GridX4) integration grid size was used for geometry optimizations. Calculations were performed using the B3LYP functional, with the resolution of identity (RI) chain-of-spheres (RIJCOSX) approximation and initiated from the crystallographic coordinates when available.[23,24] Analytical frequency calculations were performed on all optimized structures to determine whether the obtained stationary points corresponded to local minima. Chemcraft was used to visualize the calculated EAS spectra.[25] Excited states from TD-DFT were analyzed by using natural transition orbtials (NTOs) and by visualizing their difference densities between the

ground and excited states. Canonical molecular orbital isosurfaces and natural transition orbitals in the TD-DFT calculations were visualized at an isovalue of 0.05 a03 using UCSF ChimeraX.[26]

*Synthesis of [$Fe^{III}(S_2^{Me2}N_3(Et,Pr)\text{-}S^{pers}](PF_6)$ (**4**)*

Sodium methoxide (1.080 g, 20 mmol) was added to 10 mL MeOH in a 20 mL scintillation vial with a stir bar. 3-mercapto-3-methyl-2-butanone (2.364 g, 20 mmol) was added to 10 mL MeOH in a 20 mL scintillation vial, and the sodium methoxide solution was added to this solution with stirring. Iron dichloride (1.266 g, 10 mmol) was added to 30 mL MeOH in a 100 mL Schlenk flask, stirred to dissolve, and the sodium methoxide and 3-mercapto-3-methyl-2-butanone solution was added dropwise into the Schlenk flask with stirring. The reaction was allowed to stir for 15 minutes, and *N*-(2-aminoethyl)-1,3-propanediamine (1.172 g, 10 mmol) in 5 mL MeOH was added dropwise to the now cloudy brown solution in the Schlenk flask. This solution was allowed to stir for three hours, becoming clear and dark green, and ferrocenium hexafluorophosphate (3.476 g, 10.5 mmol) was added as a slurry in 5 mL MeOH. The resulting solution was stirred for twelve hours at room temperature, and the methanol solvent was removed under vacuum. The crude product is washed with diethyl ether to remove ferrocene, redissolved in a minimum of acetonitrile, and filtered to remove sodium chloride. The solution is reduced to dryness under vacuum again, and the product is recrystallized by layering a saturated MeCN solution with Et_2O in a -35 °C freezer over about 72 hours, affording very dark red needle-like crystals (1.74 g, 3.17 mmol, 31.7 % yield). This material is spectroscopically identical to the previously reported method.[5]

*Synthesis of [$Fe^{III}(S_2^{Me2}N_3(Et,Pr)](PF_6)$ (**3**)*

[$Fe^{III}(S_2^{Me2}N_3(Et,Pr)\text{-}S^{pers}](PF_6)$ (0.750 g, 1.37 mmol) was added to 15 mL MeCN in a scintillation vial and stirred to dissolve. Triphenylphosphine (0.646 g, 5.47 mmol) was added to 5 mL THF and added dropwise to the solution of **4**. The reaction was allowed to stir at room

temperature overnight, then transferred to a Schlenk flask and reduced to dryness via vacuum. The solid was washed with pentane to remove triphenylphosphine oxide, and the crude product was dissolved in a minimum of DCM and recrystallized by layering with pentane in a -35 °C freezer over about 72 hours, affording dark magenta crystals (0.474 g, 0.918 mmol, 67%). Electronic absorption (THF) λ_{max} (ε, $M^{-1}cm^{-1}$) = 490 (1320), 539 (1340), 730 (160) nm; (DCM) λ_{max} (ε, $M^{-1}cm^{-1}$) = 494 (1530), 540 (1540), 712 (360) nm; (toluene) λ_{max} = 500, 550, 735 nm. EPR (DCM/toluene glass (1:1), 110 K) *g* = 2.08, 2.03, 1.92. This material is also spectroscopically identical to the previously reported method.[5]

*Synthesis of [$Fe^{III}(\eta^2$-$S^{Me2}O)(S^{Me2}N_3(Et,Pr)](PF_6)$ (**6**) via the addition of IBX-ester to **3***

[$Fe^{III}(S_2{}^{Me2}N_3(Et,Pr)](PF_6)$ (0.100 g, 0.19 mmol) was dissolved in 10 mL DCM, and a solution of IBX-ester (0.075 g, 0.23 mmol) in 5 mL DCM was added with stirring. The solution was allowed to react for 15 minutes, then transferred to a Schlenk flask and pumped to dryness. The red solid was dissolved in a minimum of DCM and recrystallized by layering with pentane, affording red crystals. Electronic absorption (THF) λ_{max} (ε, $M^{-1}cm^{-1}$) = 530 (1610), 740 (190) nm; (DCM) λ_{max} (ε, $M^{-1}cm^{-1}$) = 530 (1740), 740 (180) nm; (toluene) λ_{max} (ε, $M^{-1}cm^{-1}$) = 530 (1500), 750 (150) nm. EPR (DCM/toluene glass (1:1), 110 K) *g* = 2.16, 2.10, 1.98.

*Formation of an intermediate via the addition of IBX-ester to **3***

A 0.500 mM solution of **3** was prepared in 4 mL of THF or DCM under an inert atmosphere in a drybox. The solution was transferred via gas-tight syringe to a custom two-neck vial equipped with a septum cap and a threaded dip-probe feed-through adaptor that had been purged with argon and contained a stir bar. The solution was cooled to -73 °C in an isopropanol/dry ice bath and a solution of 1.2 equivalents (250 µL of a 10 mM solution in THF or DCM) of IBX-ester was added, and the resulting change in absorbance was monitored by UV/visible spectroscopy.

*Formation of a green species via the addition of pyridine N-oxide (PNO) to **3***

A 0.500 mM solution of **3** was prepared in 4 mL of THF or DCM under an inert atmosphere in a drybox. The solution was transferred via gas-tight syringe to a custom two-neck vial equipped with a septum cap and a threaded dip-probe feed-through adaptor that had been purged with argon and contained a stir bar. The solution was cooled to -73 °C in an isopropanol/dry ice bath and a solution of 2 equivalents (500 μL of an 8 mM solution in THF or DCM) of was added, and the resulting change in absorbance was monitored by UV/visible spectroscopy. This species **3-PNO** could also be crystallized by adding excess PNO to a concentrated DCM solution of **3** and layering the resulting solution with pentane and allowing it to sit for approximately 72 hours in a -35 °C freezer.

Pyridine N-oxide (PNO) binding studies

Pyridine N-oxide binding studies were performed using freshly prepared solutions of $[Fe^{III}(S_2{}^{Me2}N_3(Et,Pr)](PF_6)$ (**3**) and varying concentrations of PNO in THF or DCM. The solutions were prepared in an inert atmosphere glovebox and placed in a modified 1 cm pathlength quartz air-free cuvette with a screw top equipped with a rubber septum. Measurements were performed using an UNISOKU USP-203-B cryostat and monitored with a Varian Cary 50 spectrophotometer. Spectral data was collected at 720 nm, where there is minimal overlap from the starting material **3** and the product **3-PNO**. A saturated solution of **3-PNO** was created by adding 126 equivalents of PNO to a 0.500 mM solution of **3** where further added PNO was shown to have no effect on the observed spectrum. Measurements were performed at 7 temperatures (-70 °C to -10 °C in 10 degree increments) for THF and at 11 temperatures (-90 °C to 10 °C in 10 degree increments) for DCM and at six PNO concentrations (0.500 to 1.000 mM in 0.100 mM increments) for both THF and DCM. Equilibrium constants were calculated using the following equations:[27,28]

$$[\boldsymbol{Fe-PNO}] = \frac{A - \varepsilon_{Fe}[Fe]_0}{\varepsilon_{Fe-PNO} - \varepsilon_{Fe}} \quad (2.1)$$

$$K_{eq} = \frac{[Fe-PNO]}{([Fe]_0] - [Fe-PNO])([PNO]_0 - [Fe-PNO]} \quad (2.2)$$

Thermodynamic parameters were determined from a Van't Hoff plot.

Pentafluoroiodosylbenzene (PFIB) inhibition studies

A 0.500 mM solution of **3** was prepared in 4 mL of DCM under an inert atmosphere in a drybox, both with and without 1000 added equivalents of iodopentafluorobenzene. The solution was transferred via gas-tight syringe to a custom two-neck vial equipped with a septum cap and a threaded dip-probe feed-through adaptor that had been purged with argon and contained a stir bar. The solution was cooled to -73 °C in an isopropanol/dry ice bath and a solution of 1.2 equivalents (250 μL of an 10 mM solution in DCM) of pentafluoroiodosylbezene was added, and the resulting change in absorbance was monitored by UV/visible spectroscopy.

X-ray crystallographic structure determination

A dark red prism of $[Fe^{III}(\eta^2\text{-}S^{Me2}O)(S^{Me2}N_3(Et,Pr)](PF_6)$ (**6**), measuring 0.11 x 0.10 x 0.04 mm^3 was mounted on a loop with oil. Data was collected at -173ºC on a Bruker APEX II single crystal X-ray diffractometer, Mo-radiation. Crystal-to-detector distance was 40 mm and exposure time was 10 seconds per frame for all sets. The scan width was 0.5º. Data collection was 100% complete to 25º in ϑ. A total of 58486 reflections were collected covering the indices, -23<=h<=23, -15<=k<=15, -14<=l<=14. 5555 reflections were symmetry independent and the R_{int} = 0.0698 indicated that the data was of average quality (0.07). Indexing and unit cell refinement indicated a C-centered monoclinic lattice. The space group was found to be C c (No.9).

A red block of $[Fe^{III}(\eta^2\text{-}S^{Me2}S)(S^{Me2}N_3(Pr,Pr)](PF_6)$ (**7**), measuring 0.12 x 0.15 x 0.17 mm^3 was mounted on a loop with oil. Data was collected at -173ºC on a Bruker APEX II single crystal

X-ray diffractometer, Mo-radiation. Crystal-to-detector distance was 40 mm and exposure time was xx seconds per frame for all sets. The scan width was 0.5º. Data collection was 100% complete to 25º in ϑ. A total of 11660 reflections were collected covering the indices, -16<=h<=16, -20<=k<=20, -17<=l<=17. 5937 reflections were symmetry independent and the R_{int} = 0.0176 indicated that the data was of excellent quality. Indexing and unit cell refinement indicated a monoclinic lattice. The space group was found to be P 21/n (No.14).

A green plate of $[Fe^{III}S_2^{Me2}N_3(Et,Pr)(PNO)](PF_6)$ (**3-PNO**), measuring 0.19 x 0.09 x 0.03 mm^3 was mounted on a loop with oil. Data was collected at -173ºC on a Bruker APEX II single crystal X-ray diffractometer, Mo-radiation. Crystal-to-detector distance was 40 mm and exposure time was 10 seconds per frame for all sets. The scan width was 0.5º. Data collection was 99.6% complete to 25º in ϑ. A total of 20128 reflections were collected covering the indices, -14<=h<=14, -11<=k<=11, -32<=l<=32. 5445 reflections were symmetry independent and the R_{int} = 0.0549 indicated that the data was of better than average quality (0.07). Indexing and unit cell refinement indicated a primitive monoclinic lattice. The space group was found to be P 2_1/n (No.14).

The data was integrated and scaled using SAINT, SADABS within the APEX2 software package by Bruker.[29] Solution by direct methods (SHELXT[30] or SIR97[31,32]) produced a complete heavy atom phasing model consistent with the proposed structure. The structure was completed by difference Fourier synthesis with SHELXL.[33] Scattering factors are from Waasmaier and Kirfel[34]. Hydrogen atoms were placed in geometrically idealized positions and constrained to ride on their parent atoms with C–H distances in the range 0.95-1.00 Angstrom. Isotropic thermal parameters U_{eq} were fixed such that they were 1.2U_{eq} of their parent atom Ueq for CH's and 1.5U_{eq} of their parent atom U_{eq} in case of methyl groups. All non-hydrogen atoms were refined

anisotropically by full-matrix least-squares. Structures were visualized using ORTEP-III and POV-Ray programs.[35,36]

Table 2-1. Crystal data, intensity collections[a] and structure refinement parameters for $[Fe^{III}(\eta^2\text{-}S^{Me2}O)(S^{Me2}N_3(Et,Pr)](PF_6)$ (**6**), $[Fe^{III}(\eta^2\text{-}S^{Me2}S)(S^{Me2}N_3(Pr,Pr)](PF_6)$ (**7**), and $[Fe^{III}S_2{}^{Me2}N_3(Et,Pr)(PNO)](PF_6)$ (**3-PNO**).

	6	**7**	**3-PNO**
Formula	$C_{15}\ H_{29}\ F_6\ Fe\ N_3\ O_{0.77}\ P\ S_{2.23}$	$C_{16}\ H_{31}\ F_6\ Fe\ N_3\ P\ S_3$	$C_{20}\ H_{34}\ F_6\ Fe\ N_4\ O\ P\ S_2$
Molecular Weight	536.04	562.44	611.45
Temperature (K)	100(2)	100(2)	100(2)
Crystal System	Monoclinic	Monoclinic	Monoclinic
Space Group	C_c	$P2_1/n$	$P2_1/n$
a, (Å)	17.9331(6)	12.7152(7)	11.6022(18)
b, (Å)	11.7906(4)	15.4252(8)	9.0139(14)
c, (Å)	11.1618(4)	12.8723(7)	25.653(4)
α, (°)	90	90	90
β, (°)	109.741(2)	109.603(3)	95.770(2)
γ, (°)	90	90	90
V ($Å^3$)	2221.37(14)	2378.4(2)	2669.2(7)
Z	4	4	4
R_1	0.0343	0.0243	0.0624
R_w	0.0724	0.0542	0.1549
GooF	1.039	1.043	1.047

[a] Mo Ko(α,-) (λ = 0.71070 Å) radiation; graphite monochromator; -90 ºC. [b] $R = \Sigma\ ||F_o| - |F_c|| / \Sigma\ |F_o|$. [c] $R_w = [\Sigma w(|F_o|-|F_c|)^2/\Sigma wF_o^2]^{1/2}$, where $w^{-1} = [\sigma^2_{count} + (0.05\ F^2)^2]/4F^2$.

2.3. Results and Discussion

2.3.1. Synthesis of a constrained bis-thiolate ligated iron (III) complex and its associated persulfide

Experiments with **3** were carried out to determine the effect structural constraints on how enzymes oxidize sulfur atoms. Complex **3** was originally conceived as a modification of **2** that would be incapable of supporting an ideal trigonal bipyramidal structure and thus show greater reactivity towards binding a sixth ligand.[5] Removing a methylene unit from the backbone of the ligand accomplishes just that, retaining similar Fe–S and Fe–N bond lengths while only substantially altering the S–Fe–N bond length. To produce **3**, a metal-templated Schiff-base condensation between 3-mercapto-3-methyl-2-butanone and *N*-(2-aminoethyl)-1,3-propanediamine on either iron(II) or iron(III) chloride in the presence of a base. In the case of iron(II) chloride, a ferrocenium salt (usually hexafluorophosphate) is added to oxidize the complex to Fe^{III}, and in the case of iron(III) chloride, a suitable potassium salt (such as KPF_6) is added to provide a suitable counterion for further purification steps. Unlike the similar synthesis for **2**, which produces the desired complex with no intermediate steps, this synthesis produces the persulfide ligated $[Fe^{III}(S_2{}^{Me2}N_3(Et,Pr)\text{-}S^{pers}]PF_6$ (**Scheme 2-3**, **4**). The mechanism of persulfide formation is still unknown. It is known, however, that the persulfide formation occurs after the oxidation of the iron because the Fe^{II} precursor can be isolated without a third sulfur atom (see Chapter 3.). The additional sulfur atom bound to the sixth coordination site produces an electronic absorption spectrum somewhat similar to those of other substrates ligated to **3**, with a peak at 553 nm rather than in the 700s, indicative of poorer orbital overlap.

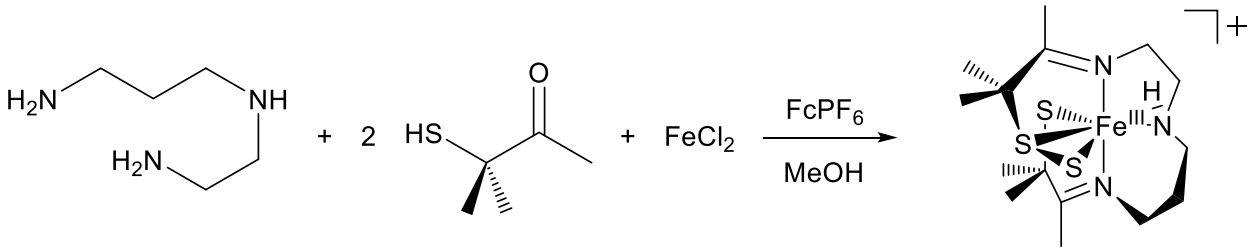

Scheme 2-3. Synthesis of $[Fe^{III}(S_2{}^{Me2}N_3(Et,Pr)\text{-}S^{pers}]PF_6$ (**4**).

The persulfide ligated **4** is indicative of **3**'s greater affinity for binding a ligand in the sixth coordination site; and can be converted into **3** by abstracting the persulfide atom with triethylphosphine. As stated previously, the steric constraints of **3** cause it to adopt a structure closer to square pyramidal than **2** (τ = 0.456 for **3** vs τ = 0.732 for **2**) with similar bond distances (**Table 2-2**) while still retaining the important biomimetic characteristics of **2**. Both have a low-spin (S = 1/2) Fe^{III} center over a wide range of temperatures, two thiolates in the coordination sphere, and an open sixth coordination site. The spontaneous formation of a persulfide also indicates that the thiolate can be easily oxidized with a suitable reagent (here likely excess 3-

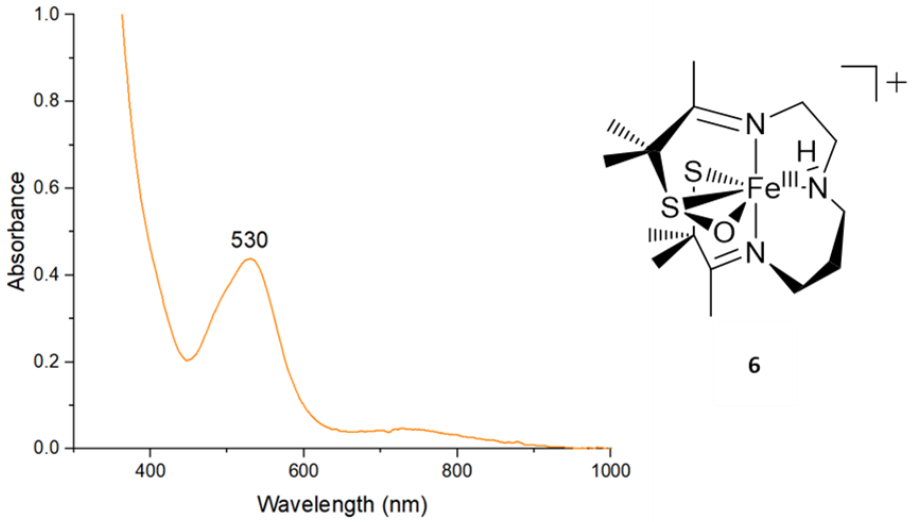

Figure 2-3. Electronic absorption spectrum of sulfenate species ($[Fe^{III}(\eta^2\text{-}S^{Me2}O)(S^{Me2}N_3(Pr,Pr)](PF_6)$, (**6**) and schematic drawing.

mercapto-3-methyl-2-butanone), and that it should be a suitable location for oxo-atom addition, as is observed with **2**.

2.3.2. Reactivity of $[Fe^{III}(S_2{}^{Me2}N_3(Et,Pr)]^+$ with oxo-atom donors

Because **2** was found to react with oxo-atom donors to produce a sulfenate ($[Fe^{III}(\eta^2\text{-}S^{Me2}O)(S^{Me2}N_3(Pr,Pr)](PF_6)$, (**5**), (**Figure 2-3**), reactions were carried out with **3** to determine if it exhibits the same reactivity. With the addition of an appropriate oxo-atom donor such as iodosylbenzene (PhIO) or isopropyl 2-iodoxybenzoate (IBX-ester), a red sulfenate is quickly formed with λ_{max} (ε, $M^{-1}cm^{-1}$) = 530 (1500). This sulfenate ($[Fe^{III}(\eta^2\text{-}S^{Me2}O)(S^{Me2}N_3(Et,Pr)](PF_6)$, (**6**) was crystallographically characterized and was shown to be substantially similar to the sulfenate formed by **2**, showing the same connectivity as it and the persulfide **4**, as well as a persulfide (**7**) formed as a byproduct in a reaction of **2** that was crystallographically characterized (**Figure 2-4**). The sulfenates show shorter Fe–O bond distances than the persulfides' Fe–S bond distances (**5**: 2.115(4) Å, **6**: 2.138(15) Å vs. **7**: 2.3644(4) Å, **4**: 2.3687(12) Å) as well as shorter O–S bond distances than the persulfides' S–S bond distances (**5**: 1.446(6) Å, **6**: 1.665(12) Å vs. **7**: 2.0073(5) Å, **4**: 2.0109(15) Å) (**Table 2-2**). These are expected, as sulfur has a larger atomic radius

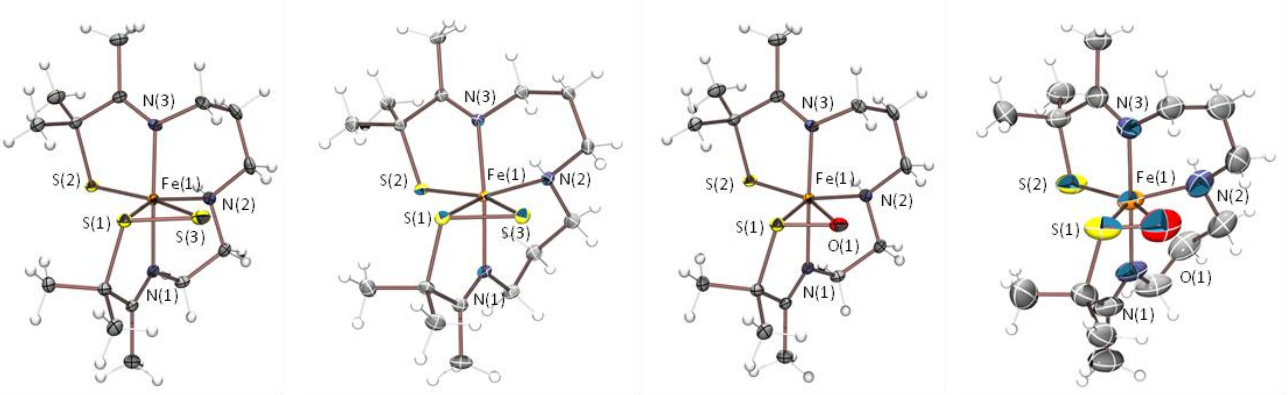

Figure 2-4. ORTEP diagrams of $[Fe^{III}(\eta^2\text{-}S^{Me2}S)(S^{Me2}N_3(Et,Pr)](PF_6)$ (**4**), $[Fe^{III}(\eta^2\text{-}S^{Me2}S)(S^{Me2}N_3(Pr,Pr)](PF_6)$ (**7**), $[Fe^{III}(\eta^2\text{-}S^{Me2}O)(S^{Me2}N_3(Et,Pr)](PF_6)$ (**6**), $[Fe^{III}(\eta^2\text{-}S^{Me2}O)(S^{Me2}N_3(Pr,Pr)](PF_6)$ (**5**), with thermal ellipsoids at the 50% probability level. Counterions removed for clarity.

than oxygen. The sulfenates also show shorter Fe–S bonds in general, especially that of the iron-sulfenate/persulfide sulfur bond (**5**: 2.1421(17) Å, **6**: 2.1779(11) Å vs. **7**: 2.2041(4) Å, **4**: 2.2209(12) Å), likely due to inductive effects from the persulfide sulfur being able to donate more electron density into the adjacent sulfur than the corresponding sulfenate oxygen.

Table 2-2. Selected metrical parameters for $[Fe^{III}(\eta^2\text{-}S^{Me2}S)(S^{Me2}N_3(Et,Pr)](PF_6)$ (**4**), $[Fe^{III}(\eta^2\text{-}S^{Me2}S)(S^{Me2}N_3(Pr,Pr)](PF_6)$ (**7**), $[Fe^{III}(\eta^2\text{-}S^{Me2}O)(S^{Me2}N_3(Et,Pr)](PF_6)$ (**6**), $[Fe^{III}(\eta^2\text{-}S^{Me2}O)(S^{Me2}N_3(Pr,Pr)](PF_6)$ (**5**)

	4	**7**	**6**	**5**
Fe–N(1) (Å)	1.944(3)	2.0044(12)	1.941(3)	1.976(4)
Fe–N(2) (Å)	1.993(4)	2.0374(12)	2.018(4)	2.044(5)
Fe–N(3) (Å)	1.971(3)	1.9886(12)	1.966(3)	1.954(4)
Fe–O/S(3) (Å)	2.3687(12)	2.3644(4)	2.138(15)	2.115(4)
Fe–S(1) (Å)	2.2209(12)	2.2041(4)	2.1779(11)	2.1421(17)
Fe–S(2) (Å)	2.1694(11)	2.1520(4)	2.1600(10)	2.1477(17)
S(1)–O/S(3) (Å)	2.0109(15)	2.0073(5)	1.665(12)	1.446(6)
N(1)–Fe–N(3) (°)	175.55(17)	174.45(5)	176.22(16)	177.99(19)
N(2)–Fe–S(1) (°)	149.86(12)	152.19(4)	145.71(11)	134.04(15)
N(2)–Fe–S(2) (°)	108.25(12)	107.62(4)	109.38(11)	113.23(15)
S(1)–Fe–S(2) (°)	100.57(4)	100.100(15)	104.04(4)	112.60(8)
N(2)–Fe–O(1) (°)	99.23(12)	100.33(4)	101.1(4)	94.4(2)
O(1)–Fe–S(1) (°)	51.85(4)	51.985(13)	45.4(4)	39.71(16)
O(1)–Fe–S(2) (°)	152.38(5)	152.049(16)	149.4(4)	152.28(17)
τ^a	0.4282	0.3710	0.5085	0.7325

[a]5-coordinate geometry index, $\tau = (\beta - \alpha)/60$. β is the largest bond angle observed, and α is the second largest bond angle.

The bond angles of the two persulfides are largely similar, with all bond angles with iron at the center being within +/- 3° of each other for **7** and **4**. This is not the case for the sulfenates, likely due to greater constraints imposed by the removal of the methylene unit as well as the shorter

Fe–O and S–O bonds. This can be seen in the τ value (disregarding the sulfenate oxygen or persulfide sulfur), where the persulfides **7** and **4** have τ = 0.371 and 0.428 respectively, and the sulfenates **5** and **6** have τ = 0.733 and 0.509 respectively. The persulfides adopt a geometry closer to square pyramidal, whereas the sulfenates are constrained to be closer to trigonal bipyramidal, and additionally remain close to the geometry indices of **2** and **3** (τ = 0.732 and 0.456 respectively), indicating that not much structural rearrangement occurs as a result of the inclusion of an oxygen atom. This could indicate that the oxygen atom does not greatly affect the electronic structure of these complexes, but more detailed theoretical studies are required to demonstrate that unambiguously.

2.3.3. Low temperature reactivity of $[Fe^{III}(S_2{}^{Me2}N_3(Et,Pr)]^+$ with oxo-atom donors

Like **2**, **3** was found to interact with oxo-atom donors at low temperature to form a green intermediate. When the reaction between **3** and IBX-ester is monitored in DCM at -40 °C, an intermediate with λ_{max} = 686 nm immediately forms. In the reaction of **2** and IBX-ester at -73 °C, the intermediate is similarly formed very quickly, and converts to the sulfenate **5** over the course

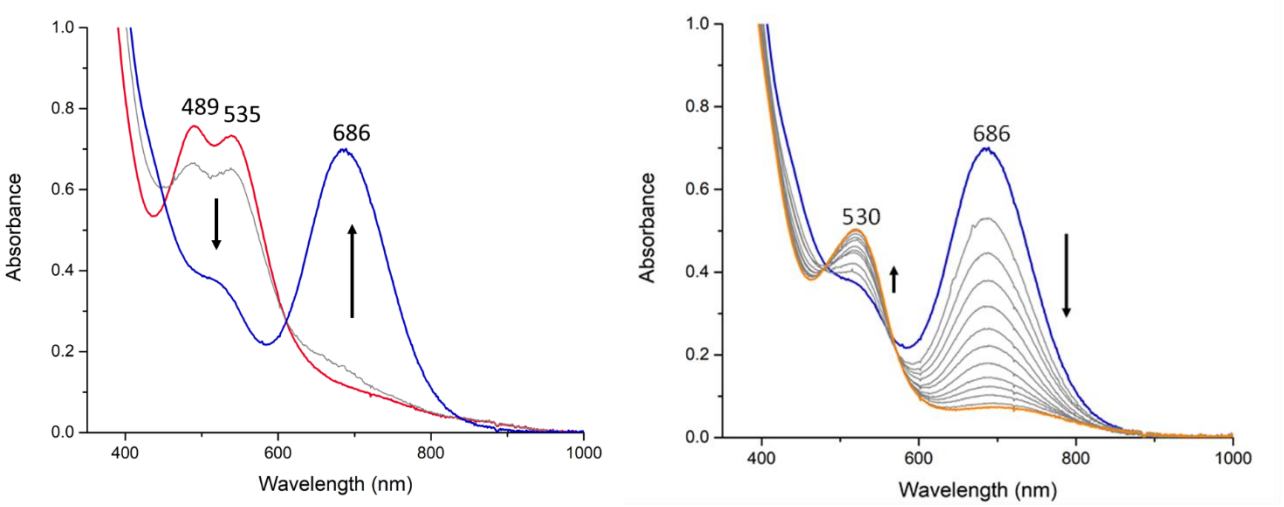

Figure 2-5. Electronic absorbance spectra for the reaction between 0.250 mM of **3** and 1.2 eq. IBX-ester at -40 °C. Left: Formation of the oxo-atom donor adduct in one minute. Right: Formation of the sulfenate **6** in four hours.

of 36 minutes. However, the intermediate of **3** and IBX-ester takes four hours to convert to the sulfenate **6** at -40 °C, and approximately three days at -73 °C (**Figure 2-5**). The identity of this intermediate is very likely an oxo-atom donor adduct species or an Fe^{V}-oxo species, which will be discussed in greater detail in the next section. The longer lifetime of the intermediate formed by **3** may be attributed to constraints imposed by the removal of the methylene unit, as both the case of an oxo-atom donor adduct converting directly to the sulfenate or an Fe^{V}-oxo converting to the sulfenate require the ligand to flex a nearby sulfur atom towards the oxygen atom in order to form the bond. Because **3** is more constrained and less flexible than **2**, the energy required to perform this motion is higher and the intermediate species will be stabilized. The product sulfenate species was not found to react further with excess added oxo-atom donor, unusual for small molecule metal thiolate complexes. As with **2**, **3** does not exhibit reactivity with oxo-atom donors when complexed with azide, indicating that the reaction is metal-centered and requires direct coordination to the metal to accomplish sulfur oxidation.

2.3.4. Possible mechanisms of oxo-atom donor reactivity

To form the sulfenate **6** in the reaction of **3** and an oxo-atom donor, first the oxo-atom donor must coordinate to the iron center in the open sixth coordination site. From this oxo-atom donor adduct species, there are two possible paths (**Scheme 2-4**). The sulfur could directly nucleophilically attack the oxygen of the oxo-atom donor coordinated to the iron, forming the sulfenate product with concomitant release of the associated aryl iodide, or the aryl iodide could dissociate from the oxygen atom without influence of a sulfur, resulting in a free aryl iodide and an Fe^{V}-oxo species. This Fe^{V}-oxo species would be highly reactive, and could either coordinate a free aryl iodide to reform the oxo-atom donor adduct, or the oxo atom could be nucleophilically attacked to form the sulfenate **6**. The observation of a single intermediate rather than the two that

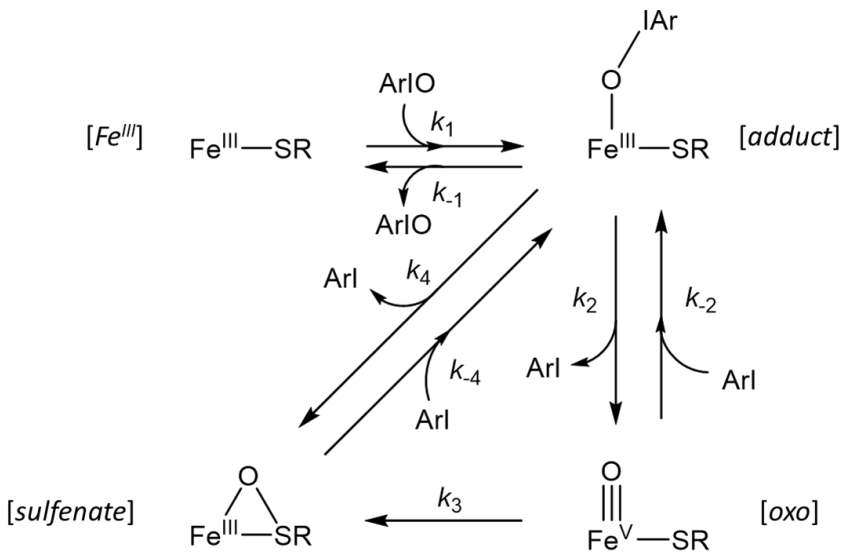

Scheme 2-4. Proposed reaction scheme for **2** + ArIO and **3** + ArIO.

are implied in this scheme indicates that either the nucleophilic attack by the sulfur on the oxygen atom or the cleavage of the I-O bond to produce an unobserved Fe^{V}-oxo is rate-determining. If the observed intermediate were an Fe^{V}-oxo, the position and intensity of the associated absorption band would remain invariant regardless of the identity of the oxo-atom donor, but using differing oxo-atom donors (iodosylbenzene and associated *para*-substituted derivatives) results in a shift of this band.

Previous work with Fe-porphyrin systems indicate that O-I bond cleavage is reversible,[37] showing that if an Fe^{V}-oxo is in the reaction pathway, the overall rate of generation of the sulfenate can be decreased by introducing a competing pathway that reverts the Fe^{V}-oxo to an oxo-atom donor adduct Fe^{III}-OAr. This approach has been used successfully to find the active oxidant in several systems.[38–42]

Using **Scheme 2-4** and its associated rate law, we can further investigate the pathway of this reaction. The full rate law, including both possible routes, is given by the equation:

$$rate = \frac{k_2 k_3 [adduct]}{k_3 + k_{-2}[ArI]} + \frac{k_1 k_4 [Fe^{III}][ArIO] + k_{-2} k_4 [oxo][ArI] + k_4 k_{-4} [sulfenate][ArI]}{k_{-1} + k_2 + k_4} - k_{-4}[sulfenate][ArI] \quad (2.3)$$

This equation can be simplified by testing if the oxo-atom donor adduct can be reformed by addition of excess aryl iodide to the sulfenate, governed by the rate k_{-4}. Performing this experiment does not show any generation of the oxo-atom donor adduct species, indicating that k_{-4} is either zero or negligibly small, and it can be disregarded. This simplifies the rate equation to:

$$rate = \frac{k_2 k_3 [adduct]}{k_3 + k_{-2}[ArI]} + \frac{k_1 k_4 [Fe^{III}][ArIO] + k_{-2} k_4 [oxo][ArI]}{k_{-1} + k_2 + k_4} \qquad (2.4)$$

The alternate pathway involves initial dissociation of the aryl iodide to form a transient Fe^{V}-oxo, which then goes on to form the sulfenate product through an intramolecular nucleophilic attack mechanism. This mechanism can be distinguished from the former mechanism through the addition of excess aryl iodide, as if k_2 is significantly larger than k_4, increasing the concentration of aryl iodide will decrease the overall rate of the reaction.

2.3.5. Investigating the presence of an Fe^{V}-oxo with inhibition studies

To further examine the rate law of the reaction in **Scheme 2-4**, studies investigating the presence of an Fe^{V}-oxo were performed. Because doubly-oxygenated hypervalent iodine oxo-atom

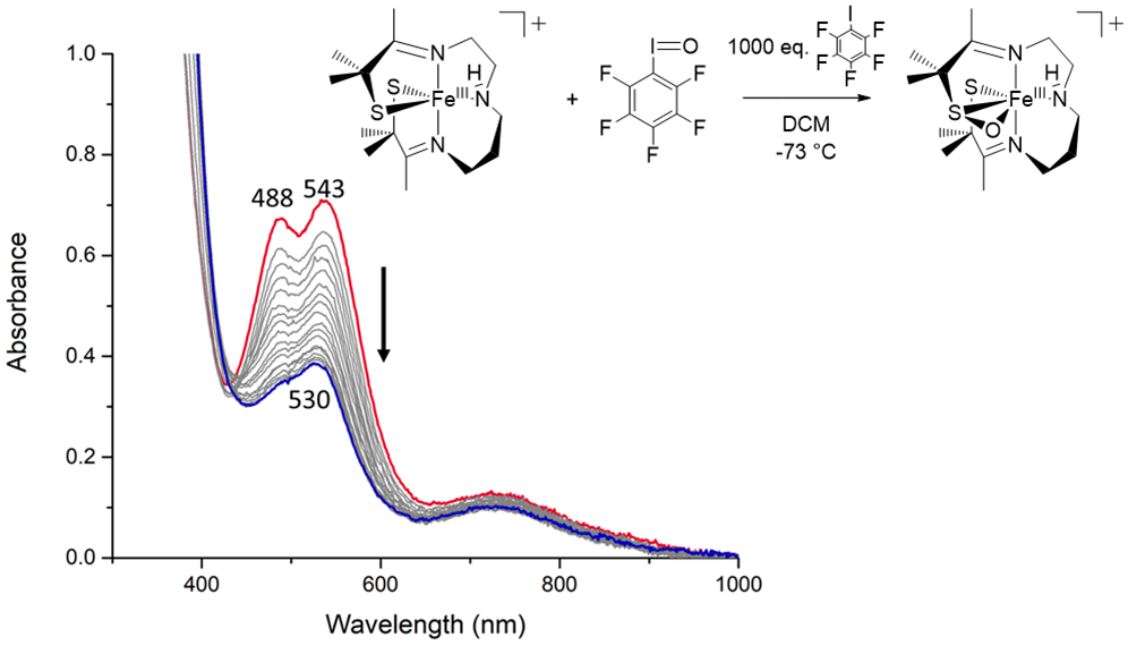

Figure 2-6. Reaction of **3** with 1.2 eq. pentafluoroiodosylbenzene in DCM at -73 °C in the presence of 1000 eq. iodopentafluorobenzene over 15 minutes.

donors such as IBX-ester create a competent singly oxygenated iodine oxo-atom donor after their first oxygen atom is donated and would thus complicate kinetic calculations, a singly oxygenated oxo-atom donor was used. Pentafluoroiodosylbenzene (PFIB) was chosen for its solubility in a wide variety of solvents (unlike PhIO, which requires methanol to dissolve) and its ability to react with **3**. No reaction was observed again with the sulfenate **6** in the presence of excess pentafluoroiodobezene ($IArF_5$), indicating that the oxo-atom donor adduct cannot be reformed from the sulfenate. At -73 °C in the absence of $IArF_5$ at, the sulfenate **6** was formed in approximately five minutes, without the observation of an intermediate. With 1000 added equivalents of $IArF_5$ in the same conditions (**Figure 2-6**), the reaction took approximately fifteen minutes (a threefold slowdown), indicating that the reaction of **3** with an oxo-atom donor likely proceeds through the pathway involving an Fe^V-oxo as outlined in **Scheme 2-4**. The same reaction performed with **2** results in a more dramatic slowdown with less added $IArF_5$, requiring only 200 equivalents of added $IArF_5$ to affect a sixfold decrease in rate.[17] Further work would be required to determine relative rate constants and thermodynamic parameters, but we may postulate that the greater slowdown observed with **2** results from a more stable Fe^V-oxo intermediate. We can attribute this to the less constrained ligand backbone allowing rearrangement more favorable for stabilizing the intermediate. Because the two competing reactions at that stage are an intramolecular rearrangement and the reverse reaction to form the oxo-atom donor adduct, the factors governing the rate of the reaction are the magnitudes of k_{-2} and k_3, as well as the concentrations of the Fe^V-oxo and the inhibitor $IArF_5$. Because a greater slowdown is observed for the reaction of **2** and PFIB than the reaction of **3** with PFIB despite the lower concentration of inhibitor, we can conclude that the intramolecular rate of reaction k_3 is slower for the Fe^V-oxo

generated by **2** than for **3**, and further that the Fe^{V}-oxo generated by **2** is more stable than that generated by **3**.

2.3.6. Thermodynamics of binding with pyridine N-oxide

To further examine the interaction of **2** and **3** and an oxo-atom donor, a similar substrate that is incapable of completely donating its oxygen atom and that has previously been used to generate stable adducts can be used.[43] Pyridine-*N*-oxide (PNO) is a weaker oxidant than hypervalent iodine oxo-atom donors, with an N-O bond strength of 72 kcal/mol[44] vs. the I-O bond strength of hypervalent iodine oxo-atom donors of approximately 44 kcal/mol.[45,46] When coordinated to both **2** or **3**, it does not transfer its oxygen atom to the metal, and binds reversibly, requiring a large excess of PNO in solution to completely generate the adduct species **3-PNO**. As a result, the thermodynamic parameters ΔH and ΔS can be calculated by using a Van't Hoff plot. With **3**, binding PNO is spontaneous at room temperature, with ΔH = -28.0 kJ/mol and ΔS = -40.6 J/molK in THF. The negative entropy of binding is as expected for an associative process. Characterization of the thermodynamics of PNO binding to **3** was also performed in DCM, finding

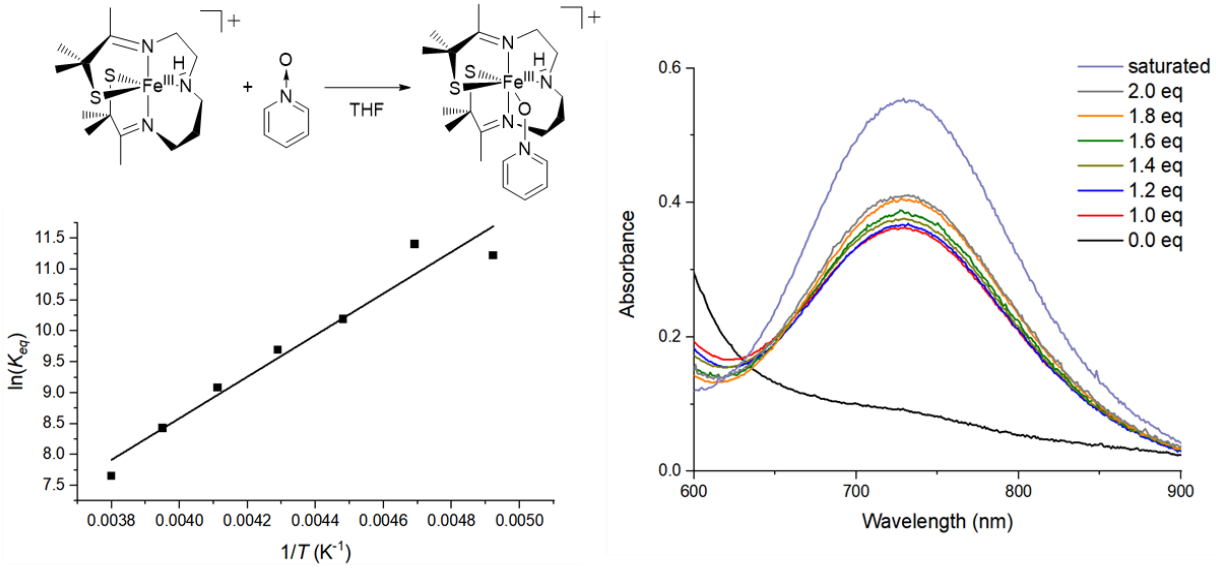

Figure 2-7. Left: Van't Hoff plot for the binding of pyridine N-oxide (PNO) to **3** to form **3-PNO** in THF. Right: electronic absorption spectrum of **3-PNO** at -40 °C with varying amounts of added PNO.

ΔH = -21.5 kJ/mol and ΔS = -31.7 J/molK. The lower enthalpy and entropy of binding are likely due to reduced interactions from the less polar solvent (polarity index for THF = 4.0; DCM = 3.1), regarding both enthalpic interactions helping to stabilize the bound PNO species and entropic interactions requiring less rearrangement of the solvent molecules.

2.3.7. X-ray crystal structure of PNO bound $[Fe^{III}(S_2{}^{Me2}N_3(Et,Pr)]^+$

Because the oxo-atom donor adduct species produced with PNO **3-PNO** is stable, it can be crystallized and a structure collected (**Figure 2-8**). Complex **3** binds PNO *trans* to one of the thiolate sulfurs and *cis* to the other, and on the N-H proton on N(2) is opposite the nitrogen from the PNO. This indicates that the amine proton is likely not involved in the formation of a sulfenate from an oxo-atom donor. The N–O bond length of PNO is 1.332(4) Å, only slightly lengthened from that of free PNO (1.31 Å).[43] In addition, a long Fe–O distance (2.131(3) Å) shows a weak interaction that does not result in the transfer of the oxo atom, expected for the relatively strong N–O bond. Because of prior evidence of an Fe^V-oxo in the pathway to form the sulfenate product, this indicates that **3** requires a somewhat weak bond to first form an Fe^V-oxo before trapping it intramolecularly rather than going through a concerted mechanism involving the nearby sulfur S(1) nucleophilically attacking the oxo atom and breaking the O–X bond of the donor.

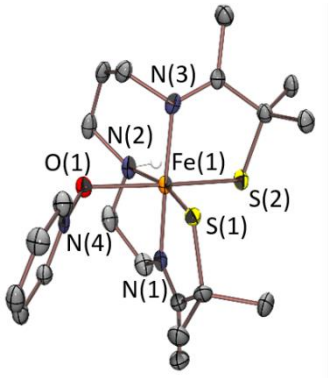

Figure 2-8. ORTEP diagram of $[Fe^{III}(S_2{}^{Me2}N_3(Et,Pr))]^+$-PNO (**3-PNO**) with thermal ellipsoids at the 50% probability level. Counterion omitted for clarity.

2.3.8. Comparisons with $[Fe^{III}(S_2{}^{Me2}N_3(Pr,Pr)]^+$-PNO

Complex **2** also binds PNO reversibly without transferring the oxo atom. Like **3-PNO**, **2-PNO** binds PNO *trans* to one sulfur and *cis* to the other, with the N–H proton facing away from the oxygen atom. **2-PNO** also does not strongly bind PNO, with an N–O bond length of 1.315(4) Å and an Fe–O bond length of 2.124(3) Å, both slightly shorter than **3-PNO**. For **2**, binding PNO is not spontaneous at room temperature, with ΔH = -35.9 kJ/mol and ΔS = -112 J/molK. Compared to **3-PNO**, **2-PNO** has a more exothermic ΔH by almost 8 kJ/mol, and a greater magnitude ΔS by just over 70 J/molK. Because of the lower entropic contribution for **3** than for **2**, it is more favorable to bind PNO to **3** at any temperature above about 110 K, under which it becomes more favorable to bind to **2** due to the larger enthalpic contribution. This is likely due to the same ligand constraints that make it initially more favorable to bind substrates to **3**; the less flexible ligand backbone means that the sixth coordination site is more open, but it also has less range of motion to stabilize the resultant product. At low temperatures, this boon becomes a curse, with the more constrained backbone putting more strain on the sixth binding site than a less constrained one would. This crossover point also helps to explain the potentially counterintuitive bond lengths found in the crystal structures, where due to the 100 K collection temperature, we find very similar bond distances for both structures but slightly shorter distances indicative of a stronger metal-donor interaction in **2-PNO**.

2-PNO and **3-PNO** retain similar bond lengths compared to each other throughout, with almost all Fe-ligand bonds within 0.05 Å of each other between the complexes. Given the identical oxidation state of iron, the same coordination environment, and the similar ΔG at the collection temperature, this is not surprising. The similarities of the bond angles found in both complexes is somewhat unexpected (**Table 2-3**). The N(2)–Fe–O(1) bond angle is 77.02(13)° in **2-PNO**, versus

78.35(13)° in **3-PNO**; and the O(1)–Fe–S(1) bond angle is 91.70(8)° in **2-PNO**, compared to 91.50(8)° in **3-PNO**. The N(1)–Fe–O(1) and N(3)–Fe–O(1) bond angles in **2-PNO** are 77.02(13)° and 97.51(15)° respectively, and 78.35(13)° and 94.31(13)° respectively in **3-PNO**. These bond angles remaining essentially unchanged implies the ligand constraints are not impactful when something is bound to the sixth coordination site, and that the flexibility of the ligand is maintained even with one methylene unit removed. Moreover, both complexes seem to be equally competent at stabilizing the intermediate, at least for this low temperature. Whether this trend changes at higher temperatures is unknown, but higher temperature data collections could result in the decomposition of the complexes due to dissociation of the PNO ligand.

Table 2-3. Selected metrical parameters for $[Fe^{III}(S_2{}^{Me2}N_3(Pr,Pr))]^+$-PNO (**2-PNO**) and $[Fe^{III}(S_2{}^{Me2}N_3(Et,Pr))]^+$-PNO (**3-PNO**)

	2-PNO	**3-PNO**
N–O (Å)	1.315(4)	1.332(4)
Fe–O (Å)	2.124(3)	2.131(3)
Fe–N(1) (Å)	1.986(3)	1.917(4)
Fe–N(2) (Å)	2.110(3)	2.055(4)
Fe–N(3) (Å)	1.957(4)	1.954(4)
Fe–S(1) (Å)	2.1780(12)	2.1924(12)
Fe–S(2) (Å)	2.1731(13)	2.1845(12)
N(2)–Fe(1)–S(1) (°)	166.68(11)	168.01(12)
N(2)–Fe(1)–S(2) (°)	95.12(11)	93.65(11)
O(1)–Fe(1)–S(1) (°)	91.70(8)	91.50(8)
O(1)–Fe(1)–S(2) (°)	171.21(9)	172.00(9)
S(2)–Fe(1)–S(1) (°)	96.58(5)	96.44(5)
N(1)–Fe(1)–O(1) (°)	88.28(14)	89.61(14)
N(2)–Fe(1)–O(1) (°)	77.02(13)	78.35(13)
N(3)–Fe(1)–O(1) (°)	97.51(15)	94.31(13)

2.3.9. Density Functional Theory Calculations

To further characterize the relative stabilities of the transient Fe-oxo species, theoretical calculations were performed. The sulfenate structures **5** and **6** were modified by removing the bond between the oxygen and the sulfur. Calculations were performed in ORCA 4.2.1[21,47] using the B3LYP functional and the polarized triple-zeta basis set def2-TZVP for both the $S = 1/2$ and $S = 3/2$ state, in the absence of an observable or characterizable intermediate to confirm the spin state. The iron-oxo moiety of the two complexes was removed after geometry optimization and the single point energy recalculated to isolate the contribution from the ligand atoms. By subtracting this contribution from the overall potential energy of the Fe^{V}-oxo complexes, the energies of the two can be compared. The energy for **2-oxo** was found to be more stable than **3-oxo** by 1.56 kcal/mol (6.52 kJ/mol) for the $S = 1/2$ species or 1.94 kcal/mol (8.12 kJ/mol) for the $S = 3/2$ species. While future work should aim to experimentally characterize the transient Fe^{V}-oxo species to assess the validity of these simulations, they do support the interpretation that **3-oxo** is less stabilized by the more constrained ligand environment.

2.4. Summary and Conclusions

Limiting ligand flexibility by the removal of one methylene unit while maintaining the rest of the structure has a large impact on the properties of a complex. The more constrained system has a greater affinity for ligands due to less reorganizational energy being required to bind a sixth ligand. This manifests in its ability to bind nitriles and other substrates at relatively high temperature, and dramatically higher rates of formation of intermediates. Additionally, this appears in a proclivity to form a persulfide species during oxidation from Fe^{II} to Fe^{III}. This persulfide complex was compared to the related unmodified ligand persulfide, as well as the two related sulfenates formed via a reaction with oxo atom donors. was that with the more flexible ligand,

incorporation of an extra sulfur atom dramatically altered the wrapping of the ligand. The less flexible ligand remained more constrained and maintained a similar geometry index to the original complex. In both complexes, incorporation of an oxygen atom does not greatly change the metrical parameters of the complex, implying that the overall electronic structure may be relatively unaffected by a sulfenate bound both to the sulfur and the neighboring metal. Reactions with oxo-atom donors at low temperatures found that the affinity for a sixth ligand did not translate to faster overall reaction rates, with the oxo-atom donor adducts of **3** having a much greater lifetime than those of **2**. Inhibition studies searching for evidence of an Fe^{V}-oxo demonstrated that the reaction rate of **3** with an oxo-atom donor to form a sulfenate is less affected than the same for **2**, potentially implying that the Fe^{V}-oxo formed by **3** is less able to be stabilized by the ligand. Experiments comparing thermodynamic parameters for binding a sixth ligand and comparisons of the crystal structures of a bound ligand show that **3** benefits entropically from the constraints upon it, but detracts enthalpically, binding ligands more strongly only due to a lower entropic term at high temperatures. This is supported by theoretical calculations finding that **2-oxo** is more stable than **3-oxo**.

2.5. References

(1) Shoner, S. C.; Barnhart, D.; Kovacs, J. A. A Model for the Low-Spin, Non-Heme, Thiolate-Ligated Iron Site of Nitrile Hydratase. *Inorg. Chem.* **1995**, *34*, 4517–4518. DOI: 10.1021/ic00122a001

(2) Nelson, M. J.; Jin, H.; Turner, I. M.; Grove, G.; Scarrow, R. C.; Brennan, B. A.; Que, L. A Novel Iron-Sulfur Center in Nitrile Hydratase from Brevibacterium Sp. *J. Am. Chem. Soc.* **1991**, *113* (18), 7072–7073. DOI: 10.1021/ja00018a074

(3) Lugo-Mas, P.; Dey, A.; Xu, L.; Davin, S. D.; Benedict, J.; Kaminsky, W.; Hodgson, K. O.; Hedman, B.; Solomon, E. I.; Kovacs, J. A. How Does Single Oxygen Atom Addition Affect the Properties of an Fe-Nitrile Hydratase Analogue? The Compensatory Role of the Unmodified Thiolate. *J. Am. Chem. Soc.* **2006**, *128* (34), 11211–11221. DOI: 10.1021/ja062706k

(4) Shoner, S. C.; Nienstedt, A. M.; Ellison, J. J.; Kung, I. Y.; Barnhart, D.; Kovacs, J. A. Structural Comparison of Five-Coordinate Thiolate-Ligated M^{II} = Fe^{II}, Co^{II}, Ni^{II}, and Zn^{II} Ions Wrapped in a Chiral Helical Ligand. *Inorg. Chem.* **1998**, *37* (22), 5721–5726. DOI:10.1021/ic980882r

(5) Schweitzer, D.; Shearer, J.; Rittenberg, D. K.; Shoner, S. C.; Ellison, J. J.; Loloee, R.; Lovell, S.; Barnhart, D.; Kovacs, J. A. Enhancing Reactivity via Structural Distortion. *Inorg. Chem.* **2002**, *41* (12), 3128–3136. DOI: 10.1021/ic0109187

(6) Sugiura, Y.; Kuwahara, J.; Nagasawa, T.; Yamada, H. Nitrile Hydratase: The First Non-Heme Iron Enzyme with a Typical Low-Spin Fe(III)-Active Center. *J. Am. Chem. Soc.* **1987**, *109* (19), 5848–5850. DOI: 10.1021/JA00253A046

(7) Brennan, B. A.; Alms, G.; Nelson, M. J.; Durney, L. T.; Scarrow, R. C. Nitrile Hydratase from Rhodococcus Rhodochrous J1 Contains a Non-Corrin Cobalt Ion with Two Sulfur Ligands. *J. Am. Chem. Soc.* **1996**, *118* (38), 9194–9195. DOI: 10.1021/JA961920D

(8) Doan, P. E.; Nelson, M. J.; Jin, H.; Hoffman, B. M. An Implicit TRIPLE Effect in Mims Pulsed ENDOR: A Sensitive New Technique for Determining Signs of Hyperfine Couplings. *J. Am. Chem. Soc.* **1996**, *118* (29), 7014–7015. DOI: 10.1021/JA960611K

(9) Ellison, J. J.; Nienstedt, A.; Shoner, S. C.; Barnhart, D.; Cowen, J. A., Kovacs, J. A. Reactivity of Five-Coordinate Models for the Thiolate-Ligated Fe Site of Nitrile Hydratase. *J. Am. Chem. Soc.* **1998**, *120* (23), 5691–5700. DOI: 10.1021/ja973129q

(10) Shearer, J.; Kung, I. Y.; Lovell, S.; Kovacs, J. A. A Co(III) Complex in a Mixed Sulfur/Nitrogen Ligand Environment: Modeling the Substrate- and Product-Bound Forms of the Metalloenzyme Thiocyanate Hydrolase. *Inorg. Chem.* **2000**, *39* (22), 4998–4999. DOI: 10.1021/ic0005689

(11) Shearer, J.; Kung, I. Y.; Lovell, S.; Kaminsky, W.; Kovacs, J. A. Why Is There an "Inert" Metal Center in the Active Site of Nitrile Hydratase? Reactivity and Ligand Dissociation from a Five-Coordinate Co(III) Nitrile Hydratase Model. *J. Am. Chem. Soc.* **2001**, *123* (3), 463–468. DOI: 10.1021/ja002642s

(12) Kung, I.; Schweitzer, D.; Shearer, J.; Taylor, W. D.; Jackson, H. L.; Lovell, S.; Kovacs, J. A. How Do Oxidized Thiolate Ligands Affect the Electronic and Reactivity Properties of a Nitrile Hydratase Model Compound? [1]. *J. Am. Chem. Soc*. **2000**, *122*, 8299–8300. DOI: 10.1021/ja0017561

(13) Shearer, J.; Jackson, H. L.; Schweitzer, D.; Rittenberg, D. K.; Leavy, T. M.; Kaminsky, W.; Scarrow, R. C.; Kovacs, J. A. The First Example of a Nitrile Hydratase Model Complex That Reversibly Binds Nitriles. *J. Am. Chem. Soc.* **2002**, *124* (38), 11417–11428. DOI: 10.1021/ja012555f

(14) Villar-Acevedo, G.; Lugo-Mas, P.; Blakely, M. N.; Rees, J. A.; Ganas, A. S.; Hanada, E. M.; Kaminsky, W.; Kovacs, J. A. Metal-Assisted Oxo Atom Addition to an Fe(III)-Thiolate. *J. Am. Chem. Soc.* **2017**, *139*, 119-129. DOI: 10.1021/jacs.6b03512

(15) Zhdankin, V. V.; Koposov, A. Y.; Litvinov, D. N.; Ferguson, M. J.; McDonald, R.; Luu, T.; Tykwinski, R. R. Esters of 2-Iodoxybenzoic Acid: Hypervalent Iodine Oxidizing Reagents with a Pseudobenziodoxole Structure. *J. Org. Chem.* **2005**, *70* (16), 6484–6491. DOI: 10.1021/JO051010R

(16) Dedushko, M. Insights into Dioxygen Bond Activation and Formation by Small Biomimetic Complexes, University of Washington, Seattle, WA, 2020.

(17) Blakeley, M. N. Insights into Dioxygen Activation by Biomimetic Alkyl Thiolate-Ligated Iron Complexes, University of Washington, Seattle, WA, 2019.

(18) IODOSOBENZENE DIACETATE. *Organic Syntheses* **1963**, *43*, 62. DOI: 10.15227/ORGSYN.043.0062

(19) Stoll, S.; Schweiger, A. EasySpin, a Comprehensive Software Package for Spectral Simulation and Analysis in EPR. *J. Magn. Reson.* **2006**, *178* (1), 42–55. DOI: 10.1016/j.jmr.2005.08.013

(20) Neese, F.; Wiley, J. The ORCA Program System. *Wiley Interdiscip. Rev. Comput. Mol. Sci.* **2012**, *2* (1), 73–78. DOI: 10.1002/WCMS.81

(21) Neese, F. Software Update: The ORCA Program System, Version 4.0. *Wiley Interdiscip. Rev. Comput. Mol. Sci.* **2018**, *8* (1), e1327. DOI: 10.1002/WCMS.1327.

(22) Grimme, S.; Ehrlich, S.; Goerigk, L. Effect of the Damping Function in Dispersion Corrected Density Functional Theory. *J. Comput. Chem.* **2011**, *32* (7), 1456–1465. DOI: 10.1002/JCC.21759

(23) Becke, A. D. Density-functional Thermochemistry. III. The Role of Exact Exchange. *J. Chem. Phys.* **1998**, *98* (7), 5648. DOI: 10.1063/1.464913

(24) Neese, F.; Wennmohs, F.; Hansen, A.; Becker, U. Efficient, Approximate and Parallel Hartree–Fock and Hybrid DFT Calculations. A 'Chain-of-Spheres' Algorithm for the Hartree–Fock Exchange. *Chem. Phys.* **2009**, *356* (1–3), 98–109. DOI: 10.1016/J.CHEMPHYS.2008.10.036

(25) Zhurko, G. A. Chemcraft – Graphical Program for Visualization of Quantum Chemistry Computations. https://chemcraftprog.com: Ivanovo, Russia 2005.

(26) Pettersen, E. F.; Goddard, T. D.; Huang, C. C.; Meng, E. C.; Couch, G. S.; Croll, T. I.; Morris, J. H.; Ferrin, T. E. UCSF ChimeraX: Structure Visualization for Researchers, Educators, and Developers. *Protein Sci.* **2021**, *30* (1), 70–82. DOI: 10.1002/PRO.3943

(27) Guidry, R. M.; Drago, R. S. Evaluation of the Thermodynamic Data Reported for the Reversible Oxygenation of the Amine Complexes of Cobalt(II) Protoporphyrin IX Dimethyl Ester. *J. Am. Chem. Soc.* **1973**, *95* (20), 6645–6648. DOI: 10.1021/JA00801A020

(28) Drago, R. S.; Epley, T. D. Enthalpies of Hydrogen Bonding and Changes in Δvoh for a Series of Adducts with Substituted Phenols. *J. Am. Chem. Soc.* **1969**, *91* (11), 2883–2890. DOI: 10.1021/JA01039A010

(29) Bruker. APEX2 (Version 2.1-4), SAINT (Version 7.34A), SADABS (Version 2007/4). BrukerAXS Inc.: Madison, WI 2007.

(30) Sheldrick, G. M. SHELXL-97, Program for the Refinement of Crystal Structures. University of Göttingen: Göttingen, Germany 1997.

(31) Altomare, A.; Cascarano, G.; Giacovazzo, C.; Guagliardi, A.; Burla, M. C.; Polidori, G.; Camalli, M.; IUCr. SIR92 – a Program for Automatic Solution of Crystal Structures by Direct Methods. *J. Appl. Cryst.* **1994**, *27* (3), 435–435. DOI: 10.1107/S002188989400021X

(32) Altomare, A.; Burla, M. C.; Camalli, M.; Cascarano, G. L.; Giacovazzo, C.; Guagliardi, A.; Moliterni, A. G. G.; Polidori, G.; Spagna, R. SIR97: A New Tool for Crystal Structure Determination and Refinement. *J. Appl. Cryst.* **1999**, *32* (1), 115–119. DOI: 10.1107/S0021889898007717

(33) Sheldrick, G. M.; IUCr. Crystal Structure Refinement with SHELXL. *Acta Cryst. C* **2015**, *71* (1), 3–8. DOI: 10.1107/S2053229614024218

(34) Waasmaier, D.; Kirfel, A. New Analytical Scattering-Factor Functions for Free Atoms and Ions. *Acta Cryst.* **1995**, *51* (3), 416–431. DOI: 10.1107/S0108767394013292

(35) Persistence of Vision Raytracer. Persistence of Vision Pty. Ltd.: Williamstown, Victoria, Australia 2004.

(36) Burnett, M. N.; Johnson, C. K. ORTEP-III: Oak Ridge Thermal Ellipsoid Plot Program for Crystal Structure Illustrations. *Oak Ridge National Laboratory Report ORNL-6895* **1996**.

(37) Song, W. J.; Sun, Y. J.; Choi, S. K.; Nam, W. Mechanistic Insights into the Reversible Formation of Iodosylarene–Iron Porphyrin Complexes in the Reactions of Oxoiron(IV) Porphyrin π-Cation Radicals and Iodoarenes: Equilibrium, Epoxidizing Intermediate, and Oxygen Exchange. *Chem.-Eur. J.* **2006**, *12* (1), 130–137. DOI: 10.1002/CHEM.200500128

(38) Hill, E. A.; Kelty, M. L.; Filatov, A. S.; Anderson, J. S. Isolable Iodosylarene and Iodoxyarene Adducts of Co and Their O-Atom Transfer and C-H Activation Reactivity. *Chem. Sci.* **2018**, *9* (19), 4493–4499. DOI: 10.1039/c8sc01167b

(39) Guo, M.; Dong, H.; Li, J.; Cheng, B.; Huang, Y. Q.; Feng, Y. Q.; Lei, A. Spectroscopic Observation of Iodosylarene Metalloporphyrin Adducts and Manganese(V)-Oxo Porphyrin Species in a Cytochrome P450 Analogue. *Nat. Commun.* **2012**, *3* (1), 1–9. DOI: 10.1038/ncomms2196

(40) Song, W. J.; Sun, Y. J.; Choi, S. K.; Nam, W. Mechanistic Insights into the Reversible Formation of Iodosylarene-Iron Porphyrin Complexes in the Reactions of Oxoiron(IV) Porphyrin π-Cation Radicals and Iodoarenes: Equilibrium, Epoxidizing Intermediate, and Oxygen Exchange. *Chem.-Eur. J.* **2006**, *12* (1), 130–137. DOI: 10.1002/chem.200500128

(41) Hong, S.; Wang, B.; Seo, M. S.; Lee, Y.; Kim, M. J.; Kim, H. R.; Ogura, T.; Garcia-Serres, R.; Clémancey, M.; Latour, J.; Nam, W. Highly Reactive Nonheme Iron(III) Iodosylarene Complexes in Alkane Hydroxylation and Sulfoxidation Reactions. *Angew. Chem. Int. Ed.* **2014**, *53* (25), 6388–6392. DOI: 10.1002/anie.201402537

(42) Nam, W.; Choi, S. K.; Lim, M. H.; Rohde, J.-U.; Kim, I.; Kim, J.; Kim, C.; Que, Jr., L. Reversible Formation of Iodosylbenzene–Iron Porphyrin Intermediates in the Reaction of Oxoiron(IV) Porphyrinπ-Cation Radicals and Iodobenzene. *Angew. Chem. Int. Ed.* **2003**, *42* (1), 109–111. DOI: 10.1002/anie.200390036

(43) Hong, S.; Gupta, A. K.; Tolman, W. B. Intermediates in Reactions of Copper(I) Complexes with N-Oxides: From the Formation of Stable Adducts to Oxo Transfer. *Inorg. Chem.* **2009**, *48* (14), 6323–6325. DOI: 10.1021/IC900435P

(44) Shaofeng, L.; Pilcher, G. Enthalpy of Formation of Pyridine-N-Oxide: The Dissociation Enthalpy of the (N–O) Bond. *J. Chem. Thermodyn.* **1988**, *20* (4), 463–465. DOI: 10.1016/0021-9614(88)90184-X

(45) Bach, R. D.; Ayala, P. Y.; Schlegel, H. B. A Reassessment of the Bond Dissociation Energies of Peroxides. An Ab Initio Study. *J. Am. Chem. Soc.* **1996**, *118* (50), 12758–12765. DOI: 10.1021/JA961838I

(46) Coleman, E. H.; Gaydon, A. G.; Vaidya, W. M. Spectrum of Iodine Oxide (IO) in Flames. *Nature* **1948**, *162* (4107), 108–109. DOI: 10.1038/162108b0

(47) Neese, F. The ORCA Program System. *Interdiscip. Rev. Comput. Mol. Sci.* **2012**, *2*, 73-78. DOI: 10.1002/wcms.81

Chapter 3. Characterization of a Constrained Reduced Complex and its Interactions with Oxygen

3.1. Introduction

Despite their structural similarity and similar proposed intermediates, IPNS and CDO complete very different catalytic pathways. CDO consists of a histidine triad and an amine and thiolate from the coordinated cysteine substrate, and an Fe^{III}-superoxo is implicated in the mechanism of formation of the eventual cysteine sulfenic acid (**Figure 3-1**). During this process, both oxygen atoms derived from dioxygen are incorporated into the final product. IPNS features two histidines, a carboxylate from an aspartic acid, a water, and a sulfur deriving from its ACV substrate. An Fe^{III}-superoxo species has been proposed as the species responsible for the first hydrogen atom abstraction and the impetus of the eventual ring closure of the β-lactam ring. After this ring closure, a high valent Fe^{IV}-oxo is formed, which proceeds to abstract a second hydrogen atom to accomplish the closure of the fused thiazolidine ring to complete the bicyclic structure of

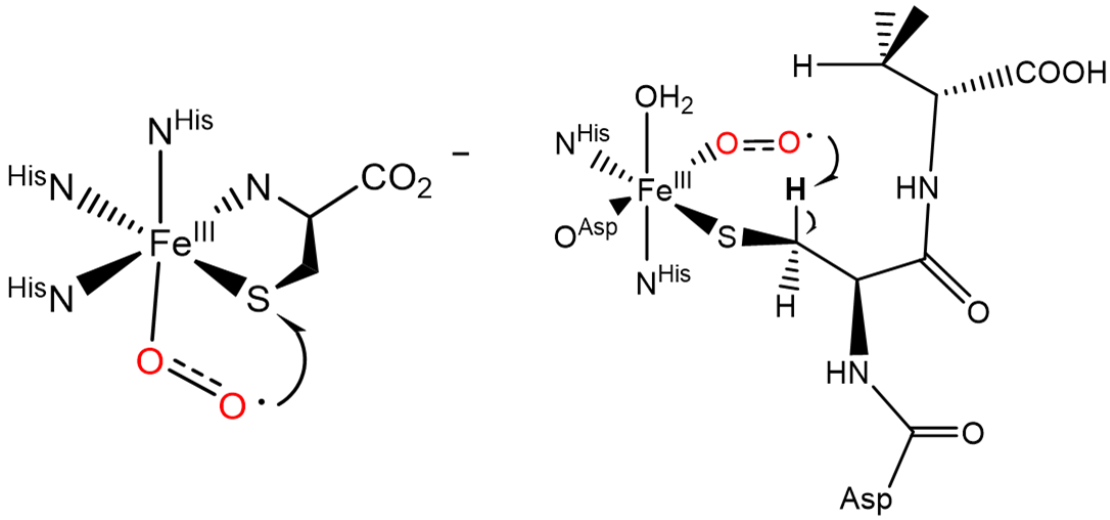

Figure 3-1. Fe^{III}-superoxo species generated by CDO (left) and IPNS (right), depicted performing their proposed reactive pathways.

the product isopenicillin N. During this process, neither oxygen atom from dioxygen is incorporated into isopenicillin N, instead being lost as water molecules.

The reasons for the differing activity of the Fe^{III}-superoxos are a pertinent area of current study. Both CDO and IPNS should be capable of hydrogen atom abstraction and sulfur oxidation respectively, yet both do not generate any appreciable quantity of side products indicative of a competing pathway.[1] Computational studies investigating the non-native pathways of both CDO and IPNS show that the preference in reactivity is governed by a small difference in the activation barrier for each reaction. In both, sulfur oxidation produces a significantly more stable end product. For IPNS, sulfur oxidation reactivity is avoided through a steric interaction between what would be the Fe–O–O–S structure that would form during sulfur oxidation and the valine side chain of ACV, an interaction which is introduced due to the shape of the substrate binding pocket. By decreasing the stability of this intermediate through steric effects, IPNS selects for hydrogen atom abstraction reactivity.[2]

Direct evidence for the formation of high-valent Fe^{III}-superoxos during these catalytic cycles is limited. In CDO, computational studies showed that CDO bound dioxygen to form an Fe^{III}-superoxo which attacked the bound sulfur of cysteine to form a bicyclic structure including a four membered Fe–O–O–S ring structure.[3,4] Using single-turnover conditions with the native enzyme observed with by transient absorption spectroscopy, an intermediate with absorption maxima at 500 and 640 nm was observed, disappearing within approximately 20 ms.[5] This intermediate was confirmed to be on-pathway via acid quench experiments, and DFT studies showed that the identity of the observed intermediate was likely to be either an Fe^{III}-superoxo species or the bicyclic ring structure.[5] In IPNS, crystallographic[6–9] and computational[10–13] studies have resulted in a proposed mechanism involving initial oxygen binding to the Fe^{II} center, resulting

in an Fe^{III}-superoxo. This then performs a hydrogen-atom abstraction from the carbon α to the cysteine sulfur, forming an Fe^{II}-hydroperoxo and a thioaldehyde. The thioaldehyde is attacked by the neighboring amide while the O–O bond is heterolytically cleaved to form the β-lactam ring and an Fe^{IV}-oxo species which abstracts a second hydrogen atom from the valine to eventually form isopenicillin N. By using stopped-flow absorption spectroscopy in single-turnover conditions to monitor the reaction of IPNS with ACV and dioxygen, an intermediate with absorption maxima at 360 and 515 nm appears over about 25 ms, disappearing within a second. Mössbauer spectra indicate that this intermediate is an Fe^{IV}-oxo, and deuterating the valine substrate showed a large effect on the decay of this intermediate, with no effect on its rate of formation, showing that the Fe^{IV}-oxo intermediate is what cleaves the valine C–H bond. Another signal is transiently observed before the formation of the Fe^{IV}-oxo intermediate at approximately 630 nm, appearing and disappearing over the course of less than 5 ms. By deuterating the carbon α to the cysteine sulfur, this intermediate accumulates more significantly, and Mössbauer spectra indicate that it is an Fe^{III} complex.[14] For both CDO and IPNS, these transient spectra comprise the entirety of the published direct evidence for these Fe^{III}-superoxo intermediates at the time of writing.

There is little direct evidence for an Fe^{III}-superoxo in these enzymatic systems, and there are similary few reported biomimetic models compared to other dioxygen derived intermediates.[15–17] Due to their high reactivity and physical characteristics, Fe^{III}-superoxos are very difficult to isolate and characterize. The superoxo radical causes complexes to be quite unstable with typically short lifetimes at low temperatures, and it can additionally couple to the metal center, potentially making the complex silent in both parallel and perpendicular modes of EPR spectroscopy. Even so, there are a few reported and thoroughly characterized non-heme metal-superoxo complexes. The first Fe^{III}-superoxo complex derived from a monoiron species was reported by Lee and

coworkers in 2014, using the pentadentate N_3O_2 ligand BDPP to generate a superoxo species by reacting the Fe^{II} complex with dioxygen. The superoxo species was characterized by electronic absorption spectroscopy, with an intense band at 330 nm; resonance Raman spectroscopy demonstrating changing vibrational frequencies with isotopic labeling of the oxygen atoms; and Mössbauer spectroscopy indicated a high-spin Fe^{III} coupled to a superoxo radical. This complex was also found to cleave the C–H bonds of dihydroanthracene (DHA) (BDE = 76.3 kcal/mol) (**Figure 3-2**, left).[18] Shortly after, Nam and coworkers reported an Fe^{III}-superoxo supported by the N_4 TAML ligand, crystallographically characterizing a side-on peroxo generated by reacting the Fe^{III} complex with KO_2. This features an absorbance band at 490 nm, and was not found to activate C-H bonds, but did cleave the O–H bond of 2,4-di-*tert*-butylphenol (BDE = 84.1 kcal/mol),[19] and could transfer its peroxo ligand to an identically coordinated manganese complex to generate a Mn^{IV}-peroxo (**Figure 3-2**, center left).[20] Hikichi and coworkers used a trispyrazolylborato ligand with a bidentate imidazolyl borate ligand to make an N_5 Fe^{II} complex that could be reacted with dioxygen to produce an Fe^{III}-superoxo complex with an electronic absorption band at 350 nm, with resonance Raman spectroscopy confirming it is a monometallic complex. They were not able to crystallographically characterize the iron complex, but a similar Co^{III}-superoxo was synthesized and characterized, showing an end-on superoxo. The Fe^{III}-superoxo complex was also able to cleave weak O–H or N–H bonds on substrates with BDE < 72.6 kcal/mol (**Figure 3-2**, center

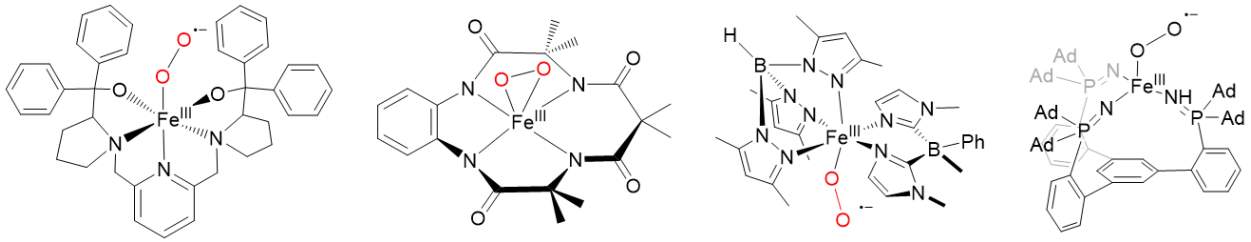

Figure 3-2. Non-heme Fe^{III}-superoxos without a thiolate in the coordination sphere. From left to right: $[Fe^{III}(BDPP)(O_2)]$,[18] $[Fe^{III}(TAML)(O_2)]^{2-}$,[20] $[Fe^{III}(L^{Ph})(Tp^{Me2})(O_2)]$,[21] and $[(L^{Ad}H)FeO_2]$.[22]

right).[21] Rittle and coworkers recently reported an unusual phosphinamide-ligated N_3 Fe^{III}-superoxo complex, using a three coordinate Fe^{II} center to react with dioxygen and produce a tetrahedral superoxo complex with absorption features at 420 nm. This complex was also crystallographically characterized and was found to be able to cleave the N–H bonds of diphenylhydrazine (BDE = 73.1) (**Figure 3-2**, right).[22]

There are several reported Fe^{III}-superoxo complexes with thiolates in the coordination sphere. The Goldberg group has used a triazacyclononane (TACN) ligand in combination with a 2-aminobenzenethiolate ligand to produce a five-coordinate N_4S_1 Fe^{II} complex. When complex was reacted with dioxygen at ambient temperature, it produced 2-aminophenyldisulfide, but at low temperature, the same conditions resulted in oxygenation of the substrate (**Figure 3-3**, left).[23] The same TACN ligand coordinated to a cobalt center in combination with the dithiolate S_2SiMe_2 was found to form a Co^{III}-superoxo that was able to be characterized via electronic absorption, resonance Raman, and EPR spectroscopies; and was found to be able to cleave the O–H bond of TEMPOH (BDE = 69.6 kcal/mol).[24] The same complex prepared with an iron center instead resulted in a peroxo-bridged dimer, implying the existence of a short-lived Fe^{III}-superoxo, which then homolytically cleaves to form an Fe^{IV}-oxo which can abstract hydrogen atoms from weak O–H bonds (BDE < 82.6 kcal/mol).[19,25] By modifying the TACN ligand with more sterically hindering isopropyl groups, they were able to more closely study factors influencing metal versus ligand

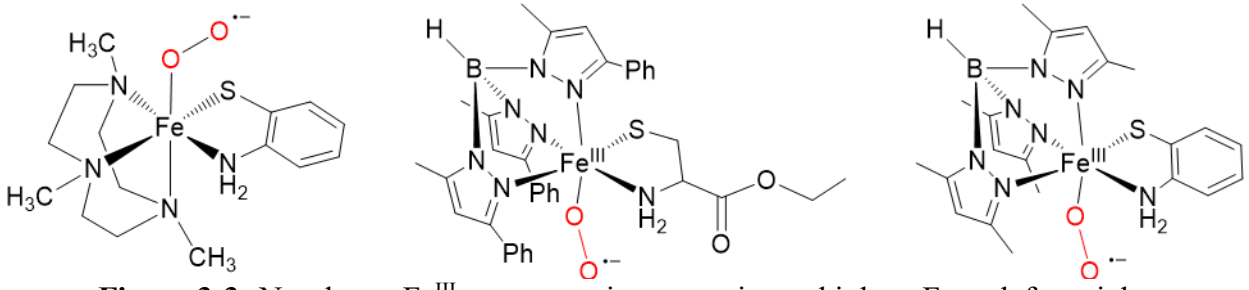

Figure 3-3. Non-heme Fe^{III}-superoxos incorporating a thiolate. From left to right: $Fe^{III}(Me_3TACN)(abt)(O_2)$,[23] $[Tp^{Me,Ph}FeCysOEt(O_2)]$,[27] and $[Fe(Tp^{Me2})(2\text{-}ATP)(O_2)]$.[29]

oxidation. They found that with added base present, the complex followed a PCET process resulting in oxidation of the metal, but in one-electron oxidation conditions, the disulfide product was formed.[26] The Limberg group used a trispyrazolylborato ligand along with L-cysteine ethyl ester bound to an iron center to produce a complex which produced a cysteine sulfenic acid when exposed to dioxygen, but did not report characterization of any intermediates (**Figure 3-3**, center).[27] The Fiedler group expanded on this work produce a cobalt complex with a modified, less sterically hindering ligand set which produces a Co^{III}-superoxo complex when exposed to dioxygen. The intermediate was characterized with EPR and resonance Raman spectroscopies and was found to reversibly bind O_2. EPR, resonance Raman, and DFT studies showed a low-spin Co^{III} center with almost complete electron transfer to the superoxide anion coordinated to it, and this complex did not show oxidation reactivity.[28] Using the same less hindered trispyrazolylborato ligand and 2-aminothiophenolate rather than L-cysteine ethyl ester, they were able to characterize an intermediate with electronic absorption maxima at 490, 655, and 860 nm which decayed at -80 °C over 10 minutes. This intermediate species was EPR-silent, consistent with an antiferromagnetically coupled Fe^{III}-superoxo; and the eventual product of the reaction is EPR-active. Resonance Raman spectroscopy and TD-DFT studies confirm the identity of the intermediate as an Fe^{III}-superoxo, although it does not oxygenate its substrate, instead transferring a proton to the superoxo anion and resulting in the formation of a dithiolate (**Figure 3-3**, right).[29]

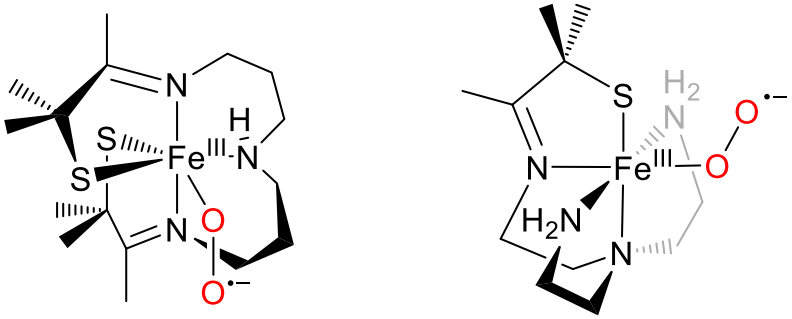

Figure 3-4. Non-heme Fe^{III}-superoxo complexes from the Kovacs group. Left: $Fe^{III}(S_2{}^{Me2}N_2NH(Pr,Pr))(O_2)$ (**2-superoxo**),[30] right: $Fe^{II}(S^{Me2}N_4(tren))(O_2)$.[36]

Previous work in the Kovacs group has also led to the formation and characterization of non-heme iron superoxo complexes. The previously discussed $Fe^{II}(S_2^{Me2}N_2NH(Pr,Pr))$ (**1**) was found to react with dioxygen at low temperatures to produce an Fe^{III}-superoxo species with electronic absorption maxima at 409, 520, and 707 nm (**Figure 3-4**, left). This superoxo species is EPR-silent, consistent with an antiferromagnetically coupled Fe^{III} and superoxo radical, and isotopic labeling studies in conjunction with resonance Raman spectroscopy confirm that it is an Fe^{III}-superoxo. As this complex decays, it converts to another species with λ_{max} = 696 nm that is likely an Fe^{III}-hydroperoxo formed via hydrogen-atom abstraction from the THF solvent (BDE = 92.1 kcal/mol). The same reaction in deuterated THF showed a kinetic isotope effect of 4.8, and the reaction rate increased with 100 added equivalents of cyclohexadiene (CHD) (BDE = 76.0 kcal/mol).[19,30] Further experiments to characterize the formation of this Fe^{III}-superoxo used stopped-flow kinetic studies to probe the binding of dioxygen in THF and methanol and found that oxygen binding was reversible in methanol, but irreversible in THF.[31] Specific findings regarding the rates of reaction will be discussed later in this chapter. The previously reported complex $[Fe^{II}(S^{Me2}N_4(tren))]^+$ was also found to react with dioxygen and produce an Fe^{III}-superoxo (**Figure 3-4**, right).[32,33] At low temperatures, this is reversible, and oxygen can be regenerated.[34] This superoxo can react with another equivalent of $[Fe^{II}(S^{Me2}N_4(tren))]^+$ to form a transient peroxo-bridged species which can homolytically cleave its O–O bond to generate two Fe^{IV}-oxos which have been shown to be capable of abstracting hydrogen atoms from the solvent to form a hydroxo species, similar to the final ring closure step of IPNS.[35]

3.2. Experimental

General Methods

All reactions were performed under an atmosphere of nitrogen in a glovebox or using standard Schlenk techniques unless otherwise indicated. Reagents purchased from commercial vendors were of the highest purity available and used without further purification. Pentane, toluene, diethyl ether (Et_2O), tetrahydrofuran (THF), acetonitrile (MeCN), and dichloromethane (DCM) were rigorously degassed and purified using solvent purification columns housed in a custom stainless-steel cabinet, dispensed a stainless steel Schlenk line (GlassContour). Methanol was distilled from magnesium turnings and iodine and degassed prior to use. 3-mercapto-3-methyl-2-butanone was synthesized according to literature precedent.[37] IBX-ester and pentafluoroiodosylbenzene were synthesized as described previously.[38–41]

^{1}H-NMR spectra were recorded on a Bruker AV-300, AV-301, or AV-500 FT-NMR spectrometer. Chemical shifts are reported in ppm and coupling constants (*J*) in Hz. EPR spectra were recorded on a Bruker EMX CW-EPR spectrometer operating at X-band frequency at 120 K or a Bruker EMXnano CW-EPR spectrometer operating at X-band frequency at 120 K. The EPR spectra were simulated using EasySpin (version 5.2.35),[42] a computational package developed by Stoll and Schweiger and based on MatLab (The MathWorks, Massachusetts, USA). Electrospray ionization mass spectrometry (ESI-MS) was performed on a Bruker Esquire LC-Ion Trap. Low-temperature electronic absorption spectra were recorded using a Varian Cary 50 or Agilent Cary 60 spectrophotometer equipped with either a fiber optic cable connected to a “dip” attenuated total reflection probe (C-technologies), with a custom built two-necked solution sample holder equipped with a threaded glass connector (sized to fit the dip probe) and purged with argon, or a UNISOKU CoolSpek USP-203 cryostat.

Calculations were performed using the ORCA v. 4.2.1 quantum chemistry package developed by Neese and coworkers,[43,44] and employed the polarized triple-zeta basis set def2-TZVP, the def2/J auxiliary basis set for Coulomb fitting, and the atom-pairwise dispersion correction of Grimme (D3BJ).[45] Tight convergence criteria were required for self-consistent field (SCF) solutions. The Grid4 (GridX4) integration grid size was used for geometry optimizations. Calculations were performed using the B3LYP functional, with the resolution of identity (RI) chain-of-spheres (RIJCOSX) approximation and initiated from the crystallographic coordinates when available.[46,47] Analytical frequency calculations were performed on all optimized structures to determine whether the obtained stationary points corresponded to local minima. Chemcraft was used to visualize the calculated EAS spectra.[48] Excited states from TD-DFT were analyzed by using natural transition orbtials (NTOs) and by visualizing their difference densities between the ground and excited states. Canonical molecular orbital isosurfaces and natural transition orbitals in the TD-DFT calculations were visualized at an isovalue of 0.05 a03 using UCSF ChimeraX.[49]

*Synthesis of $Fe^{II}(S_2^{Me2}N_3(Et,Pr))$ (**8**)*

Sodium methoxide (0.432 g, 8 mmol) was added to 5 mL MeOH in a 20 mL scintillation vial with a stir bar. 3-mercapto-3-methyl-2-butanone (0.945 g, 8 mmol) was added to 5 mL MeOH in a 20 mL scintillation vial, and the sodium methoxide solution was added to this solution with stirring. Iron dichloride (0.450 g, 4 mmol) was added to 10 mL MeOH in a 50 mL Schlenk flask, stirred to dissolve, and the sodium methoxide and 3-mercapto-3-methyl-2-butanone solution was added dropwise into the Schlenk flask with stirring. The reaction was allowed to stir for 15 minutes, and *N*-(2-aminoethyl)-1,3-propanediamine (0.469 g, 4 mmol) in 5 mL MeOH was added dropwise to the now cloudy brown solution in the Schlenk flask. The solution was allowed to stir for twelve hours, and was reduced to dryness in vacuo. The crude product was dissolved in

acetonitrile and filtered to remove sodium chloride, then reduced again to dryness in vacuo. The solid was dissolved in a minimum of DCM, filtered, and layered with pentane in a -35 °C freezer for approximately 72 hours to produce greenish brown X-ray quality crystals (0.549 g, 1.48 mmol, 37%). Electronic absorption (THF) λ_{max} (ε, $M^{-1}cm^{-1}$) = 328 (3190), 427 (1780) nm; (DCM) λ_{max} (ε, $M^{-1}cm^{-1}$) = 320 (3680), 414 (1430) nm; (toluene) λ_{max} (ε, $M^{-1}cm^{-1}$) = 328 (3250), 435 (1360) nm.

*Formation of an intermediate via the addition of O_2 to **8***

A 0.250 mM solution of **8** was prepared in 4 mL of THF, DCM, or toluene under an inert atmosphere in a drybox. The solution was placed modified 1 cm pathlength quartz air-free cuvette with a screw top equipped with a rubber septum. Measurements were performed using an UNISOKU USP-203-B cryostat and monitored with a Varian Cary 50 or Agilent Cary 60 spectrophotometer. A flask with a rubber septum was purged with dry O_2 from a cylinder for 15 or more minutes, and 5 mL of gas was drawn into a gastight syringe. The gas was injected with a long needle to the bottom of the cuvette inside the cryostat, and the solution was monitored by UV/visible spectroscopy.

Stopped-flow kinetic measurements.

Solutions were prepared in a nitrogen atmosphere glovebox and placed in Hamilton gastight syringes equipped with three-way valves. Time-resolved spectra were acquired at low temperatures using a TgK Scientific (U.K.) CSF-61DX2 Multi-Mixing CryoStopped-Flow Instrument equipped with a tungsten lamp visible light source. This instrument uses PEEK (polyether ether ketone) tubing which is inert to all solvents used inside stainless steel plumbing, a 1.00 cm^3 quartz mixing cell, and an anaerobic kit purged with an inert gas. The temperature inside the mixing cell was maintained to ± 0.1 °C, and the mixing time was 2-3 ms. All flow lines

of the instrument were extensively washed with the degassed, anhydrous solvent being used before charging the driving syringes with solutions containing the reactants. The reactions were studied by rapid scanning spectrophotometry detected by a CCD under pseudo-first order conditions with excess oxygen. Saturated solutions of O_2 were prepared by sparging the solvent with dry O_2 from a cylinder for 15 or more minutes, then allowing the solution to equilibrate in a 25 °C temperature-controlled water bath. Dilute O_2 solutions were prepared by diluting the appropriate amount of degassed solvent already inside a gastight syringe with a saturated solution of O_2 prepared as described. All concentrations are reported in the "after mixing" conditions. Experiments were performed in single-mixing mode, with a 1:1 (v/v) mixing ratio. Rates reported for oxygen dependence are the average of three different experiments. Data analysis was performed with Kinetic Studio software from TgK Scientific.[50] Data was fit to a single wavelength (520 nm) using the equation $A_t = A_\infty - (A_\infty - A_0)e^{-k_{obs}t}$. The reaction order with respect to O_2 was determined by varying the O_2 concentration over the range of 2.175 mM to 4.35 mM and the temperature from -60 °C to -25 °C in five degree increments.

*Generation of observed dioxygen intermediate via **3** and O_2*

A saturated solution of **3** was prepared in toluene by stirring an excess quantity of crystalline **3** in toluene and filtering through a syringe filter. For the reaction in the presence of DHA, 100 equivalents of DHA were added to this solution. The solution was placed modified 1 cm pathlength quartz air-free cuvette with a screw top equipped with a rubber septum. Measurements were performed using an UNISOKU USP-203-B cryostat and monitored with a Agilent Cary 60 spectrophotometer. A saturated solution of KO_2 was prepared in toluene by addition of excess KO_2 and Kryptofix® 222 was added to solubilize. 250 µL of this solution was added to the solution of **3** inside the cryostat via gastight syringe.

Hydrogen atom abstraction studies

A 0.250 mM solution of **8** and a varying concentration solution of DHA or d_4-DHA was prepared in 4 mL of DCM or toluene under an inert atmosphere in a drybox. The solution was placed modified 1 cm pathlength quartz air-free cuvette with a screw top equipped with a rubber septum. Measurements were performed using an UNISOKU USP-203-B cryostat and monitored with a Varian Cary 50 or Agilent Cary 60 spectrophotometer. A flask with a rubber septum was purged with dry O_2 from a cylinder for 15 or more minutes, and 5 mL of gas was drawn into a gastight syringe. The gas was injected with a long needle to the bottom of the cuvette inside the cryostat.

Hydrogen peroxide quantitation studies with potassium permanganate

A 1.000 mM solution of **8** was prepared in 4 mL of toluene under an inert atmosphere in a drybox. The solution was placed in a modified 1 cm pathlength quartz air-free cuvette with a screw top equipped with a rubber septum. Measurements were performed using an UNISOKU USP-203-B cryostat and monitored with a Varian Cary 50 or Agilent Cary 60 spectrophotometer. Dry O_2 was added to the reaction as described previously. The reaction was allowed to progress until the 515 nm intermediate was at a maximum, then neat trifluoroacetic acid was added to produce hydrogen peroxide. This solution was filtered through silica to remove ionic species. A 0.25 mM solution of potassium permanganate was prepared in 4mL water and placed in a modified 1 cm pathlength quartz air-free cuvette with a screw top equipped with a rubber septum. This solution was monitored by UV/vis spectroscopy and a 250 μL aliquot of the filtered solution of **8** was added, and the decay in permanganate absorbance was observed at the 547 nm wavelength.

X-ray crystallographic structure determination

A green piece of $Fe^{II}(S_2^{Me2}N_3(Et,Pr))$ (**8**), measuring 0.34 x 0.19 x 0.18 mm^3 was mounted on a loop with oil. Data was collected at -173ºC on a Nonius Kappa CCD FR590 single crystal X-ray diffractometer, Mo-radiation. Crystal-to-detector distance was 40 mm and exposure time was 60 seconds per degree for all sets. The scan width was 1º. Data collection was 99.2% complete to 25º in ϑ. A total of 15261 merged reflections were collected covering the indices, -24<=h<=23, -11<=k<=11, -27<=l<=27. 4364 reflections were symmetry independent and the R_{int} = 0.0414 indicated that the data was good (average quality 0.07). Indexing and unit cell refinement indicated a triclinic lattice. The space group was found to be P b c a (No.61).

The data was integrated and scaled using SAINT, SADABS within the APEX2 software package by Bruker.[51] Solution by direct methods (SHELXT[52] or SIR97[53,54]) produced a complete heavy atom phasing model consistent with the proposed structure. The structure was completed by difference Fourier synthesis with SHELXL.[55] Scattering factors are from Waasmaier and Kirfel[56]. Hydrogen atoms were placed in geometrically idealised positions and constrained to ride on their parent atoms with C---H distances in the range 0.95-1.00 Angstrom. Isotropic thermal parameters U_{eq} were fixed such that they were 1.2U_{eq} of their parent atom Ueq for CH's and 1.5U_{eq} of their parent atom U_{eq} in case of methyl groups. All non-hydrogen atoms were refined anisotropically by full-matrix least-squares. Structures were visualized using ORTEP-III and POV-Ray programs.[57,58]

Table 3-1. Crystal data, intensity collections[a] and structure refinement parameters for $Fe^{II}(S_2{}^{Me2}N_3(Et,Pr))$ (**8**).

	8
Formula	$C_{15}\ H_{29}\ Fe\ N_3\ S_2$
Molecular Weight	371.38
Temperature (K)	100(2)
Crystal System	Monoclinic
Space Group	P_{bca}
a, (Å)	19.7318(12)
b, (Å)	8.9395(6)
c, (Å)	21.3589(15)
α, (°)	90
β, (°)	90
γ, (°)	90
V ($Å^3$)	3767.5(4)
Z	8
R_1	0.0389
R_w	0.0878
GooF	1.126

[a] Mo Ko(α,-) (λ = 0.71070 Å) radiation; graphite monochromator; -90 ºC. [b] $R = \Sigma\ ||F_o| - |F_c|| / \Sigma\ |F_o|$. [c] $R_w = [\Sigma w(|F_o|-|F_c|)^2/\Sigma wF_o^2]^{1/2}$, where $w^{-1} = [\sigma^2_{count} + (0.05\ F^2)^2]/4F^2$.

3.3. Results and Discussion

3.3.1. Isolation of the reduced, constrained complex $Fe^{II}(S_2^{Me2}N_3(Et,Pr))$

Previously in the Kovacs group, $[Fe^{III}(S_2^{Me2}N_3(Et,Pr))]PF_6$ (**3**) was synthesized and characterized. In making this complex, it was reported that unlike $[Fe^{III}(S_2^{Me2}N_2NH(Pr,Pr))][PF_6]$ (**2**), which could be isolated in the reduced form $Fe^{II}(S_2^{Me2}N_2NH(Pr,Pr))$ (**1**) prior to oxidation to form **2**, that the "reduced compound is extremely air sensitive, making further characterization impossible."[59] While the reduced compound is indeed extremely air sensitive, careful handling of materials and rigorous degassing procedures has allowed it to be further characterized. To produce $Fe^{II}(S_2^{Me2}N_3(Et,Pr))$ (**8**), a metal-templated Schiff-base condensation between 3-mercapto-3-methyl-2-butanone and *N*-(2-aminoethyl)-1,3-propanediamine on either iron(II) in the presence of a base. Recrystallization of the crude product via layering a saturated dichloromethane solution with pentane affords large X-ray quality crystals that can be used to further characterize the complex. The reduced complex **8** is a yellow-green complex with electronic absorption maxima at λ_{max} (ε) = 414 (1200) and 318 nm (3150) in DCM (**Figure 3-5**).

The structural characteristics of **3** are very similar to **8**, and together the more constrained **3** and **8** are similar to **1** and **2**. Upon oxidation, both **1** and **8** shorten their metal-ligand bonds by

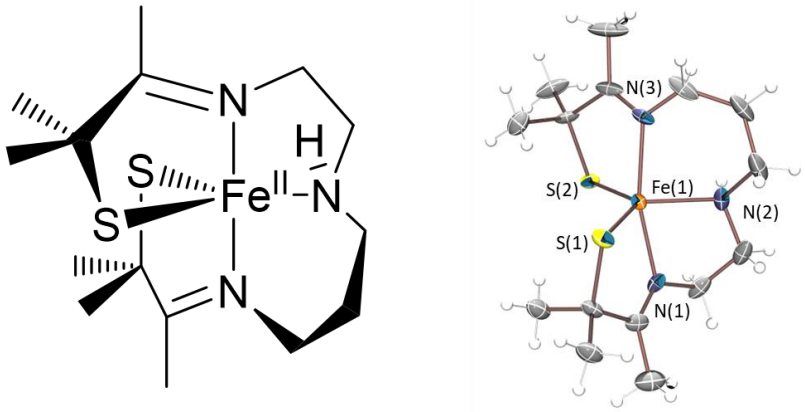

Figure 3-5. Schematic drawing (left) and ORTEP diagram (right) of $Fe^{II}(S_2^{Me2}N_3(Et,Pr))$ (**8**). Thermal ellipsoids at the 50% probability level.

about 0.2 Å and maintain the same coordination environment. They also maintain a similar geometry index (**Table 3-2**), each becoming very slightly more square pyramidal, likely due to the shorter metal-ligand bonds limiting the flexibility of the ligand. As described previously, limiting the flexibility of the complex in this way also has effects on the electronic structure of the complex due to the modified orbital overlap, with **3** being reduced at a more negative -455 mV vs SCE in MeOH compared to -400 mV for **2**.[59]

Table 3-2. Selected metrical parameters for $Fe^{II}(S_2{}^{Me2}N_3(Pr,Pr))$ (**1**), $[Fe^{III}(S_2{}^{Me2}N_3(Pr,Pr))]^+$ (**2**), $Fe^{II}(S_2{}^{Me2}N_3(Et,Pr))$ (**8**), and $[Fe^{III}(S_2{}^{Me2}N_3(Et,Pr))]^+$ (**3**)

	1	**2**	**8**	**3**
Fe–S(1) (Å)	2.3263(5)	2.133(2)	2.3396(6)	2.117(1)
Fe–S(2) (Å)	2.3306(5)	2.161(2)	2.3210(6)	2.117(1)
Fe–N(1) (Å)	2.1556(16)	1.967(4)	2.1213(18)	1.924(2)
Fe–N(2) (Å)	2.1656(16)	2.049(4)	2.206(2)	2.010(4)
Fe–N(3) (Å)	2.1815(15)	1.954(4)	2.1145(18)	1.924(2)
N(1)–Fe–N(3) (°)	172.81(6)	178.1(2)	162.39(7)	174.1(1)
N(2)–Fe–N(3) (°)	90.96(6)	86.2(2)	84.35(7)	87.9(1)
N(1)–Fe–N(2) (°)	83.80(6)	94.2(2)	78.40(7)	86.4(1)
N(3)–Fe–S(2) (°)	105.16(4)	86.4(1)	82.44(5)	86.68(7)
N(2)–Fe–S(2) (°)	107.79(4)	106.5(1)	105.81(6)	112.5(1)
N(1)–Fe–S(1) (°)	97.68(5)	86.7(1)	81.53(5)	86.68(7)
N(2)–Fe–S(1) (°)	125.70(4)	132.3(1)	128.58(6)	141.8(1)
S(2)–Fe–S(1) (°)	126.17(2)	121.0(1)	125.14(2)	105.67(5)
τ^a	0.777	0.763	0.5635	0.538

[a]5-coordinate geometry index, $\tau = (\beta - \alpha)/60$. β is the largest bond angle observed, and α is the second largest bond angle.

3.3.2. Reactivity of $Fe^{II}(S_2^{Me2}N_3(Et,Pr))$ with dioxygen

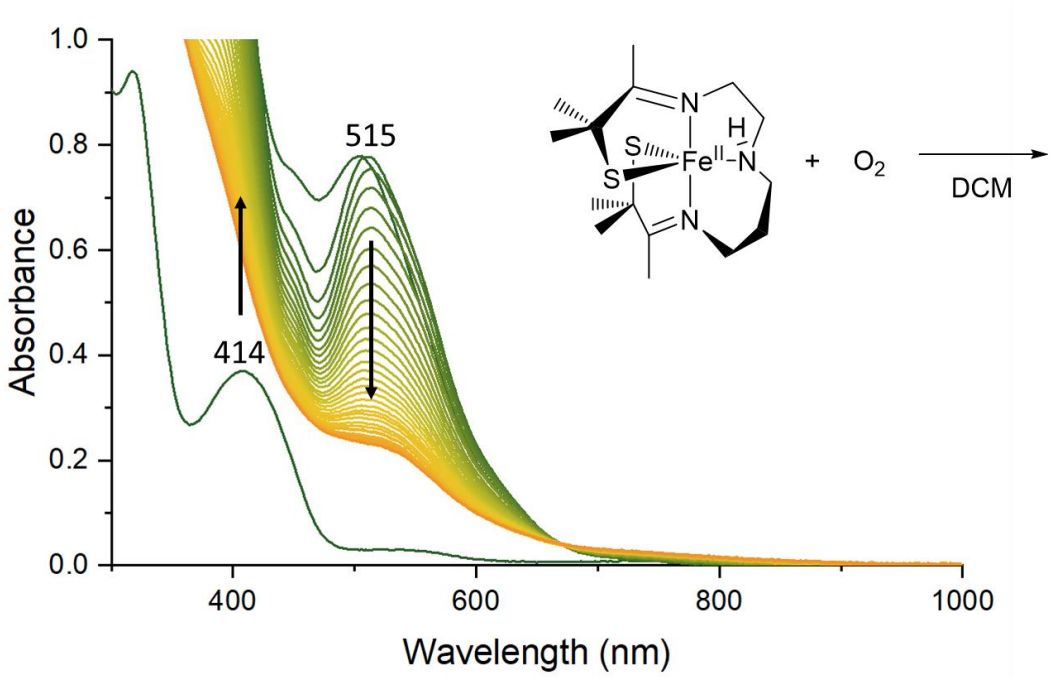

Figure 3-6. Electronic absorption spectrum of the reaction between **8** and O_2 in DCM at room temperature with a scan interval of 1 minute.

The reactivity of **8** with dioxygen was examined. By bubbling dry O_2 through a DCM solution of **8**, the solution immediately changes color from yellow-green to red, shifting the absorption maximum from 414 nm to 515 nm. This new feature exists briefly and bleaches out to a pale yellow solution, with the absorbance peak decaying to the baseline and no new feature taking its place (**Figure 3-6**). The same reactivity occurs in other solvents, with the same features and behavior being observed in THF and toluene with slightly shifted absorbance bands. Electrospray mass spectrometry (ESI-MS) of the reaction mixture showed M+16 and M+32 peaks with the ratio of M+32 to M+16 declining with time, potentially indicating an initial bound superoxo complex and single oxygenation of the complex. However, unlike the analogous reaction of **1** and dioxygen,[30] no sulfenate was able to be isolated from this reaction.

At low temperatures, an intermediate is briefly seen between the 414 nm species and the 515 nm species. This intermediate species has λ_{max} = 337, 389, and 502 nm in DCM, and converts

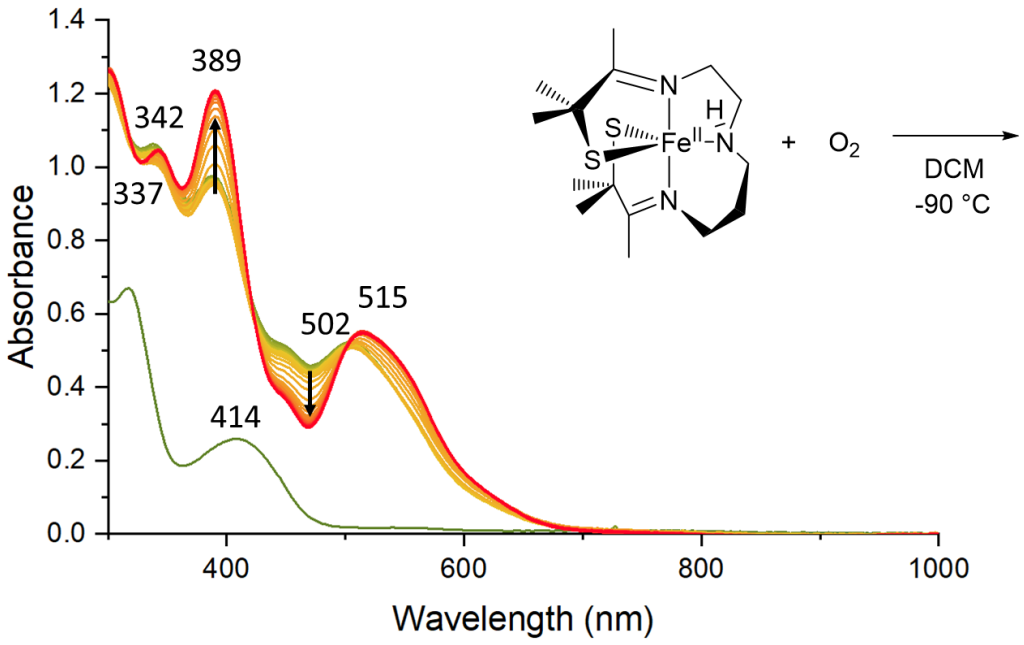

Figure 3-7. Electronic absorption spectrum of the reaction between **8** and limited O_2 in DCM at -90 °C with a scan interval of 1 minute, showing formation of an intermediate.

cleanly to the species observed at room temperature with λ_{max} = 342, 389, and 515 nm in DCM. By using a limited amount of added oxygen, this intermediate species still forms with 10 seconds at -90 °C, but its lifetime is greatly increased, implying that the decay pathway of this species is due to continued oxidation by dioxygen **(Figure 3-7**). In THF and toluene, this reaction proceeds identically with slightly shifted peak positions: an intermediate species with λ_{max} = 337, 392, and 505 nm and a final species with λ_{max} = 343, 393, and 515 nm and a slight shoulder at 560 nm in THF, and an intermediate species with λ_{max} = 339, 392, and 475 nm and a final species with λ_{max} = 339, 393, and 515 nm in toluene. Notable is the shoulder evident in the THF spectrum, where DCM and toluene have only a small asymmetry in the lowest energy peak (**Figure 3-8**). In a coordinating solvent such as methanol, addition of dioxygen to a solution of **8** results in the formation of **3** without any visible intermediates due to the sixth coordination site being blocked by the coordinated solvent, and only outer-sphere electron transfer is possible (**Figure 3-9**).

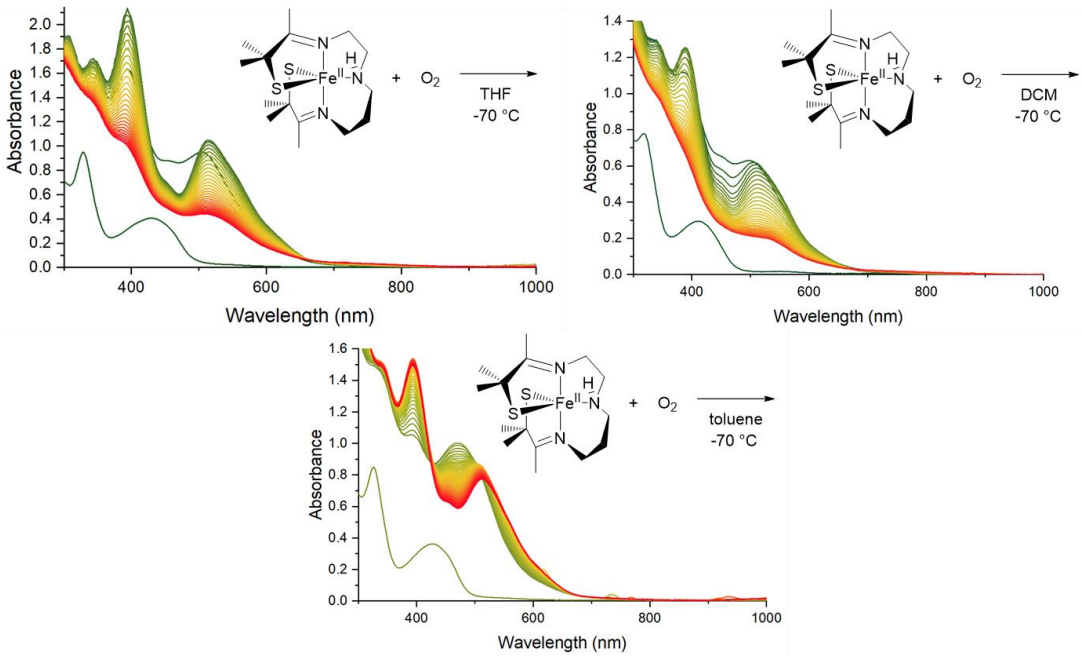

Figure 3-8. Electronic absorption spectra of the reaction between **8** and excess O_2 in (clockwise from top left) THF, DCM, and toluene at -70 °C. 1 minute between scans, 40 minutes total.

In similar conditions, **1** reacts with dioxygen to first form an Fe^{III}-superoxo, which then abstracts a hydrogen atom and converts to the sulfenate **5** in 94% yield. A likely mechanism for this reaction is analogous to that of IPNS and is given in **Scheme 3-1**, where first the Fe^{II} complex coordinates dioxygen and is oxidized, forming an Fe^{III}-superoxo complex. This superoxo can then perform hydrogen atom abstraction on a suitable substrate with a weak enough X-H bond, such as an H-atom donor like cyclohexadiene (CHD, BDE = 76 kcal/mol) or 9,10-dihydroanthracene (DHA, BDE = 76.3),[19] forming an Fe^{III}-hydroperoxo. This hydroperoxo can either homolytically or heterolytically cleave, forming an Fe^{IV}-oxo and a hydroxyl radical in the former case or an Fe^{V}-oxo and a hydroxide anion in the latter case. For IPNS, the Fe^{III}-hydroperoxo first undergoes a reduction to an Fe^{II}-hydroperoxo due to its newly generated thioalkyl radical, but the geminal dimethyl groups of **1** and **8** prevent the formation of a similar species in the model complex. In **1**,

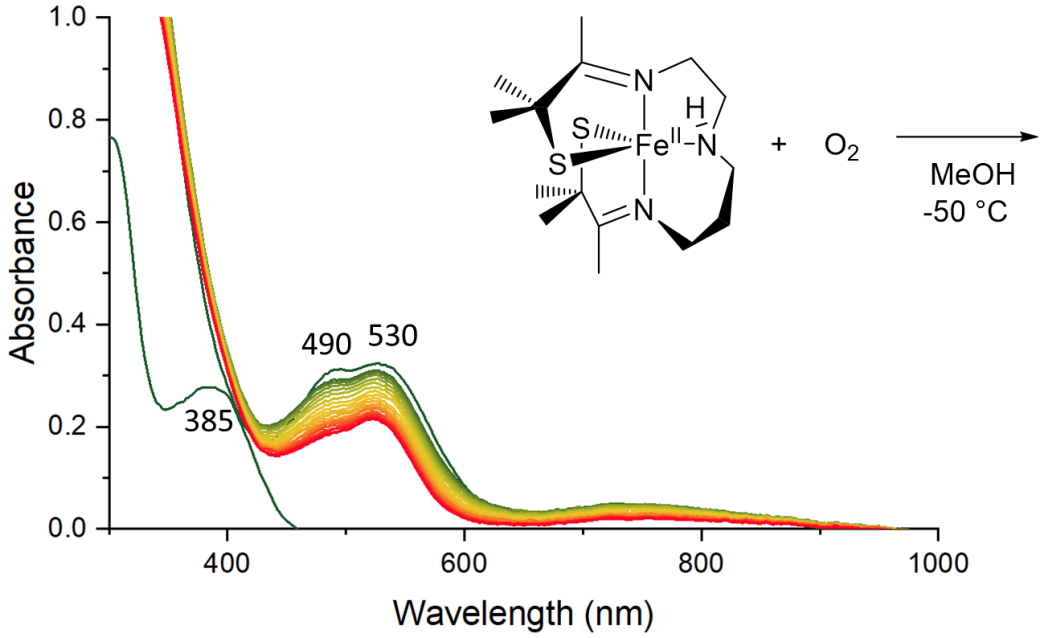

Figure 3-9. Electronic absorption spectrum of the reaction between **8** and O_2 in MeOH at -50 °C with a scan interval of 4 minutes, showing outer sphere electron transfer to form **3**.

this step forms an Fe^{III}-hydroperoxo. The newly generated high-valent Fe-oxo species is likely capable of abstracting a second hydrogen atom, but due to the significantly greater rate of intramolecular reactions versus intermolecular reactions, it undergoes nucleophilic attack from the adjacent sulfur to form the product sulfenate species. Given complex **8**'s similarity to **1**, it is likely that it follows a similar pathway. Because previous work using **3** and oxo-atom donors indicated that formation of the sulfenate progresses along a pathway involving an Fe^{V}-oxo, this reaction not producing the sulfenate product also implies that it does not progress to an Fe^{V}-oxo.

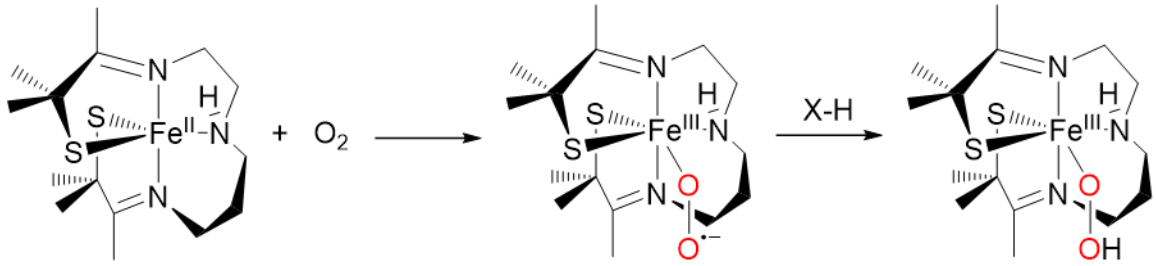

Scheme 3-1. Reaction between **8** and O_2 to produce an Fe^{III}-superoxo **3-superoxo** and subsequent hydrogen atom abstraction to produce the Fe^{III}-hydroperoxo **3-hydroperoxo.**

3.3.3. Generation of an authentic Fe^{III}-superoxo

Using superoxide and **3**, an authentic Fe^{III}-superoxo complex can be generated. Reacting **3** with a saturated potassium superoxide solution solubilized with Kryptofix® 222 in toluene at -60 °C affords an identical spectrum to that formed by **8** and dioxygen, slowly producing the species with a peak at 515 nm. Like the reaction with dioxygen, this species then slowly decays to a pale yellow solution with no spectral features (**Figure 3-10**). The slow growth of the species with a peak at 515 nm likely due to the poor solubility of both **3** and KO_2 in toluene unfortunately means that if the intermediate with a peak at 475 nm forms, it will be able to react and go on to the species with a 515 nm peak without being observed. While this experiment does not result in conclusive assignments for an Fe^{III}-superoxo or Fe^{III}-hydroperoxo complex, because of **3**'s propensity for binding ligands and a superoxide anion's fewer options for interacting with a complex compared to oxygen, we can tentatively identify the initial intermediate with λ_{max} = 475 nm as an Fe^{III}-superoxo **3-superoxo**, and the species it converts to tentatively as an Fe^{III}-hydroperoxo **3-**

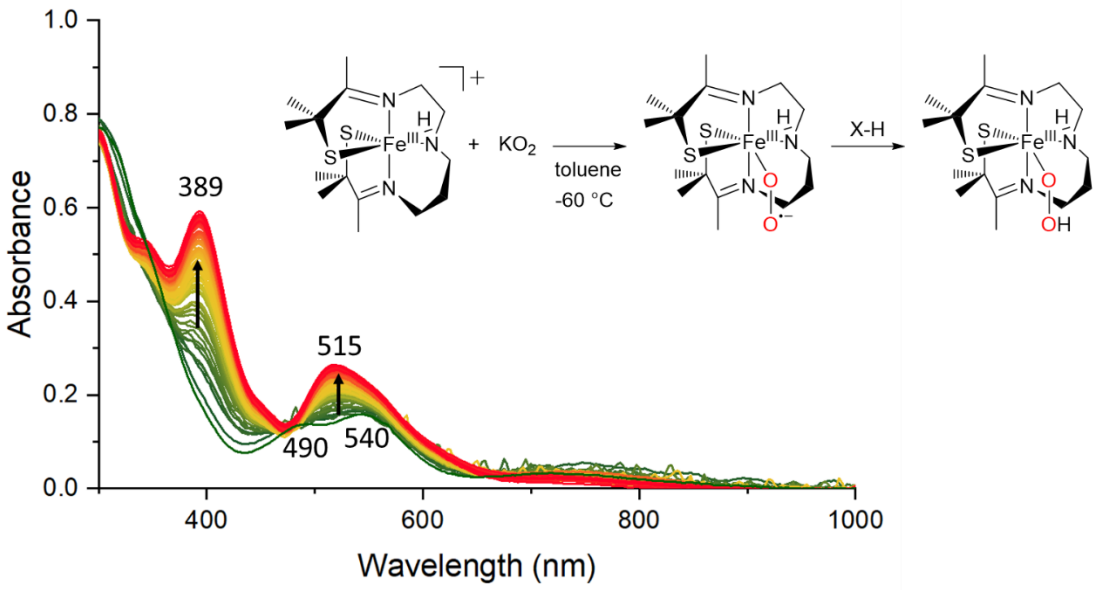

Figure 3-10. Electronic absorption spectrum of the reaction between **3** and excess KO_2 in toluene at -60 °C. 1 minute between scans, 90 minutes total.

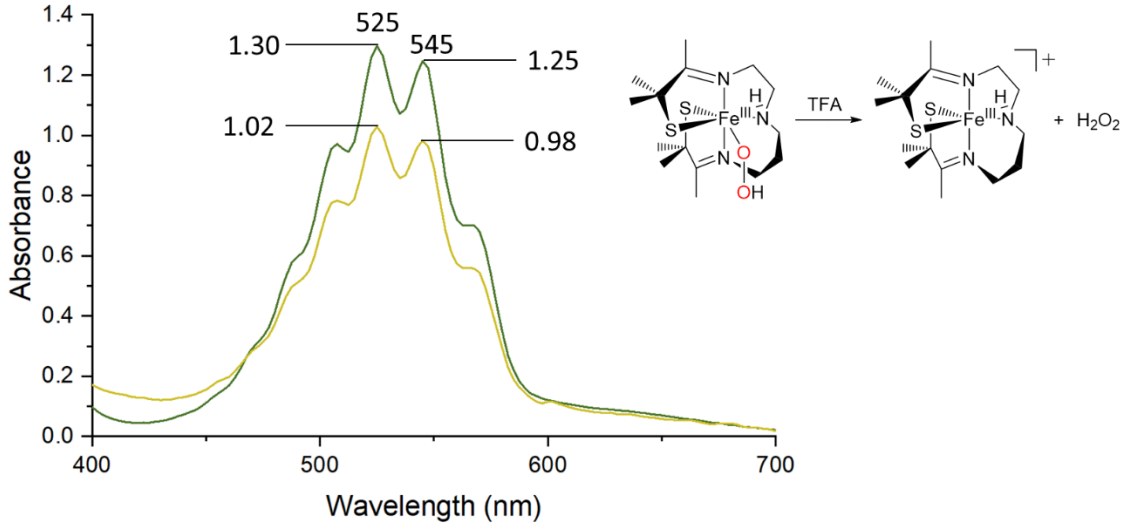

Figure 3-11. Electronic absorbance spectrum of 0.250 mM of potassium permanganate in water before and after addition of 250 µL of the acidified reaction of 1.000 mM of **8** and excess O_2 in 4 mL of THF.

hydroperoxo. The identity of the substrate for hydrogen atom abstraction is very probably the solvent, although GC/MS experiments to identify a product of this reaction were inconclusive.

In order to confirm the generation of a hydroperoxo species, a permanganate assay was performed. The proposed hydroperoxo intermediate was generated by addition of excess dioxygen to **8** in THF at low temperatures (-60 °C), first forming the proposed superoxo species and slowly converted to the proposed hydroperoxo species. Neat trifluoroacetic acid was added, the solution was allowed to stir briefly, and then filtered through a plug of silica to remove ionic species. A 250 µL aliquot was then added to an aqueous solution of potassium permanganate ($KMnO_4$) (0.25 mM) (**Figure 3-11**), and the concentration of $KMnO_4$ was monitored by UV/visible spectroscopy. According to the stoichiometry of $KMnO_4$ consumed, one equivalent of hydrogen peroxide is produced per equivalent of **8** in the starting solution, consistent with a monomeric Fe^{III}-hydroperoxo species. Addition of the hydroperoxo intermediate or trifluoroacetic acid alone to $KMnO_4$ does not result in any change to the concentration of permanganate in solution. This shows that this observed species is indeed an Fe^{III}-hydroperoxo, and because the method of formation of

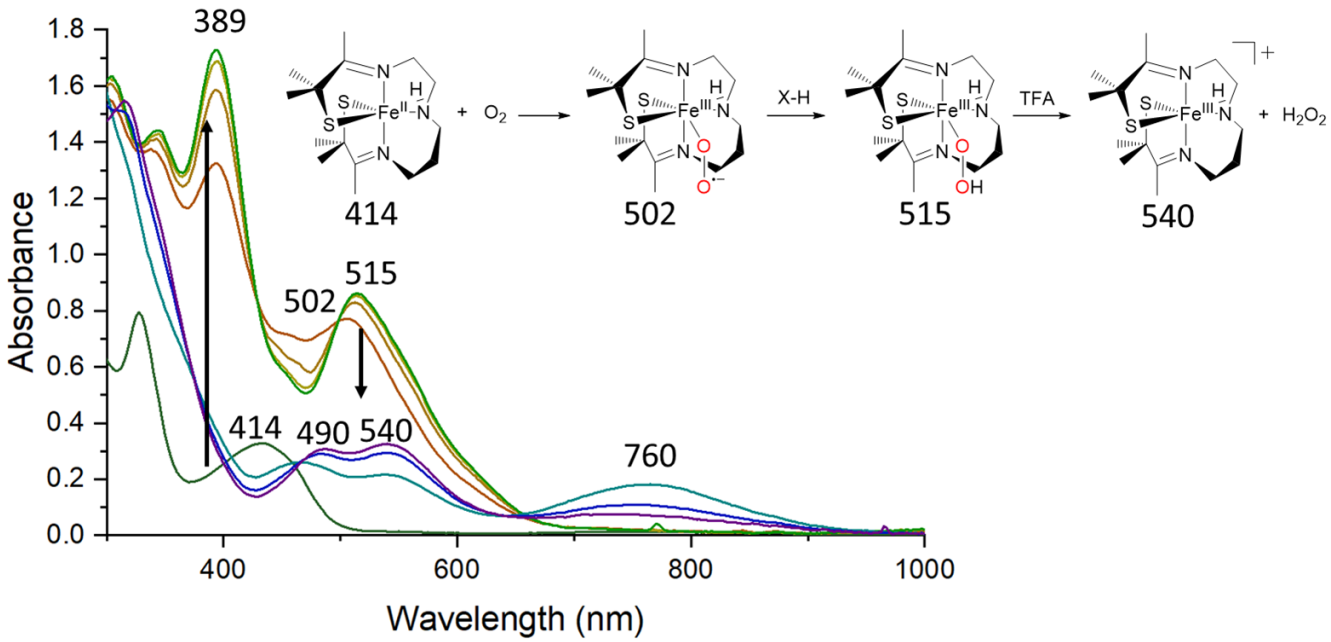

Figure 3-12. Electronic absorption spectrum of the reaction between **8** and excess O_2 at -60 °C and subsequent acidification, showing progress from **8** to **3-superoxo** to **3-hydroperoxo** to **3**, with identities of proposed species labeled by representative λ_{max}.

a hydroperoxo from dioxygen requires a hydrogen atom abstraction, that the preceding intermediate is very likely an Fe^{III}-superoxo.

The preparation of the hydrogen peroxide assay was also observed via UV/visible spectroscopy. Before the addition of trifluoroacetic acid, the reaction of **8** and dioxygen in THF proceeds as normal. Upon the addition of trifluoroacetic acid, briefly an intermediate with a low-energy peak at 760 nm appears, before converting cleanly to the Fe^{III} complex **3** in 97% yield according to its absorbance (**Figure 3-12**). The generation of **3** from **8** and acid shows that the ligand sulfur atoms are not being oxidized by direct attack of the dioxygen, and that the reaction proceeds through substrates ligated to the iron. The same reaction monitored in toluene results in an electric blue solution with λ_{max} = 620 nm due to the trifluoroacetate anion coordinating directly to the iron. After filtration through a silica plug to remove ionic species, this solution also

consumes one equivalent of permanganate per equivalent of iron in the starting solution, highlighting the effect solvent polarity has on observed species.

3.3.4. Kinetics and thermodynamics of dioxygen binding to $Fe^{II}(S_2^{Me2}N_3(Et,Pr))$

Cryogenic stopped-flow kinetic studies were performed to characterize the reaction between **8** and dioxygen. The growth of the spectral features associated with the superoxo $Fe^{III}(S_2^{Me2}N_3(Et,Pr))(O_2)$ and the hydroperoxo $Fe^{III}(S_2^{Me2}N_3(Et,Pr))(OOH)$ were monitored under pseudo first order conditions using excess O_2. Saturated solutions of O_2 were generated by bubbling dry O_2 gas into a flask sealed with a septum containing toluene for 15 minutes, followed by equilibration of the solution in a water bath at 25 °C. The solubility of O_2 in toluene was taken as 8.7 mM in toluene at 25 °C.[60,61] Dilutions were performed according to the method developed by Greiner.[31] The proposed kinetic scheme for the binding of dioxygen and abstraction of a hydrogen atom is shown in **Scheme 3-2**. The overall rate of formation of the hydroperoxo is given by **Equation 3.4**, where $[Fe^{III}]$ is the concentration of **8**, $[O_2]$ is the concentration of dioxygen, and [XH] is the concentration of abstractable hydrogen atoms. This rate law uses the steady-state approximation, assuming that the concentration of the superoxo intermediate quickly reaches an equilibrium where its rate of generation is equal to its rate of consumption. A more general expression not making this approximation is given as **Equation 3.5**.

$$Fe^{II} + O_2 \underset{k_{-1}}{\overset{k_1}{\rightleftharpoons}} Fe^{III}\text{-}O_2^{\bullet -} + XH \xrightarrow{k_2} Fe^{III}\text{-}OOH$$

Scheme 3-2. Proposed kinetic scheme for the binding of dioxygen and abstraction of a hydrogen atom by **1** and **8**.

$$\frac{d[Fe^{III}OOH]}{dt} = k_2[Fe^{III}O_2^{\cdot-}][XH] \tag{3.1}$$

$$\frac{d[Fe^{III}O_2^{\cdot-}]}{dt} = 0 = k_1[Fe^{II}][O_2] - k_{-1}[Fe^{III}O_2^{\cdot-}] - k_2[Fe^{III}O_2^{\cdot-}][XH] \tag{3.2}$$

$$[Fe^{III}O_2^{\cdot-}] = \frac{k_1[Fe^{II}][O_2]}{k_{-1} + k_2[XH]} \tag{3.3}$$

$$rate = \frac{d[Fe^{III}OOH]}{dt} = \frac{k_1k_2[Fe^{II}][O_2][XH]}{k_{-1} + k_2[XH]} \tag{3.4}$$

$$rate = \frac{k_1k_2[Fe^{II}][O_2][XH]}{k_{-1} + k_2[XH]} - \frac{k_{-1}\frac{d[Fe^{III}O_2^{\cdot-}]}{dt}}{k_{-1} + k_2[XH]} \tag{3.5}$$

In the case where k_{-1} is much larger than k_2[XH], this simplifies to $rate = \frac{k_1k_2}{k_{-1}}[Fe^{II}][O_2][XH]$, and in the case where k_{-1} is much smaller than k_2[XH], this simplifies to $rate = k_1[Fe^{II}][O_2]$. Using pseudo first order conditions, the concentrations of oxygen and of

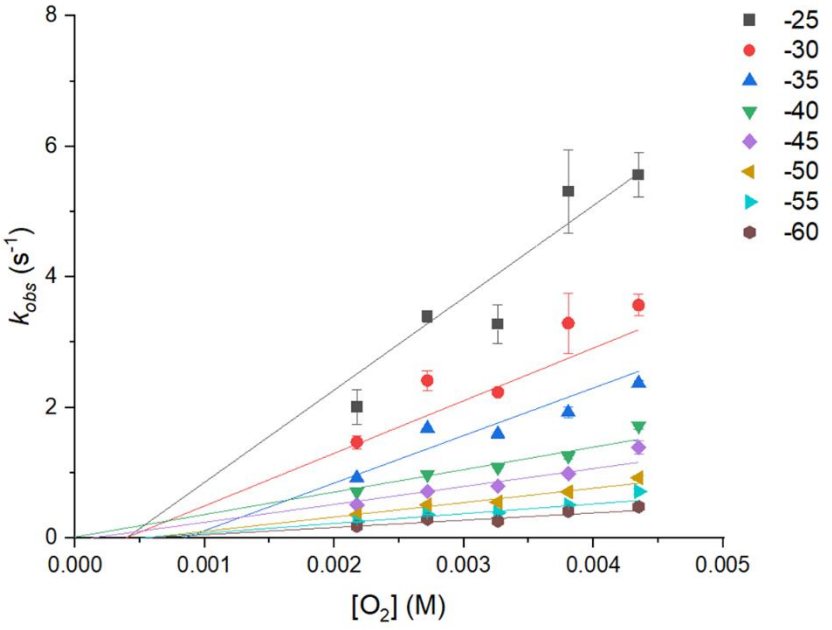

Figure 3-13. Temperature-dependent rate constants k_{obs} for the formation of proposed hydroperoxo **3-hydroperoxo** in the reaction between **8** and O_2 in toluene, plotted against [O_2]. The zero intercepts are consistent with irreversible O_2 binding. [**8**] after mixing = 0.1 mM, [O_2] listed corresponding to after mixing in the stopped-flow cell.

abstractable hydrogen bonds can be treated as constants, and the rates further simplify to $rate = k_{obs}[Fe^{II}]$ with $k_{obs} = \frac{k_1 k_2}{k_{-1}}[O_2][XH]$ in the former case and $rate = k_{obs}[Fe^{II}]$ with $rate = k_1[O_2]$ in the latter case. In both cases, the overall observed rate of formation should be dependent only on the concentration of iron. The same is true for the more general equation provided that the term $\frac{d[Fe^{III}O_2^{\cdot-}]}{dt}$ is much smaller than the term $\frac{k_1 k_2[Fe^{II}][O_2]}{k_{-1}}$.

The reaction between **8** and dioxygen was monitored by stopped-flow UV/visible spectroscopy at temperatures ranging from -60 °C to -25 °C. In all cases, the growth of only one species with an absorbance maximum at λ_{max} = 520 nm was observed. The kinetic trace of the change in absorbance at λ_{max} = 520 nm can be fit to the single exponential equation $A_t = A_\infty - (A_\infty - A_0)e^{k_{obs}t}$ with very small residuals (**Figure 3-13**).

Although the formation of the proposed hydroperoxo product of the reaction is a two step process which would imply the existence of two observable rate constants via stopped flow, we are still able to fit this process with a single exponential (**Table 3-3**). This indicates that either k_1

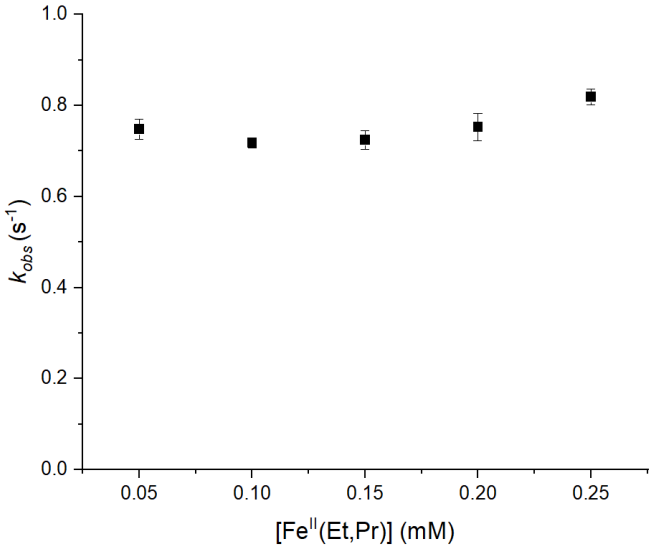

Figure 3-14. Plot of observed rate constants (k_{obs}) versus the concentration of [**8**] for the formation of **3-hydroperoxo** at -40 °C in toluene, showing a first order dependence on [**8**]. [O_2] after mixing = 4.35 mM.

or k_2 is much larger than the other, and that either upon exposure to dioxygen **8** forms a superoxo complex almost immediately, or that once the superoxo intermediate is formed that it almost immediately reacts to form a hydroperoxo. As will be discussed in the following section, studies with limiting O_2 could be helpful in elucidating the properties of this reaction.

Table 3-3. Temperature-dependent rate constants for irreversible O_2 binding to $Fe^{II}(S_2{}^{Me2}N_2NH(Pr,Pr))$ (**1**) in THF and for irreversible O_2 to $Fe^{II}(S_2N_3(Et,Pr))$ (**8**) in toluene.

Temperature (K)	**1 ($M^{-1}s^{-1}$)** THF	**8 ($M^{-1}s^{-1}$)** toluene
273.15	2.66×10^2	
268.15	2.31×10^2	
263.15	1.86×10^2	5.70×10^3
258.15	1.59×10^2	3.42×10^3
253.15	1.23×10^2	2.74×10^3
248.15	1.17×10^2	1.66×10^3
243.15	8.2×10^1	9.21×10^2
238.15	7.3×10^1	5.79×10^2
233.15	5.0×10^1	4.24×10^2
228.15		3.73×10^2
223.15		2.44×10^2
218.15		1.98×10^2
213.15		1.32×10^2
$\Delta H^{\ddagger}$ (kJ/mol)	19.3	27.4
$\Delta S^{\ddagger}$ (J/mol*K)	-127	-73.5
E_a (kJ/mol)	21.4	29.3
$\Delta G^{\ddagger}_{T=243K}$ (kJ/mol)	50.1	45.2

By varying the concentration of **8** while keeping oxygen concentration constant, the observed rate constant k_{obs} was found to be independent of the concentration of **8**, confirming the

previous findings of the permanganate assay that the reaction is first-order overall with respect to **8**, consistent with the formation of a 1:1 dioxygen adduct (**Figure 3-14**). The reaction order with respect to dioxygen was determined by varying the concentration of dioxygen over the range of $[O_2]$ = 2.175 mM to 4.35 mM in toluene. The observed rate constant k_{obs} increased linearly with increasing dioxygen concentration, consistent with a first order dependence on dioxygen. The intercept of these plots was found to be very close to zero over the course of the temperature range. Using the more general form of the rate law given in **Equation 3.5** which is in the form of $y = mx + b$, we can conclude that k_{-1} is either zero or very close to it, and that the binding of oxygen to **8** is irreversible. Because of this, we can disregard the second term in **Equation 3.5** and it becomes identical to the steady-state approximation **Equation 3.4**.

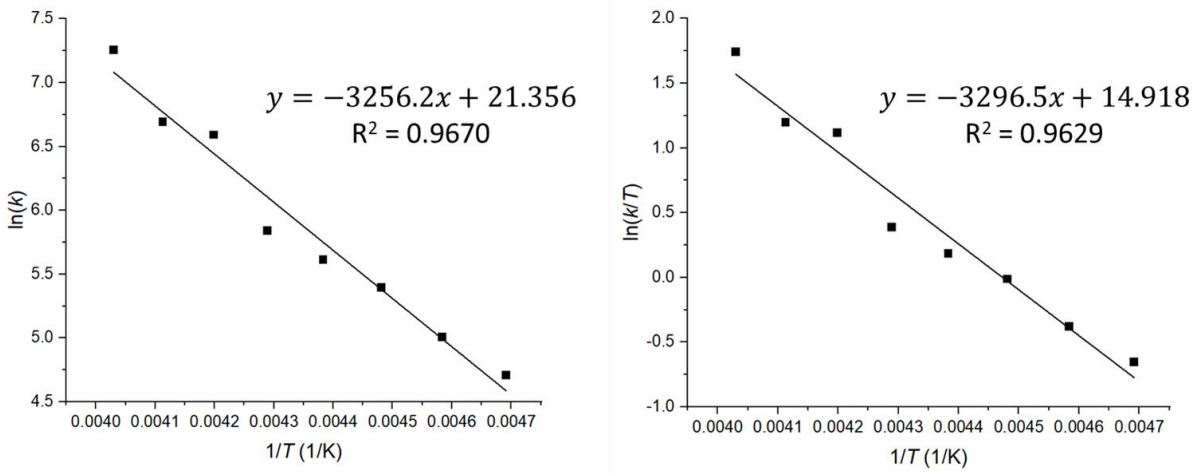

Figure 3-15. Arrhenius plot (left) and Eyring plot (right) for the reaction of **8** and O_2 in toluene from which thermodynamic parameters were obtained (**Table 3-3**). Second order rate constants (k) were obtained from the slope of k_{obs} vs. $[O_2]$ plots (**Figure 3-13**). [**8**] = 0.1 mM after mixing.

From the observed rate constants for the binding of dioxygen to **8**, k_1 was obtained at eight different temperatures and activation parameters were calculated from Eyring and Arrhenius plots (**Figure 3-15**). For the overall process of binding dioxygen to **8** and abstracting a hydrogen atom from a substrate, $\Delta H^{\ddagger}$ = 27.4 kJ/mol and $\Delta S^{\ddagger}$ = -73 J/molK. This negative entropy is expected for

an associative process involving the binding of O_2. The activation energy of the reaction, derived from an Arrhenius plot, is E_a = 29.3 kJ/mol (**Table 3-3**).

3.3.5. Examination of the rate of reaction between $Fe^{II}(S_2^{Me2}N_3(Et,Pr))$ and dioxygen in methylene chloride

To characterize the reaction between the Fe^{III}-superoxo generated by **8** and O_2, reactions with substrates with weak C–H bonds were carried out. Solutions of **8** in DCM (BDE = 95.7 kcal/mol)[19] were prepared inside a nitrogen atmosphere glovebox with varying amounts of DHA (BDE = 76.3 kcal/mol)[19] in an airtight quartz cuvette sealed with a rubber septum. The reaction was observed via UV/visible spectroscopy held at a constant temperature by a cryostat. A fixed quantity of dioxygen was bubbled through via injection by gastight syringe. Upon addition of O_2, the 414 nm species converts immediately (within the 5 second scan time of the instrument) to a new intermediate with λ_{max} = 337, 389, and 502 nm that has been proposed to be an Fe^{III}-superoxo. This Fe^{III}-superoxo converts with varying speed to a species with λ_{max} = 342, 389, and 515 nm that has been proposed earlier in the chapter to be an Fe^{III}-hydroperoxo.

While it seems counterintuitive that using a slower method of observing changes in the UV/visible spectrum results in finding an intermediate in the reaction, this can be explained by the process of combining the reactants. In the stopped-flow instrument, solutions of **8** and dioxygen are forcefully mixed inside the observation chamber, ensuring complete and even distribution of both reactants. Inside the cuvette of the cryostat-equipped UV/vis spectrometer, the solution of **8** and a substrate are already combined, and O_2 is introduced via bubbling through the reaction mixture with a syringe. Some O_2 is dissolved, but the solution does not become saturated and some portion of the oxygen stays in the headspace of the cuvette, diffusing slowly into the reaction

mixture. This lower concentration of oxygen slows the reaction to form the Fe^{III}-superoxo complex. The concentration of the superoxo is given by the equation

$$[Fe^{III}O_2^{\cdot-}] = \frac{k_1[O_2][Fe^{II}]_0}{k_2[XH] - k_1[O_2]}\left(e^{-k_1[O_2]t} - e^{k_2[XH]t}\right) \quad (3.6)$$

which can be differentiated to give

$$[Fe^{III}O_2^{\cdot-}]_{max} = [Fe^{II}]_0\left(\frac{k_2[XH]}{k_1[O_2]}\right)^{\frac{k_2[XH]}{k_1[O_2]-k_2[XH]}} \quad (3.7)$$

$$t_{max} = \frac{\ln\left(\frac{k_2[XH]}{k_1[O_2]}\right)}{k_2[XH]-k_1[O_2]} \quad (3.8)$$

With constant k_2[XH], t_{max} (the time at which concentration of the Fe^{III}-superoxo species is at a maximum) thus increases as k_1[O_2] decreases. Because this is dependent only on k_1[O_2], this does not affect measurement of k_2[XH]. [62]

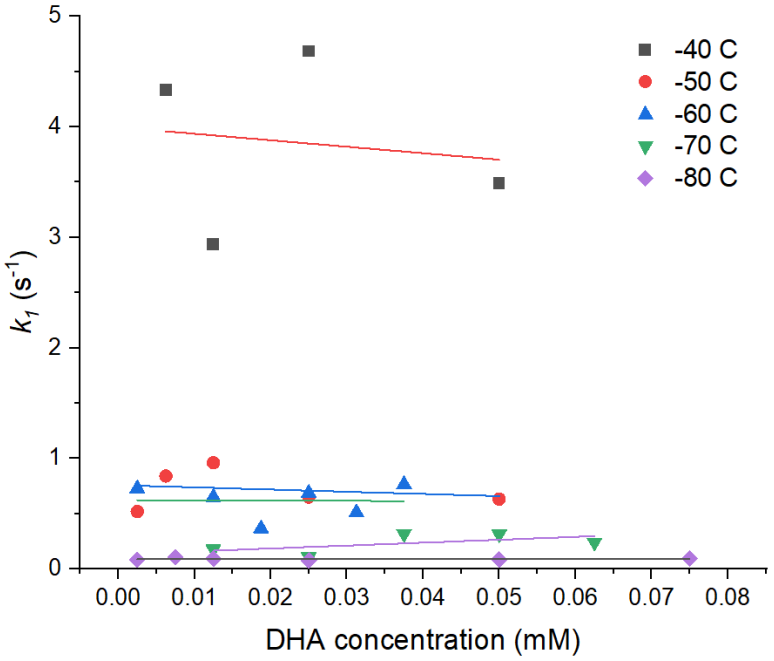

Figure 3-16. Plot of the rate constant for formation of **3-hydroperoxo** from **8** and O_2 versus 9,10-dihydroanthracene (DHA) concentration at various temperatures in DCM, showing no dependence on the concentration of DHA. [**8**] = 0.250 mM for all experiments.

By keeping the concentrations of **8** and dioxygen constant, changing the concentration of easily abstractable C–H bonds should change the rate of the reaction according to **Equation 3.4**. However, when the concentration of DHA was varied from 2.5 mM to 50 mM (10 to 200 equivalents) from -80 °C to -40 °C, no clear relationship was observed between the concentration of DHA present and the rate of the reaction, and no anthracene (the product of C-H activation of DHA) was observed by GC/MS (**Figure 3-16**). The reason for this is unclear but there are several possible explanations. It could be that the Fe^{III}-superoxo is capable of abstracting hydrogen atoms from very strong C–H bonds such as from the solvent DCM. If this is the case, the concentration of DCM in pure DCM is 15.66 M, significantly higher than the 2.5 to 50 mM of DHA added to the solution. Even with a significantly lower rate constant k_2 due to a stronger C–H bond, the term k_2[XH] will of similar magnitude or higher given the massively higher concentration, and no significant rate change would be observable due to changing the concentration of DHA. It is also possible that rather than hydrogen atom abstraction, the Fe^{III}-superoxo complex is performing halogen atom abstraction. The C–Cl bond of DCM is much weaker, with BDE = 80.8 kcal/mol.[19] Given the much greater concentration of solvent versus added DHA, the same rate considerations as the previous case apply. Another possibility is that the Fe^{III}-superoxo is obtaining a proton through an intramolecular reaction. While there is no analogous C–H bond to IPNS α to the sulfur atoms of **8**, the hydrogen atoms in the ligand backbone could feasibly be in reach of the distal oxygen of the superoxo. C–H bonds with an α-N–H are in the range of 90 kcal/mol,[19] relatively quite strong but not as tightly held as DCM. There is also the hydrogen atom bonded to the middle amine of the ligand backbone, with literature BDEs of similar compounds again around 90 kcal/mol.[19] There is also the potential that the observed reactivity is not hydrogen atom abstraction at all but proton transfer, however, there are very few if any acidic protons in solution, with the

mostly likely culprit being the N–H proton in the middle of the ligand backbone. Crystallographic evidence points to this mechanism as unlikely, as all crystal structures of **2** and **3** with a ligand bound in the sixth coordination site have that ligand bound opposite the amine nitrogen from that proton. A further intramolecular mechanism is possible where an Fe^{III}-superoxo reacts with the adjacent sulfur atom to form a four-membered Fe–O–O–S ring, which will be discussed in further detail later. The first case of hydrogen atom abstraction from the solvent would be able to be confirmed through deuteration of the solvent, but because of the possibility of halogen atom abstraction, DCM is a poor solvent for this study.

3.3.6. Examination of the rate of reaction between $Fe^{II}(S_2{}^{Me2}N_3(Et,Pr))$ and dioxygen in toluene.

Due to the possibility of halogen atom abstraction, the same experiment was performed in toluene. Toluene has a BDE of 89.7 kcal/mol for the C–H bonds of its methyl group and no other abstractable hydrogen atoms. Using the same method as in DCM, the reaction between **8** and O_2 was monitored by UV/vis. The reaction proceeds identically, with the first proposed Fe^{III}-superoxo intermediate having λ_{max} = 339, 392, and 475 nm and the final proposed Fe^{III}-hydroperoxo having λ_{max} = 339, 393, and 515 nm. Notable is that this reaction proceeds to the proposed Fe^{III}-hydroperoxo in the absence of any added DHA and any acidic protons (except the possible amine proton in the ligand backbone), implying the possibility of HAT from the solvent or from the ligand. This reaction was performed at several temperatures, and thermodynamic parameters were calculated. The activation barrier E_a of this reaction is 45.65 kj/mol, $\Delta H^{\ddagger}$ = 43.8 kJ/mol and $\Delta S^{\ddagger}$ = -79.7 J/molK. The negative entropy is again indicative of an associative process, and the high activation barrier reflects the difficulty of cleaving an X–H bond.

To determine if the presence of weak C–H bonds would increase the rate of reaction, experiments were carried out varying the concentration of DHA from 12.5 mM to 50 mM (50 to 200 equivalents vs **8**) across -55 °C to -35 °C. Once again, no clear trend between the concentration of DHA and the rate of reaction was observed (**Figure 3-17**). If the assumption is made that HAT is occurring exclusively from DHA regardless, and Eyring and Arrhenius plots are constructed, we find that the $\Delta H^{\ddagger}$ for the reaction is an enormous 63.1 kJ/mol, and the $\Delta S^{\ddagger}$ is 72.3 J/molK. The large positive entropy would reflect a dissociative process, which does not describe the reaction between an Fe^{III}-superoxo and an H-atom donor. Further, no anthracene could be detected by GC/MS from this reaction. While this does not necessarily rule out the possibility of hydrogen atom abstraction being performed by this Fe^{III}-superoxo complex, these results show that there may be confounding factors.

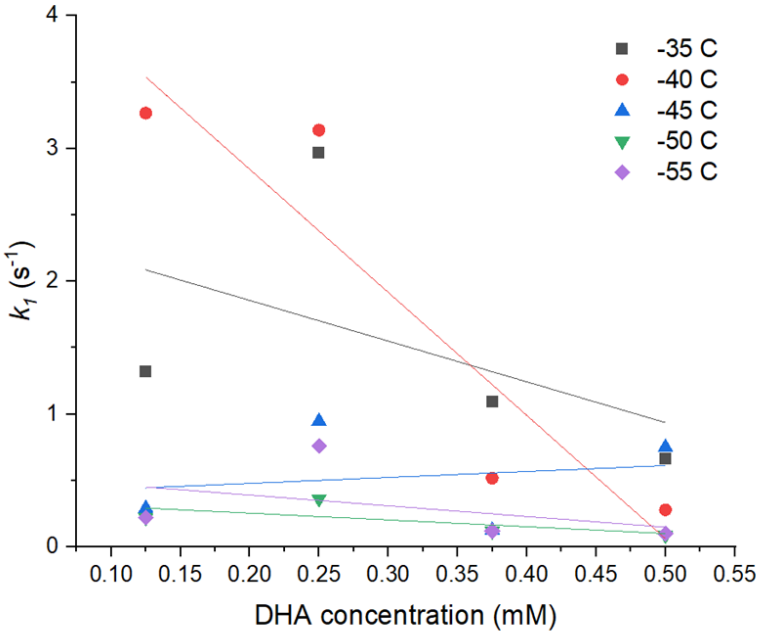

Figure 3-17. Plot of the rate constant for formation of **3-hydroperoxo** from **8** and O_2 versus 9,10-dihydroanthracene (DHA) concentration at various temperatures in toluene, showing no dependence on the concentration of DHA. [**8**] = 0.250 mM for all experiments.

3.3.7. Experiments with deuterated substrates

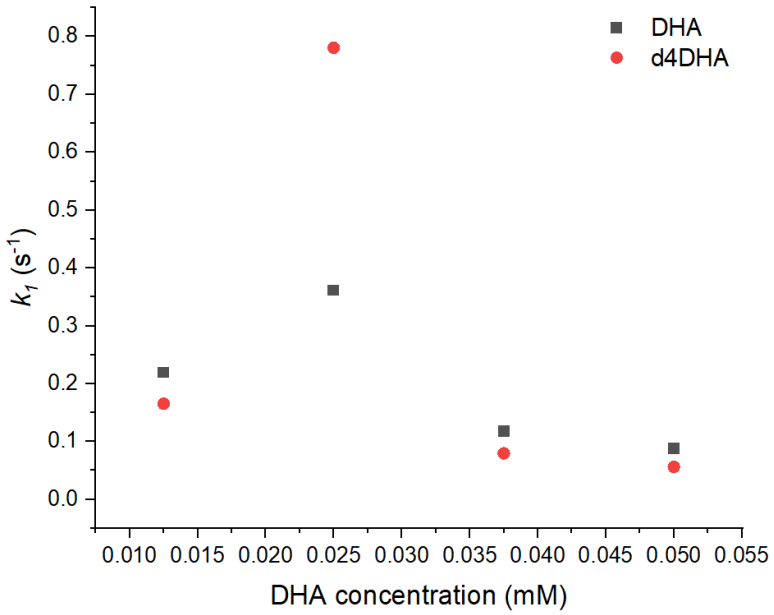

Figure 3-18. Plot of the rate constant for formation of **3-hydroperoxo** from **8** and O_2 versus 9,10-dihydroanthracene (DHA) concentration or d_4-DHA in toluene at -50 °C, showing no rate change after deuteration. [**8**] = 0.250 mM for all experiments.

While no oxidative products from the reaction between the superoxo species formed by **8** and dioxygen have been observed directly as yet, it may be possible to indirectly observe the reaction through kinetic isotope effects. To examine this, reactions were carried out using d_8-toluene a solvent or with added d_4-DHA. The reaction was performed identically to previous experiments and monitored by UV/visible spectroscopy. With d_4-DHA, there was no observed change in rate (**Figure 3-18**). If the Fe^{III}-superoxo were abstracting a hydrogen atom from DHA, a slowdown in rate on the order of 4-5 times would be expected based on those observed for similar Fe^{III}-superoxos,[63–66] or higher if a tunneling mechanism is involved.[67] This result is not surprising given the previous experiments indicating no rate dependence on the concentration of DHA and the possibility of HAT from the solvent.

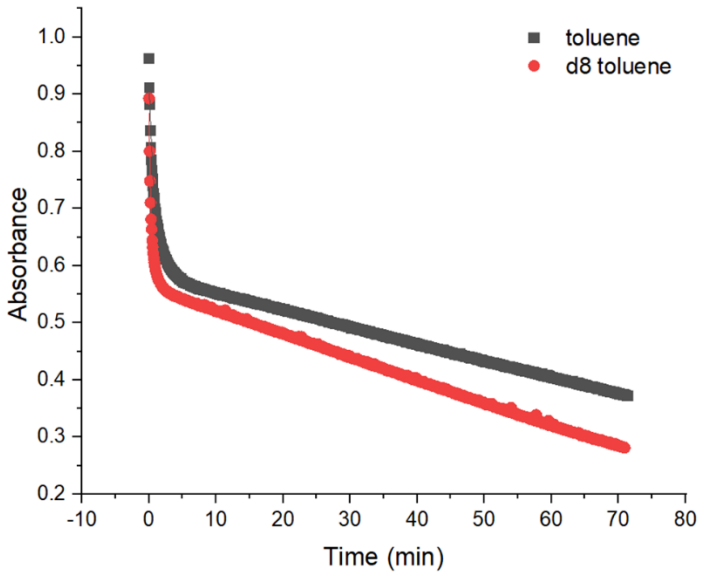

Figure 3-19. Absorbance of the reaction between **8** and O_2 at 470 nm in toluene and d_8-toluene, showing a slight *increase* in rate in deuterated solvent.

Reactions were carried out using d_8-toluene as the solvent. The reaction progressed identically to that using protiated solvent was observed via UV/visible spectroscopy. No change in rate was observed (**Figure 3-19**). The lack of any sort of kinetic isotope effect observed with deuterated substrate or solvent is not necessarily conclusive evidence that hydrogen atom transfer is not occurring, although it does warrant consideration. It is possible that a kinetic isotope effect is not observed because the rate determining step of the reaction does not involve abstracting the hydrogen atom of the solvent or substrate. It is also possible that a kinetic isotope effect is not observed because the reaction does not involve a hydrogen atom abstraction step. This process may also be confounded by saturation kinetics: it is possible that the concentration of substrate in solution (either DHA or the solvent) is past a point where more productive collisions between the Fe^{III}-superoxo and a substrate can occur, and that increasing the concentration further will not increase the rate of the two molecules coordinating to each other to react. However, saturating the solution would not prevent the observation of a kinetic isotope effect.[68,69] It also remains possible that the Fe^{III}-superoxo is abstracting a proton from its own ligand backbone, in which case only

deuteration of the ligand would result in observation of a kinetic isotope effect, and it also remains possible that the Fe^{III}-superoxo is forming a four-membered Fe–O–O–S ring.

3.3.8. Comparisons with the more flexible complex $Fe^{II}(S_2^{Me2}N_2NH(Pr,Pr))$

Previous work in the Kovacs group has characterized an Fe^{III}-superoxo generated from the reaction between **1** and O_2. This reaction was monitored by stopped-flow, and thermodynamic parameters were calculated from the corresponding rates derived from the stopped-flow kinetic studies. In THF, $\Delta H^{\ddagger}$ for the binding of dioxygen to Fe^{II} was 19.3 kJ/mol in contrast to **8**'s 27.4 kJ/mol in toluene, and $\Delta S^{\ddagger}$ was -127 J/mol*K compared to **8**'s -73 J/mol*K (**Table 3-3**). This is similar to the binding of PNO to **3** vs **2**, where the more constrained ligand is again found to have a less negative $\Delta S^{\ddagger}$ corresponding to less energy required for rearrangement. The solvent likely contributes to these values, with the more polar THF contributing more to the change in entropy and requiring more energy input enthalpically to break the solvent interactions. Unlike the binding of PNO to **3**, the more constrained ligand also has a larger $\Delta H^{\ddagger}$. Some care must be taken in comparing these values, however, as the individual rates of O_2 binding to **8** and the subsequent formation of the proposed Fe^{III}-hydroperoxo were not able to be separated. Thus, the $\Delta H^{\ddagger}$ and for **8** are representative of two bonds forming and one potentially weak bond (the H-atom donor) breaking, which would result in a larger change in enthalpy.

This previous work found that the Fe^{III}-superoxo, with λ_{max} = 409, 523, and 707 nm, converted to a proposed Fe^{III}-hydroperoxo species with λ_{max} = 696 nm. The Fe^{III}-superoxo and hydroperoxo formed by **8** and O_2, in contrast, have no lower energy transitions. DFT studies on **1** indicated that the low-energy peak is primarily due to a sulfur to metal-superoxo charge transfer band. The lack of a comparable band in **3-superoxo** and the higher energy UV/visible absorbances in general indicate that the corresponding metal-superoxo molecular orbitals are higher in energy.

2-superoxo complex was also found to be capable of abstracting hydrogen atoms from the solvent THF (BDE = 92 kcal/mol) based on the evidence of an observed kinetic isotope effect. No such effect was observed in **8**, although a proposed hydroperoxo species is observed despite this.

Most notable is that **2-hydroperoxo** converts to the previously discussed sulfenate **5** over the course of a few hours. Despite the similarity, no progression to the sulfenate **6** has been observed in any set of solvent conditions, with added H-atom donors, acid, or salts. This may be explained by what is observed in the UV/visible spectra. The lower energy peak is due to a charge transfer from the sulfur ligands into the metal and a superoxo or hydroperoxo antibonding orbital, and thus that the associated bonding orbital is correspondingly lower. Because of this, we can conclude that **3-superoxo** and hydroperoxo have a more stable O–O bonding orbital than **2-superoxo** and **2-hydroperoxo**, which would occur with a weaker Fe-O bond. This also agrees with the previous comparison of ligand binding to **2** and **3** where it was concluded that the Fe^{V}-oxo formed by **3** was less stable than that of **2**.

3.3.9. Density Functional Theory Calculations

Theoretical calculations were performed to gain a greater understanding of the processes occurring during the reaction of **8** and O_2. Geometry optimizations were performed on $S = 1/2$ structures of the proposed superoxo formed by the reaction of **8** and O_2 and the subsequent hydroperoxo complex, and TD-DFT methods were used to calculate electronic absorption spectra for those structures. Interestingly, the geometry optimized structure of the superoxo complex converged on a structure which did not have a free $O_2^{\bullet-}$, but rather a Fe–O–O–S bridged structure very much like the structure invoked in the catalytic cycle of CDO. This bridged structure was calculated to have an intense absorption band at 518 nm, similar to that previously observed in the electronic absorption spectrum of the reaction between **8** and O_2. This band is primarily attributed a superoxo O-d_{xy}(Fe^{III}) π^* → N=C π^* charge transfer and secondarily to a d_{xz}(Fe^{III}) → d_{z2}(Fe^{III})-ligand σ^* charge transfer. This structure is also calculated to have a less intense band at 437 nm,

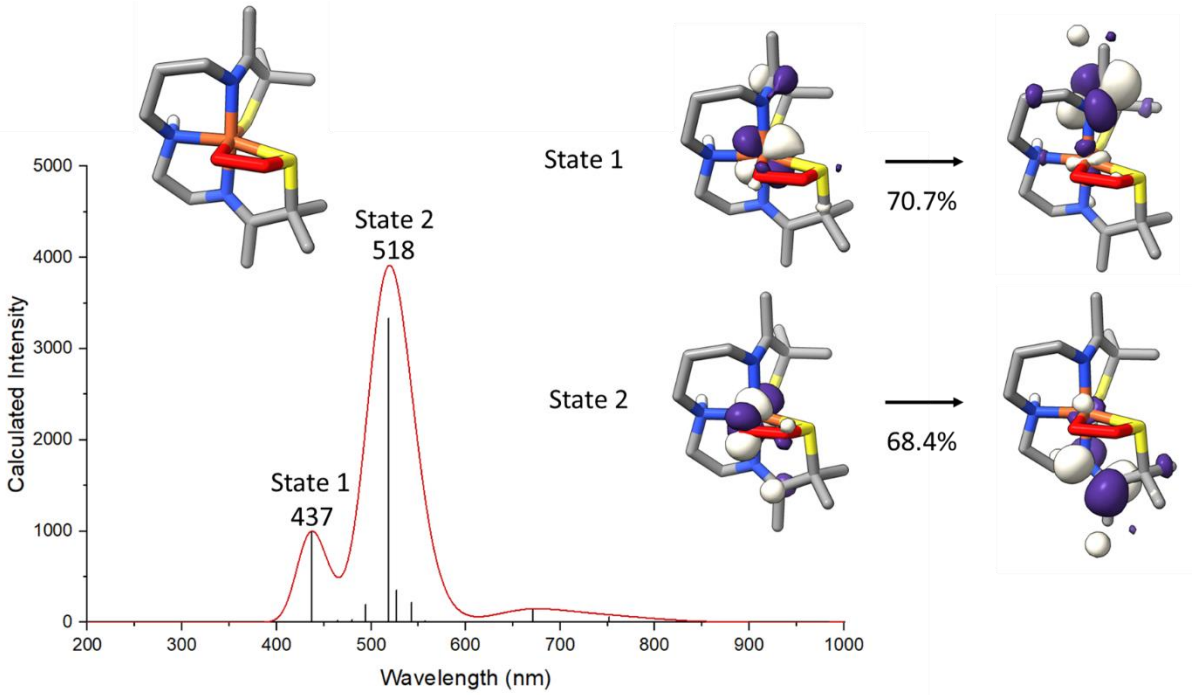

Figure 3-20. TD-DFT calculated electronic absorption spectrum of a bridged Fe–O–O–S complex generated from **8** and O_2, including natural transition orbitals (NTOs) describing the major contribution to each state.

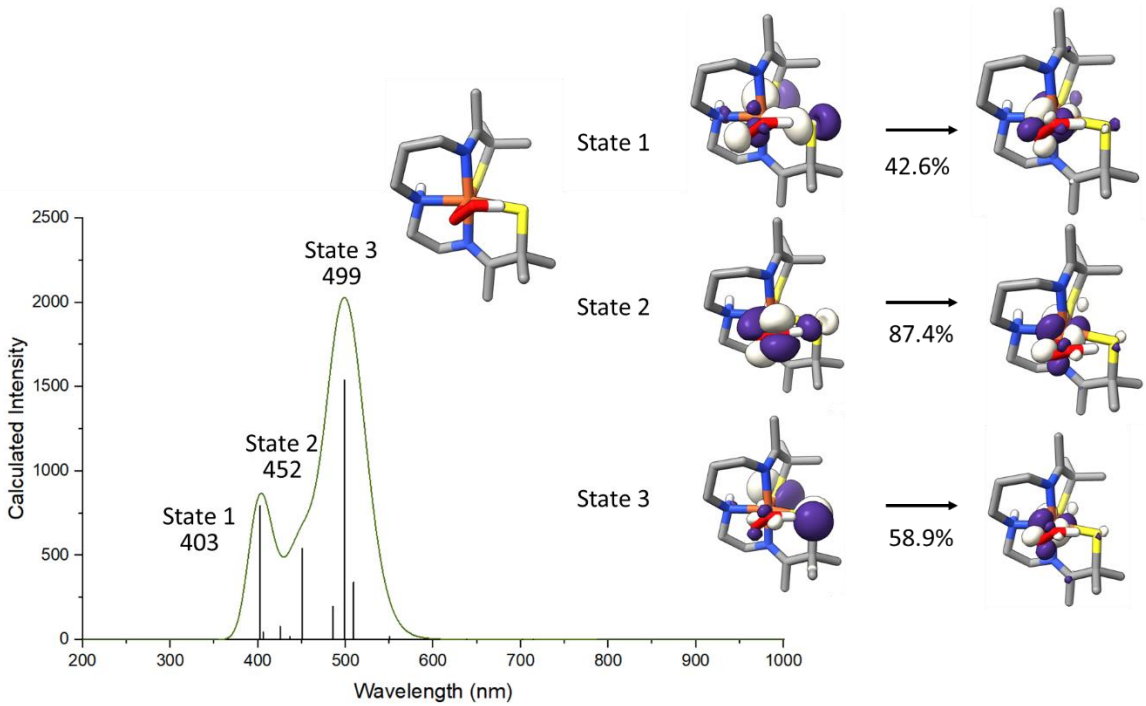

Figure 3-21. TD-DFT calculated electronic absorption spectrum of [$Fe^{III}S_2{}^{Me2}N_3$(Et,Pr))(OOH)] (**3-hydroperoxo**), including natural transition orbitals (NTOs) describing the major contribution to each state.

due to a $d_{yz}(Fe^{III})$ → N=C π* charge transfer and secondarily to a superoxo O-$d_{yz}(Fe^{III})$ π* → $d_{x2-y2}(Fe^{III})$-ligand σ* charge transfer (**Figure 3-20**).

TD-DFT methods were also used to calculate the electronic absorption spectrum for the structure of a geometry optimized hydroperoxo complex **3-hydroperoxo**. This complex orients the hydrogen atom of the hydroperoxide moiety towards the *cis* sulfur, indicative of hydrogen bonding interactions occurring. This structure was calculated to have a very similar electronic absorption spectrum to the bridged Fe–O–O–S complex, with its most intense transition occurring at 499 nm, and two less intense transitions at 403 and 452 nm. The most intense band is primarily due to a sulfur → $d_{xz}(Fe^{III})$-OOH π* charge transfer, with additional contributions from $d_{yz}(Fe^{III})$ → $d_{x2-y2}(Fe^{III})$-ligand σ* charge transfers. The lower intensity bands are due to differing contributions from the same transitions, with the 403 band arising from primarily the sulfur → $d_{xz}(Fe^{III})$-hydroperoxo O π* transition and the 452 band arising primarily from the hydroperoxo

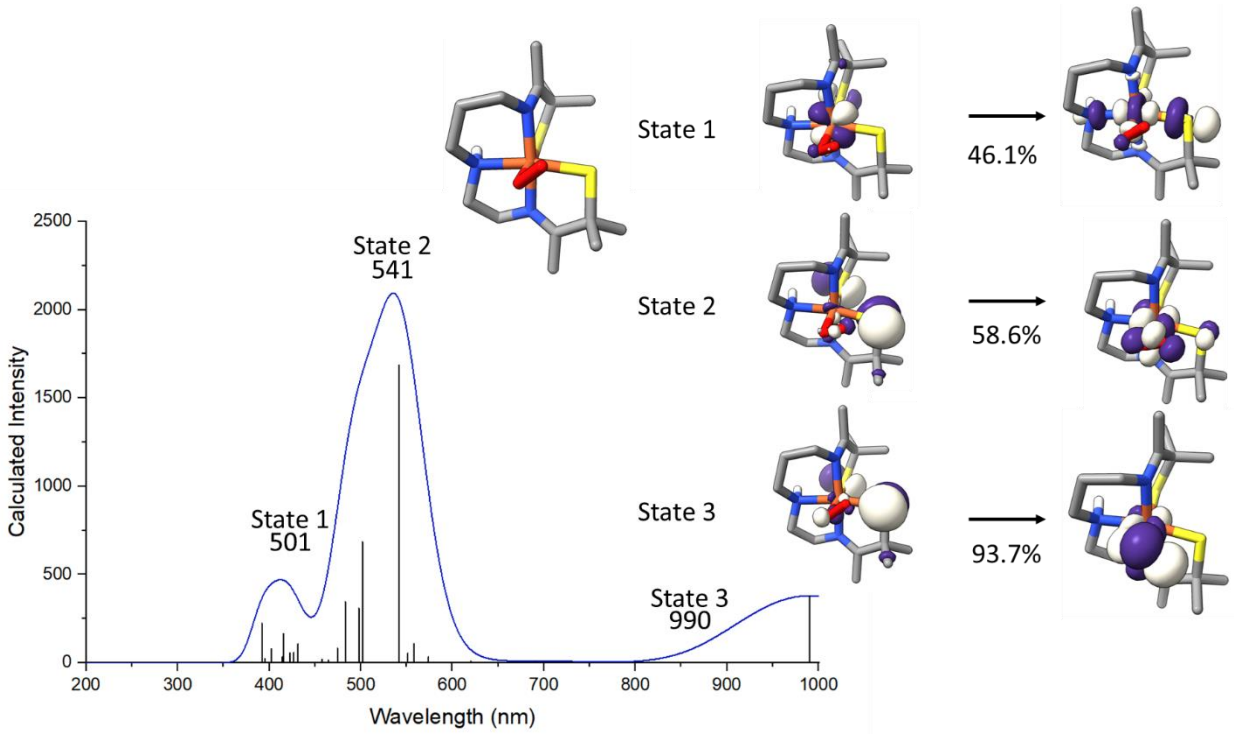

Figure 3-22. TD-DFT calculated electronic absorption spectrum of the superoxo [$Fe^{III}S_2{}^{Me2}N_3$(Et,Pr))(OO)], including natural transition orbitals (NTOs) describing the major contribution to each state.

$\pi^* \rightarrow d_{xz}(Fe^{III})$-OOH π^* transition (**Figure 3-21**). Due to the similarities between the two calculated spectra for both the bridged Fe–O–O–S structure and the Fe^{III}-hydroperoxo and both of their similarities to the observed product of the reaction, there is unfortunately not enough to rule out either structure as a possibility.

By removing the hydrogen atom of the geometry optimized Fe^{III}-hydroperoxo, TD-DFT calculations were performed on the corresponding Fe^{III}-superoxo complex. Similarly to both the bridged Fe–O–O–S complex and the Fe^{III}-hydroperoxo, it was calculated to have an intense absorbance at 541 nm, but it additionally has a series of moderately intense absorbances at 501 nm, adding up to an absorbance band with similar height to the most intense transition. The 541 band is primarily due to a sulfur $\rightarrow d_{xz}(Fe^{III})$-superoxo π transition, with additional contributions from a sulfur-d_{xz}(FeIII)-superoxo $\sigma \rightarrow d_{xz}(Fe^{III})$-OO π transition. The higher energy bands are due

in large part to a $d_{yz}(Fe^{III}) \rightarrow d_{z2}(Fe^{III})$-ligand σ* transition, with smaller contributions from the previously described transitions. It additionally has a lower energy absorbance band at 990 nm, due almost entirely to the sulfur $\rightarrow d_{xz}(Fe^{III})$-OO π transition (**Figure 3-22**). Like the two previously described structures, the calculated spectrum reproduces the spectrum tentatively assigned as a hydroperoxo species, but the presence of a secondary absorbance band of similar intensity means it more closely reproduces the spectrum tentatively assigned as a superoxo species, albeit with lower energy absorbances. Also notable is the **8**'s lack of absorbance bands in the 600-800 nm region like those observed in the less constrained ligand system **1-superoxo** or **1-hydroperoxo** are reproduced by theoretical calculations.

3.4. Summary and Conclusions

Constraining the flexibility of a ligand is again shown to have a dramatic effect on the reactivity of a complex. While we cannot make direct comparisons between the thermodynamic parameters of **1** and **8** due to **8**'s greatly higher kinetic parameters, it has been shown that limiting the degrees of freedom of a complex has a large effect on the entropic contribution to the free energy of a reaction. The rates of dioxygen binding to the complex were examined and found to be much higher than the corresponding reaction in the more constrained system, to the point where it is able to also perform a potential hydrogen atom abstraction within the same time period. To investigate the HAT activity of **8**, reactions were performed in a variety of solvents with varying concentrations of H-atom donors. No rate change was observed with increasing concentration, although this is not conclusive evidence of HAT not occurring due to potential HAT from the solvent or from the ligand backbone. Kinetic isotope studies were performed to attempt to resolve this but showed no change in rate. This could be due to a variety of factors, including that a possible hydrogen atom transfer step is after the rate determining step, and thus not observable by these

means. Despite the much faster pace of these reactions, **8** does not complete the same reactive pathway as **1** and end at the previously described sulfenate, instead slowly decaying as a proposed hydroperoxo or a peroxo-bridged Fe–O–O–S complex. The exact cause of this remains to be determined by further studies. Density functional theory calculations were used to study the potential products of the reaction, finding that both a hydroperoxo species or a peroxo bridged Fe–O–O–S complex both reproduce the observed electronic absorption spectrum.

3.5. References

(1) Ye, S.; Wu, X.; Wei, L.; Tang, D.; Sun, P.; Bartlam, M.; Rao, Z. An Insight into the Mechanism of Human Cysteine Dioxygenase: Key Roles of the Thioether-Bonded Tyrosine-Cysteine Cofactor. *J. Biol. Chem.* **2007**, *282* (5), 3391–3402. DOI: 10.1074/jbc.M609337200

(2) Goudarzi, S.; Babicz, J. T.; Kabil, O.; Banerjee, R.; Solomon, E. I. Spectroscopic and Electronic Structure Study of ETHE1: Elucidating the Factors Influencing Sulfur Oxidation and Oxygenation in Mononuclear Nonheme Iron Enzymes. *J. Am. Chem. Soc.* **2018**, *140* (44), 14887–14902. DOI: 10.1021/jacs.8b09022

(3) Aluri, S.; De Visser, S. P. The Mechanism of Cysteine Oxygenation by Cysteine Dioxygenase Enzymes. *J. Am. Chem. Soc.* **2007**, *129* (48), 14846–14847. DOI: 10.1021/ja0758178

(4) Kumar, D.; Thiel, W.; De Visser, S. P. Theoretical Study on the Mechanism of the Oxygen Activation Process in Cysteine Dioxygenase Enzymes. *J. Am. Chem. Soc.* **2011**, *133* (11), 3869–3882. DOI: 10.1021/ja107514f

(5) Tchesnokov, E. P.; Faponle, A. S.; Davies, C. G.; Quesne, M. G.; Turner, R.; Fellner, M.; Souness, R. J.; Wilbanks, S. M.; De Visser, S. P.; Jameson, G. N. L. An Iron-Oxygen Intermediate Formed during the Catalytic Cycle of Cysteine Dioxygenase. *Chem. Comm.* **2016**, *52* (57), 8814–8817. DOI: 10.1039/c6cc03904a

(6) Roach, P. L.; Clifton, I. J.; Fülöp, V.; Harlos, K.; Barton, G. J.; Hajdu, J.; Andersson, I.; Schofield, C. J.; Baldwin, J. E. Crystal Structure of Isopenicillin N Synthase Is the First from a New Structural Family of Enzymes. *Nature* **1995**, *375* (6533), 700–704. DOI: 10.1038/375700a0

(7) Roach, P. L.; Clifton, I. J.; Hensgens, C. M. H.; Shibata, N.; Long, A. J.; Strange, R. W.; Hasnain, S. S.; Schofield, C. J.; Baldwin, J. E.; Hajdu, J. Anaerobic Crystallisation of an Isopenicillin N Synthase . Fe(II) . Substrate Complex Demonstrated by X-Ray Studies. *Eur. J. Biochem.* **1996**, *242* (3), 736–740. DOI: 10.1111/j.1432-1033.1996.0736r.x

(8) Burziaff, N. I.; Rutledge, P. J.; Clifton, I. J.; Hensgens, C. M. H.; Pickford, M.; Adlington, R. M.; Roach, P. L.; Baldwin, J. E. The Reaction Cycle of Isopenicillin N Synthase Observed by X-Ray Diffraction. *Nature* **1999**, *401* (6754), 721–724. DOI: 10.1038/44400

(9) Roach, P. L.; Clifton, I. J.; Hensgens, C. M. H.; Shibata, N.; Schofield, C. J.; Hajdu, J.; Baldwin, J. E. Structure of Isopenicillin N Synthase Complexed with Substrate and the Mechanism of Penicillin Formation. *Nature* **1997**, *387* (6635), 827–830. DOI: 10.1038/42990

(10) Lundberg, M.; Kawatsu, T.; Vreven, T.; Frisch, M. J.; Morokuma, K. Transition States in a Protein Environment - ONIOM QM:MM Modeling of Isopenicillin N Synthesis. *J. Chem. Theory Comput.* **2009**, *5* (1), 222–234. DOI: 10.1021/ct800457g

(11) Lundberg, M.; Siegbahn, P. E. M.; Morokuma, K. The Mechanism for Isopenicillin N Synthase from Density-Functional Modeling Highlights the Similarities with Other Enzymes in the 2-His-1-Carboxylate Family. *Biochemistry* **2008**, *47* (3), 1031–1042. DOI: 10.1021/bi701577q

(12) Lundberg, M.; Morokuma, K. Protein Environment Facilitates O2 Binding in Non-Heme Iron Enzyme. An Insight from ONIOM Calculations on Isopenicillin N Synthase (IPNS). *J. Phys. Chem. B* **2007**, *111* (31), 9380–9389. DOI: 10.1021/jp071878g

(13) Brown-Marshall, C. D.; Diebold, A. R.; Solomon, E. I. Reaction Coordinate of Isopenicillin N Synthase: Oxidase versus Oxygenase Activity. *Biochemistry* **2010**, *49* (6), 1176–1182. DOI: 10.1021/bi901772w

(14) Tamanaha, E.; Zhang, B.; Guo, Y.; Chang, W. C.; Barr, E. W.; Xing, G.; St Clair, J.; Ye, S.; Neese, F.; Bollinger, J. M.; Krebs, C. Spectroscopic Evidence for the Two C-H-Cleaving Intermediates of Aspergillus Nidulans Isopenicillin N Synthase. *J. Am. Chem. Soc.* **2016**, *138* (28), 8862–8874. DOI: 10.1021/jacs.6b04065

(15) Sahu, S.; Goldberg, D. P. Activation of Dioxygen by Iron and Manganese Complexes: A Heme and Nonheme Perspective. *J. Am. Chem. Soc.* **2016**, *138* (36), 11410–11428. DOI: 10.1021/jacs.6b05251

(16) Ray, K.; Pfaff, F. F.; Wang, B.; Nam, W. Status of Reactive Non-Heme Metal-Oxygen Intermediates in Chemical and Enzymatic Reactions. *J Am. Chem. Soc.* **2014**, *136* (40), 13942–13958. DOI: 10.1021/ja507807v

(17) Costas, M.; Mehn, M. P.; Jensen, M. P.; Que, L. Dioxygen Activation at Mononuclear Nonheme Iron Active Sites: Enzymes, Models, and Intermediates. *Chem. Rev*. **2004**, *104* (2), 939–986. 10.1021/cr020628n

(18) Chiang, C. W.; Kleespies, S. T.; Stout, H. D.; Meier, K. K.; Li, P. Y.; Bominaar, E. L.; Que, L.; Münck, E.; Lee, W. Z. Characterization of a Paramagnetic Mononuclear Nonheme Iron-Superoxo Complex. *J. Am. Chem. Soc.* **2014**, *136* (31), 10846–10849. DOI: 10.1021/ja504410s

(19) Luo, Y.-R. *Comprehensive Handbook of Chemical Bond Energies*; Press, C. R. C., Ed.; Taylor and Francis Group: Boca Raton, FL, 2007.

(20) Hong, S.; Sutherlin, K. D.; Park, J.; Kwon, E.; Siegler, M. A.; Solomon, E. I.; Nam, W. Crystallographic and Spectroscopic Characterization and Reactivities of a Mononuclear Non-Haem Iron(III)-Superoxo Complex. *Nat. Commun.* **2014**, *5* (1), 1–7. DOI: 10.1038/ncomms6440

(21) Oddon, F.; Chiba, Y.; Nakazawa, J.; Ohta, T.; Ogura, T.; Hikichi, S. Characterization of Mononuclear Non-Heme Iron(III)-Superoxo Complex with a Five-Azole Ligand Set. *Angew. Chem. Int. Ed.* **2015**, *54* (25), 7336–7339. DOI: 10.1002/anie.201502367

(22) Winslow, C.; Lee, H. B.; Field, M. J.; Teat, S. J.; Rittle, J. Structure and Reactivity of a High-Spin, Nonheme Iron(III)-Superoxo Complex Supported by Phosphinimide Ligands. *J. Am. Chem. Soc.* **2021**, *143* (34), 13686–13693. DOI: 10.1021/jacs.1c05276

(23) Gordon, J. B.; McGale, J. P.; Prendergast, J. R.; Shirani-Sarmazeh, Z.; Siegler, M. A.; Jameson, G. N. L.; Goldberg, D. P. Structures, Spectroscopic Properties, and Dioxygen Reactivity of 5- and 6-Coordinate Nonheme Iron(II) Complexes: A Combined Enzyme/Model Study of Thiol Dioxygenases. *J. Am. Chem. Soc.* **2018**, *140* (44), 14807–14822. DOI: 10.1021/JACS.8B08349

(24) Gordon, J. B.; Vilbert, A. C.; Siegler, M. A.; Lancaster, K. M.; Moënne-Loccoz, P.; Goldberg, D. P. A Nonheme Thiolate-Ligated Cobalt Superoxo Complex: Synthesis and

Spectroscopic Characterization, Computational Studies, and Hydrogen Atom Abstraction Reactivity. *J. Am. Chem. Soc.* **2019**, *141* (8), 3641–3653. DOI: 10.1021/jacs.8b13134

(25) Gordon, J. B.; Vilbert, A. C.; Dimucci, I. M.; MacMillan, S. N.; Lancaster, K. M.; Moënne-Loccoz, P.; Goldberg, D. P. Activation of Dioxygen by a Mononuclear Nonheme Iron Complex: Sequential Peroxo, Oxo, and Hydroxo Intermediates. *J. Am. Chem. Soc.* **2019**, *141* (44), 17533–17547. DOI: 10.1021/jacs.9b05274

(26) Gordon, J. B.; McGale, J. P.; Siegler, M. A.; Goldberg, D. P. Proton-Coupled Electron-Transfer Reactivity Controls Iron versus Sulfur Oxidation in Nonheme Iron-Thiolate Complexes. *Inorg. Chem.* **2021**, *60* (9), 6255–6265. DOI: 10.1021/acs.inorgchem.0c03779

(27) Sallmann, M.; Siewert, I.; Fohlmeister, L.; Limberg, C.; Knispel, C. A Trispyrazolylborato Iron Cysteinato Complex as a Functional Model for the Cysteine Dioxygenase. *Angew. Chem. Int. Ed.* **2012**, *51* (9), 2234–2237. DOI: 10.1002/ANIE.201107345

(28) Fischer, A. A.; Lindeman, S. V.; Fiedler, A. T. Spectroscopic and Computational Studies of Reversible O2 Binding by a Cobalt Complex of Relevance to Cysteine Dioxygenase. *Dalton Trans.* **2017**, *46* (39), 13229–13241. DOI: 10.1039/c7dt01600j

(29) Fischer, A. A.; Lindeman, S. V.; Fiedler, A. T. A Synthetic Model of the Nonheme Iron-Superoxo Intermediate of Cysteine Dioxygenase. *Chem. Comm.* **2018**, *54* (80), 11344–11347. DOI: 10.1039/C8CC06247A

(30) Blakely, M., N.; Dedushko, M. A.; Poon, P. C. Y.; Villar-Acevedo, G.; Kovacs, J. A. Formation of a Reactive, Alkyl Thiolate-Ligated FeIII-Superoxo Intermediate Derived from Dioxygen. *J. Am. Chem. Soc.* **2019**, *141*, 1867-1870. DOI: 10.1021/jacs.8b12670

(31) Greiner, M. B. Kinetic Insights into Dioxygen Activation by Biomimetic Thiolate-Ligated Iron Complexes, University of Washington, Seattle, WA, 2023.

(32) Theisen, R. M.; Kovacs, J. A. Role of Protons in Superoxide Reduction by a Superoxide Reductase Analogue. *Inorg. Chem.* **2005**, *44* (5), 1169–1171. DOI: 10.1021/IC048818Z

(33) Nam, E.; Alokolaro, P. E.; Swartz, R. D.; Gleaves, M. C.; Pikul, J.; Kovacs, J. A. Investigation of the Mechanism of Formation of a Thiolate-Ligated Fe(III)-OOH. *Inorg. Chem.* **2011**, *50* (5), 1592–1602. DOI: 10.1021/IC101776M

(34) Dedushko, M. A.; Pikul, J. H.; Kovacs, J. A. Superoxide Oxidation by a Thiolate-Ligated Iron Complex and Anion Inhibition. *Inorg. Chem.* **2021**, *60* (10), 7250–7261. DOI: 10.1021/ACS.INORGCHEM.1C00336

(35) Dedushko, M. A.; Greiner, M. B.; Downing, A. N.; Coggins, M.; Kovacs, J. A. Electronic Structure and Reactivity of Dioxygen-Derived Aliphatic Thiolate-Ligated Fe-Peroxo and Fe(IV) Oxo Compounds. *J. Am. Chem. Soc.* **2021**, *2022*, 8528. DOI: 10.1021/JACS.1C07656

(36) Dedushko, M. A.; Greiner, M. B.; Downing, A. N.; Coggins, M.; Kovacs, J. A. Electronic Structure and Reactivity of Dioxygen-Derived Aliphatic Thiolate-Ligated Fe-Peroxo and Fe(IV) Oxo Compounds. *J. Am. Chem. Soc.* **2021**. DOI: 10.1021/jacs.1c07656

(37) Shoner, S. C.; Nienstedt, A. M.; Ellison, J. J.; Kung, I. Y.; Barnhart, D.; Kovacs, J. A. Structural Comparison of Five-Coordinate Thiolate-Ligated M^{II} = Fe^{II}, Co^{II}, Ni^{II}, and Zn^{II} Ions Wrapped in a Chiral Helical Ligand. *Inorg. Chem.* **1998**, *37* (22), 5721–5726. DOI: 10.1021/ic980882r

(38) Zhdankin, V. V.; Koposov, A. Y.; Litvinov, D. N.; Ferguson, M. J.; McDonald, R.; Luu, T.; Tykwinski, R. R. Esters of 2-Iodoxybenzoic Acid: Hypervalent Iodine Oxidizing Reagents with a Pseudobenziodoxole Structure. *J. Org. Chem.* **2005**, *70* (16), 6484–6491. DOI: 10.1021/JO051010R

(39) Dedushko, M. Insights into Dioxygen Bond Activation and Formation by Small Biomimetic Complexes, University of Washington, Seattle, WA, 2020.

(40) Blakeley, M. N. Insights into Dioxygen Activation by Biomimetic Alkyl Thiolate-Ligated Iron Complexes, University of Washington, Seattle, WA, 2019.

(41) Sharefkin, J. G.; Saltzman, H. IODOSOBENZENE DIACETATE. *Organic Syntheses* **1963**, *43*, 62. DOI: 10.15227/ORGSYN.043.0062

(42) Stoll, S.; Schweiger, A. EasySpin, a Comprehensive Software Package for Spectral Simulation and Analysis in EPR. *J. Magn. Reson.* **2006**, *178* (1), 42–55. DOI: 10.1016/j.jmr.2005.08.013

(43) Neese, F.; Wiley, J. The ORCA Program System. *Wiley Interdiscip. Rev. Comput. Mol. Sci.* **2012**, *2* (1), 73–78. DOI: 10.1002/WCMS.81

(44) Neese, F. Software Update: The ORCA Program System, Version 4.0. *Wiley Interdiscip. Rev. Comput. Mol. Sci.* **2018**, *8* (1), e1327. DOI: 10.1002/WCMS.1327

(45) Grimme, S.; Ehrlich, S.; Goerigk, L. Effect of the Damping Function in Dispersion Corrected Density Functional Theory. *J. Comput. Chem.* **2011**, *32* (7), 1456–1465. DOI: 10.1002/JCC.21759

(46) Becke, A. D. Density-functional Thermochemistry. III. The Role of Exact Exchange. *J. Chem. Phys.* **1998**, *98* (7), 5648. DOI: 10.1063/1.464913

(47) Neese, F.; Wennmohs, F.; Hansen, A.; Becker, U. Efficient, Approximate and Parallel Hartree–Fock and Hybrid DFT Calculations. A 'Chain-of-Spheres' Algorithm for the Hartree–Fock Exchange. *Chem. Phys.* **2009**, *356* (1–3), 98–109. DOI: 10.1016/J.CHEMPHYS.2008.10.036

(48) Zhurko, G. A. Chemcraft – Graphical Program for Visualization of Quantum Chemistry Computations. https://chemcraftprog.com: Ivanovo, Russia 2005.

(49) Pettersen, E. F.; Goddard, T. D.; Huang, C. C.; Meng, E. C.; Couch, G. S.; Croll, T. I.; Morris, J. H.; Ferrin, T. E. UCSF ChimeraX: Structure Visualization for Researchers, Educators, and Developers. *Protein. Sci.* **2021**, *30* (1), 70–82. DOI: 10.1002/PRO.3943

(50) Kinetic Studio. Jplus Consulting Pty Ltd: United Kingdom 2020.

(51) Bruker. APEX2 (Version 2.1-4), SAINT (Version 7.34A), SADABS (Version 2007/4). BrukerAXS Inc.: Madison, WI 2007.

(52) Sheldrick, G. M. SHELXL-97, Program for the Refinement of Crystal Structures. University of Göttingen: Göttingen, Germany 1997.

(53) Altomare, A.; Cascarano, G.; Giacovazzo, C.; Guagliardi, A.; Burla, M. C.; Polidori, G.; Camalli, M.; IUCr. SIR92 – a Program for Automatic Solution of Crystal Structures by Direct Methods. *J. Appl. Cryst.* **1994**, *27* (3), 435–435. DOI: 10.1107/S002188989400021X

(54) Altomare, A.; Burla, M. C.; Camalli, M.; Cascarano, G. L.; Giacovazzo, C.; Guagliardi, A.; Moliterni, A. G. G.; Polidori, G.; Spagna, R. SIR97: A New Tool for Crystal Structure Determination and Refinement. *J. Appl. Cryst.* **1999**, *32* (1), 115–119. DOI: 10.1107/S0021889898007717

(55) Sheldrick, G. M.; IUCr. Crystal Structure Refinement with SHELXL. *Acta. Cryst. C* **2015**, *71* (1), 3–8. DOI: 10.1107/S2053229614024218

(56) Waasmaier, D.; Kirfel, A. New Analytical Scattering-Factor Functions for Free Atoms and Ions. *Acta Cryst. A* **1995**, *51* (3), 416–431. https://doi.org/10.1107/S0108767394013292

(57) Persistence of Vision Raytracer. Persistence of Vision Pty. Ltd.: Williamstown, Victoria, Australia 2004.

(58) Burnett, M. N.; Johnson, C. K. ORTEP-III: Oak Ridge Thermal Ellipsoid Plot Program for Crystal Structure Illustrations. *Oak Ridge National Laboratory Report ORNL-6895* **1996**.

(59) Schweitzer, D.; Shearer, J.; Rittenberg, D. K.; Shoner, S. C.; Ellison, J. J.; Loloee, R.; Lovell, S.; Barnhart, D.; Kovacs, J. A. Enhancing Reactivity via Structural Distortion. *Inorg. Chem.* **2002**, *41* (12), 3128–3136. DOI: 10.1021/ic0109187

(60) Lawrence Clever, H.; Battino, R.; Miyamoto, H.; Yampolski, Y.; Young, C. L. IUPAC-NIST Solubility Data Series. 103. Oxygen and Ozone in Water, Aqueous Solutions, and Organic Liquids (Supplement to Solubility Data Series Volume 7). *J. Phys. Chem. Ref. Data* **2014**, *43* (3), 033102. DOI: 10.1063/1.4883876

(61) Kryatov, S. V.; Rybak-Akimova, E. V.; Schindler, S. Kinetics and Mechanisms of Formation and Reactivity of Non-Heme Iron Oxygen Intermediates. *Chem. Rev.* **2005**, *105* (6), 2175–2226. DOI: 10.1021/CR030709Z

(62) Espenson, J. H. *Chemical Kinetics and Reaction Mechanisms*; McGraw-Hill: New York, 1981.

(63) Schneider, J. E.; Goetz, M. K.; Anderson, J. S. Statistical Analysis of C-H Activation by Oxo Complexes Supports Diverse Thermodynamic Control over Reactivity. *Chem. Sci.* **2021**, *12* (11), 4173–4183. DOI: 10.1039/d0sc06058e

(64) Sacramento, J. J. D.; Albert, T.; Siegler, M.; Moënne-Loccoz, P.; Goldberg, D. P. An Iron(III) Superoxide Corrole from Iron(II) and Dioxygen. *Angew. Chem. Int. Ed.* **2022**, *61* (2), e202111492. DOI: 10.1002/anie.202111492

(65) Goetz, M. K.; Anderson, J. S. Experimental Evidence for p Ka-Driven Asynchronicity in C-H Activation by a Terminal Co(III)-Oxo Complex. *J. Am. Chem. Soc.* **2019**, *141* (9), 4051–4062. DOI: 10.1021/jacs.8b13490

(66) Baldwin, J. E.; Abraham, E. The Biosynthesis of Penicillins and Cephalosporins. *Nat. Prod. Rep.* **1988**, *2*, 129–145. DOI: 10.1039/NP9880500129

(67) Klinman, J. P.; Offenbacher, A. R. Understanding Biological Hydrogen Transfer Through the Lens of Temperature Dependent Kinetic Isotope Effects. *Acc. Chem. Res.* **2018**, *51* (9), 1966–1974. DOI: 10.1021/acs.accounts.8b00226

(68) Huynh, M. H. V.; Meyer, T. J. Proton-Coupled Electron Transfer from Phosphorus: A P−H/P−D Kinetic Isotope Effect of 178. *Angew. Chem. Int. Ed.* **2002**, *41* (8), 1395–1398. DOI: 10.1002/1521-3773(20020415)41:8<1395::AID-ANIE1395>3.0.CO;2-Z

(69) Huynh, H. V.; Meyer, T. J. Colossal Kinetic Isotope Effects in Proton-Coupled Electron Transfer. *P. Natl. Acad. Sci. USA* **2004**, *101* (36), 13138–13141. DOI: 10.1073/pnas.0405086101

Chapter 4. Characterization of an Asymmetric Complex Bound with a Thiolate and an Alkoxide

4.1. Introduction

Non-heme iron enzymes that bind dioxygen such as CDO and IPNS perform difficult chemical transformations by using the chemical energy stored in dioxygen bonds. A frequently occurring residue pattern that supports this is the 2-histidine-1-carboxylate facial triad family, which allows an Fe^{II} to bind dioxygen and a substrate in close proximity and perform a variety of different reactions. Enzymes which activate dioxygen often contain a cysteine in the coordination sphere, which help to lower the activation barrier of O_2 and to stabilize the generated Fe^{III}-superoxo intermediate.[1–3] The high covalency of this bond and the nephelauxetic (cloud-expanding) effect of sulfur's orbitals lowers the metal's reduction potential.[4,5] Being able to delocalize electron density off of the metal due to this highly covalent bond favors lower spin states.[6] These effects from incorporating a thiolate coordinated to the metal center have been shown by computational studies to lower the energy required to bind oxygen by 26 kcal/mol versus a complex with another nitrogen atom bound to the metal center.[7] In heme systems, the role of a thiolate is better characterized, with studies finding that the thiolate incorporated *trans* to the binding site of dioxygen helps to strengthen the Fe–O bond through stabilization of a low spin-state in the iron center, and that the *trans* effect of the sulfur atom helps to promote cleavage of the O–O bond rather than the Fe–O bond.[8–10] In contrast, studies in non-heme iron systems found that the same effect helped to weaken the Fe–O bond and left the O–O bond unperturbed.[2,11,12]

The role of sulfur in non-heme iron enzymes is not always directly modeled, with very few studies modifying the ligand at the site of the thiolate to determine its role in the activation of dioxygen. A previous study in the Kovacs group is one of the few, investigating how changing the

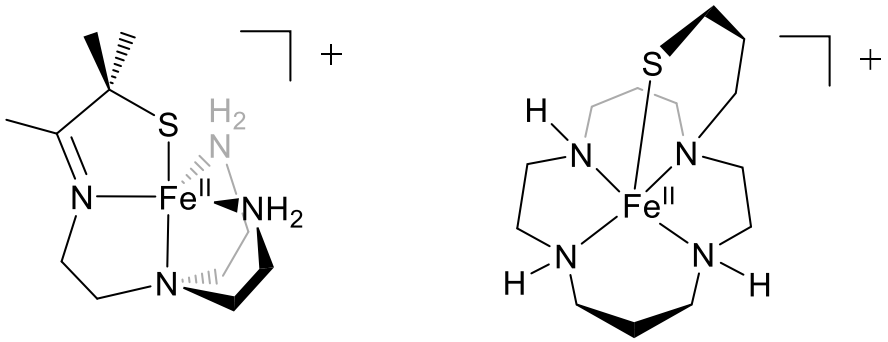

Figure 4-1. Schematic drawings of $[Fe^{II}(S^{Me2}N_4(tren))]^+$ (left)[46] and $[Fe^{II}(cyclam\text{-}PrS)]^+$ (right).[13]

thiolate for an alkoxide or an amine affects the properties of the complex. Using the tris(2-aminoethyl)amine based ligand $[Fe^{II}(S^{Me2}N_4(tren))]^+$ as a basis for one series and the 1,4,8,11-tetraazacyclotetradecane based $[Fe^{II}(cyclam\text{-}PrS)]^+$ as the basis for another, two series of complexes were made (**Figure 4-1**). With a thiolate incorporated, the metal ion Lewis acidity was lower than with alkoxide or an amine, which helps to maintain an open coordination site. Changing a thiolate for an alkoxide also shifted the reduction potential of these complexes cathodically, stabilizing the iron in the +3 oxidation state but still allowing easy access the +2 oxidation state. The two series are also notable structurally, as the $[Fe^{II}(S^{Me2}N_4(tren))]^+$ has the open sixth coordination site located *cis* to the thiolate, where the $[Fe^{II}(cyclam\text{-}PrS)]^+$ series has the sixth coordination site *trans* to the thiolate. The thiolate-ligated complexes demonstrate a strong *trans* effect, which further helps maintain an open coordination site.[13]

The reactivity of these series of complexes with dioxygen has been studied. $[Fe^{II}(S^{Me2}N_4(tren))]^+$ reacts readily with O_2, reversibly forming an Fe^{III}-superoxo before reacting with another equivalent of Fe^{II} to form a peroxo-bridged dimer. This dimer then homolytically cleaves its O–O bond to form two Fe^{IV}-oxo complexes which are capable of abstracting hydrogen atoms from methanol. This generates an Fe^{III}-hydroxo complex which reacts with another complex in solution to produce one water molecule and an oxo-bridged Fe^{III} dimer.[14] DFT studies on these

complexes demonstrated the influence of the *cis* thiolate on the oxo species, namely that it helps to stabilize a low-spin iron center.[15] Stopped-flow studies helped to characterize the kinetics and thermodynamics of dioxygen binding to the metal center. The reaction proceeds extremely quickly, with a very low barrier to O_2 binding ($\Delta H^{\ddagger}$ = 34 kJ mol^{-1}, E_a = 36 kJ mol^{-1}), similar to IPNS.[14] Studies using nitric oxide as a stable analogue to an Fe^{III}-superoxo complex were able to structurally and electronically characterize the nature of the iron-ligand interactions, finding that the *cis* sulfur helped to activate the N–O bond.[4] A low-spin Fe^{III}-hydroperoxo adduct was also studied, with EXAFS experiments finding a short Fe–O bond and an O–O bond stretch lower than normal, indicating a weakened O–O bond.[16] No studies with an alkoxide replacing the thiolate were reported with an iron center, however, studies with the related complex $[Mn^{II}(S^{Me2}N_4$(6-Me-DPEN))$]^+$ and $[Mn^{II}(O^{Me2}N_4$(6-Me-DPEN))$]^+$ were performed, finding via vibrational spectroscopy and theoretical calculations that a coordinated alkylperoxo ligand was significantly stabilized with a *cis* alkoxide versus a *cis* thiolate.[17,18]

The reactivity of the $[Fe^{II}$(cyclam-PrS)$]^+$ with dioxygen was also studied. Using superoxide and an external proton source, $[Fe^{II}$(cyclam-PrS)$]^+$ generates a high-spin Fe^{III}-hydroperoxo complex with the hydroperoxo putatively *trans* to the thiolate. Vibrational data and theoretical studies indicated that the Fe-O bond was significantly destabilized upon the introduction of a *trans* thiolate versus an amine or an alkoxide.[19] The alkoxide analogue $[Fe^{II}$(cyclam-PrO)$]^+$ was found to not have a strong affinity to bind a sixth ligand, although whether this was due to steric or electronic effects could not be determined.[13] To further investigate the role of the thiolate in dioxygen activation, the NO derivative was produced, surprisingly showing binding *cis* to the thiolate ligand.[20] Theoretical studies to elucidate the binding mode of a superoxide on a *cis* or *trans* ligated were inconclusive.[21]

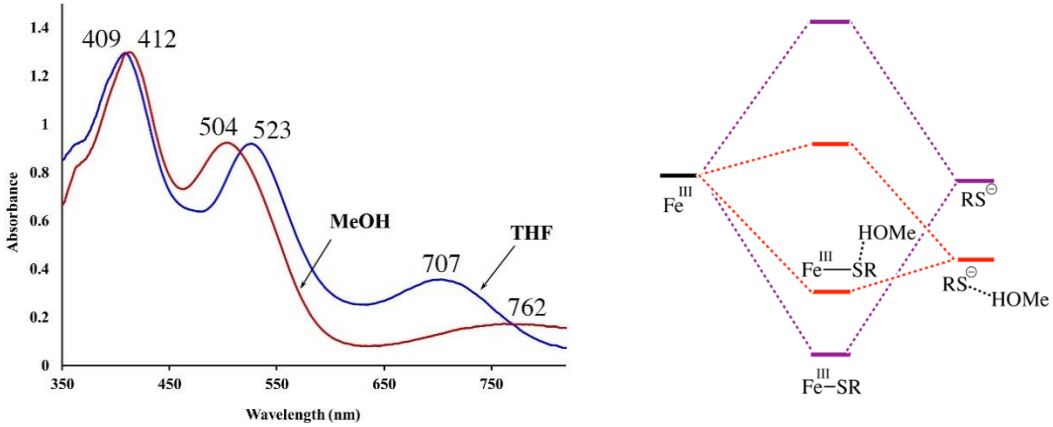

Figure 4-2. Left: Electronic absorption spectrum of Fe^{III}-superoxo **2-superoxo** (0.25 mM) in THF vs MeOH. Right: Influence of H-bonds on the energy of the **π**-symmetry sulfur orbitals and the stabilization of the resulting Fe^{III}-SR (purple) versus H-bonded Fe^{III}-SR bonds (red). Reproduced from "Kinetic Insights into Dioxygen Activation by Biomimetic Thiolate-Ligated Iron Complexes", Greiner, M. B.

The bis-thiolate ligated complex $Fe^{II}(S_2{}^{Me2}N_2NH(Pr,Pr))$ (**1**) has also been the subject of various studies to characterize how it interacts with dioxygen. Notable for **1** versus the previously discussed $[Fe^{II}(S^{Me2}N_4(tren))]^+$ and $[Fe^{II}(cyclam\text{-}PrS)]^+$ are its two thiolate ligands, necessitating exogenous ligands to bind to its open site both *cis* and *trans* to a thiolate. Studies binding nitric oxide to the oxidized complex **2** found a linear NO moiety with π-back-donation into the iron. This lengthens the mean Fe-S distance and helps to elongate the N–O bond.[22] The *trans* thiolate was shown to have a role in labilizing the ligand in the sixth coordination site, allowing reversible binding of possible substrates.[23–26] **1** experiences a blue shift in the thiolate-to-metal charge transfer band in protic solvents, and theoretical calculations show that this is a result of hydrogen bonding to one of the thiolate ligands (**Figure 4-2**). This is also observed in the spectrum of its Fe^{III}-superoxo, where absorption peaks are shifted to higher energy in protic solvents.[21] Through hydrogen bonding, the strength of the Fe-S interaction is diminished, affecting the kinetics and thermodynamics of the reaction significantly.

4.2. Experimental

General Methods

All reactions were performed under an atmosphere of nitrogen in a glovebox or using standard Schlenk techniques unless otherwise indicated. Reagents purchased from commercial vendors were of the highest purity available and used without further purification. Pentane, toluene, diethyl ether (Et_2O), tetrahydrofuran (THF), acetonitrile (MeCN), and dichloromethane (DCM) were rigorously degassed and purified using solvent purification columns housed in a custom stainless-steel cabinet, dispensed a stainless steel Schlenk line (GlassContour). Methanol was distilled from magnesium turnings and iodine and degassed prior to use. 3-mercapto-3-methyl-2-butanone was synthesized according to literature precedent.[27]

^{1}H-NMR spectra were recorded on a Bruker AV-300, AV-301, or AV-500 FT-NMR spectrometer. Chemical shifts are reported in ppm and coupling constants (*J*) in Hz. Electrospray ionization mass spectrometry (ESI-MS) was performed on a Bruker Esquire LC-Ion Trap. Low-temperature electronic absorption spectra were recorded using a Varian Cary 50 or Agilent Cary 60 spectrophotometer equipped with either a fiber optic cable connected to a "dip" attenuated total reflection probe (C-technologies), with a custom built two-necked solution sample holder equipped with a threaded glass connector (sized to fit the dip probe) and purged with argon, or a UNISOKU CoolSpek USP-203 cryostat.

Calculations were performed using the ORCA v. 4.2.1 quantum chemistry package developed by Neese and coworkers,[28,29] and employed the polarized triple-zeta basis set def2-TZVP, the def2/J auxiliary basis set for Coulomb fitting, and the atom-pairwise dispersion correction of Grimme (D3BJ).[30] Tight convergence criteria were required for self-consistent field (SCF) solutions. The Grid4 (GridX4) integration grid size was used for geometry optimizations.

Calculations were performed using the B3LYP or the CAM-B3LYP functional, with the resolution of identity (RI) chain-of-spheres (RIJCOSX) approximation and initiated from the crystallographic coordinates when available.[31,32] Analytical frequency calculations were performed on all optimized structures to determine whether the obtained stationary points corresponded to local minima. Chemcraft was used to visualize the calculated EAS spectra.[33] Excited states from TD-DFT were analyzed by using natural transition orbtials (NTOs) and by visualizing their difference densities between the ground and excited states. Canonical molecular orbital isosurfaces and natural transition orbitals in the TD-DFT calculations were visualized at an isovalue of 0.05 a03 using UCSF ChimeraX.[34]

Synthesis of 3-[3-(3-aminopropylamino)propylimino]-2-methyl-2-butanol

Bis(3-aminopropyl)amine (10.92 g, 83.2 mmol) was added to 20 mL MeOH in a round bottom flask. 3-hydroxy-3-methyl-2-butanone (4.25 g, 41.6 mmol) was added to 20 mL MeOH. The 3-hydroxy-3-methyl-2-butanone solution was added via addition funnel over the course of 2 hours, and the solution was heated to 50 °C overnight. The methanol was removed in vacuo and the crude reaction mixture was then fractionally distilled at 210 °C to afford 3-[3-(3-aminopropylamino)propylimino]-2-methyl-2-butanol as a pale yellow oil (4.6 g, 21.3 mmol, 51.3%). ^{1}H-NMR (300 MHz, $CDCl_3$): δ = 3.34 (t, 2H, *J* = 6.6 Hz), 2.27 (t, 2H, *J* = 6.5 Hz), 2.68 (tt, 4H, *J* = 7.0, 6.5 Hz), 1.86 (s, 3H), 1.63 (tt, 4H, *J* = 7.0, 6.5 Hz), 1.29 (s, 6H), 1.18 (s, 3H).

*Synthesis of $Fe^{II}(S^{Me2},O^{Me2}N_2NH(Pr,Pr))$ (**9**)*

Sodium methoxide (0.452 g, 8.36 mmol) was added to 5 mL MeOH in a 20 mL scintillation vial with a stir bar. 3-[3-(3-aminopropylamino)propylimino]-2-methyl-2-butanol (1.000 g, 4.64 mmol) was added to 5 mL MeOH in a 20 mL scintillation vial, and added to the sodium methoxide solution dropwise with stirring. Iron dichloride (0.530 g, 4.18 mmol) was added to 5 mL MeOH,

stirred to dissolve, and was added to the sodium methoxide solution with stirring, producing a cloudy green solution. 3-mercapto-3-methyl-2-butanone (0.494 g, 4.18 mmol) was dissolved in 5 mL MeOH in a 20 mL scintillation vial and added dropwise to the iron solution with stirring. The green solution was allowed to stir for 12 hours, then transferred to a 50 mL Schlenk flask and the solvent was removed by vacuum. The crude product was redissolved in MeCN, filtered to remove sodium chloride, and the solvent was removed again by vacuum. The crude product was washed with minimal diethyl ether, then dissolved in a minimum of DCM and layered with pentane. The solution was allowed to mix for approximately 72 hours in a -35 °C freezer, affording green crystals (0.694 g, 1.88 mmol, 45%). Electronic absorption (THF) λ_{max} (ε, $M^{-1}cm^{-1}$) = 319 (960) nm, 420 (520) nm.

*Synthesis of [$Fe^{III}(S^{Me2},O^{Me2}N_2NH(Pr,Pr))][PF_6]$ (**10**)*

Sodium methoxide (0.452 g, 8.36 mmol) was added to 5 mL MeOH in a 50 mL Schlenk flask with a stir bar. 3-[3-(3-aminopropylamino)propylimino]-2-methyl-2-butanol (1.000 g, 4.64 mmol) was added to 5 mL MeOH in a 20 mL scintillation vial, and added to the sodium methoxide solution dropwise with stirring. Iron dichloride (0.530 g, 4.18 mmol) was added to 5 mL MeOH, stirred to dissolve, and was added to the sodium methoxide solution with stirring, producing a cloudy green solution. 3-mercapto-3-methyl-2-butanone (0.494 g, 4.18 mmol) was dissolved in 5 mL MeOH in a 20 mL scintillation vial and added dropwise to the iron solution with stirring. Ferrocenium hexafluorophosphate (1.535 g, 4.64 mmol) was added to 10 mL MeOH and the solution was added to the Schlenk flask. The dark brown solution was allowed to stir for 12 hours and the solvent was removed by vacuum. The crude product was redissolved in MeCN, filtered to remove sodium chloride, and the solvent was removed again by vacuum. The crude product was washed with diethyl ether, and subsequently dissolved in a minimum of DCM and layered with

pentane. The solution was allowed to mix for approximately 72 hours in a -35 °C freezer, affording brown crystals (0.520 g, 1.01 mmol, 24.3%). Electronic absorption (THF) λ_{max} (ε, $M^{-1}cm^{-1}$) = 414 (1300) nm.

*Formation of an intermediate via the addition of O_2 to **9**.*

A 0.250 mM solution of **9** was prepared in 4 mL of THF under an inert atmosphere in a drybox. The solution was placed in a modified 1 cm pathlength quartz air-free cuvette with a screw top equipped with a rubber septum. Measurements were performed using an UNISOKU USP-203-B cryostat and monitored with a Agilent Cary 60 spectrophotometer at -40 °C. A flask with a rubber septum was purged with dry O_2 from a cylinder for 15 or more minutes, and 5 mL of gas was drawn into a gastight syringe. The gas was injected with a long needle to the bottom of the cuvette inside the cryostat, and the resulting change was monitored by UV/visible spectroscopy.

*Formation of an intermediate via the addition of IBX-ester to **10.***

A 0.500 mM solution of **10** was prepared in 4 mL of THF under an inert atmosphere in a drybox. The solution was transferred via gas-tight syringe to a custom two-neck vial equipped with a septum cap and a threaded dip-probe feed-through adaptor that had been purged with argon and contained a stir bar. The solution was cooled to -73 °C in an isopropanol/dry ice bath and a solution of 10 equivalents (250 μL of an 80 mM solution in THF) of IBX-ester was added, and the resulting change in absorbance was monitored by UV/visible spectroscopy.

*Evans Method of $[Fe^{III}(S^{Me2},O^{Me2}N_2NH(Pr,Pr))][PF_6]$ (**10**)*

^{1}H-NMR spectra were recorded on Bruker AV 301 FT-NMR spectrometers and are referenced to residual protio-solvent. Chemical shifts are reported in ppm. The magnetic moment of **1** was determined to be μ_{eff} = 4.69 B.M (MeOH), and μ_{eff} =4.08 B.M. (THF) using the Evans method.

X-ray crystallographic structure determination

A green needle of $Fe^{II}(S^{Me2},O^{Me2}N_2NH(Pr,Pr))$ (**9**), measuring 0.02 x 0.03 x 0.15 mm^3 was mounted on a loop with oil. Data was collected at -173ºC on a Nonius Kappa CCD FR590 single crystal X-ray diffractometer, Mo-radiation. Crystal-to-detector distance was 40 mm and exposure time was 90 seconds per degree for all sets. The scan width was 1º. Data collection was 100% complete to 25º in ϑ. A total of 6287 merged reflections were collected covering the indices, 0<=h<=10, 0<=k<=24, -24<=l<=24. 3355 reflections were symmetry independent and the R_{int} = 0.1669 indicated that the data was worse than average quality (average quality 0.07). Indexing and unit cell refinement indicated a triclinic lattice. The space group was found to be Pbca (No.61).

A red needle of $[Fe^{III}(S^{Me2},O^{Me2}N_2NH(Pr,Pr))][PF_6]$ (**10**), measuring 0.03 x 0.04 x 0.24 mm^3 was mounted on a loop with oil. Data was collected at -173ºC on a Nonius Kappa CCD FR590 single crystal X-ray diffractometer, Mo-radiation. Crystal-to-detector distance was 40 mm and exposure time was 90 seconds per degree for all sets. The scan width was 1º. Data collection was 99.9% complete to 25º in ϑ. A total of 8954 merged reflections were collected covering the indices, -16<=h<=16, -15<=k<=15, -18<=l<=18. 4628 reflections were symmetry independent and the R_{int} = 0.1382 indicated that the data was of worse than average quality (average quality 0.07). Indexing and unit cell refinement indicated a triclinic lattice. The space group was found to be P 2_1/c (No.14).

The data was integrated and scaled using SAINT, SADABS within the APEX2 software package by Bruker.[35] Solution by direct methods (SHELXT[36] or SIR97[37,38]) produced a complete heavy atom phasing model consistent with the proposed structure. The structure was completed by difference Fourier synthesis with SHELXL.[39] Scattering factors are from Waasmaier and Kirfel[40]. Hydrogen atoms were placed in geometrically idealised positions and constrained to ride on their

parent atoms with C---H distances in the range 0.95-1.00 Angstrom. Isotropic thermal parameters U_{eq} were fixed such that they were $1.2U_{eq}$ of their parent atom Ueq for CH's and $1.5U_{eq}$ of their parent atom U_{eq} in case of methyl groups. All non-hydrogen atoms were refined anisotropically by full-matrix least-squares. Structures were visualized using ORTEP-III and POV-Ray programs.[41,42]

Table 4-1. Crystal data, intensity collections[a], and structure refinement parameters for $Fe^{II}(S^{Me2},O^{Me2}N_2NH(Pr,Pr))$ (**9**) and $[Fe^{III}(S^{Me2},O^{Me2}N_2NH(Pr,Pr))](PF_6)$ (**10**).

	9	**10**
Formula	C_{16} H_{31} Fe N_3 $O_{0.84}$ $S_{1.16}$	C_{16} H_{31} F_6 Fe N_3 $O_{0.80}$ P $S_{1.20}$
Molecular Weight	371.97	517.54
Temperature (K)	100(2)	100(2)
Crystal System	Orthorhombic	Monoclinic
Space Group	P_{bca}	$P_{21/c}$
a, (Å)	9.207(5)	13.0383(9)
b, (Å)	20.195(10)	12.0531(8)
c, (Å)	20.468(10)	14.7542(13)
α, (°)	90	90
β, (°)	90	101.923(3)
γ, (°)	90	90
V (Å^3)	3806(3)	2268.6(3)
Z	8	4
R_1	0.0485	0.0556
R_w	0.0674	0.0900
GooF	0.0803	0.998

[a] Mo Ko(α,$^-$) (λ = 0.71070 Å) radiation; graphite monochromator; -90 ºC. [b] $R = \Sigma ||F_o| - |F_c|| / \Sigma |F_o|$. [c] $R_w = [\Sigma w(|F_o|-|F_c|)^2/\Sigma wF_o^2]^{1/2}$, where $w^{-1} = [\sigma^2_{count} + (0.05\ F^2)^2]/4F^2$.

4.3. Results and Discussion

4.3.1. Making an asymmetric ligand system

To develop a platform where the influence of a *trans* versus a *cis* thiolate could be elucidated, the mixed thiolate/alkoxide ligand $Fe^{II}(S^{Me2},O^{Me2}N_2NH(Pr,Pr))$ (**9, Scheme 4-1**) complex was developed. Extensive previous work established a synthetic procedure to create **1** and **3** by performing a metal-templated Schiff base condensation.[23,25,26,43] This procedure involves reacting 3-mercapto-3-methyl-2-butanone with either bis(3-aminopropyl)amine or N-(2-aminoethyl)-1,3-propanediamine to form a long chain with thiolates at each end before subsequent addition to an iron (II) or (III) salt. This process creates a symmetric complex, as both ends of the amine backbone are open for a condensation reaction to occur and there is no kinetic or thermodynamic preference for reacting with one end of the amine over the other. This presents a problem for creating an asymmetric ligand, as the amines are also far enough apart where addition at one end of the molecule does not affect the rate of addition at the other end. This presents an issue for protecting one end of the amine to prevent further reaction, as reaction conditions which protect one end of the amine will be able to protect both ends of the amine.

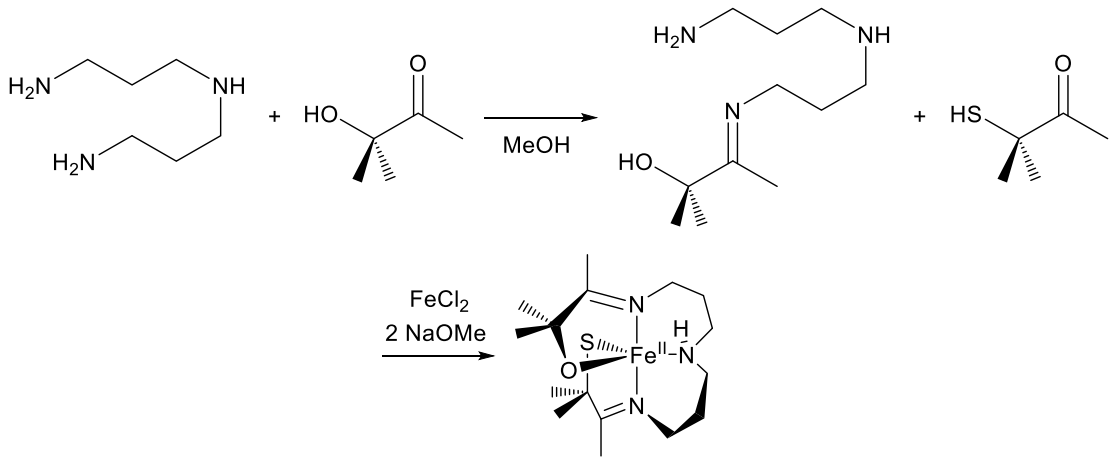

Scheme 4-1. Synthetic scheme for the production of $Fe^{II}(S^{Me2},O^{Me2}N_2NH(Pr,Pr))$ (**9**).

An attempt was made to produce **9** by sequential addition of one equivalent of 3-mercapto-3-methyl-2-butanone and one equivalent of 3-hydroxy-3-methyl-2-butanone to a dilute solution of a bis(3-aminopropyl)amine and iron, however, mass spectrometry of the solution showed that this results in a statistical mixture of the bis-thiolate, bis-alkoxide, and the desired mixed alkoxide/thiolate complex. Several attempts were made at reacting one equivalent of amine with one equivalent of a protecting group such as a *tert*-butyl carbamate and chromatographically separating the desired singly condensed ligand from the doubly condensed and uncondensed amine, but the long chain and polar amine made this infeasible. To successfully produce a singly condensed amine, 3-hydroxy-3-methyl-2-butanone was added dropwise to a dilute solution of excess bis(3-aminoethyl)amine. After the reaction was completed, the excess amine was distilled away, leaving primarily the singly condensed ligand with a small amount of doubly condensed impurity. This singly condensed ligand can then be reacted with iron (II) chloride and 3-mercapto-3-methyl-2-butanone to produce the desired complex. It can be crystallized by layering a DCM solution with pentane to produce X-ray quality crystals. The reduced complex **9** can then be oxidized with ferrocenium hexafluorophosphate to produce $[Fe^{III}(S^{Me2},O^{Me2}N_2NH(Pr,Pr))][PF_6]$ (**10, Figure 4-3**). Examination of the electronic structure of **9** shows an absorbance with λ_{max} = 415 nm. Oxidation to **10** does not greatly affect the electronic absorption spectrum, with a more intense peak at λ_{max} = 415 nm, a shoulder at 550 nm and a weak and broad transition at 800 nm. The oxidized complex **10** was found to have μ_{eff} = 1.99 at room temperature, corresponding to S = 1/2 (μ_{eff} = 1.73) via the Evans method. This is unusual for Fe^{III} thiolate complexes, but is similar to what is observed with **2** and **3**, which are S = 1/2 at low temperatures and a spin mixture at ambient temperature and S = 1/2 at room temperature respectively.[23,26]

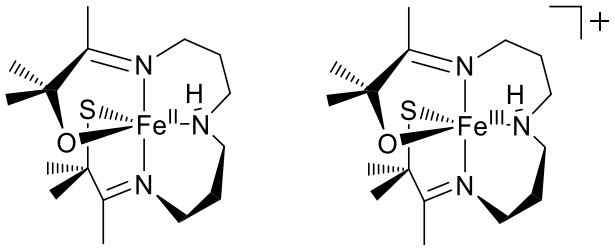

Figure 4-3. Schematic drawings of $Fe^{II}(S^{Me2},O^{Me2}N_2NH(Pr,Pr))$ (**9**) (left) and $[Fe^{III}(S^{Me2},O^{Me2}N_2NH(Pr,Pr))]^+$ (**10**) (right).

Mass spectrometry experiments were performed on both **9** and **10** to determine the amount of bis-thiolate and bis-alkoxide species present, as well as to characterize how **9** interacts with dioxygen. Mass spectrometry of **10** found an M+ peak at 369 m/z, showng with a smaller peak at 353 m/z, indicative of either a small amount of a bis-alkoxide impurity or a fragmentation losing the oxygen atom. There is initially only a small peak at 385 m/z, indicative of either a bis-thiolate impurity or the addition of one oxygen atom, but as the scan progresses, the 385 m/z peak grows steadily. Since the solution being injected into the spectrometer is homogenous, this could show the incorporation of an oxygen atom derived from O_2, but whether it is a sulfenate species like that found in **2** or **3** cannot be determined from mass spectrometry experiments alone. The reduced complex **9** was similarly found to have an M+ peak at 369 m/z, along with a peak arising at 403 m/z at M+32. This could indicate either an additional sulfur atom or two oxygen atoms, which both have a weight of 32 Da. This 403 m/z peak lowers in intensity as the solution ages with the concomitant increase in the intensity of the 385 m/z peak, implying that it is a result of **9** reacting with O_2 to form a transient superoxo (or other O_2-derived species) that proceeds to some product that incorporates an oxygen derived from O_2.

4.3.2. X-ray crystal structures of $Fe^{II}(S^{Me2},O^{Me2}N_2NH(Pr,Pr))$ and $[Fe^{III}(S^{Me2},O^{Me2}N_2NH(Pr,Pr))]^+$

Crystallographic experiments were carried out to characterize **9** and **10** (**Figure 4-4**). Like the symmetric complexes, they are roughly trigonal bipyramidal and coordinatively unsaturated. The reduced complex **9** has a geometry index of $\tau = 0.689$, which upon oxidation to **10** becomes 0.806. When oxidized, the bonds to the metal center correspondingly shorten by approximately 0.1 Å each (**Table 4-2**). The complexes crystallize with the sulfur and oxygen atoms disordered over both positions equally, indicating no preference for one configuration over another, and no preference for the thiolate or alkoxide being nearer to the N(2) amine proton. It is currently undetermined if this affects ligand binding to the open coordination site, as the symmetric complexes tend to bind ligands across the amine from its proton. The molecule also shows no preference for one enantiomer over another, with both complexes crystallizing in space groups with inversion centers, indicating a 1:1 ratio of both enantiomers. The two ends of the ligand exhibit very different bond lengths, as would be expected from a thiolate versus an alkoxide. In **9**,

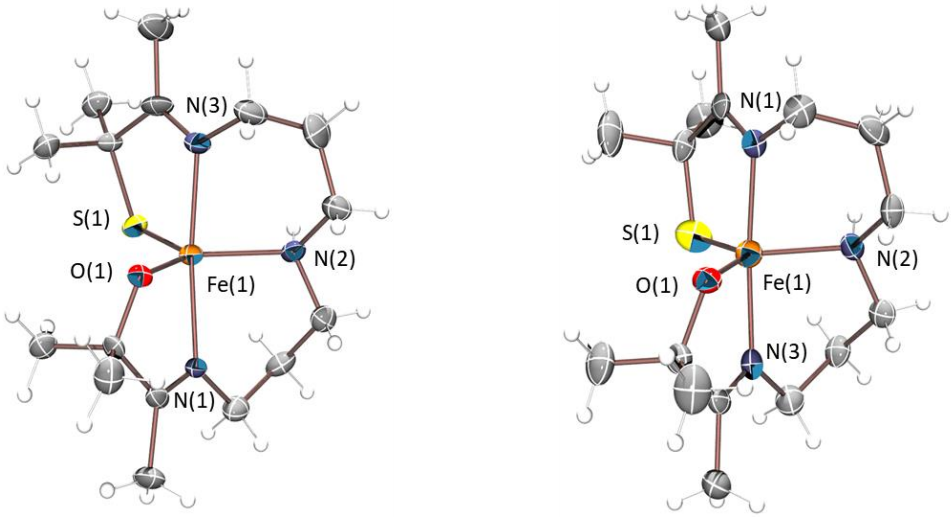

Figure 4-4. ORTEP diagrams of $Fe^{II}(S^{Me2},O^{Me2}N_2NH(Pr,Pr))$ (**9**) (left) and $[Fe^{III}(S^{Me2},O^{Me2}N_2NH(Pr,Pr))]^+$ (**10**) (right). Thermal ellipsoids at the 50% probability level, counterions omitted for clarity.

the Fe–O bond is 1.975(5) Å and the Fe-S bond is 2.3332(16) Å, and when oxidized to **10** those lengths become 1.876(11) and 2.171(3) Å respectively. Upon oxidation, the ligand becomes slightly more constrained due to shortening bond lengths, and accordingly, the bond angles shift slightly. The most open O–Fe–N(2) angle closes somewhat, going from 133.0(2)° to 125.7(5)°, correspondingly opening the O–Fe–S angle from 117.9(2)° to 123.0(5)° and the N(2)–Fe–S angle from 109.6(11)° to 111.25(13)°.

Table 4-2. Selected metrical parameters for $Fe^{II}(S_2{}^{Me2}N_2NH(Pr,Pr))$ (**1**), $Fe^{II}(S^{Me2},O^{Me2}N_2NH(Pr,Pr))$ (**9**), $[Fe^{III}(S_2{}^{Me2}N_2NH(Pr,Pr))](PF_6)$ (**2**), and $[Fe^{III}(S^{Me2},O^{Me2}N_2NH(Pr,Pr))](PF_6)$ (**10**).

	1	**9**	**2**	**10**
Fe–S(1)/O(1) (Å)	2.3263(5)	1.975(5)	2.133(2)	1.876(11)
Fe–S(2)/S(1) (Å)	2.3306(5)	2.3332(16)	2.161(2)	2.171(3)
Fe–N(1) (Å)	2.1556(16)	2.177(4)	1.967(4)	2.052(4)
Fe–N(2) (Å)	2.1656(16)	2.180(4)	2.049(4)	2.103(3)
Fe–N(3) (Å)	2.1815(15)	2.156(4)	1.954(4)	2.051(4)
N(1)–Fe(1)–N(3) (°)	172.81(6)	171.34(16)	178.1(2)	174.06(15)
N(2)–Fe(1)–N(3) (°)	90.96(6)	85.66(16)	86.2(2)	84.56(14)
N(1)–Fe(1)–N(2) (°)	83.80(6)	89.54(15)	94.2(2)	91.61(14)
N(3)–Fe(1)–S(2)/S(1) (°)	105.16(4)	80.70(12)	86.4(1)	78.1(3)
N(2)–Fe(1)–S(2)/S(1) (°)	107.79(4)	109.06(11)	106.5(1)	125.7(5)
N(2)–Fe(1)–S(1)/O(1) (°)	125.70(4)	133.0(2)	86.7(1)	87.20(13)
N(1)–Fe(1)–S(1)/O(1) (°)	97.68(5)	77.9(2)	132.3(1)	111.25(13)
S(2)/S(1)–Fe(1)–S(1)/O(1) (°)	126.17(2)	117.9(2)	121.0(1)	123.0(5)
τ^a	0.777	0.689	0.763	0.806

[a]5-coordinate geometry index, $\tau = (\beta - \alpha)/60$. β is the largest bond angle observed, and α is the second largest bond angle.

4.3.3. Comparisons with symmetric complexes

The exchange of a thiolate for an alkoxide has large effects on the structure and properties of the complex. Foremost, the smaller oxygen atom leads to smaller Fe–O bonds than Fe–S bonds, 1.975(5) Å versus 2.3263(5) Å in the reduced complex and 1.876(11) Å and 2.133(2) Å (**Table 4-2**) in the oxidized complex. For the most part, the rest of the bond lengths involving the metal center stay largely unchanged. This single shorter bond length causes the ligand to be more constrained, affecting the bond angles of the complexes and the geometry indices. The mixed alkoxide/thiolate complex has a geometry index of $\tau = 0.689$ in its reduced form **9** and $\tau = 0.806$ in its oxidized form **10**, changed from $\tau = 0.777$ and $\tau = 0.763$ for **1** and **2** respectively. In the reduced complex, this change to a slightly more open complex is driven primarily by the shorter Fe–O bond, causing the O/S(1)–Fe–N(2) bond angle to open from 125.70(4)° in the bis-thiolate complex to 133.0(2)° in the mixed complex. This is accompanied by a contraction in the O/S(1)–Fe–S(2) bond angle, from 126.17(2)° in the bis-thiolate to 117.9(2)°. The most dramatic change occurs unexpectedly in the N(3)–Fe–S bond angle, contracting from 105.16(4)° in the bis-thiolate complex to 80.70(12)° in the mixed complex. This shortening is driven by a rotation of carbon-carbon bond linking N(3) and the sulfur which allows the sulfur to be more evenly spaced between the oxygen and N(2). This same effect may not be observed in the bis-thiolate complex because the longer Fe–S bonds allow both sulfurs in the equatorial plane the range of motion to relax equally. In the oxidized complex, the shorter Fe–O bond causes the complex to become more trigonal bipyramidal, counter to what is observed in the reduced complex. The O/S–Fe–N(2) angle widens from 106.5(1)° to 125.7(5)°, accompanied by a greater contraction in the S(2)–Fe–N(2) angle from 132.3(1)° to 111.25(13)°. This lowers the variance of the equatorial bond angles, reducing the difference between the largest and smallest angles from 25.8° to just 14.5°.

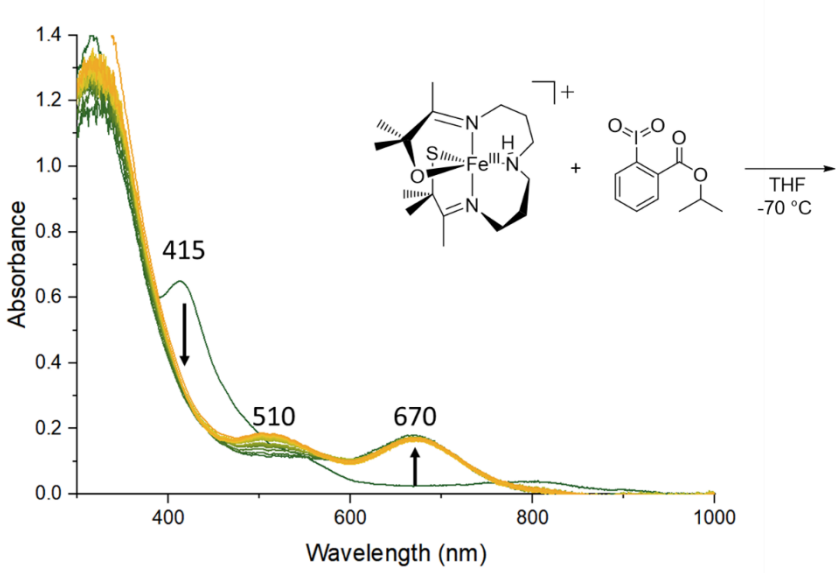

Figure 4-6. Electronic absorption spectrum of the reaction of $[Fe^{III}(S^{Me2},O^{Me2}N_2NH(Pr,Pr))]^+$ (**10**) with IBX-ester in THF at -70 °C. Scans are 3 minutes apart.

Preliminary reactions were carried out with the mixed alkoxide/thiolate complex to determine whether it retained the same chemical properties as the bis-thiolate complex. The oxidized complex **10** was reacted with the oxo-atom donor IBX-ester at -73 °C to determine

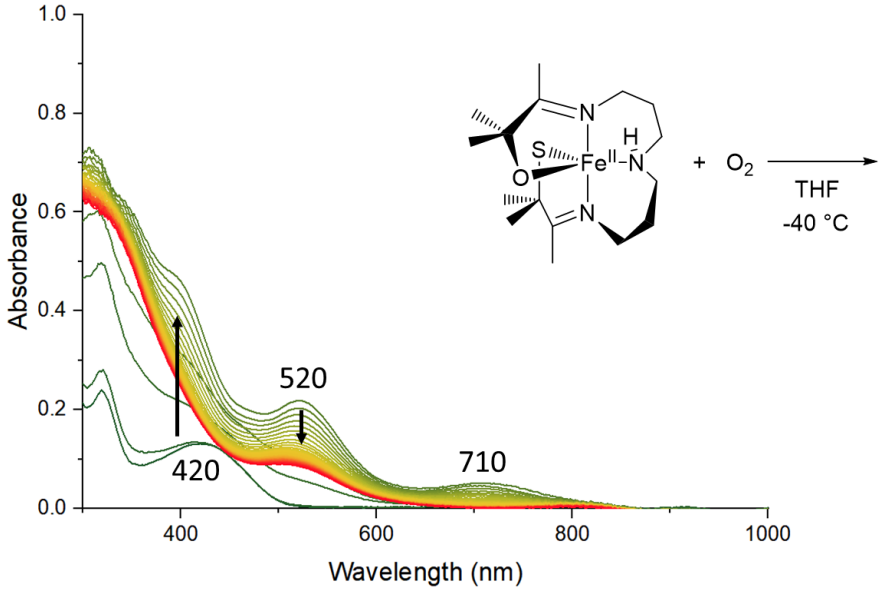

Figure 4-5. Electronic absorption spectrum of the reaction between $Fe^{II}S^{Me2},O^{Me2}N_2NH(Pr,Pr))$ (**9**) in THF at -40 °C. Scans are 1 minute apart.

whether a sulfenate complex could be formed, similar to complexes **2** and **3**. Upon addition of excess IBX-ester, **10** immediately forms a species with λ_{max} = 670 nm, with a second peak growing more slowly at λ_{max} = 510 nm (**Figure 4-6**). This intermediate remains unchanged at low temperatures, and upon warming, both peaks decay to the baseline. No sulfenate was able to be isolated from this reaction, which could indicate that the complex is being decomposed by the addition of another oxygen atom. It could also be that the complex continues to react with the excess oxo-atom donor, and that multiple oxidations cause the complex to fall apart. The addition of dioxygen to the reduced **9** at -40°C results in the dramatic growth of a band in the region of 300 nm, with shoulders at 390 and 520 nm, and a weak and broad absorbance at 750 nm (**Figure 4-5**). When warmed, this absorbance decays, with absorbances at 390 and 750 decaying faster than the 520 band before the spectrum becomes featureless. While more experiments are necessary to determine the specifics of these reactions, they bear marked similarity to those of **1** and **2**. Like **2**, the oxidized complex **10** has an absorbance band at 415 nm, and like **2**, addition of an oxo atom donor leads to the growth of a low-energy absorbance band at approximately 670 nm. However, unlike **2**, the reaction of **10** and IBX-ester does not seem to proceed to a sulfenate, potentially indicating that the role of the second sulfur atom is to stabilize the transient Fe^{V}-oxo required for sulfenate formation. Like **1**, the reaction between **9** and dioxygen leads to a transient species with a peak at 520 nm and a low energy band at 750 nm, but again unlike **1**, the reaction between **9** and O_2 does not seem to proceed to a sulfenate. Because a sulfenate necessarily requires binding the source of the oxygen atom *cis* to the sulfur atom, the sulfenate not being observed could also be due to a sixth ligand coordinating *trans* to the sulfur.

4.3.4. Density Functional Theory calculations

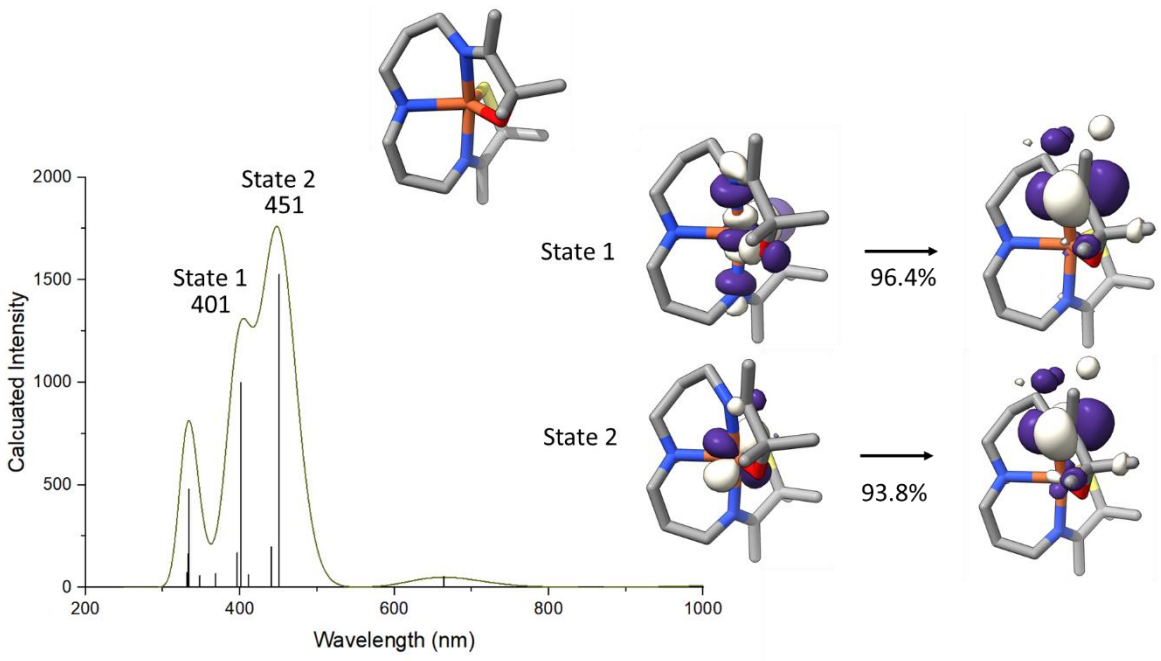

Figure 4-7. TD-DFT calculated electronic absorption spectrum of $Fe^{II}S^{Me2}$,$O^{Me2}N_2NH$(Pr,Pr)) (**9**) . including natural transition orbitals (NTOs) describing the major contribution to each state.

To further characterize how removing a thiolate in favor of an alkoxide affects the electronic structure of **9** and **10**, theoretical calculations were performed. Calculations were also performed to determine whether binding a substrate (in this case, dioxygen) was more favorable *cis* or *trans* to the sulfur atom. Calculations were performed on all possible spin states (S = 0, 1, or 2 for **9** and S = 1/2, 3/2, and 5/2 for **10**), and their structural parameters in addition to their calculated electronic absorption parameters were compared to empirical parameters. For **9**, the spin state that best reproduced the empirical data was the S = 2 spin state. This high spin state is not unusual for five-coordinate ferrous complexes.[23,44] For **10**, the spin state which best reproduced observed data was the S = 1/2 state, which matches what was found with Evans method.

Time-dependent density functional theory (TD-DFT) calculations were performed to examine the transitions involved in the electronic absorption spectra of **9** and **10**. The reduced complex **9** was calculated to have absorption maxima at 451 and 401 nm, similar to the 415 nm

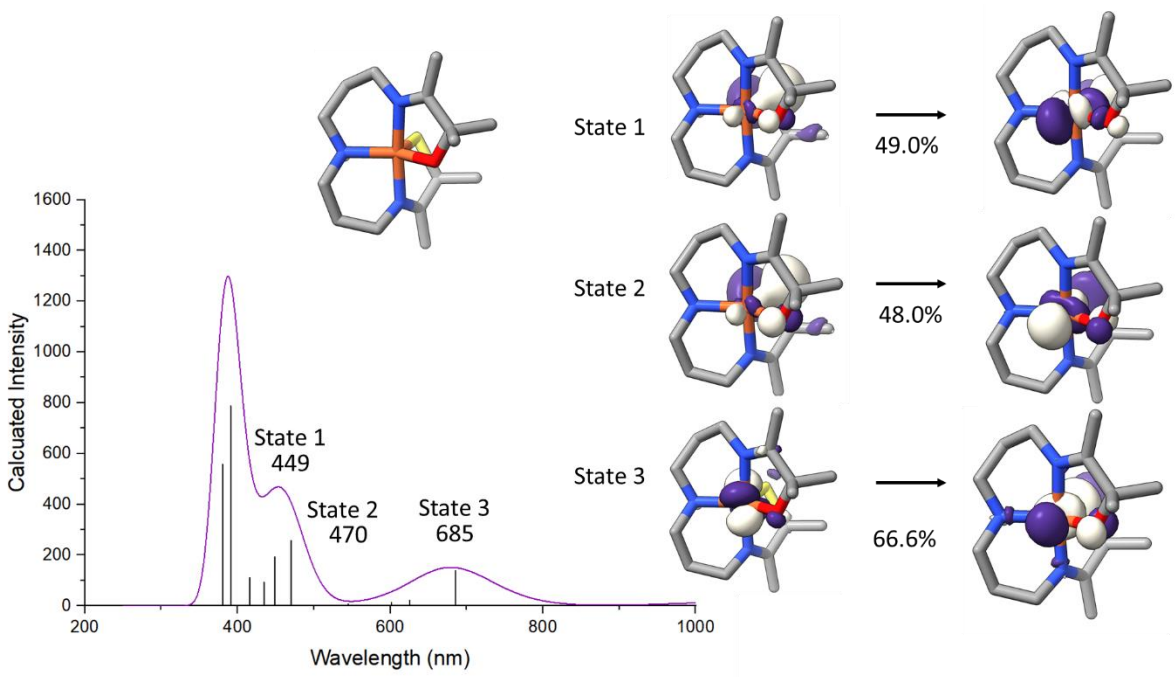

Figure 4-8. TD-DFT calculated electronic absorption spectrum of $[Fe^{III}S^{Me2},O^{Me2}N_2NH(Pr,Pr))]^+$ (**10**) . including natural transition orbitals (NTOs) describing the major contribution to each state.

band observed empirically. The lower energy band was calculated to be a $d_{xz}(Fe^{II}) \rightarrow C{=}N\ \pi^*$ transition, and the higher energy band a ligand-$d_{x2-y2}(Fe^{II})\ \sigma^* \rightarrow C{=}N\ \pi^*$ transition (**Figure 4-7**). In both cases, the C=N bond in question is the bond closest to the alkoxide, with the thiolate staying largely uninvolved. The oxidized complex **10** sees a much greater contribution from the thiolate, with the calculated lowest energy 685 nm band occurring due to a $d_{yz}(Fe^{III}) \rightarrow$ ligand-$d_{z2}(Fe^{III})\ \sigma^*$ transition. The higher energy transitions at 470 and 449 nm are due to a thiolate S-$d_{xz}(Fe^{III})\ \pi \rightarrow$ ligand-$d_{z2}(Fe^{III})\ \sigma^*$ transition and a combination of a thiolate S-$d_{xz}(Fe^{III})\ \pi \rightarrow$ thiolate S-$d_{xz}(Fe^{III})\ \pi^*$ transition and a thiolate S-$d_{yz}(Fe^{III})\ \sigma \rightarrow$ thiolate S-$d_{z2}(Fe^{III})\ \sigma^*$ respectively (**Figure 4-8**).

Using the hybrid exchange-correlation functional with Coulomb attenuating method function CAM-B3LYP, calculations were performed on structures incorporating a superoxo moiety either *cis* or *trans* to the thiolate sulfur. The calculated energies for the *cis* and *trans* structures are somewhat close, favoring the *trans* structure by 12 kcal/mol. However, this energy is reflective

most of the number of atoms and the number of bonds. During geometry optimization of the *cis* superoxo structure, the N(2) amine of the ligand backbone drifts away from the iron center and breaks the Fe–N(2) bond. This is likely due to the high degree of backdonation from the thiolate which is *trans* to that nitrogen and the well-established *trans* effect of thiolates.[45] While bond lengths cannot be compared to values obtained from a crystal structure of this complex, when compared to the similar **2-superoxo** complex and the calculations performed on it, both the *cis* and *trans* structures match closely to previously computed values (**Table 4-3**). Fe–N, Fe–S/O, and Fe–OO distances are comparable for all three calculated structures with the exception of the *cis* thiolate complex, which has long Fe–N(2) and Fe–OO bonds, likely due to the influence of a tightly bound thiolate, with a Fe–S bond of just 2.200 Å.

Table 4-3. Comparison of empirical and calculated bond lengths of $[Fe^{III}(S_2^{Me2}N_2NH(Pr,Pr))]^+$ (**2**), $Fe^{III}(S_2^{Me2}N_2NH(Pr,Pr))(O_2)$ (**2-superoxo**), and $Fe^{III}(S^{Me2},O^{Me2}N_2NH(Pr,Pr))(O_2)$ (**10**) with the superoxo anion bound *cis* (*cis*-**10**-superoxo) and *trans* (*trans*-**10**-superoxo).

Bond	2	2-superoxo	*cis*-10-superoxo	*trans*-10-superoxo
Fe–S/O(1)cis (Å)	2.133(2)	2.203	2.200	1.838
Fe–S/O(2)trans (Å)	2.161(2)	2.256	1.894	2.288
Fe–N(1) (Å)	1.967(4)	1.981	2.015	1.994
Fe–N(2) (Å)	2.049(4)	2.111	2.434	2.102
Fe–N(3) (Å)	1.954(4)	1.981	2.048	1.958
Fe–O (Å)	N/A	1.947	2.009	1.960
O–O (Å)	N/A	1.289	1.303	1.307

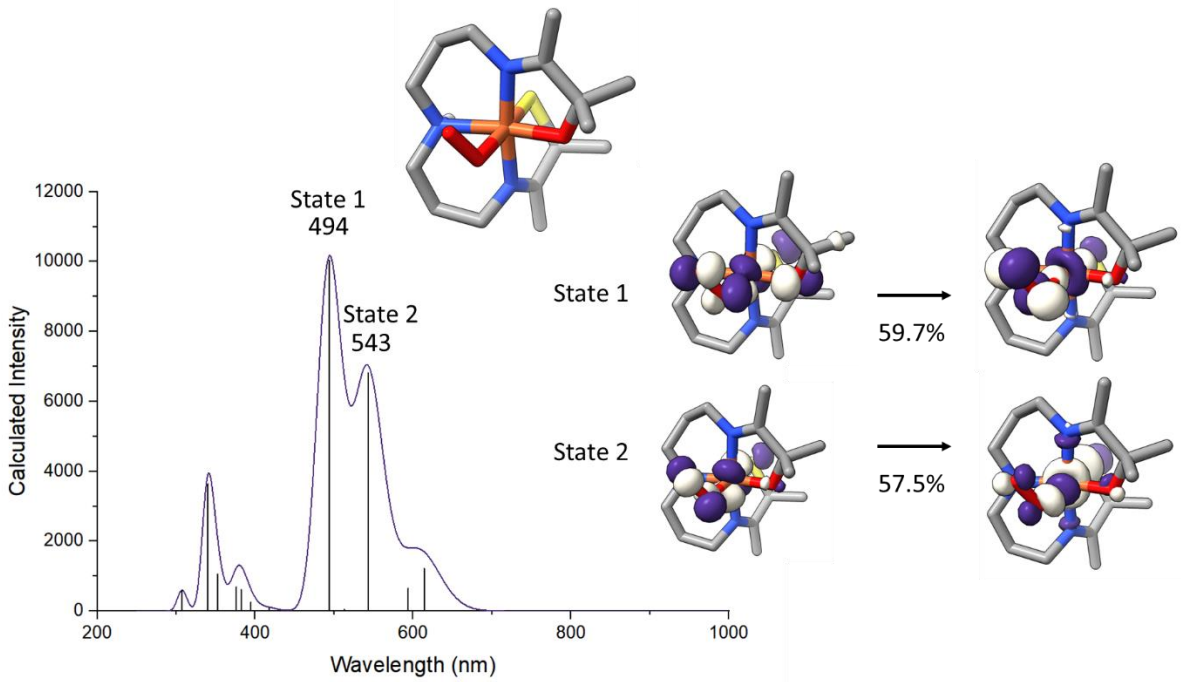

Figure 4-9. TD-DFT calculated electronic absorption spectrum of a superoxo complex formed from **9** and O_2 with the superoxo bound *trans* to the thiolate, including natural transition orbitals (NTOs) describing the major contribution to each state.

Despite the *cis* thiolate structure's dissimilarity to the other calculated structures, its calculated electronic absorbance spectrum is much closer to the observed **2-superoxo** than the *trans* thiolate structure's. The *trans* superoxo's calculated electronic absorbance spectrum has a broad absorbance band in the 500-600 nm region caused by two strong absorbances at 494 and 543 nm (**Figure 4-9**). These are caused by a ligand-$d_{yz}(Fe^{III})$-superoxo nonbonding → $d_{z2}(Fe^{III})$-superoxo σ* transition and a $d_{yz}(Fe^{III})$-superoxo σ → thiolate S-$d_{z2}(Fe^{III})$-superoxo σ* transition respectively, with overall little contribution from the thiolate. In contrast, the *cis* thiolate structure's calculated electronic absorption spectrum has absorbances at 726, 551, and 423 nm, similar to **2-superoxo**'s empirically observed 707, 523, and 409 nm and absorbance bands and the bands observed in the reaction between **9** and dioxygen (**Figure 4-10**). These bands are due to a thiolate S p_x → $d_{xz}(Fe^{III})$-superoxo σ*, a thiolate S-$d_{z2}(Fe^{III})$ σ* → $d_{xz}(Fe^{III})$-superoxo σ*, and an alkoxide O-$d_{xz}(Fe^{III})$-superoxo π* → $d_{yz}(Fe^{III})$-superoxo σ* transition respectively.

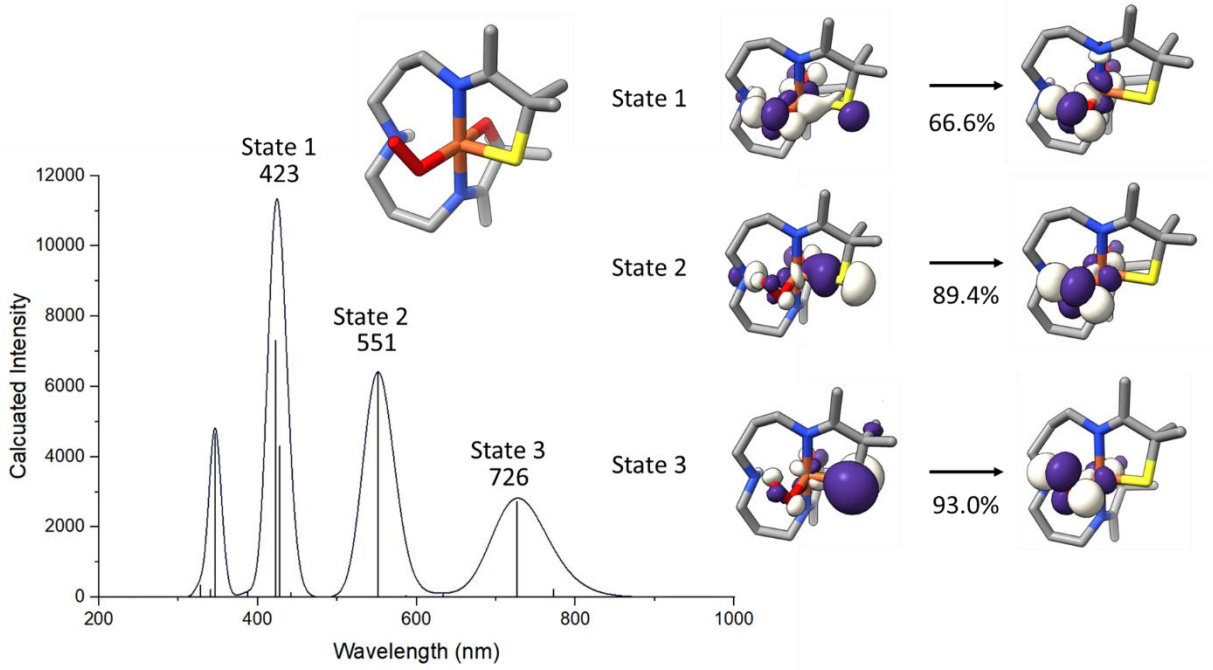

Figure 4-10. TD-DFT calculated electronic absorption spectrum of a superoxo complex formed from **9** and O_2 with the superoxo bound *cis* to the thiolate, including natural transition orbitals (NTOs) describing the major contribution to each state.

The strong similarity of the *cis* thiolate's electronic absorption spectrum to the observed spectrum of **2-superoxo** would seem to imply that despite the broken Fe-N(2) bond, it would still be the likely isomer for the binding of a substrate. However, the *trans* thiolate's calculated electronic absorption matches that of **3-superoxo** somewhat closely. Examination of the lower energy bands in these systems reveals they are largely due to sulfur-to-metal charge transfer bands, and in the more constrained system or the system with fewer thiolates, the required orbital interactions may not be present. Further characterization would be required to state definitively whether a substrate binds *cis* or *trans* to the thiolate, with the most effective method likely being crystallization with a dioxygen mimic such as azide or nitric oxide.

4.4. Summary and Conclusions

Exchange of a thiolate for an alkoxide has been preliminarily shown to have an effect on the properties of **1** and **2**, but not as strong an effect as might be expected. Primarily, the major

effect of the second sulfur atom seems to be the stabilization of the transient Fe^{V}-oxo intermediate required for formation of a sulfenate. Beyond the shortening of the Fe–O bond due to the smaller radius of an oxygen atom versus a sulfur atom, structural properties are more or less maintained, with the complexes remaining roughly trigonal bipyramidal. Complex **10** is still able to bind an oxo-atom donor and form an adduct species, although a sulfenate species resulting from this reaction is not observed. Complex **9** reacts with dioxygen to form a transient species with a similar absorbance profile to the reaction of **1** and dioxygen, but a sulfenate species originating from this reaction is also unobserved. Mass spectrometry of these complexes demonstrates that an oxygen atom can be incorporated to them via reaction with dioxygen, but whether it is a metal-centered transformation remains undetermined. Theoretical calculations suggest that the reduced complex in a high-spin state, and that the oxidized complex becomes low-spin. Calculations that were performed to determine the most probable mode of substrate binding to the mixed-alkoxide/thiolate complex were inconclusive, with structural data suggesting that a substrate binding *trans* to a thiolate is preferred, and calculated spectra showing that binding a substrate *cis* to a thiolate better reproduces the empirical data.

4.5. References

(1) Brown, C. D.; Neidig, M. L.; Neibergall, M. B.; Lipscomb, J. D.; Solomon, E. I. VTVH-MCD and DFT Studies of Thiolate Bonding to {FeNO}7/ {FeO2}8 Complexes of Isopenicillin N Synthase: Substrate Determination of Oxidase versus Oxygenase Activity in Nonheme Fe Enzymes. *J. Am. Chem. Soc.* **2007**, *129* (23), 7427–7438. DOI: 10.1021/ja071364v

(2) Kovacs, J. A.; Brines, L. M. Understanding How the Thiolate Sulfur Contributes to the Function of the Non-Heme Iron Enzyme Superoxide Reductase. *Acc. Chem. Res.* **2007**, *40* (7), 501–509. DOI: 10.1021/ar600059h

(3) Kennepohl, P.; Neese, F.; Schweitzer, D.; Jackson, H. L.; Kovacs, J. A; Solomon, E. I. Spectroscopy of Non-Heme Iron Thiolate Complexes: Insight into the Electronic Structure of the Low-Spin Active Site of Nitrile Hydratase. *Inorg. Chem.* **2005**, *44*, 1826–1836. DOI: 10.1021/ic0487068

(4) Villar-Acevedo, G.; Nam, E.; Fitch, S.; Benedict, J.; Freudenthal, J.; Kaminsky, W.; Kovacs, J. A. Influence of Thiolate Ligands on Reductive N-O Bond Activation. Probing the O2- Binding Site of a Biomimetic Superoxide Reductase Analogue and Examining the Proton-Dependent Reduction of Nitrite. *J. Am. Chem. Soc.* **2011**, *133* (5), 1419–1427. DOI: 10.1021/ja107551u

(5) Shearer, J.; Scarrow, R. C.; Kovacs, J. A. Synthetic Models for the Cysteinate–Ligated Non–Heme Iron Enzyme Superoxide Reductase: Observation and Structural Characterization by XAS of an FeIII–OOH Intermediate. *J. Am. Chem. Soc.* **2002**, *124*, 11709-11717. DOI: 10.1021/ja012722b

(6) Green, M. T. Role of the Axial Ligand in Determining the Spin State of Resting Cytochrome P450 [7]. *J. Am. Chem. Soc*. **1998**, *120* (41), 10772–10773. DOI: 10.1021/ja980994h

(7) Goudarzi, S.; Babicz, J. T.; Kabil, O.; Banerjee, R.; Solomon, E. I. Spectroscopic and Electronic Structure Study of ETHE1: Elucidating the Factors Influencing Sulfur Oxidation and Oxygenation in Mononuclear Nonheme Iron Enzymes. *J. Am. Chem. Soc.* **2018**, *140* (44), 14887–14902. DOI: 10.1021/jacs.8b09022

(8) Mak, P. J.; Denisov, I. G.; Victoria, D.; Makris, T. M.; Deng, T.; Sligar, S. G.; Kincaid, J. R. Resonance Raman Detection of the Hydroperoxo Intermediate in the Cytochrome P450 Enzymatic Cycle. *J. Am. Chem. Soc.* **2007**, *129* (20), 6382–6383. DOI: 10.1021/ja071426h

(9) Hunt, A. P.; Lehnert, N. The Thiolate Trans Effect in Heme {FeNO}6 Complexes and Beyond: Insight into the Nature of the Push Effect. *Inorg. Chem.* **2019**, *58* (17), 11317–11332. DOI: 10.1021/acs.inorgchem.9b00091

(10) Denisov, I. G.; Makris, T. M.; Sligar, S. G.; Schlichting, I. Structure and Chemistry of Cytochrome P450. *Chem. Rev*. **2005**, *105* (6) 2253–2277. DOI: 10.1021/cr0307143

(11) Namuswe, F.; Kasper, G. D.; Narducci Sarjeant, A. A.; Hayashi, T.; Krest, C. M.; Green, M. T.; Moënne-Loccoz, P.; Goldberg, D. P. Rational Tuning of the Thiolate Donor in Model Complexes of Superoxide Reductase: Direct Evidence for a Trans Influence in Fe^{III}-OOR Complexes. *J. Am. Chem. Soc.* **2008**, *130* (43), 14189–14200. DOI: 10.1021/ja8031828

(12) Mathé, C.; Weill, C. O.; Mattioli, T. A.; Berthomieu, C.; Houée-Levin, C.; Tremey, E.; Nivière, V. Assessing the Role of the Active-Site Cysteine Ligand in the Superoxide Reductase from Desulfoarculus Baarsii. *J. Biol. Chem.* **2007**, *282* (30), 22207–22216. DOI: 10.1074/jbc.M700279200

(13) Brines, L. M.; Villar-Acevedo, G.; Kitagawa, T.; Swartz, R. D.; Lugo-Mas, P.; Kaminsky, W.; Benedict, J. B.; Kovacs, J. A. Comparison of Structurally-Related Alkoxide, Amine, and Thiolate-Ligated MII (M = Fe, Co) Complexes: The Influence of Thiolates on the Properties of Biologically Relevant Metal Complexes. *Inorg. Chim. Acta* **2008**, *361* (4), 1070–1078. DOI: 10.1016/j.ica.2007.07.038

(14) Dedushko, M. A.; Greiner, M. B.; Downing, A. N.; Coggins, M.; Kovacs, J. A. Electronic Structure and Reactivity of Dioxygen-Derived Aliphatic Thiolate-Ligated Fe-Peroxo and

Fe(IV) Oxo Compounds. *J. Am. Chem. Soc.* **2021**, *144*, 8515-8528. DOI: 10.1021/JACS.1C07656

(15) Dedushko, M. Insights into Dioxygen Bond Activation and Formation by Small Biomimetic Complexes, University of Washington, Seattle, WA, 2020.

(16) Shearer, J.; Scarrow, R. C.; Kovacs, J. A. Synthetic Models for the Cysteinate-Ligated Non-Heme Iron Enzyme Superoxide Reductase: Observation and Structural Characterization by XAS of an FeIII-OOH Intermediate. *J. Am. Chem. Soc.* **2002**, *124* (39), 11709–11717. DOI: 10.1021/ja012722b

(17) Coggins, M. K.; Toledo, S.; Shaffer, E.; Kaminsky, W.; Shearer, J.; Kovacs, J. A. Characterization and Dioxygen Reactivity of a New Series of Coordinatively Unsaturated Thiolate-Ligated Manganese(II) Complexes. *Inorg. Chem.* **2012**, *51* (12), 6633–6644. DOI: 10.1021/ic300192q

(18) Downing, A. N.; Coggins, M. K.; Poon, P. C. Y.; Kovacs, J. A. Influence of Thiolate versus Alkoxide Ligands on the Stability of Crystallographically Characterized Mn(III)-Alkylperoxo Complexes. *J. Am. Chem. Soc.* **2021**, *143* (16), 6104–6113. DOI: 10.1021/jacs.0c13001

(19) Kitagawa, T.; Dey, A.; Lugo-Mas, P.; Benedict, J. B.; Kaminsky, W.; Solomon, E.; Kovacs, J. A. A Functional Model for the Cysteinate-Ligated Non-Heme Iron Enzyme Superoxide Reductase (SOR). *J. Am. Chem. Soc.* **2006**, *128* (45), 14448–14449. DOI: 10.1021/ja064870d

(20) Kitagawa, T. Biomimetic Modeling of Superoxide Reductase, University of Washington, Seattle, WA, 2007.

(21) Greiner, M. B. Kinetic Insights into Dioxygen Activation by Biomimetic Thiolate-Ligated Iron Complexes, University of Washington, Seattle, WA, 2023.

(22) Schweitzer, D.; Ellison, J. J.; Shoner, S. C.; Lovell, S.; Kovacs, J. A. A Synthetic Model for the NO-Inactivated Form of Nitrile Hydratase. *J. Am. Chem. Soc.* **1998**, *120* (42), 10996–10997. DOI: 10.1021/ja981117e

(23) Ellison, J. J.; Nienstedt, A.; Shoner, S. C.; Barnhart, D.; Cowen, J. A., Kovacs, J. A. Reactivity of Five-Coordinate Models for the Thiolate-Ligated Fe Site of Nitrile Hydratase. *J. Am. Chem. Soc.* **1998**, *120* (23), 5691–5700. DOI: 10.1021/ja973129q

(24) Shearer, J.; Kung, I. Y.; Lovell, S.; Kaminsky, W.; Kovacs, J. A. Why Is There an "Inert" Metal Center in the Active Site of Nitrile Hydratase? Reactivity and Ligand Dissociation from a Five-Coordinate Co(III) Nitrile Hydratase Model. *J. Am. Chem. Soc.* **2001**, *123* (3), 463–468. DOI: 10.1021/ja002642s

(25) Shearer, J.; Jackson, H. L.; Schweitzer, D.; Rittenberg, D. K.; Leavy, T. M.; Kaminsky, W.; Scarrow, R. C.; Kovacs, J. A. The First Example of a Nitrile Hydratase Model Complex That Reversibly Binds Nitriles. *J. Am. Chem. Soc.* **2002**, *124* (38), 11417–11428. DOI: 10.1021/ja012555f

(26) Schweitzer, D.; Shearer, J.; Rittenberg, D. K.; Shoner, S. C.; Ellison, J. J.; Loloee, R.; Lovell, S.; Barnhart, D.; Kovacs, J. A. Enhancing Reactivity via Structural Distortion. *Inorg. Chem.* **2002**, *41* (12), 3128–3136. DOI: 10.1021/ic0109187

(27) Shoner, S. C.; Nienstedt, A. M.; Ellison, J. J.; Kung, I. Y.; Barnhart, D.; Kovacs, J. A. Structural Comparison of Five-Coordinate Thiolate-Ligated M^{II} = Fe^{II}, Co^{II}, Ni^{II}, and Zn^{II} Ions Wrapped in a Chiral Helical Ligand. *Inorg. Chem.* **1998**, *37* (22), 5721–5726. DOI: 10.1021/ic980882r

(28) Neese, F.; Wiley, J. The ORCA Program System. *Wiley Interdiscip. Rev. Comput. Mol. Sci.* **2012**, *2* (1), 73–78. DOI: 10.1002/WCMS.81

(29) Neese, F. Software Update: The ORCA Program System, Version 4.0. *Wiley Interdiscip. Rev. Comput. Mol. Sci.* **2018**, *8* (1), e1327. DOI: 10.1002/WCMS.1327

(30) Grimme, S.; Ehrlich, S.; Goerigk, L. Effect of the Damping Function in Dispersion Corrected Density Functional Theory. *J. Comput. Chem.* **2011**, *32* (7), 1456–1465. DOI: 10.1002/JCC.21759

(31) Becke, A. D. Density-functional Thermochemistry. III. The Role of Exact Exchange. *J. Chem. Phys.* **1998**, *98* (7), 5648. DOI: 10.1063/1.464913.

(32) Neese, F.; Wennmohs, F.; Hansen, A.; Becker, U. Efficient, Approximate and Parallel Hartree–Fock and Hybrid DFT Calculations. A 'Chain-of-Spheres' Algorithm for the Hartree–Fock Exchange. *Chem. Phys.* **2009**, *356* (1–3), 98–109. DOI: 10.1016/J.CHEMPHYS.2008.10.036

(33) Zhurko, G. A. Chemcraft – Graphical Program for Visualization of Quantum Chemistry Computations. https://chemcraftprog.com: Ivanovo, Russia 2005.

(34) Pettersen, E. F.; Goddard, T. D.; Huang, C. C.; Meng, E. C.; Couch, G. S.; Croll, T. I.; Morris, J. H.; Ferrin, T. E. UCSF ChimeraX: Structure Visualization for Researchers, Educators, and Developers. *Protein Sci.* **2021**, *30* (1), 70–82. DOI: 10.1002/PRO.3943

(35) Bruker. APEX2 (Version 2.1-4), SAINT (Version 7.34A), SADABS (Version 2007/4). BrukerAXS Inc.: Madison, WI 2007.

(36) Sheldrick, G. M. SHELXL-97, Program for the Refinement of Crystal Structures. University of Göttingen: Göttingen, Germany 1997.

(37) Altomare, A.; Cascarano, G.; Giacovazzo, C.; Guagliardi, A.; Burla, M. C.; Polidori, G.; Camalli, M.; IUCr. SIR92 – a Program for Automatic Solution of Crystal Structures by Direct Methods. *J. Appl. Cryst.* **1994**, *27* (3), 435–435. DOI: 10.1107/S002188989400021X

(38) Altomare, A.; Burla, M. C.; Camalli, M.; Cascarano, G. L.; Giacovazzo, C.; Guagliardi, A.; Moliterni, A. G. G.; Polidori, G.; Spagna, R. SIR97: A New Tool for Crystal Structure Determination and Refinement. *J. Appl. Cryst.* **1999**, *32* (1), 115–119. DOI: 10.1107/S0021889898007717

(39) Sheldrick, G. M.; IUCr. Crystal Structure Refinement with SHELXL. *Acta Cryst. C* **2015**, *71* (1), 3–8. DOI: 10.1107/S2053229614024218

(40) Waasmaier, D.; Kirfel, A. New Analytical Scattering-Factor Functions for Free Atoms and Ions. *Acta Cryst. A* **1995**, *51* (3), 416–431. DOI: 10.1107/S0108767394013292

(41) Persistence of Vision Raytracer. Persistence of Vision Pty. Ltd.: Williamstown, Victoria, Australia 2004.

(42) Burnett, M. N.; Johnson, C. K. ORTEP-III: Oak Ridge Thermal Ellipsoid Plot Program for Crystal Structure Illustrations. *Oak Ridge National Laboratory Report ORNL-6895* **1996**.

(43) Blakely, M. N.; Dedushko, M. A.; Poon, P. C. Y.; Villar-Acevedo, G.; Kovacs, J. A. Formation of a Reactive, Alkyl Thiolate-Ligated Fe^{III}-Superoxo Intermediate Derived from Dioxygen. *J. Am. Chem. Soc.* **2019**, *141*, 1867-1870. DOI: 10.1021/jacs.8b12670

(44) Gordon, J. B.; McGale, J. P.; Prendergast, J. R.; Shirani-Sarmazeh, Z.; Siegler, M. A.; Jameson, G. N. L.; Goldberg, D. P. Structures, Spectroscopic Properties, and Dioxygen Reactivity of 5- and 6-Coordinate Nonheme Iron(II) Complexes: A Combined

Enzyme/Model Study of Thiol Dioxygenases. *J. Am. Chem. Soc.* **2018**, *140* (44), 14807–14822. DOI: 10.1021/JACS.8B08349

(45) Hunt, A. P.; Lehnert, N. The Thiolate Trans Effect in Heme {FeNO}6 Complexes and Beyond: Insight into the Nature of the Push Effect. *Inorg. Chem.* **2019**, *58* (17), 11317–11332. DOI: 10.1021/ACS.INORGCHEM.9B00091

(46) Shearer, J.; Nehring, J.; Lovell, S.; Kaminsky, W.; Kovacs, J. A. Modeling the Reactivity of Superoxide Reducing Metalloenzymes with a Nitrogen and Sulfur Coordinated Iron Complex. *Inorg. Chem.* **2001**, *40* (22), 5483–5484. DOI: 10.1021/ic0102211

Chapter 5. Synthetic Heterometallic "Open" $NaMn_3O_4$ Cubane Clusters Containing an Exchangeable Exogenous Hydroxide Ligand

5.1. Introduction

The oxygen-evolving complex (OEC) is a heterometallic cubane cluster, $Mn_{dang}CaMn_3O_5$, involved in photosynthetic water oxidation.[1–7] The redox-inactive Ca^{II} ion is essential for catalytic activity, but its precise role in the catalysis of the OEC is presently unknown.[8,9] The cubane core of the OEC is flexible, especially in the lower S_1, S_2, and S_3 oxidation states of its catalytic cycle, and it forms both "open" and "closed" structures that are easily interconverted.[1,6,7,10] It has been proposed that the interconversion between these two forms acts as a mechanism for gating access to higher S_i states,[2] and that it limits the availability of reactive sites. The "open" conformation is deemed open because central oxo atom O(5) is closer to the "dangling" manganese atom and one of the cubane core Mn–O distances is longer than a covalent bond, and the "closed" conformation is deemed as such because the O(5) atom is closer to the rest of the cubane (**Figure 5-1**).[11] This longer distance in the "open" conformation may be because the oxo atom is protonated.[3] For the S_2 state, the OEC exists in a low- or high-spin form depending on whether it is in the "open" or

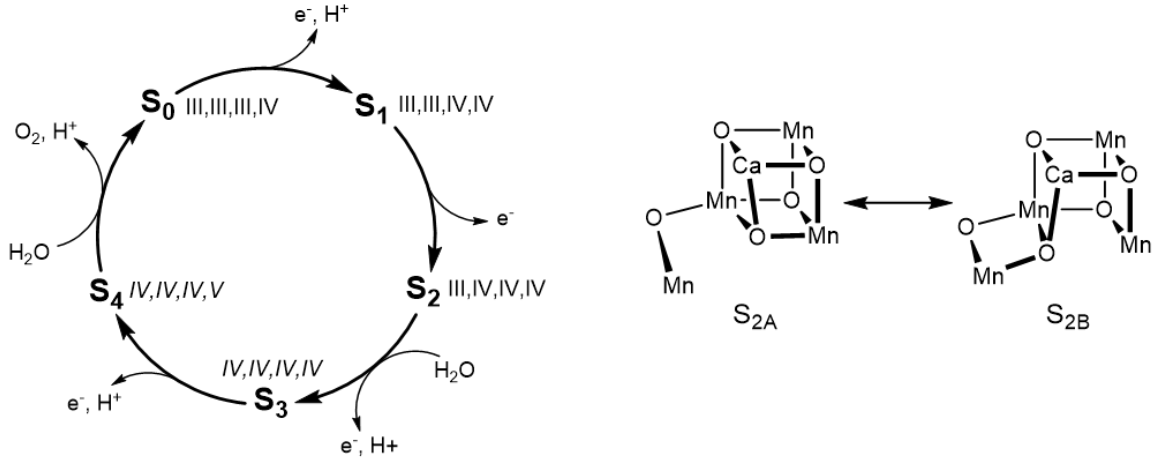

Figure 5-1. Left: The Kok cycle and right: two proposed structures for "closed" (S_{2A}) and "open" (S_{2B}) conformations of the S_2 state.

"closed" conformation respectively.[10,12] The origin of this flexibility is currently not entirely understood, but it has been proposed to be due to Jahn-Teller effects.[13]

The exact mechanism of O–O bond formation by the oxygen-evolving complex is currently unknown. Many mechanisms of O–O bond formation have been proposed, but two leading mechanisms are the radical coupling mechanism wherein two Mn^{IV}-oxyl radicals couple to form a peroxo intermediate,[14] and a nucleophilic attack mechanism where a Ca^{II}-OH nucleophically attacks Mn^{V}-oxo to form an O–O bond (**Figure 5-2**, left).[15,16] The role of calcium within this process is currently unclear, but the O_2 evolution of the complex has been shown to decrease when the Ca^{II} ion is replaced with Sr^{II}, and ceases entirely when it is replaced with Ba^{II}.[7,17] This indicates that calcium is directly involved in the O_2 evolution process, although whether it is involved directly in O–O bond formation or is present to modulate the electronic structure of the OEC is unclear.[18] Computational studies have indicated that the mechanism of O–O bond formation proceeds through the radical coupling mechanism, specifically invoking first a hydroxide bridging between a cubane manganese and the calcium atom, and transformation of that hydroxide to an oxyl radical which can then form a bond with the bridging O(5) molecule (**Figure 5-2**, right).[19–21] These studies have found support from a variety of experimental evidence from direct observation of the OEC, including X-ray free-electron laser studies finding a short O•••O distance supporting

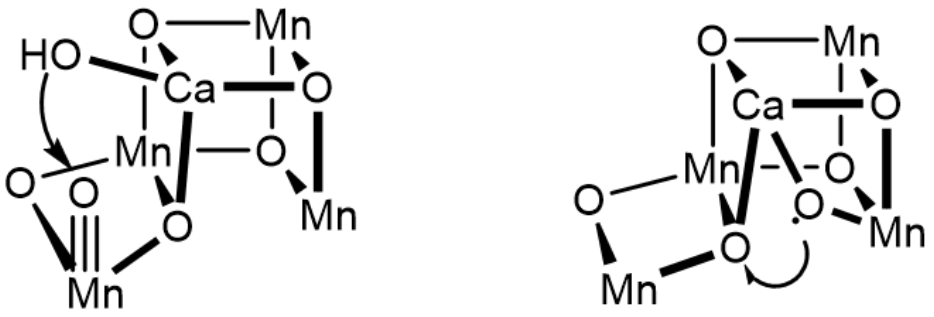

Figure 5-2. Two proposed mechanisms of O–O bond formation. Left: the nucleophilic attack mechanism. Right: the radical coupling mechanism.

an oxyl mechanism;[22] serial femtosecond X-ray crystallography and X-ray emission spectroscopy finding intricate structural rearrangement between the S_2 and S_0 states;[23] and ^{17}O electron-electron double resonance-detected NMR spectroscopy identified a bridging μ-oxo that exchanges on a timescale similar to the previously identified substrate.[24] The radical coupling mechanism has been favored in theoretical studies due to the lower energetic barrier for O–O bond formation, however, there is no precedence in small-molecule manganese model chemistry for this mechanism,[25] and limited evidence in materials chemistry.[26–28]

Model chemistry of the OEC commonly attempts to model both the structure and function of the OEC, however, the two groups rarely overlap. While many functional analogues were designed with the intention of also being structural analogues with the knowledge of the time, greater understanding of the OEC stemming from higher and higher quality crystallographic and electronic experiments means that very few, if any, could still be considered structural analogues.[3,29,30] The enormous breadth of functional analogues prevents detailed discussion here, but there are several extensive reviews on the subject.[31–33] Structural analogues which incorporate both manganese and calcium are also limited, and as such there is a dearth of fundamental studies on the role of calcium. The Agapie group's Mn_3CaO_4 cubane complex was contrasted with an

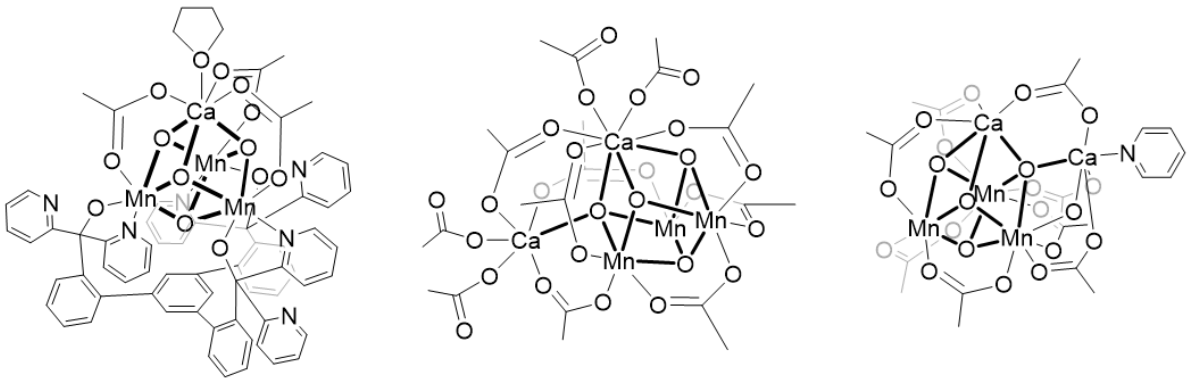

Figure 5-3. Structural analogues of the oxygen-evolving complex containing manganese and calcium atoms. Left to right: $LMn^{IV}_3CaO_4(OAc)_3(THF)$,[34] $[Mn^{IV}_3Ca_2O_4(O_2C^tBu)_8(^tBuCO_2H)_4]$,[36] and $[Mn_4CaO_4(Bu^tCO_2)_8(Bu^tCO_2H)_2(py)]$[37]

identically ligated Mn_4O_4 cubane to investigate possible effects of a redox-inactive ion in the cubane (**Figure 5-3**, left). It was found that the calcium ion allowed for the buildup of localized positive charges in the manganese ions, allowing reductions to occur at potentials more than 1 V more negative compared to the entirely manganese complex. Additionally, calcium's lack of redox activity prevents the comproportionation of a high-valent and a low-valent manganese center, allowing higher oxidation states to be reached. Incorporation of a calcium ion also slightly lowers the average Mn•••Mn distances in the cubane.[34] They have also been able to add a fifth metal center to this cluster through the addition of silver trifluoromethanesulfonate. This fifth metal was shown to increase the basicity of a nearby oxo atom via the desymmetrization of the cluster and through its coordination.[35] The Christou group has reported a self-assembled $Mn_3Ca_2O_4$ cubane with a dangling calcium atom, modeling the less symmetric OEC and allowing study of the magnetic properties of the cubane to be characterized, finding that it mimicked the $S = 9/2$ state of found in the S_2 state of the OEC (**Figure 5-3**, center).[36] The Zhao group has produced a self-assembled Mn_4CaO_4 complex, allowing the characterization of the "dangling" manganese ion's contribution to the magnetic structure of the cubane core (**Figure 5-3**, right). It was found that this cluster reproduced the observed magnetic structure of the OEC in the S_2 state with an $S = 9/2$ core antiferromagnetically coupled to an $S = 2$ "dangling" manganese. They also reported derivatives of this cubane with differing ligands coordinated to the calcium ion or dangling manganese, but they did not characterize how those ligands altered the properties of the cluster as a whole.[37]

5.2. Experimental

General Methods

All manipulations were performed in a glovebox under an atmosphere of N_2 unless otherwise noted. Reagents purchased from commercial vendors were of the highest purity available and used without further purification. Toluene, tetrahydrofuran, and diethyl ether were rigorously degassed and purified using solvent purification columns housed in a custom steel cabinet, dispensed via a stainless steel Schlenk-line (GlassContour). Methanol was distilled from magnesium methoxide and degassed prior to use. Pyridine was dried over NaOH and fractionally distilled and degassed prior to use. All solvents were additionally stored over molecular sieves for at least 24 hours prior to use.

*Synthesis of 1-(3,5-di-tert-butyl-2-hydroxyphenyl) ethanone (**A**)*

Titanium tetrachloride, $TiCl_4$ (0.832 g, 4.4 mmol), was slowly added to 2,4-di-*tert*-butylphenol (0.826 g, 4 mmol) in a Schlenk flask flushed with N_2 at room temperature. $TiCl_4$ acts as a Lewis acid for direct of *ortho*-acylation of 2,4-di-*tert*-butylphenol, according to a previously reported procedure.[38] The resulting dark cherry-red mixture was stirred at r.t. for 15 minutes until gas evolution has stopped. Following this, acetyl chloride (0.235 g, 3 mmol) was added to the solid and the resulting thick dark-red solution was stirred at r.t. for 15 minutes. The reaction mixture was then brought up to 120 °C and left to stir at this temperature for an additional hour. The reaction mixture was then cooled to room temperature, diluted with 15 mL DCM and quenched with 15 mL DI H_2O. A cloudy dark-orange solution was obtained which was extracted with 3 x 10 mL CH_2Cl_2. The organic layer was washed with 2 x 30 mL DI H_2O, dried over Na_2SO_4 for 30 minutes, and concentrated under reduced pressure. ^{1}H NMR (300 MHz, $CDCl_3$): 12.99 (s, OH), 7.56 (s, Ar C-H), 2.65 (s, $CH_3C(O)$), 1.43 (s, ^{t}Bu), 1.32 (s, ^{t}Bu).

*Synthesis of 2-acetyl-4,6-di-tert-butylphenyl acetate (**B-Me**)*

In a glovebox, a solution of **A** (2.48 g, 10.0 mmol) in 20 mL anhydrous THF was added dropwise to a rigorously stirred solution of insoluble NaH (0.264 g, 11.0 mmol) in 60 mL THF in a 250 mL round-bottom Schlenk flask. The resulting neon-yellow mixture was stirred at 25 ˚C for 15 minutes until H_2 gas evolution has stopped and no trace of unreacted NaH solid was observed. Then, acetyl chloride (0.71 mL, 10.0 mmol) was added to the reaction mixture and stirred for 12 hours. The reaction mixture was removed from the glovebox and quenched with a mixture of ice (9 g) and 1N HCl (15 mL). The organic phase was extracted with 3 x 20 mL ethyl acetate, washed with 2 x 20 mL brine and 2 x 20 mL DI H_2O. The organic layer was dried over $NaSO_4$ for 30 minutes, filtered, and concentrated under reduced pressure. The desired product was obtained as a white powder in 74% yield (2.22 g). ^{1}H NMR (300 MHz, $CDCl_3$): δ = 1.34 (s, 9H, ^{t}Bu), 1.37 (s, 9H, ^{t}Bu), 2.34 (s, 3H, CH_3), 2.53 (s, 3H, CH_3), 7.57 (d, J = 2.4 Hz, 1H, ArH), 7.59 (d, J = 2.4 Hz 1H, ArH).

*Synthesis of 1-(3,5-di-tert-butyl-2-hyroxyphenyl)butane-1,3-dione (**C-Me**).*

To a stirring solution of **B-Me** (1.00 g, 3.45 mmol) in 80 mL anhydrous THF, a solution of KO^{t}Bu (0.387 g, 3.45 mmol) in 20 mL THF was added in a glovebox. The reaction was stirred at ambient temperatures for 12 hours, after which time the pH was adjusted to pH= 3 using 3M HCl. The reaction mixture was then concentrated on rotary evaporator to give a brown oil, which was extracted with 100 mL DCM. The organic layer was washed with 2 x 100 mL 5% $NaHCO_3$, 2 x 100 mL DI H_2O, and 2 x 100 mL brine, and then dried over Na_2SO_4, filtered, and concentrated on a rotary evaporator. The resulting oily residue was recrystallized and washed with cold hexanes to give a white powder in 47% yield (0.47 g). ^{1}H NMR (300 MHz, $CDCl_3$): δ = 1.31 (s, 9H, ^{t}Bu),

1.43 (s, 9H, ^{t}Bu), 1.79 (s, 3H, CH_3), 2.91 (s, 2H, CH_2), 7.57 (d, J = 2.6 Hz, 1H, ArH), 7.81 (d, J = 2.6 Hz, 1H, ArH), 12,65 (s, 1H, ArOH).

*Synthesis of Mn(hydroxyphenyldiimine)(Cl) (**11**)*

To a stirred solution of **C-Me** (0.450 g, 1.54 mmol) in 20 mL diethyl ether in air was added a solution of ethylenediamine (0.046 g, 0.77 mmol) in 10 mL diethyl ether. The solution was allowed to stir for 12 hours and the solvent was removed in vacuo. 0.100 g of the white solid was dissolved in 15 mL MeOH, and a slurry of calcium hydroxide (0.012 g, 0.17 mmol) and manganese dichloride (0.021 g, 0.17 mmol) in 10 mL MeOH was added and allowed to stir for 12 hours. The dark greenish brown solution was then reduced to dryness via rotary evaporator, and crystals suitable for X-ray diffraction were grown via layering a saturated MeOH solution with diethyl ether and allowing the solution to mix over approximately 72 hours (0.047 g, 0.07 mmol, 40%).

*Synthesis of [(en)NaMn$_3$O$_4$(L$_3$)(OH)] (**12**)*

To a stirred solution of 1-(3,5-di-*tert*-butyl-2-hydroxyphenyl)butane-1,3-dione (**C-Me**, 60 mg, 0.207 mmol) and NaOMe (11 mg, 0.207 mmol) in 10 mL of MeOH was added dropwise a solution of $MnCl_2$ (26 mg, 0.207 mmol) in 5 mL of MeOH (Scheme S2). The resulting yellow solution was stirred for an hour, after which time a solution of ethylenediamine (12.4 mg, 0.207 mmol) in 1 mL of MeOH was added dropwise. The solution was allowed to stir overnight. The resulting golden yellow solution was reduced in volume to approximately 5 mL, and crystals suitable for X-ray diffraction were grown via vapor diffusion of the methanol solution and toluene. Yield: 42 mg (0.03 mmol, 49%).

*Synthesis of [(en)NaMn$_3$O$_4$(L$_3$)(OMe)] (**13**)*

Ethylene diamine (0.082 g, 1.37 mmol) was added to **C-Me** (0.300 g, 1.03 mmol) in 10 mL of anhydrous THF resulting in an immediate color change to bright yellow. After stirring for

one hour, NaOMe (0.054 g, 1.03 mmol) was added, and the reaction mixture was allowed to stir for additional 15 minutes, after which time $MnSO_4 \cdot H_2O$ (1.03 mmol, 0.169 g) was added. The reaction mixture was allowed to stir for 12 hours, and the resulting orange-red reaction mixture was filtered through a bed of celite, the solvent was pumped off under vacuum, and the resulting red powder was redissolved in a minimal amount of toluene. Crystals suitable for X-ray diffraction of **2** were grown by layering DCM on a toluene solution.

*Synthesis of [(py)NaMn$_3$O$_4$(L$_3$)(OH)] (**14**)*

To a stirred solution of 1-(3,5-di-*tert*-butyl-2-hydroxyphenyl)butane-1,3-dione (**C-Me**, 60 mg, 0.207 mmol) in 5 mL of diethyl ether was added a solution of ethylenediamine (12.4 mg, 0.207 mmol) in 5 mL of diethyl ether and stirred overnight. The resulting yellow solution was evaporated to dryness, re-dissolved in 8 mL of THF, followed by the dropwise addition of a solution of $NaN(TMS)_2$ (38 mg, 0.207 mmol) in THF. This solution was stirred for an hour and then evaporated to dryness. The resulting yellow solid was re-dissolved in 10 mL of pyridine, and a solution of $MnCl_2$ (26 mg, 0.207 mmol) in 5 mL of pyridine was added. The reaction mixture was then allowed to stir overnight. The volume of the solution was reduced to approximately 3 mL, and crystals suitable for X-ray diffraction were grown via vapor diffusion of this solution and ether. Yield: 37 mg (0.029 mmol, 42%).

X-ray crystallographic structure determination

A brown needle of singly metalated complex **11**, measuring 0.30 x 0.05 x 0.04 mm^3 was mounted on a loop with oil. Data was collected at -173°C on a Bruker APEX II single crystal X-ray diffractometer, Mo-radiation. Crystal-to-detector distance was 40 mm and exposure time was 60 seconds per frame for all sets. The scan width was 0.5°. Data collection was 99.8% complete to 25° in ϑ. A total of 15652 reflections were collected covering the indices, -44<=h<=44, -

12<=k<=12, -31<=l<=31. 8076 reflections were symmetry independent and the R_{int} = 0.1589 indicated that the data was of moderate quality (0.07). Indexing and unit cell refinement indicated a C-centered monoclinic lattice. The space group was found to be C 2/c (No.15).

A gold prism of [(en)$NaMn_3O_4(L_3)$(OH)] (**12**) measuring 0.08 x 0.11 x 0.12 mm^3 was mounted on a loop with oil. Data was collected at -173 ºC on a Bruker APEX II single crystal X-ray diffractometer, with Mo-radiation. The crystal-to-detector distance was 40 mm and exposure time was 30 seconds per frame for all sets. The scan width was 0.5º. Data collection was 99.9% complete to 25º in ϑ. A total of 19494 reflections were collected covering the indices, $-21 \leq h \leq 21$, $-22 \leq k \leq 22$, $-22 \leq l \leq 22$. 38916 reflections were symmetry independent and the R_{int} = 0.0920 indicated that the data was of slightly worse than average quality (0.07). Indexing and unit cell refinement indicated a triclinic lattice. The space group was found to be P -1 (No.2).

A gold prism of [(en)$NaMn_3O_4(L_3)$(OMe)] (**13**) measuring 0.09 x 0.06 x 0.05 mm^3 was mounted on a loop with oil. Data was collected at -173 ºC on a Bruker APEX II single crystal X-ray diffractometer, with Mo-radiation. The crystal-to-detector distance was 40 mm and exposure time was 30 seconds per frame for all sets. The scan width was 0.5º. Data collection was 100% complete to 25º in ϑ. A total of 89545 reflections were collected covering the indices, $-18 \leq h \leq 18$, $-20 \leq k \leq 20$, $-22 \leq l \leq 22$. 18011 reflections were symmetry independent and the R_{int} = 0.1139 indicated that the data was of somewhat worse than average quality (0.07). Indexing and unit cell refinement indicated a triclinic lattice. The space group was found to be P -1 (No.2).

A gold prism of [(py)$NaMn_3O_4(L_3)$(OH)] (**14**) measuring 0.13 x 0.06 x 0.06 mm^3 was mounted on a loop with oil. Data was collected at -173 ºC on a Bruker APEX II single crystal X-ray diffractometer, with Mo-radiation. Crystal-to-detector distance was 40 mm and exposure time was 30 seconds per frame for all sets. The scan width was 0.5º. Data collection was 98.3%

complete to 25° in ϑ. A total of 25830 reflections were collected covering the indices, $-20 \leq h \leq 20$, $-18 \leq k \leq 20$, $-22 \leq l \leq 23$. 14370 reflections were symmetry independent and the $R_{int} = 0.0828$ indicated that the data was of about average quality (0.07). Indexing and unit cell refinement indicated a triclinic lattice. The space group was found to be P -1 (No.2).

The data was integrated and scaled using SAINT, SADABS within the APEX2 software package by Bruker.[39] Solution by direct methods (SHELXT[40] or SIR97[41,42]) produced a complete heavy atom phasing model consistent with the proposed structure. The structure was completed by difference Fourier synthesis with SHELXL.[43] Scattering factors are from Waasmaier and Kirfel[44]. Hydrogen atoms were placed in geometrically idealised positions and constrained to ride on their parent atoms with C---H distances in the range 0.95-1.00 Angstrom. Isotropic thermal parameters U_{eq} were fixed such that they were $1.2U_{eq}$ of their parent atom Ueq for CH's and $1.5U_{eq}$ of their parent atom U_{eq} in case of methyl groups. All non-hydrogen atoms were refined anisotropically by full-matrix least-squares. Structures were visualized using ORTEP-III and POV-Ray programs.[45,46]

The asymmetric unit of all three cubane compounds consists of one complete molecule with additional solvent molecule(s), in the case of **13** and **14**. In the case of **12**, all solvent molecules were removed via SQUEEZE[47–49], however, with **13** the crystal was of sufficient quality to resolve one toluene molecule, and with **14** the crystal was of sufficient quality to also resolve one disordered pyridine and one Et_2O molecule.

T**able 5-1**. Crystal data, intensity collections[a], and structure refinement parameters for Mn(hydroxyphenyldiimine)(Cl) (**11**), [(en)$NaMn_3O_4(L_3)(OH)$] (**12**), [(en)$NaMn_3O_4(L_3)(OMe)$] (**13**), and [(py)$NaMn_3O_4(L_3)(OH)$] (**14**)

	11	**12**	**13**	**14**
Formula	C_{40} H_{60} Cl_5 Mn N_2 O_5	C_{62} H_{99} Mn_3 N_8 Na O_7	C_{70} H_{109} Mn_3 N_8 Na O_7	C_{74} H_{111} Mn_3 N_8 Na O_8
Molecular Weight	881.09	1256.30	1362.46	1428.51
Temperature (K)	100(2)	100(2)	100(2)	100(2)
Crystal System	Monoclinic	Triclinic	Triclinic	Triclinic
Space Group	$C_{2/c}$	P_{-1}	P_{-1}	P_{-1}
a, (Å)	37.583(6)	16.3953(18)	14.0391(16)	16.3457(17)
b, (Å)	10.4011(17)	16.5727(17)	15.6116(18)	16.3492(17)
c, (Å)	26.386(5)	16.7750(18)	17.2259(18)	18.7332(19)
α, (°)	90	60.415(4)	80.111(3)	67.655(4)
β, (°)	119.278(9)	80.346(5)	80.350(3)	64.312(4)
γ, (°)	90	83.344(5)	81.918(4)	60.052(4)
V ($Å^3$)	8997(3)	3904.7(7)	3642.4(7)	3822.1(7)
Z	8	2	2	2
R_1	0.0939	0.0619	0.05147	0.0595
R_w	0.2373	0.1221	0.1029	0.1132
GooF	0.979	0.894	1.002	0.997

[a] Mo Ko(α,$^-$) (λ = 0.71070 Å) radiation; graphite monochromator; -90 ºC. [b] $R = \Sigma ||F_o| - |F_c|| / \Sigma |F_o|$. [c] $R_w = [\Sigma w(|F_o|-|F_c|)^2/\Sigma wF_o^2]^{1/2}$, where $w^{-1} = [\sigma^2_{count} + (0.05\ F^2)^2]/4F^2$.

5.3. Results and Discussion

5.3.1. Synthesis of a Schiff-base-type binucleating ligand

To investigate the proposed mechanisms of O–O bond formation in the OEC and to characterize the electronic structure of reactive intermediates in the process, a ligand framework supporting a bimetallic Mn/Ca or a Mn/Mn system was proposed. A site-differentiated binucleating ligand was designed to allow for a high-valent manganese atom and another metal in close proximity. To accomplish this, a salen-derivative was chosen, as *o*-vanillin salen derivatives have previously been shown to be able to incorporate both a high-valent manganese and an alkaline earth metal.[50] The diketone 1-(3,5-di-*tert*-butyl-2-hydroxylphenyl)butane-1,3-dione was reacted with ethylenediamine to afford the a Schiff-base enolate ligand, which could then be deprotonated in the presence of manganese to afford the singly metalated Mn(hydroxyphenyldiimine)(Cl) complex **11** (**Figure 5-4**).

The singly-metalated manganese complex could be crystallized and characterized via single-crystal X-ray diffraction. Unexpectedly, rather than binding in the N_2O_2 pocket of the binucleating ligand, the manganese inserted in the O_4 pocket, coordinated in an octahedral

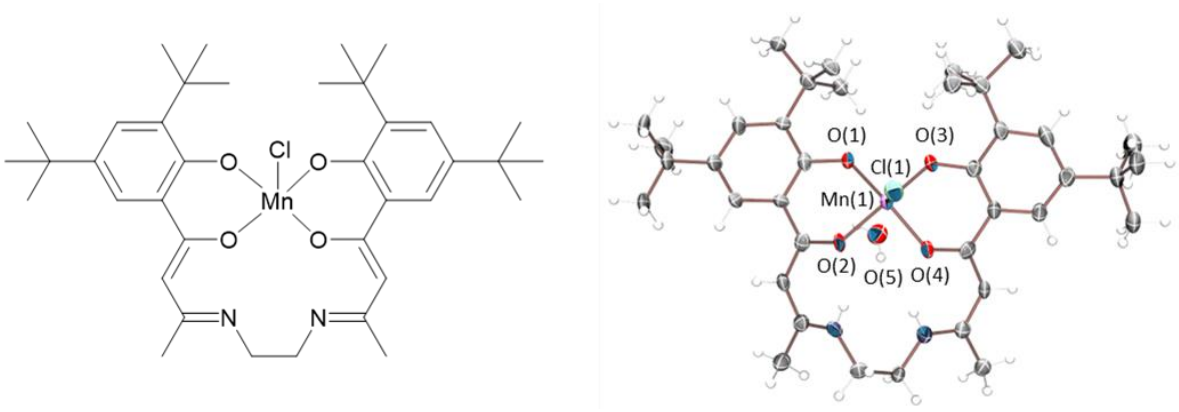

Figure 5-4. Schematic drawing (left) and ORTEP diagram (right) of Mn(hydroxyphenyldiimine)(Cl) (**11**). Thermal ellipsoids at the 50% probability level.

geometry to two alkoxide oxygens and two phenoxide oxygens, with the fifth and sixth coordination sites being ligated with a chloride anion and with a water molecule 2.8 Å away respectively (**Figure 5-4**). Due to the absence of other anions in the crystal structure, this implies that the oxidation state of the manganese center is +5. The Mn–O distances are similar to those observed in other Mn^{V} complexes in similar environments,[50] with an average bond length of 1.880 Å (**Table 5-2**). Experiments were carried out to attempt to metalate the second coordination site with calcium, however, these were largely unsuccessful and no calcium-containing products were able to be isolated. It is possible that the chloride anion could be replaced with another coordinating or noncoordinating ligand, as the long Mn–Cl bond length of 2.470(2) Å implies the possibility of lability, but no ligand replacement experiments were attempted.

Table 5-2. Selected bond lengths for Mn(hydroxyphenyldiimine)(Cl) (**11**)

	Bond length (Å)
O(1)–Mn(1)	1.864(5)
O(2)–Mn(1)	1.915(5)
O(3)–Mn(1)	1.855(5)
O(4)–Mn(1)	1.911(5)
Cl(1)–Mn(1)	2.470(2)
O(5)–Mn(1)	2.797(5)

5.3.2. Synthesis of Mn_3Na cubane complexes

In the course of these experiments, a fortuitous product was isolated from modified reaction conditions for **11**. By reacting 1-(3,5-di-*tert*-butyl-2-hydroxylphenyl)butane-1,3-dione, ethylenediamine, manganese dichloride, and sodium methoxide in inert atmosphere, we were able to produce a series of $NaMn_3O_4$ cubane complexes of similar structure to the core of the OEC (**Scheme 5-1**). These clusters are composed of a flexible ligand that supports an "open" cubane structure as well as incorporating an exogenous hydroxide or methoxide ligand opposite the sodium atom. The sodium atom is ligated with an ethylenediamine molecule but can be replaced with a pyridine molecule by condensing the dione ligand with ethylenediamine and isolating it prior to adding the metal. These complexes contain a sodium atom as a byproduct of their method of synthesis which could feasibly be replaced with a differing alkaline or alkaline earth metal by judicious choice of base. This was attempted with calcium hydroxide and calcium methoxide, and while no product was able to be isolated from the reaction mixture, we believe that with fine-tuning of the reaction conditions and isolation conditions that it can be successful. These complexes were able to be crystallized and characterized via single-crystal X-ray diffraction, but further attempts at producing these cubanes in bulk for analysis via cyclic voltammetry and other methods were not successful.

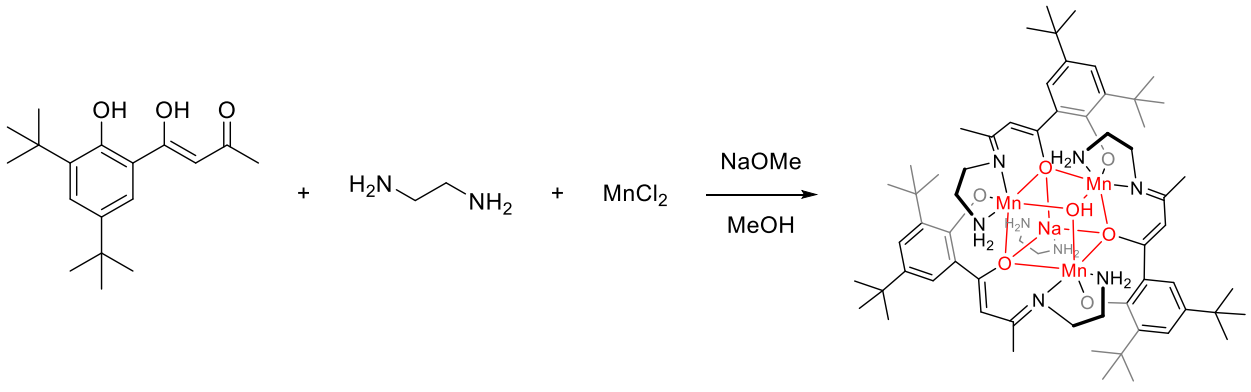

Scheme 5-1. Synthesis of $[(en)NaMn_3O_4(L_3)(OH)]$ (**12**).

5.3.3. X-ray crystal structures of three distinct cubane complexes

Three distinct heterometallic cubane clusters were isolated and characterized. All three clusters, [(en)NaMn$_3$O$_4$(L$_3$)(OH)] (**12**), [(en)NaMn$_3$O$_4$(L$_3$)(OMe)] (**13**), and [(py)NaMn$_3$O$_4$(L$_3$)(OH)] (**14**), feature manganese ions each ligated by one primary amine (N(1), N(3), or N(5), one imine nitrogen (N(2), N(4), or N(6)), a phenoxide oxygen (O(2), O(4), or O(6)), and an enolate oxygen (O(1), O(3), or O(5)) all derived from the same ligand, as well as in some cases an enolate oxygen provided by an adjacent manganese ion's ligand. The phenoxide oxygens are terminal, whereas the enolate oxygens form vertices of the cubane and bridge manganese and/or sodium ions. The hydroxide or methoxide is loosely bound and exchangeable, shown by the isolation of two clusters containing different exogenous ligands via the same synthetic method. Additionally, based on the bond lengths of the cubane, O(7) is terminal in **13**, doubly bridging in **12**, and triply bridging in **14**, demonstrating the flexibility of the ligand structure. All three cubanes have each of their manganese atoms in either five- or six-coordinate N_2O_3 or N_2O_4 environments, exhibiting a range of Mn–O bond lengths despite the pseudo-C_3 helical symmetry of the ligand

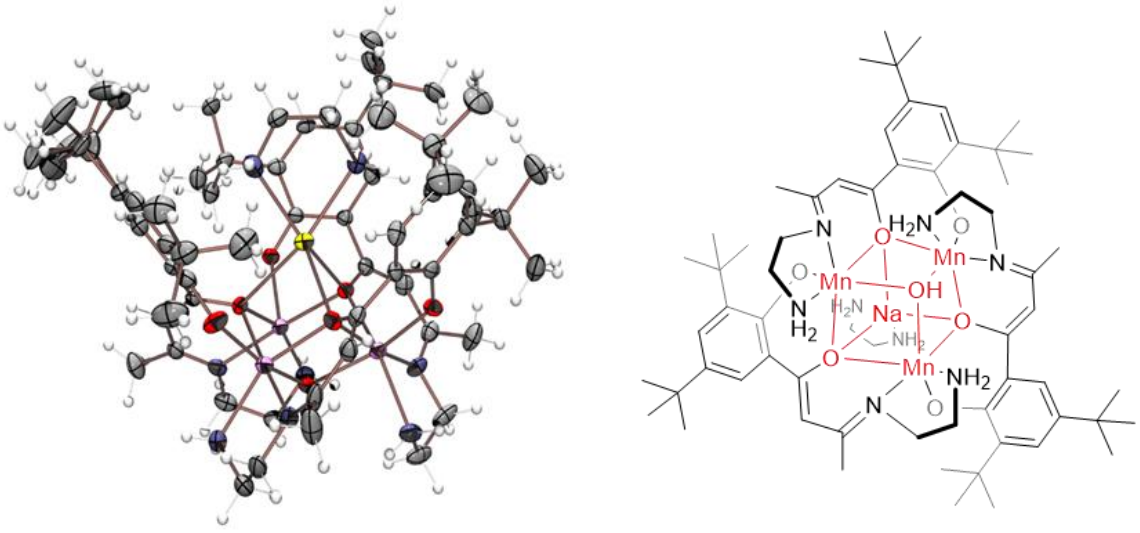

Figure 5-5. ORTEP diagram of [(en)NaMn$_3$O$_4$(L$_3$)(OH)] (**12**) (left) with thermal ellipsoids at 50% probability level and schematic drawing of [(en)NaMn$_3$O$_4$(L$_3$)(OH)] (**12**) (right).

environment. Each cluster incorporates either a hydroxide or a methoxide diagonally opposite the sodium ion and above a triangular arrangement of three manganese ions. The sodium atom is ligated by either ethylenediamine or pyridine, allowing modification of its Lewis acidity. The chelated enolate oxygens rather than oxos limit the number of exchangeable sites inside the cubane core versus a self-assembled cubane, limiting the number of variables and allowing more specific analysis of the role the exogenous ligands play.

5.3.4. Structural comparisons of three distinct cubane complexes

The differing electron density of the three cubane cores caused by varying the exogenous ligand and the sodium atom's Lewis acidity causes more structural variation than might be expected. The ethylenediamine bound cubanes **12** and **13** are open at the corner containing the exogenous hydroxide or methoxide ligands, with Mn(1)•••O(7) separations (2.255(2) Å for **12**, 2.2515(19) Å for **13**) and Mn(2)•••O(7) (2.2450(19) Å for **13**), longer than the sum of their covalent radii (2.20 Å) (**Table 5-3**).[51] These differences are also significantly longer than all reported five or six coordinate Mn(II)–O alkoxide, phenoxide, or carboxylate bonds (approximately 2.115-2.18 Å).[52,53] In contrast, **14** is not open at any bond involving O(7), but is open between Mn(3)•••O(1) (2.235(3) Å) and Mn(2)•••O(5) (2.237(3) Å), with slightly shorter Mn•••Mn distances relative to **12** and **13**, reflecting its more compact structure. The distances between the oxygens support O(7) being protonated in **12** and **14**, as the overage distance between O(7) and other core oxygens O(7)•••O_{avg} is 2.77 Å in **12** and 2.75 Å in **14**, compared to the distances between other core oxygens and each other, O•••O_{avg} = 3.14 Å in **12** and 3.16 Å in **14**. The asymmetry in the cubane can be observed by the deviations from mean distances in the clusters, such as that for the Mn–O(7) distance in **14** (±0.003 Å) vs. **12** (± 0.04 Å), indicating the hydroxide is more symmetrically bound in **14** than in **12**. Additionally, the asymmetry observed in

the clusters is independent of the exogenous group, with the deviation from the mean distances for Mn-O(7) for **13** being approximately the same as in **12** (± 0.01 Å vs. ± 0.04 Å). In contrast, for pyridine-ligated **14**, the mean Mn•••Mn separation is slightly larger than in **12** or **13** (3.3440(2) Å in **14** vs. 3.410(6) Å in **12** and 3.43(5) Å in **13**); and the largest deviation from the mean is for the methoxide cluster **13** (± 0.05 Å).

Table 5-3. Comparison of selected bond lengths (Å), volumes, and deviations from key geometrical parameters for cubane clusters [(en)$NaMn_3O_4(L_3)(OH)$] (**12**), [(en)$NaMn_3O_4(L_3)(OMe)$] (**13**), and [(py)$NaMn_3O_4(L_3)(OH)$] (**14**).

	12	**13**	**14**
Mn(1)–O(7)	2.255(2)	2.2515(19)	2.210(3)
Mn(2)–O(7)	2.188(2)	2.2450(19)	2.206(3)
Mn(3)–O(7)	2.189(3)	2.219(2)	2.203(3)
Mn(1)–O(1)	2.150(2)	2.1544(18)	2.167(3)
Mn(2)–O(3)	2.177(2)	2.1306(18)	2.172(3)
Mn(3)–O(5)	2.178(2)	2.1512(19)	2.169(3)
Mn(1)–O(3)	2.190(2)	2.2048(19)	2.220(3)
Mn(2)–O(5)	2.223(2)	2.2191(19)	2.237(3)
Mn(3)–O(1)	2.211(2)	2.2250(19)	2.235(3)
$Mn•••Mn_{avg}$	3.410(6)	3.43(5)	3.440(2)
$O•••O(7)_{avg}$	2.77(2)	2.78(4)	2.75(1)
$Na•••O_{\sigma}$	0.034	0.005	0.012
$Mn•••O(7)_{\sigma}$	0.028	0.014	0.002
$\tau_{Mn(1)}$	0.29	0.24	0.056
$\tau_{Mn(2)}$	N/A	0.14	0.022
$\tau_{Mn(3)}$	N/A	N/A	N/A
$\sigma_{\theta(oct)2}$ Mn(1)	95.8	120.5	114.1
$\sigma_{\theta(oct)2}$ Mn(2)	125.4	157.8	119.3
$\sigma_{\theta(oct)2}$ Mn(3)	119.6	100.3	119.2
Volume ($Å^3$)	10.341	10.401	10.278

These distortions in the cubane structure can be further quantified by examining the volumes of the cores,[54] metrical parameters, octahedral angle variance,[55] and the τ value of the five coordinate

manganese ions (**Table 5-3**); all of which are influenced by the exogenous ligands coordinated to the sodium ion (ethylenediamine vs. pyridine) and the manganese ions (OH^- vs. MeO^-). The volume of the cluster trends from smallest to largest in the order **14**, **12**, **13** (10.278 $Å^3$, 10.341 $Å^3$, and 10.401 $Å^3$ respectively); decreasing with increasing Na^+ coordination number and with OH^- compared to MeO^-. When MeO^- (pK_a (MeOH) = 15.5) is replaced by the slightly more basic OH^- (pK_a (HOH) =15.7), electron density is drawn from the manganese ions, making them more Lewis acidic; Mn–O(7) bonds become slightly smaller ($Mn•••O(7)_{avg}$ = 2.24(2) for **13** and 2.21(4) for **12**), and the core volume shrinks by 0.060 $Å^3$. When bidentate ethylenediamine is replaced by monodentate pyridine, the coordination number of the sodium decreases from five to four, in turn decreasing electron density on the sodium ion and increasing its Lewis acidity. This shrinks the core volume further by 0.063 $Å^3$, and Na–O distances also become shorter ($Na•••O_{avg}$ = 2.45(5) in **12** and 2.40(2) in **14**). Without looking at individual bonds, the regularity or symmetry of the clusters can be quantified by the standard deviation of the Mn–OR and Na–O distances, which are smaller in **14** compared to **12** and **13** ($Na•••O_\sigma$ = 0.012, $Mn•••O(7)_\sigma$ = 0.002; $Na•••O_\sigma$ = 0.034, $Mn•••O(7)_\sigma$ = 0.028; and $Na•••O_\sigma$ = 0.005, $Mn•••O(7)_\sigma$ = 0.014 respectively), indicating that **14** is more compact, and that **13** is somewhat more symmetric than **12**. Further, upon exchanging the ethylenediamine for pyridine, the Na•••O(7) distance becomes notably shorter, going from 3.735(3) Å in **12** to 3.613(3) Å in **14**. In contrast, while this distance does change upon exchange of OH^- for MeO^-, it lengthens only slightly, from 3.735(3) Å in **12** to 3.755(2) Å in **13**. This indicates that the Lewis acidity of the sodium ion has a dramatic effect on the cubane core, much more than the identity of the exogenous ligand OH^- vs. MeO^-. As Ca^{2+} is more Lewis acidic than Na^+, demonstrated by the large difference in pK_a of their aquo complexes ($pK_a(Ca\text{-}OH_2)$ = 12.60

vs. $pK_a(Na\text{-}OH_2)$ = 14.77, a qualitative measure of Lewis acidity),[56] it can be expected that exchange of the sodium ion for a calcium ion would affect the cubane core even more.

Table 5-4. Comparison of Selected Bond Distances (Å) for cluster **12** and the 1.9 Å structure of the OEC.

Bond (Å)	**6**	**OEC**
Na/Ca-Mn(1)	3.3203(15)	3.5
Na/Ca-Mn(2)	3.4469(14)	3.3
Na/Ca-Mn(3)	3.3421(14)	3.4
Mn(1)-Mn(2)	3.4162(7)	2.8
Mn(2)-Mn(3)	3.4117(8)	2.9
Mn(1)-Mn(3)	3.4121(8)	3.3

Examining the manganese ions individually also demonstrates the heterogeneity between the clusters. The octahedral angle variance $\sigma_{\theta(oct)^2}$, where $\sigma_{\theta(oct)^2} = 0$ is an ideal octahedron and higher values correspond to a more distorted octahedron, can be used to compare the local environments of the manganese ions. These range from $\sigma_{\theta(oct)^2}$ = 95.8 – 125.4 for **12**, 110.3 – 157.8 for **13**, and 114.1 – 119.3 for **14**; indicating that while all manganese ions are in quite distorted environments, they are more similarly distorted and thus the cubane is more symmetric in **14** compared to **12** and **13**, evidenced by the smaller spread of angle variances. The τ values of

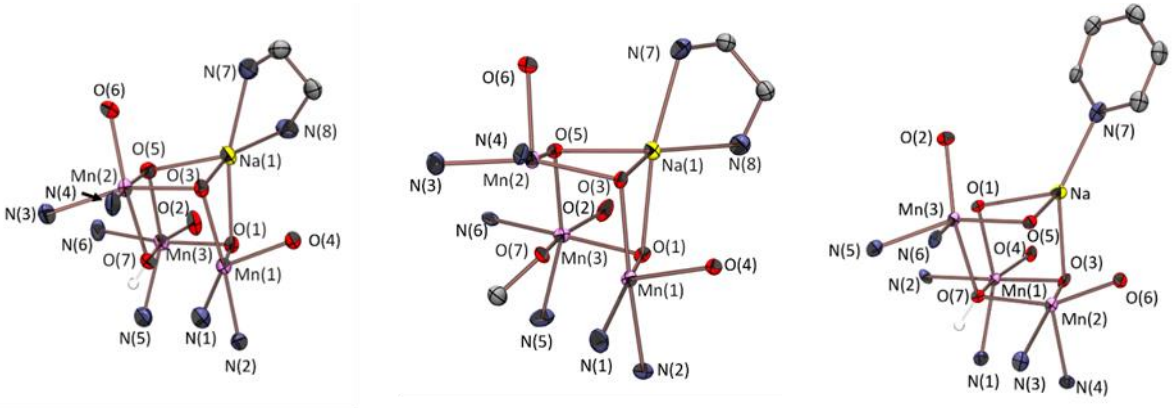

Figure 5-6. ORTEP diagrams of the cores of $[(en)NaMn_3O_4(L_3)(OH)]$ (**12**), $[(en)NaMn_3O_4(L_3)(OMe)]$ (**13**), and $[(py)NaMn_3O_4(L_3)(OH)]$ (**14**) with thermal ellipsoids at the 50% probability level.

the five-coordinate manganese ions reflect this as well, with **14**'s manganese atoms lying in a roughly square pyramidal geometry (τ(Mn(1) = 0.056, τ(Mn(2) = 0.022) compared to **12** and **13**'s more distorted ligand environments (τ(Mn(1) = 0.29 for **12**; τ(Mn(2) = 0.24 and τ(Mn(3) = 0.20 for **13**). These parameters demonstrate that the cubane core supported by this ligand environment is quite flexible, and further that it can be dramatically influenced by small changes in Lewis acidity of participant metal ions or the basicity of exogenous ligands which in turn affect metal ion Lewis acidity. It also suggests that the flexibility and the existence of "open" and "closed" forms of the OEC are not necessarily due to Jahn-Teller distortions, given that a d^5 Mn^{II} ion would not be expected to exhibit these effects.

While these clusters are not directly comparable to the OEC at any stage of the Kok cycle due to their comparatively lower oxidation state, measurements have been performed on the OEC to which they are comparable, namely the 1.9 Å structure collected by Umena et al.[57] Structures of the OEC collected via X-ray diffraction suffer from photoreduction of the manganese ions due to incident X-rays,[58] and in the case of the 1.9 Å structure, that according to a bond-valence sum analysis the manganese ions have oxidation states of +2.8, +2.7, +2.5, and +2.1 for Mn(1) – Mn(4) respectively, consistent with assignments of III-III-II-II oxidations states corresponding to a nonphysiological S_{-3} state of the Kok cycle.[59,60] In doing so, we can observe that the cation-manganese distances match quite closely, with all of them in both the 1.9 Å structure and the cubane core of **12** being approximately 3.4 Å (**Table 5-4**). The intermanganese distances differ, likely as a result of differing oxidation states or effects stemming from the dangling manganese, which is not included in these model clusters.

5.4. Summary and Conclusions

These clusters demonstrate that an "open" heterometallic $NaMn_3O_4$ cubane cluster core forms in a flexible ligand framework when the manganese ions are in lower oxidation states. We also conclude that the longer Mn•••O separations in the "open" OEC structure are not necessarily due to Jahn-Teller distortions, as our clusters incorporate only d^5 Mn(II) ions, which are not subject to Jahn-Teller distortions. Rather, the "open" nature of these clusters can be explained by effects stemming from the ligand environment of the cluster, especially the Lewis acidity of the sodium atom, which is governed by the basicity of the amine bound to it. This work also shows for the first time that an exchangeable protonated oxo (OH^-) can be incorporated into the cubane core, which can be replaced with an exogenous MeO^-. While they are not perfectly analogous to the OEC, these clusters demonstrate potential sources of structural inhomogeneity other than Jahn-Teller distortions, and that the redox-inactive ion in these cubanes and the OEC has a dramatic influence on the structure of the cluster, including the core volume and the overall symmetry of the cluster. Detailed analysis of the structural characteristics of these complexes was performed, and provides a window into the myriad ways the OEC may control its structural flexibility.

Further study of these clusters of these clusters should involve foremost attempts to replace the sodium cation with a more Lewis acidic calcium cation, which should further distort the five-coordinate manganese ions and make them more accessible to external substrates. While difficult to synthesize, the alternate method used to form **14** can be adapted and fine-tuned to exclude sodium atoms in favor of calcium atoms, allowing for the formation of a cluster that is even more similar to the OEC. Examination of the spin state and the Mn–Mn interactions has yet to be performed, and could be used to further examine the causes of the "open" and "closed" states of the OEC and how they influence the reactivity of the OEC along the Kok cycle. These clusters

may also be able to be chemically oxidized to states similar to those involved in the Kok cycle, and once oxidized and isolated, can be used to examine their reactivity with oxo-atom donors to investigate the nucleophilic attack method of O–O bond formation.

5.5. References

(1) Ibrahim, M.; Fransson, T.; Chatterjee, R.; Cheah, M. H.; Hussein, R.; Lassalle, L.; Sutherlin, K. D.; Young, I. D.; Fuller, F. D.; Gul, S.; Kim, I. S.; Simon, P. S.; de Lichtenberg, C.; Chernev, P.; Bogacz, I.; Pham, C. C.; Orville, A. M.; Saichek, N.; Northen, T.; Batyuk, A.; Carbajo, S.; Alonso-Mori, R.; Tono, K.; Owada, S.; Bhowmick, A.; Bolotovsky, R.; Mendez, D.; Moriarty, N. W.; Holton, J. M.; Dobbek, H.; Brewster, A. S.; Adams, P. D.; Sauter, N. K.; Bergmann, U.; Zouni, A.; Messinger, J.; Kern, J.; Yachandra, V. K.; Yano, J. Untangling the Sequence of Events during the S2 → S3 Transition in Photosystem II and Implications for the Water Oxidation Mechanism. *P. Natl. Acad. Sci. USA* **2020**, *117* (23), 12624–12635. DOI: 10.1073/pnas.2000529117

(2) Pantazis, D. A. Missing Pieces in the Puzzle of Biological Water Oxidation. *ACS Catal*. **2018**, *8* (10), 9477–9507. DOI: 10.1021/acscatal.8b01928

(3) Suga, M.; Akita, F.; Hirata, K.; Ueno, G.; Murakami, H.; Nakajima, Y.; Shimazu, T.; Yamashita, K.; Yamamoto, M.; Ago, H.; Shen, J. -R. Native Structure of Photosystem II at 1.95 A˚Resolution Viewed by Femtosecond X-Ray Pulses. *Nature* **2015**, *517*, 99-103. DOI: 10.1038/nature13991

(4) Young, I. D.; Ibrahim, M.; Chatterjee, R.; Gul, S.; Fuller, F. D.; Koroidov, S.; Brewster, A. S.; Tran, R.; Alonso-Mori, R.; Kroll, T.; Michels-Clark, T.; Laksmono, H.; Sierra, R. G.; Stan, C. A.; Hussein, R.; Zhang, M.; Douthit, L.; Kubin, M.; De Lichtenberg, C.; Vo Pham, L.; Nilsson, H.; Cheah, M. H.; Shevela, D.; Saracini, C.; Bean, M. A.; Seuffert, I.; Sokaras,

D.; Weng, T. C.; Pastor, E.; Weninger, C.; Fransson, T.; Lassalle, L.; Bräuer, P.; Aller, P.; Docker, P. T.; Andi, B.; Orville, A. M.; Glownia, J. M.; Nelson, S.; Sikorski, M.; Zhu, D.; Hunter, M. S.; Lane, T. J.; Aquila, A.; Koglin, J. E.; Robinson, J.; Liang, M.; Boutet, S.; Lyubimov, A. Y.; Uervirojnangkoorn, M.; Moriarty, N. W.; Liebschner, D.; Afonine, P. V.; Waterman, D. G.; Evans, G.; Wernet, P.; Dobbek, H.; Weis, W. I.; Brunger, A. T.; Zwart, P. H.; Adams, P. D.; Zouni, A.; Messinger, J.; Bergmann, U.; Sauter, N. K.; Kern, J.; Yachandra, V. K.; Yano, J. Structure of Photosystem II and Substrate Binding at Room Temperature. *Nature* **2016**, *540* (7633), 453–457. DOI: 10.1038/nature20161

(5) Yano, J.; Yachandra, V. Mn4Ca Cluster in Photosynthesis: Where and How Water Is Oxidized to Dioxygen. *Chem. Rev.* **2014**, *114* (8), 4175–4205. DOI: 10.1021/cr4004874

(6) Cox, N.; Retegan, M.; Neese, F.; Pantazis, D. A.; Boussac, A.; Lubitz, W. Electronic Structure of the Oxygen-Evolving Complex in Photosystem II Prior to O-O Bond Formation. *Science* **2014**, *345* (6198), 804–808. DOI: 10.1126/science.1254910

(7) Cox, N.; Pantazis, D. A.; Neese, F.; Lubitz, W. Biological Water Oxidation. *Acc. Chem. Res.* **2013**, *46* (7), 1588–1596. DOI: 10.1021/ar3003249

(8) Yachandra, V. K.; Yano, J. Calcium in the Oxygen-Evolving Complex: Structural and Mechanistic Role Determined by X-Ray Spectroscopy. *J. Photochem. Photobiol. B* **2011**, *104*, 51-59. DOI: 10.1016/j.photobiol.2011.02.019

(9) Cinco, R. M.; McFarlane Holman, K. L.: Robblee, J. H.; Yano, J.; Pizarro, S. A.; Bellacchio, E.; Sauer, K.; Yachandra, V. K. Calcium EXAFS Establishes the Mn-Ca Cluster in the Oxygen-Evolving Complex of Photosystem II. *Biochemistry* **2002**, *41*, 12928-12933. DOI: 10.1021/bi026569p

(10) Pantazis, D. A.; Ames, W.; Cox, N.; Lubitz, W.; Neese, F. Two Interconvertible Structures That Explain the Spectroscopic Properties of the Oxygen-Evolving Complex of Photosystem II in the S2 State. *Angew. Chem. Int. Ed.* **2012**, *51* (39), 9935–9940. DOI: 10.1002/anie.201204705

(11) Retegan, M.; Krewald, V.; Mamedov, F.; Neese, F.; Lubitz, W.; Cox, N.; Pantazis, D. A. A Five-Coordinate Mn(IV) Intermediate in Biological Water Oxidation: Spectroscopic Signature and a Pivot Mechanism for Water Binding. *Chem. Sci.* **2016**, *7* (1), 72–84. DOI: 10.1039/c5sc03124a

(12) Haddy, A.; Lakshmi, K. V.; Brudvig, G. W.; Frank, H. A. Q-Band EPR of the S2 State of Photosystem II Confirms an S = 5/2 Origin of the X-Band g = 4.1 Signal. *Biophys. J.* **2004**, *87* (4), 2885–2896. DOI: 10.1529/biophysj.104.040238

(13) Ames, W.; Pantazis, D. A.; Krewald, V.; Cox, N.; Messinger, J.; Lubitz, W.; Neese, F. Theoretical Evaluation of Structural Models of the S 2 State in the Oxygen Evolving Complex of Photosystem II: Protonation States and Magnetic Interactions. *J. Am. Chem. Soc.* **2011**, *133* (49), 19743–19757. DOI: 10.1021/ja2041805

(14) Siegbahn, P. E. M. O-O Bond Formation in the S4 State of the Oxygen-Evolving Complex in Photosystem II. *Chem.-Eur. J.* **2006**, *12* (36), 9217–9227. DOI: 10.1002/chem.200600774

(15) McEvoy, J. P.; Brudvig, G. W. Water-Splitting Chemistry of Photosystem II. *Chem. Rev.* **2006**, *106* (11), 4455–4483. DOI: 10.1021/CR0204294

(16) Betley, T. A.; Wu, Q.; Van Voorhis, T.; Nocera, D. G. Electronic Design Criteria for O-O Bond Formation via Metal-Oxo Complexes. *Inorg. Chem.* **2008**, *47* (6), 1849–1861. DOI: 10.1021/ic701972n

(17) Yocum, C. F. The Calcium and Chloride Requirements of the O2 Evolving Complex. *Coord. Chem. Rev*. **2008**, *252*, 296–305. DOI: 10.1016/j.ccr.2007.08.010

(18) Ghanotakis, D. F.; Babcock, G. T.; Yocum, C. F. Calcium Reconstitutes High Rates of Oxygen Evolution in Polypeptide Depleted Photosystem II Preparations. *FEBS Lett.* **1984**, *167* (1), 127–130. DOI: 10.1016/0014-5793(84)80846-7

(19) Siegbahn, P. E. M. Water Oxidation Mechanism in Photosystem II, Including Oxidations, Proton Release Pathways, O—O Bond Formation and O2 Release. *BBA - Bioenergetics* **2013**, *1827* (8–9), 1003–1019. DOI: 10.1016/J.BBABIO.2012.10.006

(20) Siegbahn, P. E. M. Structures and Energetics for O2 Formation in Photosystem II. *Acc. Chem. Res.* **2009**, *42* (12), 1871–1880. DOI: 10.1021/AR900117K

(21) Siegbahn, P. E. M. O-O Bond Formation in the S4 State of the Oxygen-Evolving Complex in Photosystem II. *Chem.-Eur. J.* **2006**, *12* (36), 9217–9227. DOI: 10.1002/CHEM.200600774

(22) Suga, M.; Akita, F.; Yamashita, K.; Nakajima, Y.; Ueno, G.; Li, H.; Yamane, T.; Hirata, K.; Umena, Y.; Yonekura, S.; Yu, L. J.; Murakami, H.; Nomura, T.; Kimura, T.; Kubo, M.; Baba, S.; Kumasaka, T.; Tono, K.; Yabashi, M.; Isobe, H.; Yamaguchi, K.; Yamamoto, M.; Ago, H.; Shen, J. R. An Oxyl/Oxo Mechanism for Oxygen-Oxygen Coupling in PSII Revealed by an x-Ray Free-Electron Laser. *Science* **2019**, *366* (6463), 334–338. DOI: 10.1126/SCIENCE.AAX6998

(23) Kern, J.; Chatterjee, R.; Young, I. D.; Fuller, F. D.; Lassalle, L.; Ibrahim, M.; Gul, S.; Fransson, T.; Brewster, A. S.; Alonso-Mori, R.; Hussein, R.; Zhang, M.; Douthit, L.; de Lichtenberg, C.; Cheah, M. H.; Shevela, D.; Wersig, J.; Seuffert, I.; Sokaras, D.; Pastor, E.; Weninger, C.; Kroll, T.; Sierra, R. G.; Aller, P.; Butryn, A.; Orville, A. M.; Liang, M.;

Batyuk, A.; Koglin, J. E.; Carbajo, S.; Boutet, S.; Moriarty, N. W.; Holton, J. M.; Dobbek, H.; Adams, P. D.; Bergmann, U.; Sauter, N. K.; Zouni, A.; Messinger, J.; Yano, J.; Yachandra, V. K. Structures of the Intermediates of Kok's Photosynthetic Water Oxidation Clock. *Nature* **2018**, *563* (7731), 421–425. DOI: 10.1038/s41586-018-0681-2

(24) Rapatskiy, L.; Cox, N.; Savitsky, A.; Ames, W. M.; Sander, J.; Nowaczyk, M. M.; Rögner, M.; Boussac, A.; Neese, F.; Messinger, J.; Lubitz, W. Detection of the Water-Binding Sites of the Oxygen-Evolving Complex of Photosystem II Using W-Band 17O Electron-Electron Double Resonance-Detected NMR Spectroscopy. *J. Am. Chem. Soc.* **2012**, *134* (40), 16619–16634. DOI: 10.1021/JA3053267

(25) Liu, F.; Concepcion, J. J.; Jurss, J. W.; Cardolaccia, T.; Templeton, J. L.; Meyer, T. J. Mechanisms of Water Oxidation from the Blue Dimer to Photosystem II. *Inorg. Chem.* **2008**, *47* (6), 1727–1752. DOI: 10.1021/IC701249S

(26) Wiechen, M.; Zaharieva, I.; Dau, H.; Kurz, P. Layered Manganese Oxides for Water-Oxidation: Alkaline Earth Cations Influence Catalytic Activity in a Photosystem II-like Fashion. *Chem. Sci.* **2012**, *3* (7), 2330–2339. DOI: 10.1039/C2SC20226C

(27) Wiechen, M.; Berends, H. M.; Kurz, P. Water Oxidation Catalysed by Manganese Compounds: From Complexes to 'Biomimetic Rocks.' *Dalton Trans.* **2011**, *41* (1), 21–31. DOI: 10.1039/C1DT11537E

(28) Lang, S. M.; Zimmermann, N.; Bernhardt, T. M.; Barnett, R. N.; Yoon, B.; Landman, U. Size, Stoichiometry, Dimensionality, and Ca Doping of Manganese Oxide-Based Water Oxidation Clusters: An Oxyl/Hydroxy Mechanism for Oxygen-Oxygen Coupling. *J. Chem. Phys. Lett.* **2021**, *12* (22), 5248–5255. DOI: 10.1021/ACS.JPCLETT.1C01299

(29) Zouni, A.; Witt, H. T.; Kern, J.; Fromme, P.; Krauss, N.; Saenger, W.; Orth, P. Crystal Structure of Photosystem II from Synechococcus Elongatus at 3.8 Å Resolution. *Nature* **2001**, *409* (6821), 739–743. DOI: 10.1038/35055589

(30) Guskov, A.; Kern, J.; Gabdulkhakov, A.; Broser, M.; Zouni, A.; Saenger, W. Cyanobacterial Photosystem II at 2.9-Å Resolution and the Role of Quinones, Lipids, Channels and Chloride. *Nat. Struct. Mol. Biol.* **2009**, *16* (3), 334–342. DOI: 10.1038/nsmb.1559

(31) Kärkäs, M. D.; Verho, O.; Johnston, E. V.; Åkermark, B. Artificial Photosynthesis: Molecular Systems for Catalytic Water Oxidation. *Chem. Rev.* **2014**, *114* (24), 11863–12001. DOI: 10.1021/CR400572F

(32) Ashford, D. L.; Gish, M. K.; Vannucci, A. K.; Brennaman, M. K.; Templeton, J. L.; Papanikolas, J. M.; Meyer, T. J. Molecular Chromophore-Catalyst Assemblies for Solar Fuel Applications. *Chem. Rev.* **2015**, *115* (23), 13006–13049. DOI: 10.1021/ACS.CHEMREV.5B00229

(33) Hunter, B. M.; Gray, H. B.; Müller, A. M. Earth-Abundant Heterogeneous Water Oxidation Catalysts. *Chem. Rev.* **2016**, *116* (22), 14120–14136. DOI: 10.1021/ACS.CHEMREV.6B00398

(34) Kanady, J. S.; Tsui, E. Y.; Day, M. W.; Agapie, T. A Synthetic Model of the Mn_3Ca Subsite of the Oxygen-Evolving Complex in Photosystem II. *Science* **2011**, *333*, 733-736. DOI: 10.1126/science.1206036

(35) Kanady, J. S.; Lin, P. H.; Carsch, K. M.; Nielsen, R. J.; Takase, M. K.; Goddard, W. A.; Agapie, T. Toward Models for the Full Oxygen-Evolving Complex of Photosystem II by Ligand Coordination to Lower the Symmetry of the Mn3CaO4 Cubane: Demonstration

That Electronic Effects Facilitate Binding of a Fifth Metal. *J. Am. Chem. Soc.* **2014**, *136* (41), 14373–14376. DOI: 10.1021/ja508160x

(36) Mukherjee, S.; Stull, J. A.; Yano, J.; Stamatatos, T. C.; Pringouri, K.; Stich, T. A.; Abboud, K. A.; Britt, R. D.; Yachandra, V. K.; Christou, G. Synthetic Model of the Asymmetric [Mn 3CaO 4] Cubane Core of the Oxygen-Evolving Complex of Photosystem II. *P. Natl. Acad. Sci. USA* **2012**, *109* (7), 2257–2262. DOI: 10.1073/PNAS.1115290109

(37) Zhang, C.; Chen, C.; Dong, H.; Shen, J. R.; Dau, H.; Zhao, J. A Synthetic Mn4Ca-Cluster Mimicking the Oxygen-Evolving Center of Photosynthesis. *Science* **2015**, *348* (6235), 690–693. DOI: 10.1126/science.aaa6550

(38) Bensari, A.; Zaveri, N. T. Titanium(IV) Chloride-Mediated Ortho-Acylation of Phenols and Naphthols. *Synthesis (Stuttg)* **2003**, No. 2, 0267–0271. DOI: 10.1055/s-2003-36822

(39) Bruker. APEX2 (Version 2.1-4), SAINT (Version 7.34A), SADABS (Version 2007/4). BrukerAXS Inc.: Madison, WI 2007.

(40) Sheldrick, G. M. SHELXL-97, Program for the Refinement of Crystal Structures. University of Göttingen: Göttingen, Germany 1997.

(41) Altomare, A.; Cascarano, G.; Giacovazzo, C.; Guagliardi, A.; Burla, M. C.; Polidori, G.; Camalli, M.; IUCr. SIR92 – a Program for Automatic Solution of Crystal Structures by Direct Methods. *J. Appl. Cryst.* **1994**, *27* (3), 435–435. DOI: 10.1107/S002188989400021X

(42) Altomare, A.; Burla, M. C.; Camalli, M.; Cascarano, G. L.; Giacovazzo, C.; Guagliardi, A.; Moliterni, A. G. G.; Polidori, G.; Spagna, R. SIR97: A New Tool for Crystal Structure Determination and Refinement. *J. Appl. Cryst.* **1999**, *32* (1), 115–119. DOI: 10.1107/S0021889898007717

(43) Sheldrick, G. M.; IUCr. Crystal Structure Refinement with SHELXL. *Acta Cryst. C* **2015**, *71* (1), 3–8. DOI: 10.1107/S2053229614024218

(44) Waasmaier, D.; Kirfel, A. New Analytical Scattering-Factor Functions for Free Atoms and Ions. *Acta Cryst. A* **1995**, *51* (3), 416–431. DOI: 10.1107/S0108767394013292

(45) Persistence of Vision Raytracer. Persistence of Vision Pty. Ltd.: Williamstown, Victoria, Australia 2004.

(46) Burnett, M. N.; Johnson, C. K. ORTEP-III: Oak Ridge Thermal Ellipsoid Plot Program for Crystal Structure Illustrations. *Oak Ridge National Laboratory Report ORNL-6895* **1996**.

(47) Spek, A. L.; IUCr. Single-Crystal Structure Validation with the Program PLATON. *J. Appl. Cryst.* **2003**, *36* (1), 7–13. DOI: 10.1107/S0021889802022112

(48) Van Der Sluis, P.; Spek, A. L. BYPASS: An Effective Method for the Refinement of Crystal Structures Containing Disordered Solvent Regions. *Acta Cryst. A* **1990**, *46* (3), 194–201. DOI: 10.1107/S0108767389011189

(49) Spek, A. L. Structure Validation in Chemical Crystallography. *Acta Cryst. D* **2009**, *65* (2), 148–155. DOI: 10.1107/S090744490804362X

(50) Chantarojsiri, T.; Reath, A. H.; Yang, J. Y.; Hantarojsiri, T. C.; Reath, A. H.; Ang, J. Y. Y. Cationic Charges Leading to an Inverse Free-Energy Relationship for N−N Bond Formation by MnVI Nitrides. *Angew. Chem. Int. Ed.* **2018**, *57* (43), 14037–14042. DOI: 10.1002/ANIE.201805832

(51) Shannon, R. D.; Prewitt, C. T.; IUCr. Effective Ionic Radii in Oxides and Fluorides. *Acta Cryst. B* **1969**, *25* (5), 925–946. DOI: 10.1107/S0567740869003220

(52) Mukhopadhyay, S.; Gandhi, B. A.; Kirk, M. L.; Armstrong, W. H. A New Class of Oxo-Bridged High-Valent Hexamanganese Clusters Supported by Sterically Hindered Carboxylate Ligands. *Inorg. Chem.* **2003**, *42* (25), 8171–8180. DOI: 10.1021/IC034641H

(53) Gelasco, A.; Kirk, M. L.; Kampf, J. W.; Pecoraro, V. L. The [Mn2(2-OHsalpn)2]2-,-,0,+ System: Synthesis, Structure, Spectroscopy, and Magnetism of the First Structurally Characterized Dinuclear Manganese Series Containing Four Distinct Oxidation States. *Inorg. Chem.* **1997**, *36* (9), 1829–1837. DOI: 10.1021/IC970140I

(54) Carney, M. J.; Kovacs, J. A.; Zhang, Y. P.; Papaefthymiou, G. C.; Spartalian, K.; Frankel, R. B.; Holm, R. H. Comparative Electronic Properties of Vanadium-Iron-Sulfur and Molybdenum-Iron-Sulfur Clusters Containing Isoelectronic Cubane-Type [VFe3S4]2+and [MoFe3S4l3+Cores. *Inorg. Chem.* **1987**, *26* (5), 719–724. DOI: 10.1021/ic00252a016

(55) Robinson, K.; Gibbs, G. V.; Ribbe, P. H. Quadratic Elongation: A Quantitative Measure of Distortion in Coordination Polyhedra. *Science (1979)* **1971**, *172* (3983), 567–570. https://doi.org/10.1126/science.172.3983.567.

(56) Reath, A. H.; Ziller, J. W.; Tsay, C.; Ryan, A. J.; Yang, J. Y. Redox Potential and Electronic Structure Effects of Proximal Nonredox Active Cations in Cobalt Schiff Base Complexes. *Inorg. Chem.* **2017**, *56* (6), 3713–3718. DOI: 10.1021/acs.inorgchem.6b03098

(57) Umena, Y.; Kawakami, K.; Shen, J. R.; Kamiya, N. Crystal Structure of Oxygen-Evolving Photosystem II at a Resolution of 1.9Å. *Nature* **2011**, *473* (7345), 55–60. DOI: 10.1038/nature09913

(58) Yano, J.; Kern, J.; Irrgang, K. D.; Latimer, M. J.; Bergmann, U.; Glatzel, P.; Pushkar, Y.; Biesiadka, J.; Loll, B.; Sauer, K.; Messinger, J.; Zouni, A.; Yachandra, V. K. X-Ray Damage to the Mn4Ca Complex in Single Crystals of Photosystem II: A Case Study for

Metalloprotein Crystallography. *P. Natl. Acad. Sci. USA* **2005**, *102* (34), 12047–12052. DOI: 10.1073/pnas.0505207102

(59) Galstyan, A.; Robertazzi, A.; Knapp, E. W. Oxygen-Evolving Mn Cluster in Photosystem II: The Protonation Pattern and Oxidation State in the High-Resolution Crystal Structure. *J. Am. Chem. Soc.* **2012**, *134* (17), 7442–7449. DOI: 10.1021/ja300254n

(60) Grundmeier, A.; Dau, H. Structural Models of the Manganese Complex of Photosystem II and Mechanistic Implications. *BBA - Bioenergetics*. **2012**, *1817*, 88–105. DOI: 10.1016/j.bbabio.2011.07.004

VITA

Dylan Meamber Rogers completed his Bachelor of Arts in Chemistry and Mathematics and Master of Science in Organic Chemistry at Northwestern University in 2016. Under Prof. Danna Freedman, he contributed to research investigating how proximity of adjacent nuclear spins contributes to the lifetime of a qubit candidate. Under Prof. Julia Kovacs at the University of Washington, he studied how structural modifications altered the reactivity of thiolate-ligated biomimetic transition metal complexes.